Durham E-Theses

Understanding and Control of Calcium Carbonate Crystal Growth on Model Substrates in Dishwasher

HONG, YUEXIAN

How to cite:

Use policy

Yuexian Hong

Durham University

Supervisor: Prof. Jonathan W. Steed

A thesis submitted for the partial fulfillment of the requirements for the degree of

Doctor of Philosophy

Department of Chemistry

Durham University

2016

Table of Contents

Abstract

This thesis presents the understanding and control of calcium carbonate crystal growth on model substrates under dishwasher conditions.

The study was conducted to understand why calcium carbonate crystals grow on the surface of kitchenware under dishwasher conditions, especially the severe deposition observed on plastic samples. **Chapter 1** gives reviews on the current crystallization theories, with a particular focus on the current understanding of surface crystallization and mineral crystal growth control on the surface. **Chapter 2** and **Chapter 3** present the underlying reasons that promote the mineral growth under dishwasher conditions. **Chapter 2** focuses on assessing how the different ingredients in the prototype dishwasher formula affect the 'shine' on the surface. **Chapter 3** further explores the reason of shine loss by looking into the system parameters (pH, temperature and phosphate ions). Poly (methyl methacrylate) slide and soda-lime glass slides are used as two main model substrates. It is observed that the dishwasher conditions (high pH, high temperature, high Ca concentration), in any way, promotes the formation of calcium carbonate growth. The polymer, one of the ingredients in the prototype dishwasher formulation, encourages this process, especially for plastic samples.

Chemical inhibition methods are still the most efficient way of limiting mineral formation on the surface. **Chapter 4** examines the X-ray crystal structures of a range of newly synthesized calcium compounds with oligocarboxylate candidate inhibitors so as to understand the exact structure and calcium binding mode of each potential inhibitor. **Chapter 5** presents the screening results of inhibition performance for thirty-nine different phosphate-free inhibitors, in order to find an alternative phosphorus-free inhibitor to the currently used phosphate-containing inhibitor 1-hydroxyethane 1,1-diphosphoric acid (HEDP). Two phosphate-free, cyclic poly(carboxylic acids) inhibitors were found to be effective replacements.

Chapter 6 summarizes the main findings and conclusions towards the $CaCO_3$ crystallization under dishwasher conditions and the structural characteristics of an efficient $CaCO_3$ inhibitor. It was concluded that an effective inhibitor should achieve a critical charge density. While the exact structure requirements of an efficient inhibitor for $CaCO_3$ is still unknown, factors such as balanced flexibility and rigidity in the backbone are desirable.

Declaration & Statement of Copyright

The copyright of this thesis rests with the author. No quotation from it should be published without her proper consent and information derived from it should be acknowledged in the form of a reference.

Acknowledgements

Without their support and help, my thesis writing, especially English writing, cannot finish in a good quality.

Abbreviations

a	Activity
a, b, c	Lattice parameter in crystal
Å	Angstrom
ACC	Amorphous calcium carbonate
ADW	Automatic dishwasher
AFM	Atomic force microscopy
AFP	antifreeze proteins
ATR-IR	Attenuated total reflectance infrared spectroscopy
Acusol 588G	Sulfonated polyacrylates Acusol 588
BCA	Benzenecarboxylic acids
BHCA	Benzene hexacarboxylic acid
BPA	Benzenepentacarboxylic Acid
BTCA	Benzene-1,3,5-tricarboxylic acid
BTTCA	1,2,4,5-Benzenetetracarboxylic acid
c	Concentration
cm	Centimeter
$CaCl_2$	Calcium chloride
CCD	Charge-coupled device
CIF	Crystallographic information file
CHDAA	1,1-Cyclohexanediacetic acid
CHDA	cis-1,2-cyclohexanedicarboxylic acid
CHHCA	1,2,3,4,5,6-Cyclohexanehexacarboxylic acid monohydrate
CHTTCA	Cyclohexane-1,2,4,5-tetracarboxylic acid

COSY	Correlation spectroscopy
CPTCA	cis,cis,cis,cis-1,2,3,4-Cyclopentanetetracarboxylic acid
CPCA	Cyclic polycarboxylic acids
CSD	Crystal structure database
CHTCA-135	1α,3α,5α-Cyclohexanetricarboxylic acid
CHTCA-124	(1a,2a,3a)-1,3,5,-Cyclohexanetricarboxylic acid
1D	One-dimensional
2D	Two-dimensional
3D	Three-dimensional
DHDAD	1.3-Dihydroxyacetone dimer
DHHPA	2-Dihydroxyphosphonyl-2-hydroxypropionic
DI water	Deionized water
DPA	Dipicolinic acid
EDX	Energy-dispersive X-ray spectroscopy
EF	Electric field
ENTMP	Ethylenediaminetetramethylene phosphonic acid
F	Flat faces
FA	Fulvic acid
FDA	2.5-Furandicarboxylic acid
FTIR	Fourier transform infrared spectroscopy
ΔG	Free energy/ overall Gibbs free energy of the system
$\Delta_r G^{\phi}$	Standard molar Gibbs free energy of reaction
$\Delta_f G^{\phi}$	Standard Gibbs free energy of formation at 25 °C
$\Delta_r H$	Standard change of reaction in enthalpy at 25 °C

$\varDelta G_V$	Free energy of cluster volume
$\varDelta G_S$	Free energy of the surface
$\varDelta G^*$	Activation energy
GOF	Goodness of fit
GTDH	Glyoxal trimeric dihydrate
GLTA	D-(+)-Galacturonic acid
HEDP	1-Hydroxy ethylidene-1,1-diphosphonic acid
heter	Heterogeneous
Hexa.	Hexagonal
homo	Homogeneous
HMBC	Heteronuclear multiple-bond correlation spectroscopy
HSQC	Heteronuclear single-quantum correlation spectroscopy
IAP	Ionic activity product
ICSD	Inorganic crystal structure database
IR	Infrared spectroscopy
J	Nucleation rate
K	Kinked faces
K_{aff}	Affinity constant
K_B	Boltzmann constant
Ks_p	Solubility product
kV	Kilovolts
L-L/LL	Liquid to liquid diffusion
m	Medium / lattice mismatch
mA	Milliampere

mM	Millimole
min(s)	Minute(s)
M^+	Activity of the cation in solution
MA	Mellitic acid
MCC	Monohydrated calcium carbonate
MD	Mellitic acid
MF	Magnetic field
Mg^{2+}	Magnesium
MGDA	Methylglycinediacetic acid
MS	Mass spectrometer
Mono.	Monoclinic
nm	Nanometer
Na_2CO_3	Sodium carbonate
nil-P	Nil-phosphate
NMR	Nuclear magnetic resonance
NOESY	nuclear Overhauser effect spectroscopy (
NTMP	Nitrilotrimethylene phosphonic acid
Ortho.	Orthorhombic
Ortho-P.	Orthophosphate
PA	Phytic acid dipotassium salt
PBTCA	2-Phosphonobutane-1,2,4 tricarboxylic acid
PDA-12	1,2-Phenylenediacetic acid
PDA-13	1,3-Phenylenediacetic acid
PDF	Powder diffraction file

PE	Polyethylene
PGA	Polyglutamic acid
P & G	Procter & Gamble
PMA	Pyromellitic acid
PMMA	Polymethylmethacrylate
PO_4^{3-}	Phosphate
PS	Polystyrene
PVS	Polyvinyl sulfonate
PXRD	Powder X-ray diffraction
PZDA	2,3-Pyrazinedicarboxylic acid
QA	Quinic acid
Q	Number of ions in solution
QCM	Quartz crystal microbalance
R	Gas constant
r	Nucleus size
$r*$	Critical size of nucleus
R_i	Growth rates in the presence of inhibitor
R_o	Growth rates in the absence of inhibitor
R_{wp}	Weighted profile R-factor
R_p	Expected R-factor
R_{brag}	Bragg R-factor
RT	Room temperature
S	Solubility / Stepped faces
s	Strong

S_A	Absolute supersaturation
SA	Salicylic acid
Saturation pH	pH_s
SEM	Scanning electron microscopy
SFG	Sum frequency generation
SI	Saturation index
S_R	Relative supersaturation
STPP	Sodium tripolyphosphate
$S.S.$	Supersaturation
SE	Slow evaporation
T	Temperature
T_{max}	Maximum temperature in the main dishwasher cycle
T_r	Kinetic roughening
TA	Tannic acid
TEM	Transmission electron microscopy
TGA	Thermogravimetric analysis
THFTCA	Tetrahydrofurantetracarboxylic acid
TMCPDA	(1R,3S)-1,2,2-Trimethylcyclopentane-1,3-dicarboxylic acid
TTCDTCA	1,4,7,10-Tetraazacyclododecane-1,4,7,10-tetraacetic Acid
TPCHTCA	cis,cis,cis-1,3,5-Tripropyl-1,3,5-cyclohexanetricarboxylic acid
V	Volume occupied by cluster
v	Number of ions in 1 mole of electrolyte
w	Weak / Water

WAXS	Wide angle X-ray scattering
XRD	X-ray diffraction
α , β , γ	Angle parameters in crystal lattice
z	Charges
λ	Kinetic coefficient / Wavenumber
μ	Chemical potential
μm	Micrometer
σ	Interfacial energy
Ω	Pre-exponential factor

1   Introduction and Literature Review

1.1   General Considerations about CaCO$_3$ Growth in Dishwashers

It is an unsolved problem that solid, inorganic minerals can form and deposit on the surface of kitchenware during washing, rinsing or drying in dishwashers (Figure 1.1). In a dishwasher, crystals of these inorganic minerals can be formed in three different ways via different mechanisms. Initially, during the first cycle, there is no crystalline material in the system. Crystallization on a surface needs nuclei for subsequent growth. The formation of nuclei is via heterogeneous nucleation. Crystals can then be formed directly on the surface with little contribution from the adhesion of particles in solution.[1] In the second and subsequent cycles, crystals grow on the prescaled deposits, which act as nuclei for the new crystallization cycle. Crystallization, in this case, occurs on the existing layer of crystalline material and may follow secondary nucleation or epitaxy, where the growth mode is orientated by the existing crystals.[2]
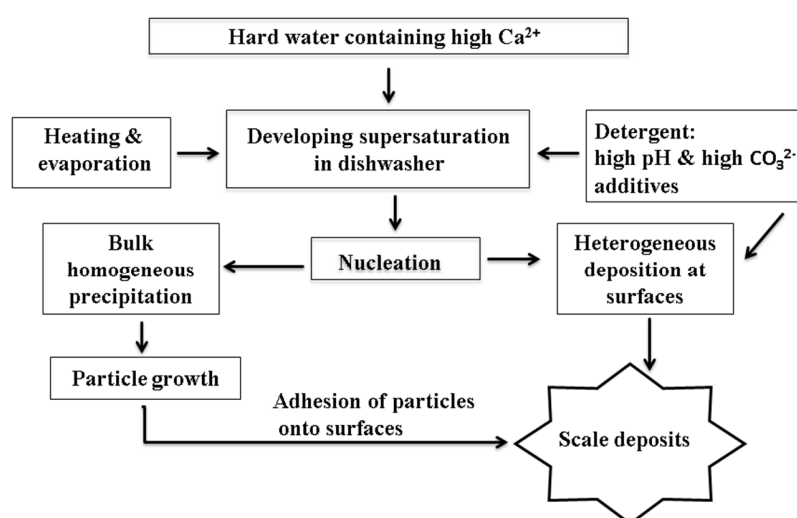
Figure 1.1 The possible deposition pathways of CaCO$_3$ inside a dishwasher.

FTIR and X-ray diffraction have identified the deposits on the surface as calcium carbonate.[3] Conditions inside dishwashers such as water hardness, high temperature, high pH and high ionic strength all contribute to the crystallization of calcium carbonate. Strategies are needed to prevent surface deposition of minerals so a surface with a visually clean outcome can be achieved.

Proposed ideas for solutions to this problem can be classified into two parts: (a) using tailored $CaCO_3$ inhibitors to prevent surface crystallization or (b) installing an ion exchange resin to soften the water before it enters the machine. In this project, we will focus on the chemical ways of controlling $CaCO_3$ deposition. Due to increasing government regulation aimed towards discontinuation of the use of phosphate-containing additives, a non-phosphate containing $CaCO_3$ inhibitor will be developed to replace the phosphate-containing inhibitor currently used in Western Europe, which is 1-hydroxy ethylidene-1,1-diphosphonic acid (HEDP).

In this chapter, the crystallization mechanism for bulk precipitation and surface deposition will be reviewed by introducing the most important factors involved in the development of crystals, both with and without additives. The emphasis will be placed on the surface deposition and inhibition.

1.2 Classical Crystallization Theories

According to Mullin's definition, crystallization is a complex process including processes of nucleation, crystal growth, and Ostwald ripening.[2] Nucleation, as the most critical step, can result in the formation of nuclei in a supersaturated solution, which undergoes further crystal growth. Nucleation, crystal growth and Oswald ripening together determine the final properties of the crystals.[4]

For crystallization to occur, two conditions are needed: supersaturation and the existence of an induction center.[4-5] Supersaturation is essential for both the formation of crystal nuclei and its subsequent growth, but it alone is not sufficient for the occurrence of crystallization. An induction center in the form of a substrate, embryo, seed, nuclei or any external stimulus is also needed to induce the occurrence of crystallization.

1.2.1 Supersaturation

At a given temperature, the solubility of a substance in water is expressed as the number of moles of the pure substance in a solution divided by one liter of the solvent at equilibrium.[6] Based on different solubility properties, salts in water can generally be split into two groups. A normal soluble salt is one whose solubility increases when the temperature rises, such as NaCl and

$NaNO_3$. In contrast, inverse salts, like $CaSO_4$, $Ca_3(PO_4)_2$ and $CaCO_3$ decrease in solubility as the temperature goes up.

Crystallization from solution is also a process of crystal precipitation and dissolution. At a given temperature, the conditions under which a solution is in equilibrium with its soluble solid phase is called the saturation point.[2] If a solute concentration exceeds its saturation concentration without precipitating out, the solution is in a supersaturated state. For precipitation to occur, an ionic salt needs to exceed the equilibrium saturation concentration to achieve a supersaturated state, which acts as a driving force to push the crystal to precipitate out upon the induction centers. In this case, the equilibrium shown below will move towards the left-hand side.[6]

$$M_nX_m \rightleftharpoons nM^{Z+} + mX^{Z-}$$

where, n and m are the charges of the anion and cation, z^+, z^-, are the valences form M and X, respectively, $[M^{z+}]$ and $[X^{z-}]$ are the activity of the ions in solution, expressed as mol L^{-1}. (The calculation is attached in Appendix 1). The activity of a solid is defined as equal to 1, the ionic activity product (K_{IP}) of solution is calculated as follows:

$$K_{IP} = \gamma_{\pm}^{m+n}[M^{z+}]^n[X^{z-}]^m \qquad \text{Equation 1.1}$$

where $\gamma_{\pm}$ is the mean activity coefficient. The solubility product (K_{sp}) is introduced to represent the saturation point. At the saturation point, K_{sp} is equal to the ionic activity product (K_{IP}) provided $\gamma_{\pm} = 1$. The values of K_{sp} are often recorded and expressed as pK_{sp} for convenience. The relative supersaturation (S_R) is often used to express the saturated state of a solution as given in Equation 1.2

$$S_R = K_{IP}/K_{sp} \qquad \text{Equation 1.2}$$

More commonly, the saturation index (SI) is used to determine the saturation state of solution with respect to K_{sp} of the given mineral:

$$SI = Log_{10}(K_{IP}/K_{sp}) \qquad \text{Equation 1.3}$$

When the saturation index (SI) is equal to 0, the value of K_{sp} is equal to that of the ionic activity product (K_{IP}) and the solution is at the saturation point. When the $SI < 0$, which means the value

of K_{sp} is larger than that of the K_{IP}, the solution is undersaturated and, precipitation will not occur. When SI > 0, precipitation is possible (for details refer to Section 1.2.2). If precipitation does happen, it will continue until the value of K_{sp} becomes equal to or greater than that of K_{IP}.[6]

The value of K_{IP} is calculated based on the activity of the solute in solution, K_{sp} is constant for a given temperature and can be calculated as shown in according to Equation 1.4 and Equation 1.6.[2, 7] The value of K_{sp} at the standard temperature (25 $^\circ$C) can be calculated by the standard molar Gibbs free energy of reaction ($\Delta_r G^\emptyset$):

$$-RTln\left(K_{sp}\right) = \Delta_r G^\emptyset \qquad\qquad \text{Equation 1.4}$$

where, T is the temperature of the solution (K), R is the gas constant, equal to 8.314 J mol^{-1} K^{-1}. The standard molar Gibbs free energy of reaction ($\Delta_r G^\emptyset$) can be obtained from the values of standard Gibbs free energy of formation ($\Delta_f G^\emptyset$) at 25°C of the pure compounds from the literature.[8]

$$\Delta_r G^\emptyset = (\Delta_f G^\emptyset)_{\,products} - (\Delta_f G^\emptyset)_{\,reactants} \qquad\qquad \text{Equation 1.5}$$

where, $(\Delta_f G^\emptyset)_{\,products}$ and $(\Delta_f G^\emptyset)_{\,reactants}$ are the free energies of formation of the products and the reactants, respectively in units of J mol^{-1}.

At a specific temperature, Equation 1.6 is used obtain the value of $\Delta_r G^\emptyset$ and hence the value of K_{sp}.[7]

$$-RTln\left(K_{sp}\right) = \Delta_r G^\emptyset = \frac{T}{298.15}\Delta_r G^{298} + \left(1 - \frac{T}{298.15}\right)\Delta_r H^{298} \qquad \text{Equation 1.6}$$

where $\Delta_r G^{298}$ and $\Delta_r H^{298}$ are the standard change of reaction in Gibbs free energy and in enthalpy at 25 °C and can be obtained from the literature.[8] Thus the value of K_{sp} at other temperatures can be calculated. It is obvious that the value of K_{sp} is highly related to the change of temperature.

1.2.2 Nucleation

1.2.2.1 Classification of Nucleation

The relationships of various forms of nucleation are shown in Figure 1.2.[2] There are two types of nucleation: primary nucleation and secondary nucleation. The occurrence of crystallization that is assisted by existing crystals in solution is termed as secondary nucleation. When there is no crystalline material initially present in the system, the formation of nuclei is referred to as primary nucleation. Primary nucleation can be further divided into homogeneous and heterogeneous nucleation. Homogeneous nucleation refers to nucleation of a species of the same component phase, which occurs spontaneously. Heterogeneous nucleation refers to the nucleation of a species upon an external stimulus, which can be a substrate, impurity or irregularity.[2, 9] As seen from Figure 1.3, it is easier for heterogeneous nucleation to occur since homogeneous nucleation needs to overcome a higher activation energy for the formation of critical nuclei. This will be explained in the following section.
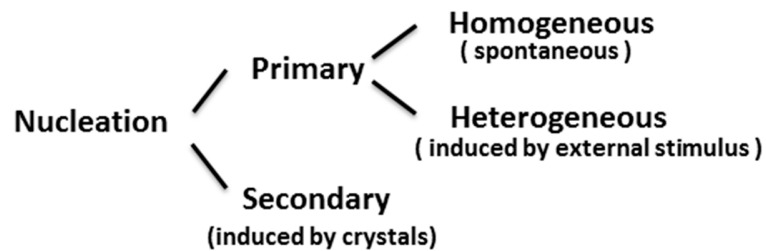
Figure 1.2 The relationships between the various forms of nucleation.[2]
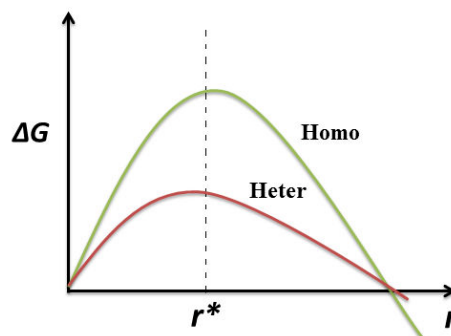
Figure 1.3 Comparison of the energy barrier for heterogeneous and homogeneous nucleation.[10]

1.2.2.2   Homogeneous Nucleation

It is hard to find a system free of any impurities, so heterogeneous nucleation is a more common process even though the process of homogeneous nucleation is simpler. The understanding of the process of homogeneous nucleation is based on classical nucleation theory. Hence it is important to understand the calculation of activation energy (ΔG_N) for the formation of crystal nucleus because it indicates what factors need to be taken into consideration for the occurrence of crystallization.[2]

In the supersaturated solution, the system is not stable. The formation of molecular clusters is spontaneous, but they are also falling apart at a rate that hinders the development of a new solid phase. Any formation of a new stable phase requires the creation of the new interface, which needs an amount of work. Therefore, the free energy needed to form a nucleus in solution (ΔG_N) can be expressed by the difference between bulk energy released to form the clusters in bulk solution (ΔG_B) and the free energy required for the creation of interface between the cluster and bulk solution (ΔG_I).[2]

$$\Delta G_N = \Delta G_B + \Delta G_I \qquad\qquad \text{Equation 1.7}$$

Figure 1.3 shows the variation of bulk free energy (ΔG_B) and interfacial free energy (ΔG_I) against the nucleus size (r). In a classical picture, the nucleus is assumed to have a spherical shape. For the creation of a new interface, work needs to be done to bring the molecules from the bulk interior to the surface. The interfacial energy is always positive and is a function of surface area, while the bulk energy is a function of volume of the clusters. The bulk energy is the energe released to form clusters in bulk solution, therefore, it is a negative value. The interfacial energy therefore increases proportionally to r^2 whereas the bulk free energy decreases with r^3, hence the bulk free energy term always dominates at a large r.[2]

$$\Delta G_I = 4\pi r^2 \sigma \qquad\qquad \text{Equation 1.8}$$

$$\Delta G_B = \frac{4}{3}\pi r^3 \Delta G_V \qquad\qquad \text{Equation 1.9}$$

$$\Delta G_N = 4\pi r^2 \sigma + \frac{4}{3}\pi r^3 \Delta G_V \qquad\qquad \text{Equation 1.10}$$

where r is the size of the cluster and σ is surface tension or interfacial tension ("surface tension" being used when one of the phases at the interface is a gas), which is equivalent to the free energy needed per unit surface area, with a unit of N m^{-1}. ΔG_V is the free energy change upon forming the bulk condensed phase per unit volume.[2]
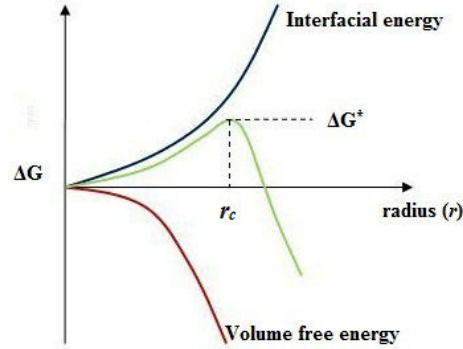
Figure 1.4 Variation of volume free energy (ΔG_B) and interfacial energy (ΔG_I) against the size of the cluster.[11]

The excess free energy of ΔG_N for the formation of a stable nucleus is a combination of ΔG_B and ΔG_I.[2] Figure 1.4 shows the curve that tells the variation of free energy of nucleus formation against the radius of the cluster. At a critical size (r^*), it passes through a maximum point of free energy (ΔG_N^*), which corresponds to the activation energy of the homogeneous nucleation. The free energy at this point can be obtained by maximizing Equation 1.10 by setting $d\Delta G_N/dr = 0$

$$\frac{d\Delta G_N}{dr} = 8\pi r\sigma + 4\pi r^2 \Delta G_V = 0$$

The critical size of the nucleus and the activation energy are expressed as

$$r_c = -2\sigma/\Delta G_V \qquad\qquad \text{Equation 1.11}$$

$$\Delta G_N^* = \frac{4}{3}\pi r_c^2 \sigma \qquad\qquad \text{Equation 1.12}$$

According to the *Gibbs-Thomson* equation of non-electrolyte solution,

$$lnS_R = 2V_m\sigma/KTr \qquad\qquad \text{Equation 1.13}$$

V_m is the molecular volume ($V_m = M/\rho$, where M is the molecular weight and ρ is the density), S_R refers to the relative supersaturation (see Equation1.2); K_B is the Boltzmann constant (K_B =1.380×10^{-23} J mol^{-1}) and T is temperature (K). From Figure 1.12 and Equation 1.13, activation energy (ΔG_N^*) can also be expressed as follows:[2]

$$\Delta G_N^* = \frac{4}{3}\pi r_c^2 \sigma = \frac{4}{3}\pi\sigma * (2V_m\sigma/RT ln S_R)^2 = \frac{16}{3}\pi\sigma^3 V_m^2/(K_B T ln S_R)^2 \qquad \text{Equation1.14}$$

The nucleation rate of the homogeneous nucleation is defined as the number of nuclei formed in a unit volume per second. The general expression of growth rate for homogeneous nucleation is given by

$$J_{hom} = \Omega_{hom} * exp(-\Delta G_{hom}^*/K_B T) \qquad \text{Equation 1.15}$$

where, Ω_{hom} is the pre-exponential factor, which is not very dependent upon the supersaturation compared to the exponential factor and so can often be regarded as a constant. Typical values of Ω_{hom} range from ~10^{25} -10^{35} cm^{-3} s^{-1}. ΔG_{hom}^* is the activation energy needed for the formation of a stable critical nucleus.[9]

In classical nucleation theory, the formation of a critical nucleus through homogeneous nucleation requires overcoming an activation barrier.[2] The nucleation rate is highly dependent on this activation barrier as can be seen from the calculation equations above: activation energy in Equation 1.14 and nucleation rate in Equation 1.15. Factors of great importance in determining nucleation processes are: the temperature (T), relative supersaturation (S_R) and the interfacial tension (σ).[2, 12] It is clear that for a constant supersaturation, the higher the temperature, the lower the value of the activation barrier and the higher nucleation rate, hence benefiting the formation of critical nuclei and further growth, though of course a higher temperature typically decreases the supersaturation as for most materials, solubility increases with temperature. An increase in supersaturation, i.e. S_R, typically induces a significantly higher rate of nucleation rate and crystal growth. In pure solution, the increase in S_R can produce a sudden increase in the nucleation rate as can be seen from the Figure 1.5, if the S_R exceeds S_R^*. However, it is also discussed by Mullin[2] that an over increase in S_R experimentally can lead to an increase in viscosity, restricting the movement of the molecules and inhibiting the formation of nuclei. However, this is not within the scope of S_R in this project and so this situation will not be discussed further. Interfacial

tension (σ), on the other hand, has marked effects on both activation energy (ΔG_N^*) and the nucleation rate (J_{hom}). The activation energy is proportional to the cube of the interfacial energy ($\Delta G_N^* \propto \sigma^3$). The interfacial energy is the amount of work needed to be done to overcome the cohesive forces in the bulk. The more work required to be done, the higher value of the activation energy, hence a lower rate of nucleation.
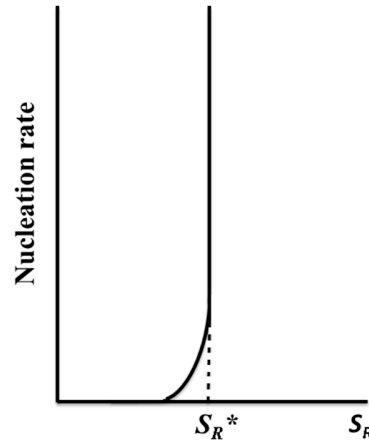
Figure 1.5 The nucleation rate (J_{hom}) plotted against the relative supersaturation.[13] (Reproduced with the permission of ref.13 Copyright @ Dr. Sharon Cooper).

1.2.2.3   Heterogeneous Nucleation

For homogeneous nucleation from solution, the crystal nuclei are formed within the bulk solution. Heterogeneous nucleation, on the other hand, occurs on a substrate surface and so involves three phases, which are the (typically) solid substrate (s), the crystalline phase (c) and the liquid phase (l). Figure 1.5 illustrates the interfacial tensions for three phases in contact. The relationship between the interfacial tensions can be expressed by resolving these forces in the horizontal direction.

$$\sigma_{sl} = cos\theta\sigma_{cl} + \sigma_{cs} \qquad \text{Equation 1.16}$$

or

$$cos\theta = \sigma_{sl} - \sigma_{cs}/\sigma_{cl} \qquad \text{Equation 1.17}$$

where, σ_{sl} is the interfacial tension between the solid substrate and the liquid phase; σ_{cs} is the interfacial tension between the crystalline phase and the solid substrate; σ_{cl} is the interfacial tension between the crystalline phase and the liquid phase.
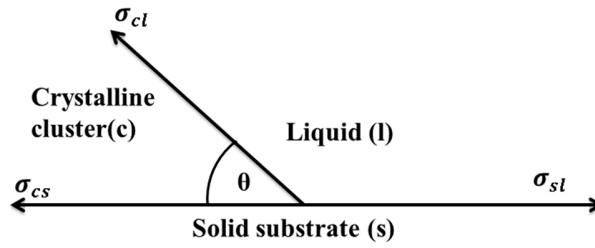
Figure 1.6 Illustration of the three interfacial tensions for heterogeneous nucleation.[2]

It is shown at the beginning of this section in Figure 1.3 that the activation barrier for heterogeneous nucleation is lower than that for homogeneous nucleation due to the presence of the substrates inducing the nucleation. The overall free energy change associated with formation of a critical nucleus on a solid substrate and that of the crystal in contact with solution can be expressed as in Equation 1.18

$$\Delta G^*_{\text{crit}} = \emptyset \Delta G_{\text{crit}} \qquad \text{Equation 1.18}$$

where the factor $\emptyset$ is highly dependent on the angle between the solid substrate and the crystalline phase and can be obtained from the value of $cos\theta$:

$$\emptyset = (2 + cos\theta)(1 - cos\theta)^2/4 \qquad \text{Equation 1.19}$$

In fact, $\emptyset$ represents the ratio of the heterogeneous critical nucleus volume to that of the homogeneous critical nucleus volume. This shows that the reduction in the nucleation barrier for heterogeneous nucleation compared to homogeneous nucleation arises from the small size of the critical nucleus for the heterogeneous case. When θ lies between 0 and 180°, $\emptyset < 1$, therefore,

$$\Delta G^*_{\text{crit}} < \Delta G_{\text{crit}}$$

In the case of partial contact, $0 < \theta < 180°$, the activation energy needed is less that that required for homogeneous nucleation. This is where heterogeneous nucleation occurs. The expression of the nucleation rate is similar to that of homogeneous nucleation but with different values of Ω_{het} and ΔG^*_{het}

$$J_{\text{het}} = \Omega_{\text{het}} * exp(-\Delta G^*_{\text{het}}/K_\text{B}T) \qquad \text{Equation 1.20}$$

where: ΔG^*_{het} is the activation energy required for the formation of critical nucleus for heterogeneous nucleation. The pre-exponential factor (Ω_{het}) is the range of 10^{17} - 10^{22} cm^{-2} s^{-1},

and is also typically not very dependent upon supersaturation. The value of ΔG^*_{het} depends upon the shape of the critical nucleus and the type of substrate. Compared to homogeneous nucleation, the activation barrier for heterogeneous nucleation is lower due to the interaction between the crystalline phase and substrate being stronger than that between the crystals and solvent. The strength of the interaction at the interface of the crystalline phase and substrate is not just decided by the crystalline material but also the properties of the substrate surfaces. The surface properties include the chemistries and the structure of the foreign surface as they affect the interfacial tension between the solid substrate and the crystalline phase. This will be further discussed in Section 1.3.6.[2, 12]

When $\theta = 180$ °, $cos\theta = $ -1 and $\emptyset = 1$, therefore, we have

$$\Delta G^*_{crit} = \Delta G_{crit} \qquad \text{Equation 1.21}$$

In this case, there is no contact between the crystalline phase and the solid substrate. The homogeneous nucleation occurs. When $\theta = 0$, $\emptyset = 1$, and $\Delta G^*_{crit} = 0$, this suggests there is no nucleation barrier, although in fact a small energy barrier still arises as the critical nucleus now has a monolayer disc shape, and so the edge tension between the crystal and surrounding solution needs to be considered. This case corresponds to secondary nucleation, where crystalline material is already present in the system, and also to crystal growth via 2D surface nucleation (see Section 1.2.3.3).[2, 12]

The equations for the calculation of the activation energy for both homogeneous nucleation and heterogeneous nucleation discussed above are based on the assumption that the nucleus shape is spherical. If the nucleus is, in fact, another shape, a shape coefficient needs to be included, but the overall conclusions on nucleation thermodynamics and kinetics will not change significantly. Classical nucleation theories have their limits, however, principally because of the assumption that the critical crystal nucleus can be viewed as having the same properties as the bulk crystalline phase cannot be true if the critical nucleus only contains 10's or 100's of molecules or ions. Further discussion of the limitations of classical nucleation theories is not within the research field of this project, but further information can be found in the references available.[2, 9] Non-classical crystallization theories provide an alternative, which may provide a more realistic

picture of the crystallization process, albeit that these theories are necessarily more complicated than the simple classical approaches.[2]

1.2.2.4   Ostwald Ripening and Agglomeration

Crystal growth increases the size of the nuclei. Larger particles are formed at the expense of smaller particles, which are less thermodynamically favored. This is called Ostwald ripening, a special kind of crystal growth.[4] When the nuclei grow into small particles, agglomeration can take place. Small particles can agglomerate together and form larger particles under conditions close to equilibrium. Agglomeration process can be affected by the supersaturation, hydrodynamics, surface changes and the interaction between the particles.[14]

1.2.3 Crystal Growth

1.2.3.1   Crystal Growth Theories

Once the nucleus becomes larger than the critical nucleus, crystal growth will come into play. There are three theories that have been proposed to explain the process of crystal growth: theories of surface energy, diffusion, and adsorption layer.[2]

Surface energy theory, also known as Gibbs-Wulff theory, assumes that a crystal will grow to its minimum surface energy for a given volume. Gibbs proposed that surface energy will determine the equilibrium morphology of a crystal. Wulff furthered this theory and proposed that equilibrium morphology is dominated by the slow growing faces. Faces with high surface energy will grow out and disappear in the resulting crystal morphology. This theory has been used to predict the growth morphology and equilibrium morphology of $CaCO_3$ by using atomistic simulation.[15] However, this approach suffers some limitations by not considering the influences of supersaturation and stirring, and by ignoring that crystal growth is a kinetic process and can occur under conditions that are not close to equilibrium.[16]

Diffusion theory considers crystallization as a continuous process, where deposition of the solid on the face of a growing crystal is essentially a diffusional process. The impacts of the concentration, diffusion rate, and crystal size are taken into consideration. The rate of crystal growth is controlled by the concentration difference between the solute at the growing solid surface and bulk solution.[16]

Adsorption layer theory takes crystallization as a discontinuous process.[16] When growth units arrive at the surface of the crystal, they are not immediately integrated into the lattice but migrate over the crystal face, forming a loosely adsorbed layer of solute ions or molecules at the interface. This adsorbed layer will contribute to the crystal growth by providing incorporation sites. In this theory, the growth mode on a smooth or rough surface has been studied. Growth mechanisms such as two dimensional nucleation, polynucleation, Kossel's model of a growing crystal surface and screw dislocation have been proposed.[2]

1.2.3.2   Classification of Crystal Faces

Crystal faces can be divided into two types: rough crystal faces and atomically smooth flat faces (defectless).[2, 9, 12] Faces with the lowest surface tension typically contain most densely packed arrays of strongly bonded atoms and will be atomically flat. Flat (F) faces are those that are parallel to at least two dense atomic rows. However, when the temperature goes above the roughening temperature, T_r, or the system suffers from a kinetic roughening (this will be explained in the 2D nucleation process in Section 1.2.3.3), F faces will become rough and follow the continual growth mechanism. Rough crystal faces include the stepped (S) face and kinked (K) face. S faces are those that are parallel to one dense atomic row and K faces are not parallel to any dense atomic rows. Figure 1.7 shows different types of crystal faces. Crystal faces that are parallel to a ⟨100⟩, b ⟨010⟩ and c ⟨001⟩ directions, are F faces. S faces are the terminations of separated flat faces represented as (110), (101) and (011) in Figure 1.7. K face (111) is the face which terminates individual rows in steps. Three different crystal sites are defined accordingly (refer to Figure 1.18, Figure 1.19 and Figure 1.20): terrace, steps, and kinks. The terraces or the flat surfaces are relatively smooth, and large areas exist between steps. Steps and kinks are two active sites for molecule or ion incorporation for surface controlled growth. Step sites are defined as the termination of one or more monolayers of the crystal lattice on the crystal surface and separate terraces. Kink sites are the termination of individual rows of lattice ions in steps. Kink sites have the highest favorable attachment energy for ion incorporation. Thus the more kink sites distributed in a crystal surface, the more active the face will be.[2, 9, 12]
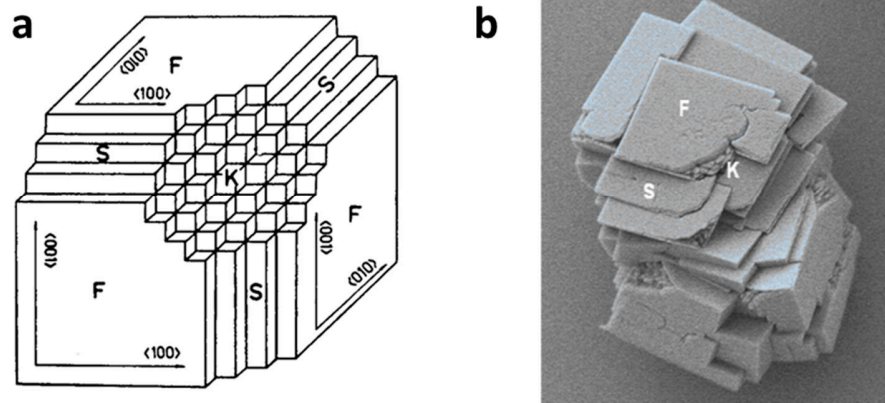
Figure 1.7 (a) Classification of crystal faces. *F* represents the flat faces contain *a* (100), *b* (010) and *c* (001). Faces (110), (101) and (011) are step faces, represented by *S*. Face (111) is kink face, labeled with *K*.[2] (b) SEM image of a calcite crystal illustrating F, S, and K surfaces.[1a] (Image a is reproduced with the permission of ref.14. Copyright @ Dr. Sharon Cooper; Inage b reprinted with the permission of ref.1a. Copyright @ Dr. Tommy Nylander).

1.2.3.3 Crystal Growth Mechanism

Crystal growth is a process involving the continuous transportation of growth units to the surface and subsequent incorporation into lattice sites.[2, 12, 17] How fast the nuclei grow depends on the rates at which the growth units attach and/or remove themselves from the nuclear surface. The rate-determining step for the growth can be the diffusion of the growth units through the reaction zone and solution to the surface of the crystal or the surface reaction, where the growth units are incorporated into the sites on the surfaces. Whether the crystal growth is diffusion controlled or adsorption controlled depends on the degree of supersaturation. Different supersaturation levels will lead to different changes on *F* faces and thus follow a different growth mode. A summary of growth mechanisms under different supersaturation levels has been listed in Table 1.1 and will be explained below. The general growth rate can be expressed by the supersaturation level of the solution, in the form of a power law[12]

$$J_G = k(S_A)^X$$

where, k is the rate constant, S_A is the absolute supersaturation and the value of power x is dependent on the mode of growth. Considering supersaturation levels from high to low, the value of x is in four main scenarios as shown in Table 1.1.

When the supersaturation level is very high, the growth is diffusion controlled. Nuclei, in this case, grow very fast because rough surfaces (including a flat surface which has become very rough because it is favorable at such high supersaturations for growth units to be incorporated, i.e. kinetic roughening has occurred) have a high density of kinks, hence high binding energy for ion incorporation.[13]

Table 1.1 Different supersaturation level leads to different growth mechanism in F faces.[13]

Supersaturation level	Growth mechanism	Equation
$S \leq 1\%$ (far below S_C)	Screw Dislocations	$x = 2$
S_c reached	2-D Nucleation	$x = 1$
In high SL	Multilayer Mechanism	$x > 2$
In higher SL	Kinetic Roughening	$x = 1$

*S=supersaturation; S_c= critical supersaturation; SL = supersaturation level

The two-dimensional nucleation (the 2D equivalent of classical homogeneous nucleation), multilayer nucleation and screw dislocation are adsorption or surface controlled. Two-dimensional nucleation proceeds on smooth F faces periodically. In one periodic process, as can be seen from Figure 1.18, a monolayer island nucleus, usually called a 'two-dimensional nucleus' (2D nucleus), is firstly formed on the crystal surface. This is the rate-determine step. This nucleus, which is the source of steps and kinks, favors the incorporation of crystal forming elements. The incorporation spreads laterally and continues until the whole crystal layer is completely covered and become flat. For further incorporation, a new two-dimensional nucleus is required. However, it requires an energy barrier to generate a new nucleus on a defectless, atomically smooth F face due to the edge tension. Hence a critical supersaturation level (S_c) is required for the creation of a new 2D nucleus. This periodic process proceeds in this way until the supersaturation essentially relieved.[2, 17]

When the supersaturation level rises, multiple 2D nuclei are formed on the crystal surface, resulting in multiple two-dimensional nucleations at the same time. At high supersaturation, F faces tend to follow the polynucleation of surface growth islands.[2, 17]

However, as the supersaturation level goes higher, more 2D nuclei are formed at the expense of the integration of adatoms at any lattice. Smooth *F* faces then become rough, and the growth mode switches from a surface controlled to a diffusion controlled mechanism. This process is called kinetic roughening. Kinetic roughening can be caused by very high supersaturation or high temperature.[2, 17]

If the reaction above exhausts the ions or molecules in solution, this leads to a drop in the supersaturation, especially when the supersaturation, S, is below 1% of the critical supersaturation, the level of supersaturation above which surface nucleation will occur instantaneously.[18] In this case, a screw dislocation mechanism comes into play (Figure 1.8).[19] Stress caused by impurities, vacancies or misalignment inside the crystal lattice will result in defects in the crystal lattice. These defects or dislocations on the crystal surface act as steps, providing a way for crystal growth to occur under very low supersaturations, i,e, lower than the critical value required for surface nucleation, albeit very slowly. [2, 17]
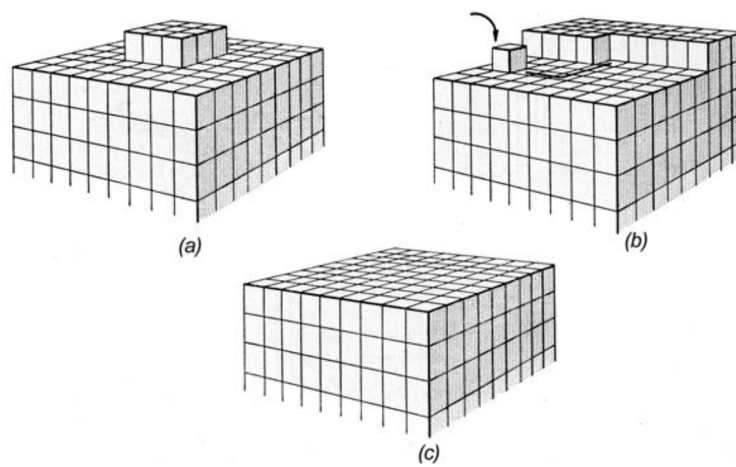
Figure 1.8 Two dimensional nucleation. a) Creation of a 2-D nucleus, b) incorporation toward desired sites, c) completion of crystal layer.[16] (Reprinted with the permission of ref.16. Copyright @ 2001 Elsevier).
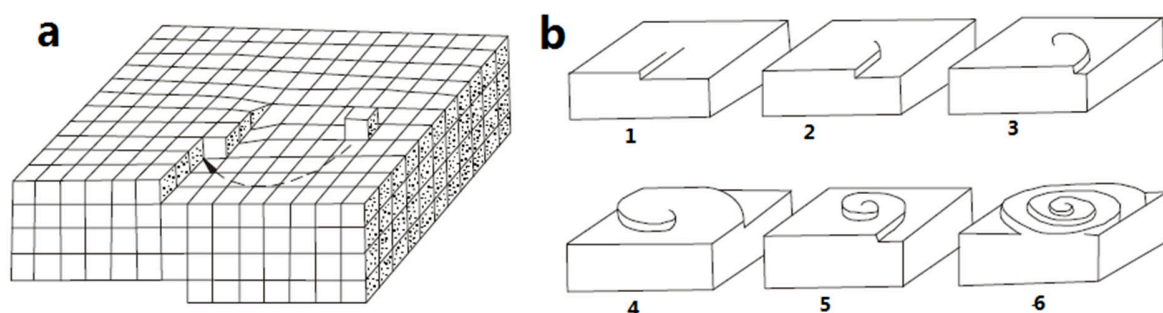
Figure 1.9 Spiral growth occurs along screw dislocations a) defects in the structure of crystal lattice. b) development of a spiral growth starting from a screw dislocation.[16] (Reprinted with the permission of ref.16. Copyright @ 2001 Elsevier).

1.2.3.4 The Kossel-Stranski Model

Kossel's model (see Figures 1.8 and Figure 1.10) is proposed based on the absorption layer theory and provides a simplified model for crystal growth.[17] This model assumes the pre-existence of active sites on a flat surface: kinks and steps. Kinks and steps are integration sites for growth units. Kink sites have three faces bonding to neighboring molecules, and three surfaces unbound, making the attaching and detaching of growth units easier than the completed step edges and embedded sites in flat surfaces.[20] Incorporation at a kink site is the most energetically preferred, for one reason, because incorporation into current kink provides a new kink site in steps for further incorporation, thus makes it as a repeatable procedure for crystal formation. Another explanation for kink site being most energetically preferred is that they have the structural and stereochemical requirements for incorporation ions/additives, hence, greatest stability after they fit in.[12] As illustrated in Figure 1.10, the integration of growth units (ion or molecules) into kink sites has five consecutive steps, and each step is reversible. Firstly, the growth unit diffuses from the bulk solution to the flat surface (step 1), from where the growth unit is dehydrated and adsorbed to the crystal surface (step 2). Growth units migrate into step sites (step 3), and then move to the kink sites (step 4), where the growth unit is incorporated (step 5).[12] Under a given solute concentration, the growth rate is dependent on the kink site density. Faces covered with more kinks will grow faster.[12]
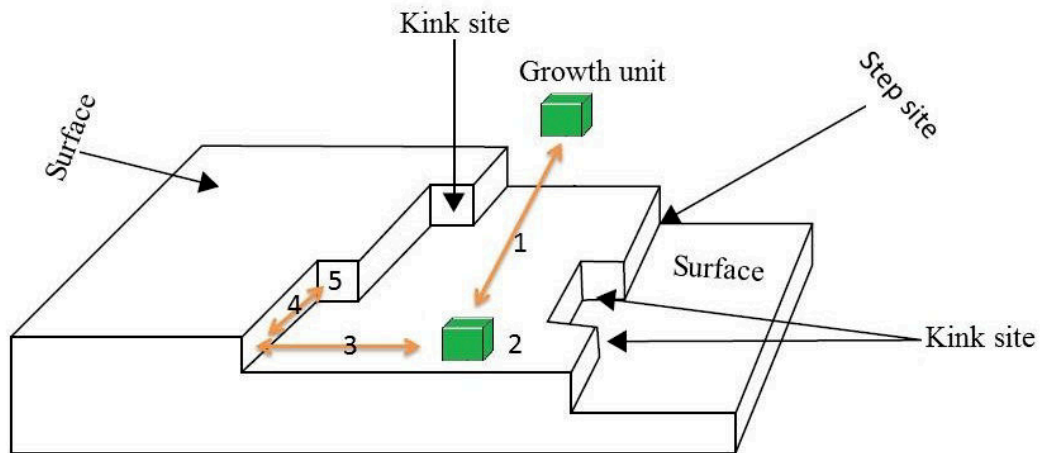
Figure 1.10 A graphical representation of Kossel's model of crystal growth. Migration of the green cubic growth unit onto the surface structure of a growing crystal may take place at three possible sites. They are labeled as kinks, steps, and the flat surface. The migration process from the solution into kink sites includes five steps and each step is reversible (indicated with orange arrow): 1) Ions diffuse from bulk solution to the flat surface; 2) ions are dehydrated when adsorbed to the crystal surface; 3) 2-dimensional (2-D) diffusion from the flat surface to the step sites; 4) 1-dimensional (1-D) diffusion from the step sites to the kink sites; 5) kink site incorporation.[12, 21] (Reproduced with the permission of ref.12. Copyright © Oxford University Press 2016).

1.3 Calcium Carbonate Crystallization

The precipitated calcium carbonate forming either in bulk solution or on a solid surface is the result of the combined effects of various factors. These factors include the supersaturation level, temperature, agitation, pH and type of additives, among which, the surface-active additives (ions and inhibitors) exhibit significant effects.[22] In this section, all the observed polymorphs of $CaCO_3$ are briefly introduced and the difference between different polymorphs in terms of morphology and site specificity is discussed. Two different pathways for $CaCO_3$ crystallization both in solution and on a surface are discussed. The primary focus is any factors that may be relevant to surface deposition of $CaCO_3$. These factors can be classified into three categories: process parameters (pH, temperature, and agitation), surface characteristics and additives. Each factor is discussed based on its impact on the nucleation rate and the resulting crystals formed on the

surface. Finally, some important principles of molecular recognition at the interface are discussed to help unravel the mysteries of mineral interaction with additives/substrates.

1.3.1 Observed Calcium Carbonate Polymorphs
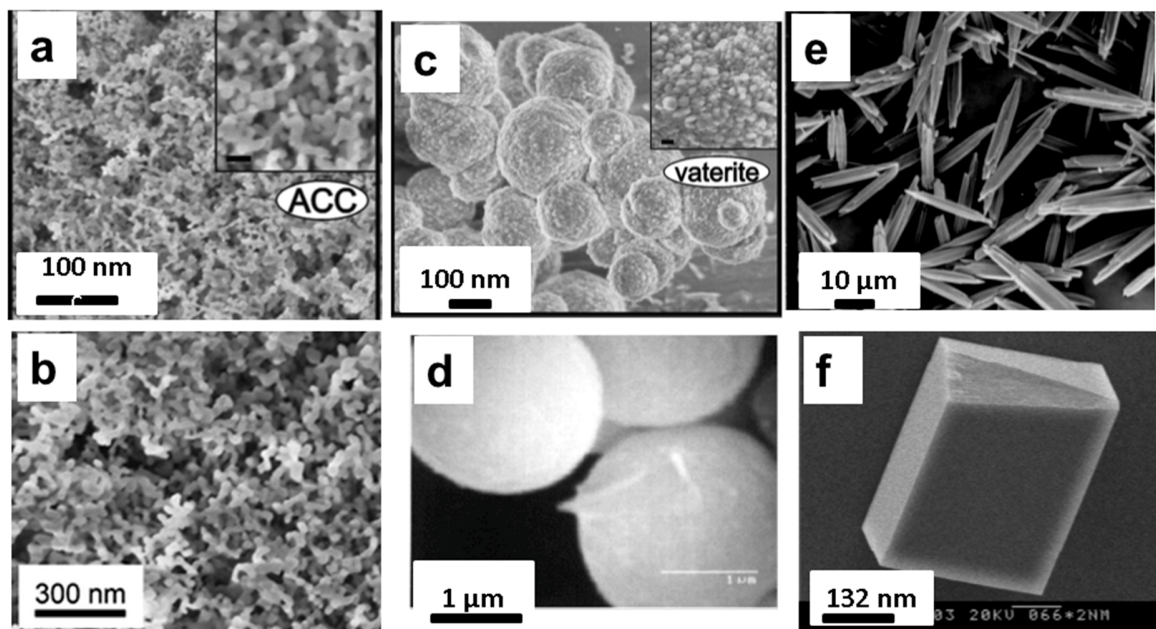
Figure 1.11 The most commonly observed shapes of non-biogenic calcium carbonate polymorphs:[24] (a&b): Amorphoud calcium carbonate (ACC); (c&d): vaterite; (e) aragonite; (f) calcite. (Image a & c reproduced with the permission ref.24a, Copyright 2012 American Chemical Society; Image b reproduced with the permission ref.24b, Copyright 2010 Royal Society of Chemistry; Image d reproduced with the permission ref.24c, Copyright 2000 Springer; Image e reproduced with the permission ref.24d, copyright 2001 Elsevier Science B.V.; Image f reproduced with the permission ref.24e, Copyright 2002 Elsevier Science B.V.)

Under ambient conditions, the observed polymorphs of $CaCO_3$ can be divided into three groups.[12] These are: three anhydrous forms of $CaCO_3$, which are calcite, aragonite, and vaterite; two hydrated forms: calcium carbonate monohydrate (MCC) and calcium carbonate hexahydrate (HCC); and amorphous calcium carbonate (ACC). Their occurrence is highly dependent on environment conditions such as temperature, flow speed and the type of substrate and additives. MCC and HCC are transient phases and only stable under low temperature and not within the scope of this project.[34] The properties of the three anhydrous $CaCO_3$ forms and ACC will be primarily discussed. ACC is often the precursor for all the other crystalline products.[23]

Amorphous calcium carbonate (ACC), with the highest solubility in solution, is the only non-crystalline form of calcium carbonate.[25] ACC is a hydrated amorphous phase and is usually

expressed as $CaCO_3 \cdot nH_2O$. It is often highly unstable and is difficult to detect as it is usually a transient species.[26] ACC, which has the lowest activation barrier of formation, is favored to form spontaneously but ACC nuclei are also falling apart at a rate that hinders the development of clusters. The formation of stable ACC needs to achieve a critical size.[26] ACC can be stabilized without converting into a solid form of $CaCO_3$ and can appear in different shapes.[25] Biogenetic ACC is often observed inside organisms with the presence of macromolecules or polysaccharides (like polyphosphonates,[27] polysaccharides[28] and ions like magnesium[29]). The non-biogenetic ACC, produced in the laboratory, is commonly observed in a spherical shape, with a diameter of less than 1 µm. Unlike the anhydrous polymorphs of $CaCO_3$, no intense peaks or sharp band can be observed in XRD and Raman pattern. However, it has characteristics of short-range order, as can be shown by X-ray absorption spectroscopy studies (XAS)[30] or TEM.[23]

The three anhydrous polymorphs (calcite, aragonite, and vaterite) with decreasing thermodynamic stability have different solubilities, morphologies, and crystallographic properties. Calcite is the most stable polymorph of calcium carbonate and is frequently observed as rhombohedra, cubic or tetrahedral.[31] Aragonite has a needle-like shape, belonging to the orthorhombic system.[32] It has a density of 2.94 g cm^{-3} and is the densest solid form of calcium carbonate. Vaterite belongs to the hexagonal crystal system and is usually seen in a spherical shape.[33] The summarized crystallographic information for different $CaCO_3$ polymorphs is attached in Appendix 2. Figure 1.11 shows the most commonly observed shapes for calcium carbonate polymorphs. In the first column, we can see the typical shape of the amorphous calcium carbonate without rigid shape.[24a] The anhydrous calcium carbonate polymorphs have relatively clear edges and are shown in the second and third columns. The shape of the rough and smooth vaterite samples in the second column are obtained in the absence and presence of the inhibitor, respectively.[24c] Column three shows the typical needle-like aragonite[24d] and rhombohedral calcite produced from pure solution.[24e] It should be mentioned that the morphologies of $MgCO_3$ and $CaMg(CO_3)_2$ also appear as rhombohedra,[34] therefore, morphology is not a valid method for polymorph identification for $CaCO_3$. Identification based on the crystal structure is a much more reliable method for characterization.

1.3.1.1　Site Specificity of Calcium Carbonate

The site specificity of the calcium carbonate polymorphs can be explained based on their crystal structures. Firstly, the coordination numbers for Ca^{2+} ions in the different lattices of the polymorphs are different. It is six for calcite, nine for aragonite and eight for vaterite. Secondly, at ambient temperatures and pressures, the distribution of the carbonate ions in the crystal structures of calcite, aragonite, and vaterite are different (Figure 1.12). Structures of calcite, aragonite and vaterite are similar, and all are composed of alternating layers of calcium ions and carbonate ions perpendicular to the *c* axis. The calcium ions in the polymorph lattices occupy almost the same lattice positions in the *c* plane, and the carbonate ions lie parallel to the *ab* layer. In calcite, carbonate ions are all oriented in one direction, whereas they are arranged in two different orientations in aragonite and three orientations in vaterite.[35] This is probably how polymorph selectivity is possible in nature.[36] One well-studied example is the mollusk shell, which has a calcitic layer outside and an aragonitic layer inside (see Section 1.3.7.4 for details).[37]
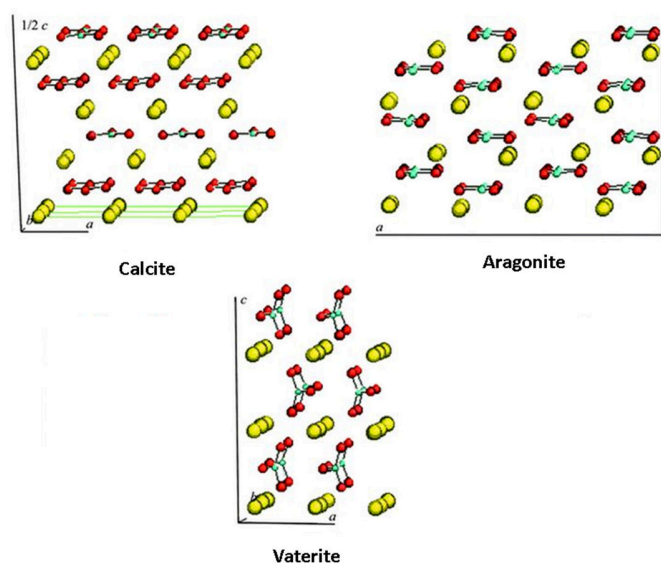
Figure 1.12 Crystal structures of calcite, aragonite and vaterite.[38] (Reproduced with the permission of Ref.38. Copyright 2000 Royal Society of Chemistry)

The feasibility of face selectivity for $CaCO_3$ polymorph may be due to the different distances of carbonate to carbonate in different planes. The carbonate to carbonate distance is often expressed as calcium to calcium distance (Ca-Ca). Table 1.2 shows the Ca-Ca distance for the most commonly observed faces of $CaCO_3$ polymorphs. The different distribution of cations and anions

in the mineral lattice forms a characteristic distribution of charge/polarity on different crystal surfaces in different polymorphs. If an additive/template can recognize this and fit in, specific nucleation can be promoted. This will be further discussed in sections below.

Table 1.2 Ca-Ca spacing on crystal faces of different calcium carbonate polymorphs.[39]

Polymorph	hkl	Ca-Ca distance (Å)
	104	4.014; 4.990
	102	4.048; 4.048
Calcite	001	4.990; 4.990
Aragonite	001	4.960; 7.970
	002	4.130; 4.130
	020	4.130; 4.240
	101	5.918; 5.918
	021	4.130; 9.432
	120	4.240; 10.925
Vaterite	062	4.130; 13.373

1.3.2 Calcium Carbonate Crystallization in Solution

1.3.2.1 Two Crystallization Pathways

Crucial features of crystals are determined at the nucleation stage and the subsequent crystal growth. Even though a full picture of $CaCO_3$ crystallization has not yet been obtained,[40] two crystallization mechanisms are proposed as shown in Figure 1.13: classical crystallization and non-classical crystallization. In classical crystallization, stable nucleation clusters are built via ion-by-ion attachment and then further develop into a single crystal (path a, Figure 1.13). Supported by experimental evidence, non-classical crystallization proceeds along particle-based reaction channels through oriented attachment (path b, Figure 1.13) and mesocrystal formation

(path c, Figure 1.13)..[41][42] Particle mediated crystallization observed in synthetic, biogenic, and geologic environments has been reviewed by De Yoreo.[43] The strict definition of mesocrystals is given as 'colloidal crystals that are built up from individual nanocrystals and are aligned in a common crystallographic register'.[41a] Mesocrystals are intermediate species between single crystals and crystals and can be self-assembled into different shapes. X-ray scattering for a mesocrystal shows that it has a similar behavior to a polycrystal.[44]
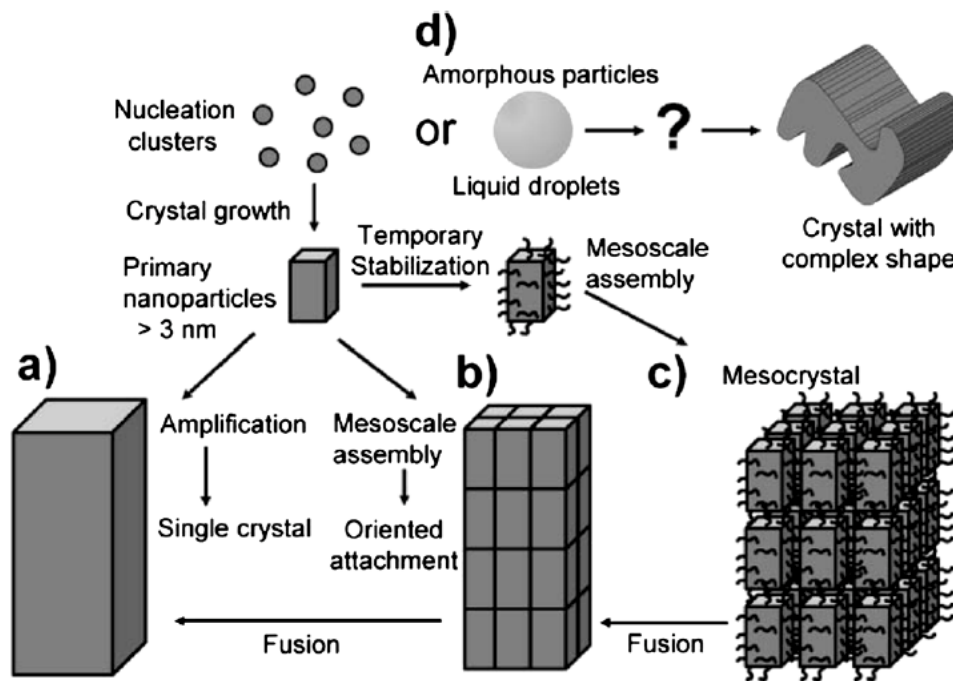
Figure 1.13 Schematic illustration of classical (a) and non-classical crystallization (b, c & d): a) The classical crystallization pathway, where nucleation clusters formed via ion-by-ion addition until they reach critical size and grow into a primary nanoparticle, which is amplified to a single crystal. b) The primary nanoparticles can also arrange to form an isooriented crystal, where the nanocrystalline building units can crystallographically lock in and fuse to form a single crystal. c) When a polymer or other additives are present in the system and adsorbed onto the primary nanoparticles, undergoes a mesoscale self-assemble, a mesocrystal is formed and fuses to form a single crystal. d) Instead of primary nanoparticles, lattice ions can aggregate to form amorphous particles, which can transform before or after their assembly to more complicated morphologies.[45] (Reproduced with the permission from ref.45, Copyright 2008 John Wiley & Sons Ltd).

However, research is focused more on amorphous particles due to their important precursor role in most situations. The formation of crystals through the assembly and transformation of amorphous precursor particles was demonstrated for $CaCO_3$ (path d, Figure 1.13). Moreover,

Gebauer[47] further demonstrates that nucleation of ACC occurs by aggregation of the stable, amorphous, precritical clusters, which have a size of about 2 nm in diameter. The nucleated ACC phase subsequently crystallizes to generate the final stable crystal product. Meldrum[40] tried to reconcile classical nucleation theory with non-classical theory by questioning whether the stable preclusters are actually stabilized by impurities in the system; hence a cluster containing 70 ions can neither shrink nor grow. The evidence that unites the classical and non-classical theories is observed from ion-association complexes during the biomimetic nucleation of calcium phosphate.[48] We should probably assume that both classical and non-classical crystallization belong to the general crystallization picture. They can be two competitive/optional nucleation pathways, and the one which dominates is dependent on the actual conditions.[49]

1.3.2.2 Phase Transformation

The transformation sequence of $CaCO_3$ polymorphs from supersaturated Ca^{2+} solution is controlled by the thermodynamics and kinetics of a system (Figure 1.14). It is known that the required supersaturation level to form calcite is larger than that of ACC, vaterite, and aragonite.[50] We would expect a more stable product, which is calcite to form first (Figure 1.14, pathway Thermodynamic A). This is only observed under excessive supersaturation, where ACC rapidly transformed into calcite.[51] However, most crystallization processes are often a sequential process (Figure 1.14, pathway Kinetically B)[24a, 50]

Thermodynamic control, in this case, only takes over when near termination.[53] This empirical observation of kinetic control is known as Ostwald's rule.[54] In Ostwald's rule, ACC phase transforms into the stable crystal products with increasing thermodynamic stability in a multistage process. However, not all possible polymorphs will appear in the sequence of this kinetic control line[54-55]. For example, the ACC phase can transform into vaterite, which can undergo a further transform into calcite but not aragonite.[41a, 56] However, this does not mean aragonite can not be obtained. With the presence of additives, aragonite can also be obtained through ACC.[57]
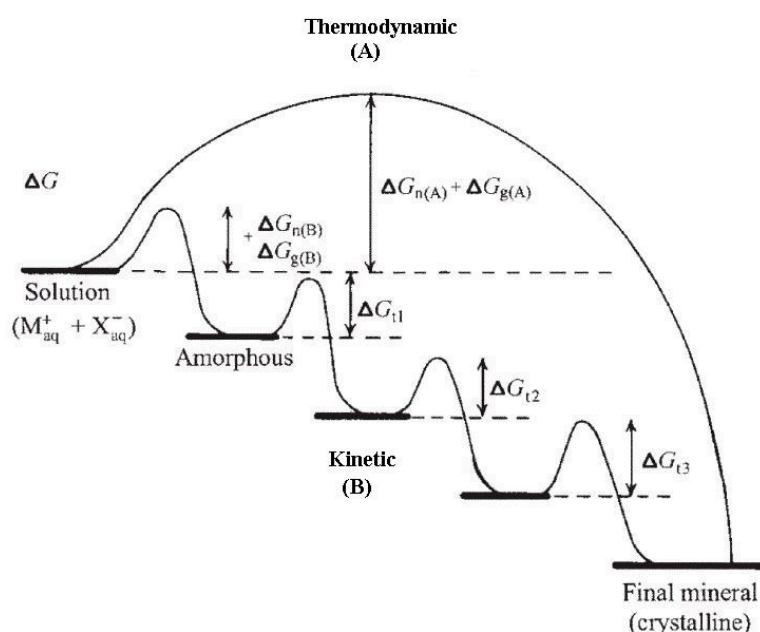
Figure 1.14 Simplified scheme of the crystallization pathways under thermodynamic and kinetic control. Whether a system follows a one-step route to the final mineral phase (pathway A) or proceeds by sequential precipitation (pathway B) depends on the free energy of activation associated with nucleation (n), growth (g) and the phase transformation (t), a manifestation of Ostwald's step rule. This rule allows an empirical prediction of the formation sequence of phases in a crystallization event.[52] (Reproduced with the permission of ref.52, Copyright © 2003 WILEY-VCH Verlag GmbH & Co. KGaA, Weinheim).

1.3.3 Surface Crystallization of Calcium Carbonate

Traditionally, studies of scale formation are more focused on bulk precipitation.[24b, 58] Recently, the difference between the surface deposition and bulk precipitation has been demonstrated.[59] It is shown that surface deposition and bulk precipitation follow different crystallization mechanisms. Surface deposition is a heterogeneous crystallization process, while bulk precipitation is a homogeneous process.[59b] Deposits found on surface mainly result from the direct surface crystallization with little contribution from adhesion of particles in solution.[1b, 60] Under dishwasher conditions, a similar conclusion for $CaCO_3$ growth on surfaces is obtained.[1a] In this project, the study will be restricted to the understanding of surface crystallization and deposit control on surfaces and how the deposition rate and the properties of the resulting crystals on a surface change under different conditions.

The crystallization pathways of $CaCO_3$ on a surface may be different under different conditions, but surface deposition can generally be divided into three stages: (1) induction period, no stable crystal plane is observed on the surface; (2) nucleation and growth on the surface of a substrate, a stable crystal plane starts to form on the surface and grows slowly as time elapses; (3) nucleation and growth of crystals on a pre-scaled surface. One example for surface crystallization of $CaCO_3$ on a silicon slide at 80 ^{o}C is shown in Figure1.15. The induction period and subsequent growth of crystal planes can be monitored by using *in situ* synchrotron radiation wide angle X-ray scattering (WAXS). The induction time is short at high temperature, approximately 6 mins. Individual planes from various polymorphs emerge and subsequently disappear under the hydrodynamic conditions in this stage. The majority of these planes can be assigned to aragonite (110) and aragonite (111). After the initially unstable phase, stable crystals start to appear on the surface. Crystals that are observed in the first layer of crystals are the (104), (110) and (113) planes of calcite. Once the first layer of crystal has formed, the growth rate of crystal increases dramatically.[59a] When crystallization has finished, calcite is the dominant polymorph. Even if it is still not clear whether the formation of calcite is via thermodynamically controlled transformation from ACC or via kinetic transformation from aragonite/vaterite via a dissolution-reprecipitation process, we can see that the formation of the first layer crystal highly promotes the nucleation rate. In the following section, the focus will be on understanding the formation of the first layer crystals, which is of vital importance in crystal growth and control.
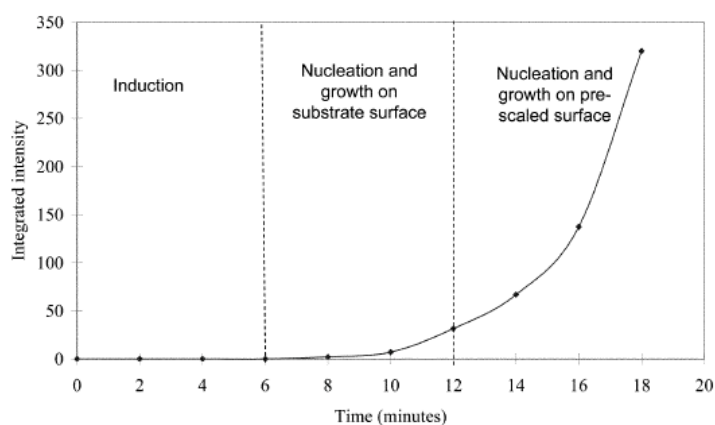

Figure 1.15 Crystallization of CaCO$_3$ on silicon slide expressed in terms of the evolution of X-ray diffraction integrated intensity peaks of calcite (104) crystals at 80 ^{o}C.[59a] (Reproduced with the permission of ref.59a. Copyright 2007 Royal Society of Chemistry)

1.3.3.1 Surface Nucleation

Similar to nucleation in solution and supported by experimental evidence, the most accepted two surface nucleation mechanisms are ion-by-ion nucleation (top, Figure 1.16) and particle mediated nucleation (bottom, Figure 1.16). The former follows heterogeneous nucleation (Section 1.2.2.3), where the formation of the critical nucleus is required to overcome an energy barrier before the system enters into the crystal growth stage. The particle mediated nucleation, on the other hand, is preceded by the aggregation of the amorphous phase, leading to an amorphous cluster, which subsequently crystallizes to generate stable crystal products.[53] The amorphous clusters might occur preferentially via ion aggregation to an amorphous phase or via the formation of stable prenucleation $CaCO_3$ clusters.[47]
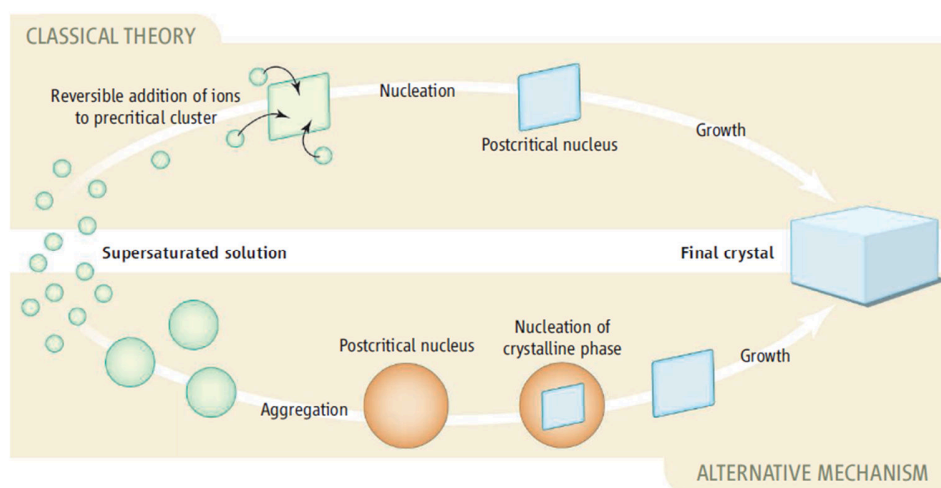
Figure 1.16 The surface crystallization of $CaCO_3$. Ion-by-ion nucleation (top): the classical heterogeneous nucleation proceeds by addition of ions to a single cluster. Particle mediated nucleation (down): aggregation of pre-nucleation clusters on the surface, which form ACC. Crystalline domains formed within the ACC when in contact with the substrate.[40] (Reproduced with permission from ref 40. Copyright Science 2008)
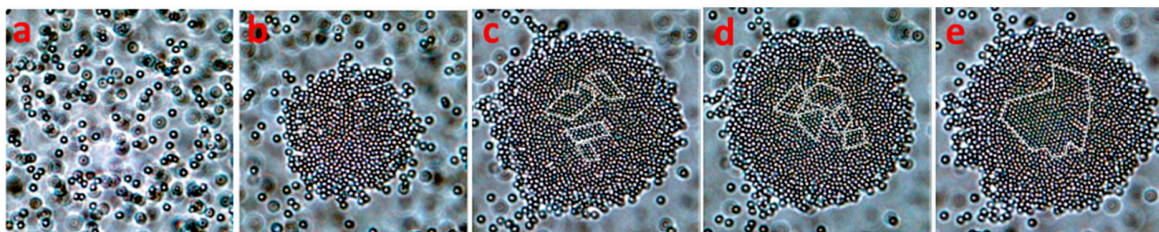
Figure 1.17 Evolution of crystalline structures inside the amorphous phase assembly of polystyrene spheres. (a) Small subcrystalline nuclei are initially created in the droplets that disappear and (b) reappear until they fuse to form (c) a stable, mature crystalline nucleus (d&e).[61] (Reproduced with the permission from ref.61, Copyright 2007 American Chemical Society)

When amorphous clusters are formed on a surface, how do they evolve into crystal products? A possible evolution process has been demonstrated recently by Zhang[61] using polystyrene spheres of ~1 μm and narrow polydispersity (~5%) in an electric field at the low volume fraction of 0.03% (Figure 1.17). It is demonstrated that surface crystallization occurs firstly via the aggregation of the amorphous phase (Figure 1.17a), followed by the formation of an amorphous cluster (Figure1.17b). Some subcrystalline nuclei start to appear and disappear within the amorphous cluster before a critical nucleus is obtained within the amorphous cluster (Figure1.17c-e). In a sufficiently large amorphous cluster, the critical nucleus is formed via coalescence of several subcrystalline nuclei. We can see that the phase behaviour of colloidal suspensions in atomic and molecular systems are similar and follow Ostwald ripening in that the stable crystalline nucleus is formed at the expense of the unstable subcrystalline nuclei.[62] Similar work has been carried out for $CaCO_3$ nucleation on a surface of a Langmuir monolayer,[63] with the finding that a crystal formed within ACC after ACC attached to a surface. However, the formation of a crystal is only possible when the crystal orientation is favorable to the monolayer. In other cases, it will disintegrate again.[63]

1.3.3.2 Factors that Affect the Surface Deposition

Theoretically, the rate of nucleation can be expressed as below (details see Section 1.2.2.3).

$$J_{het} = \Omega_{het} * \exp(-\Delta G^*_{het}/K_B T) = \Omega_{het} * \exp(-\emptyset\Delta G^*_{hom}/K_B T) \qquad \text{Equation 1.22}$$

$$\Delta G^*_{hom} = \frac{16}{3}\pi\sigma^3 V_m^2/(K_B T ln S_R)^2 \qquad \text{Equation 1.23}$$

The rate of nucleation is frequently expressed through the induction time, which is inversely proportional to the nucleation rate (Figure 1.24). Induction time refers to the period of time that elapses between the achievement of supersaturation and the observation of the first nuclei or crystals (Figure 1.26).[64] The induction time ($ln t_{ind}$) can be deduced as follows from Equation 1.22 and Equation 1.23:

$$t_{ind} = 1/J_{het} \qquad \text{Equation 1.24}$$

$$lnt_{\text{ind}} = ln\,1/\Omega_{het} + \frac{16\pi V_m^2}{3K_B^3}\frac{\sigma^3}{T^3}\frac{\emptyset}{(lnS_R)^2} \qquad\qquad \text{Equation 1.25}$$

$$lnt_{\text{ind}} = C_1 + C_2\left(\frac{\sigma^3}{T^3}\frac{\emptyset}{(lnS_R)^2}\right) \qquad\qquad \text{Equation 1.26}$$

The value of $\emptyset$ can be obtained from the Equation 1.18 and Equation 1.19 in Section 1.2.2.3. The subsequent growth of the crystal (Section 1.2.3.3) is expressed as

$$J_G = k(S_A)^X \qquad\qquad \text{Equation 1.27}$$

From Equation 1.25 and Equation 1.26, we can see that the formation of the first layer of crystals and the subsequent growth on a prescaled crystal are controlled by different factors. The factors that affect the surface crystallization of the first layer are surface properties (interfacial energy and the angle between the crystal phase and solution), the temperature of the solution and the supersaturation level. The subsequent growth of stable nuclei is mainly controlled by the supersaturation of solution. Therefore, a long induction period can be regulated by a low supersaturation level, a low temperature, and a non-wettable surface.[65] Nucleation delay is of utmost importance in scale control. This will be further discussed in Section 1.3.7.1

In the following sections, three classes of parameters in the system that affect the surface deposition will be discussed: (1) system parameters: pH, temperature of the solution and the flow rate; (2) the nature of the substrate: surface energy, surface roughness and surface chemistries; (3) the chemistry of the solution. Importance will be placed on the effects of additives.

1.3.4 The Effect of pH and Temperature

In a general crystallization picture, supersaturation is the thermodynamic driving force for the occurrence of precipitation, assessing to what extent a solution can be out of equilibrium. The degree of supersaturation is the key variable in any precipitation and governs the rate of nucleation and growth.[2, 55b] When additives are absent, the supersaturation level in pure solution can be affected by changes in temperature, the pH of the solution or the composition that is related to the evaporation of the solvent or ionic activities.[12] The temperature comes to play here by its effects on the value of K_{sp}. Calcium carbonate, as an inverse salt, decreases its solubility product when the temperature is increased. The value of K_{sp}, in the case of $CaCO_3$, is different for

different polymorphs. The value of K_{IP} is calculated based on the activity of the solute in solution while K_{sp} is constant for the given temperature. The calculating methods of K_{sp} under different temperature are shown in Section1.1.1. Available data and equations have been done by Elfil[66] and can be seen from Table 1.3. Temperature also affects the distribution of the CaCO$_3$ polymorphs. Without the presence of additives in solution, non-biogenic ACC can transform into vaterite and calcite in minutes at low temperatures (10-30 °C). At high temperatures (40-50 °C), a mix of vaterite, aragonite and calcite are observed. At higher temperature (60-80 °C) aragonite tends to be the dominant phase.[67] It is observed that the induction time of CaCO$_3$ on a silicone slide is 40 mins at 25 °C and 6 mins when at 80 °C. The formation of the first layer of crystals takes an hour more at 25 °C but only 14 mins at 80 °C. Deposition rate is faster at high temperature.

Table 1.3 Solubility constants for the different calcium carbonate polymorphs at 25 °C and their corresponding calculation form.[66]

Polymorphs	pk_{sp} at 298.15 K	$log(K_{sp})$ (T in K)
ACC	6.28	$6.1987 + 0.00053369(T\text{-}273.15) + 0.0001096(T\text{-}273.15)^2$ (283.15 < T < 328.15 K)
Vaterite	7.913 ± 0.020	$-172.1295 - 0.077993T + 3074.688/T + 71.595\log T$ (273.15< T < 363.15 K)
Aragonite	8.336 ± 0.020	$-171.9773 - 0.07793T + 2903.293/T + 71.595 \log T$ (273.15< T < 363.15 K)
Calcite	8.480 ± 0.020	$-171.9065 - 0.077993T + 2839.319/T + 71.595 \log T$ (273.15< T < 363.15 K)

The pH value of the solution influences the distribution of the carbonate species and hence influences the deposition rate and the distribution of CaCO$_3$ polymorphs. Increase in pH converts the bicarbonate into carbonate, hence favoring the precipitation of CaCO$_3$.[68] When pH < 6,

carbonic acid is the dominant species. Between pH ~ 6 and 9, the bicarbonate ion dominates. When the pH goes above 9, the carbonate ion dominates.[69] It has been shown that pH has a significant effect on the pathways and mechanisms of the transformation of ACC into crystalline $CaCO_3$. A neutral starting pH drives the system towards a direct crystallization of ACC to calcite. Conversely, a high starting pH promotes the formation of the metastable intermediate, vaterite, driving the system towards calcite through a secondary dissolution-recrystallization step.[70] It is also suggested that aragonite tends to form in highly alkaline solution.[71]

When additives are absent, high temperature and high pH promote the precipitation of $CaCO_3$, especially the nucleation of aragonite on a solid surface. Temperature exerts greater effects on the nucleation of aragonite. This can be seen from Figure 1.18. At low temperature but high pH, only calcite is observed, while at high temperature and high pH, spindle-like aragonite and rhombohedral calcite are both observed on the surface. The nucleation of aragonite may also be due to the presence of Mg, which also favors the nucleation of aragonite.[1a]
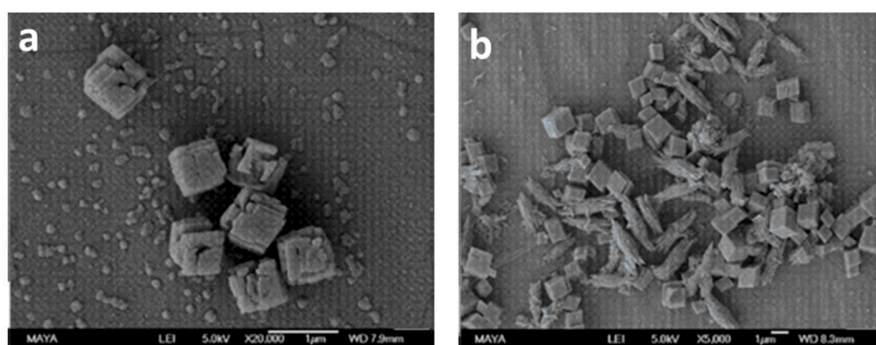

Figure 1.18 SEM images of CaCO₃ crystals deposition on the surface of stainless steel at pH=10 after 1 h with the presence of Mg: (a) at T = 25 °C, only calcite is observed. (b) at T = 55 °C, both spindle-like aragonite and rhombohedral calcite are observed, no vaterite is found.[1a] **(With the permission of ref.1a for reproduction, Copyright 2013 American Chemical Society)**

1.3.5 The Effects of Agitation

The increase in flow rate shortens the induction time and increases the deposition rate of crystals on a surface.[72] How fast the nuclei grow depends on the rates at which growth units attach and/or remove themselves from the nuclei surface. When the effects of agitation are involved, both deposition rate and the rate of crystal removal from the surface should be taken into consideration, especially when the flow rate is high.[1b] The overall scale rate is equal to the deposition rate of crystal minus the removal rate caused by hydrodynamic force.[65]

Comparing to a static mode, agitation can highly promote the formation of crystals.[73] Studies on the fouling process in pipes shows that the increase in velocity of fluid flow increases the rate of deposition of $CaCO_3$ on a surface.[74] However, it has been observed by Bott[75] that the lowest thickness of scale tends to be obtained at a high velocity of flow rate; thicker deposits are formed at an intermediate and a low velocity of flow rate. This suggests the importance of removal rate at high velocity of flow rate. When the flow rate is high, the removal rate of deposits increases faster than that of deposition rate, hence overall scale rate is reduced.[76] Agitation promotes the deposition process on the surface, but overall scaling rate is dependent on the velocity range, which is a combination of deposition rate and removal rate of crystals on the surface.

It is found that agitation has an obvious influence on the morphologies of particles and particle size, especially for metastable or intermediate phases, but has little effect on the resulting stable polymorphs.[77] During the carbonation of $CaCl_2$ solution, Han *et al.* found that fine vaterite particles form and aggregate into dense particles at low stirring rates, while aggregated vaterite particles at high stirring rates appear less.[78] Literature evidence shows that a reasonably high velocity of flow increases the amount of deposits formed on the surface, favoring the formation of calcite and suppressing the formation of aragonite.[79] This is consistent with the observation from Chien,[73] who further states that agitation enhances and accelerates the phase transformation from vaterite to calcite/aragonite. This can be seen in Figure 1.18 and Table 1.4. At higher stirring rates, vaterite completely transforms into calcite or aragonite. When additives are absent, the formation of calcite is enhanced with the increase of stirring rate in solution. When polyethylene glycol (PEG) is included as an additive, aragonite crystals other than the calcite tend to precipitate. When the stirring rate is 100 rpm, the formation of aragonite is enhanced. When increased to 500 rpm, vaterite totally transforms into calcite and aragonite. Additives have a profound effect on polymorphs control. Agitation seems to enhance and accelerate the crystallization process.

Table 1.4 Polymorph distribution of CaCO$_3$ in saturated Ca(HCO$_3$)$_2$ solution with and without the addition of PEG, after 60mins at 80 ^{o}C.[73]

Stirring rate (rpm)	Ratio of calcite: aragonite: vaterite	
	No PEG	2 wt% PEG
0	1: 1: 2	13: 1: 3
100	21: 1: 3	1: 9: 1
500	16: 1: 0	1: 2: 0

1.3.6 The Effects of the Substrate

From Equation 1.26 ($lnt_{ind} = C_1 + C_2 \left(\frac{\sigma^3}{T^3} \frac{f(\theta)}{(lnS_R)^2} \right)$) and Equation 1.27 ($J_G = k(S_A)^X$), we know that once the initial first layer of deposits is formed, the deposition rate become independent of surface properties. This is confirmed by experimental observations.[60, 80] Therefore, discussion can be restricted mainly to how surface properties influence the nucleation rate and the formation of nuclei on the first layer of deposits. The surface properties that affect surface crystallization have been studied so far include surface energy, surface roughness and surface chemistry. The contribution of each factor is dependent on the specific system under consideration and surface deposition is always a comprehensive consideration of all surface properties, especially for polymer surfaces.[60] Calvert and Rieke[81] stated that mineral growth at inorganic and organic interfaces are distinctly different. Organic surfaces are inherently more flexible and may have specific binding capacities for the ions in solution. Inorganic substrates, on the other hand, tend to be rigid and stable, surface deposition is largely determined by epitaxial lattice matching or surface topography.[82] Study of the fouling phenomenon on stainless steel surfaces shows that it is the surface roughness, rather than the surface chemistry, that makes a difference in the induction period when surfaces of carbon steel, stainless steel and admiralty steel are exposed to brackish water.[83] While in the case of polymer surfaces, all surface properties must be taken into consideration, especially the surface chemistry.[56b]

1.3.6.1 Surface Energy

From Equation 1.26 ($lnt_{\text{ind}} = C_1 + C_2 \left(\frac{\sigma^3}{T^3} \frac{\emptyset}{(lnS_R)^2} \right)$), it can be seen that the induction time of crystallization on a surface is directly proportional to the cube of the interfacial tension (σ_{cl}) and factor $\emptyset$.(function of the angle between the solid substrate and the crystalline phase in heterogeneous nucleation, see Equation1.18 and Equation 1.19 in Section 1.2.2.3) The interfacial tension σ_{cl} ($cos\theta\sigma_{cl} = \sigma_{sl} - \sigma_{cs}$), on the other hand, is determined by the interfacial tension of the substrate/liquid (σ_{sl}), substrate/crystal (σ_{cs}) and the corresponding contact angle. Factor $\emptyset$ is also a function of contact angle. Hence, contact angle is frequently used to assess the effects of a substrate on surface crystallization. Contact angle is a measurement of the surface energy.[56b] Efforts have been made to build up the relationship between the surface energy and scaling tendency. It is reported that a low-energy surface leads to a lower nucleation rate compared to a high-energy surface.[84] In a study of induction time measurement for supersaturated $CaCO_3$ solutions held in cells made of different materials, it is found that the induction time is the highest and the lowest for polyvinylchloride (PVC) material and polished stainless steel surface, respectively because the former has a lower energy surface.[85] Also, deposits on a low-energy surface are easier to remove under hydrodynamic conditions due to weak binding at the substrate–liquid interface.[86]

1.3.6.2 Surface Roughness

However, there are investigations that negate a direct correlation between surface energy and fouling tendency,[87] and associate the induction time with a degree of roughness on the surface; this is very applicable for the study of surface deposition on stainless steel.[88] On rough surfaces, there is a distribution of hills and valleys. The hills provide nucleation sites,[89] while the valleys act as shelters for deposits against the removal by shear stress. It is reported that the tensile stress needed to break away the scaling layer attached to a rough surface is several time greater than that for the case of smooth one. Under non-flow boiling conditions, the amount of deposit increases with surface roughness at low velocity (1m s^{-1}), but was negligibly small and independent of surface roughness when the velocity of flow is high (2m s^{-1}).[90] Rough surfaces provide more contact area for crystal growth and are found to have a higher deposition rate and shorter induction time. However, when a surface has a microroughness or local smoothness, it can be taken as smooth surface or locally smooth surface.[86] In these two extreme cases, the

contact area between the crystal and substrate is highly reduced.[91] As reported by McGuire and Swartzel[92], the deposition rate is independent of surface roughness when the surfaces of polished stainless steel, rough stainless steel, polytetrafluoroethylene coating and aluminosilicate coating have a R_a value of 0.04 mm, 0.41 mm 1.93 mm and 2.31 mm, respectively (R_a is the arithmetic average of the roughness profile).

1.3.6.3   Surface Chemistry

It has been long realised that the surface chemistry of a substrate can affect the nucleation rate and the phase behaviors of $CaCO_3$.[12, 93] In some situations, the additive in solution can absorb onto the surface of the substrate. The substrate with an adsorbed additive on the surface regulates the surface crystallization of $CaCO_3$. This is observed when deposition of thin films of $CaCO_3$ on a tailored functional polymer, hydroxylated poly(methyl methacrylate) (HyPMMA) with poly(acrylic acid) (PA) as an additive in solution.[94] PA adsorbs onto the surface of the polymer matrix through electrostatic interactions. The concerted interplay of interactions between the insoluble polymer matrix (HyPMMA) and the soluble additive (PA) determines the growth and morphology of $CaCO_3$ by influencing the phase transformation from ACC into the crystalline phases. Other examples, such as poly(aspartic acid), adsorb onto sulfonated polystyrene and regulate the specific nucleation of calcite (001).[95] Poly(isocyano peptides) adsorb to the glass slide and induced nucleation of calcite (011).[96] Surface chemistry of a substrate can be from original properties of the substrate itself or the adsorbed additives on the substrate. Biominerals are results of the synergistic control by the template and additive.[26, 53, 97] For an overview of the roles of soluble additives and templates in different stages of crystallization the reader can refer to Song.[97]

The crystallization pathway on a surface and the effects of the substrate in determining the formation of the first layer of crystals is still not systematically understood. Two nucleation mechanisms have been proposed to understand the underlying mechanism. Regardless of the difference, both nucleation pathways are affected by the surface properties of the substrate. The substrate, on the one hand, serves as a template for heterogeneous nucleation; on the other hand, it promotes the nucleation process by lowering the activation barrier. The promotion of nucleation can be specific or non-specific. The promotion of non-specific nucleation means that the substrate lowers the activation energy of the formation of the critical nucleus, but the

mineralization outcome is not affected[12]. For example, the polymorph species or the resulting morphologies are not altered. The promotion of specific nucleation is more complicated, but three possible outcomes can take place: polymorph selectivity, face selectivity and the crystallographic alignment of the nuclei on the substrate. The three outcomes can take place together or independently if just one of them is favored.[12] This will be further discussed in molecular recognition in Section 1.3.8.

1.3.7 The Effects of Additives

Water-soluble additives can play a dual role in crystallization. When molecularly dispersed they can attach to primary particles or the growing mineral phase, thereby influencing the formation of critical nuclei or the growth rate of various faces. Hence the growth of the crystal is interrupted. Additives, in this case, can be potent growth inhibitors. On the other hand, the adsorption of additives decreases the solid-liquid interfacial tension and enhances the formation rate of critical nuclei which can form a surface at which preferential nucleation occurs, so micelles can be a powerful nucleation promoter.[98]

1.3.7.1 Nucleation Promoter

Additives usually perform multiple roles in a crystallization process, which start with the complexation of ions, generate local ion enrichment, and decrease the supersaturation of solutions. If primary particles are formed, these are the next species after the constituent ions themselves, which can interact with additives. Subsequently, nucleation can be influenced by additives with coded control over crystal size, morphology, and polymorphic form.[97] The presence of additives can not only promote face selectivity but also polymorph selectivity. Carboxylate and sulfate monolayers can regulate the formation of the (110) and (001) face of calcite, respectively.[99] Chitosan gel can stabilize and preferentially promote the formation of vaterite (001).[100]

Additives promote crystallization via aggregation or bridging. The inclusion of the additives changes the surface characteristics of the growing phase,[101] which may cause aggregation of small entities to occur, yielding either randomly oriented polycrystalline aggregates or, in favorable cases, well-oriented, larger aggregates.[53] Aggregation of crystals can also be due to the bridging of those additives between two or more crystallites.[102]

1.3.7.2   Additives as Potent Inhibitors

Now imagine the situation when the nuclei are still unstable as they are below the critical size. Adsorption of the additives onto a prenucleation cluster delays the process of nuclei reaching the critical size, resulting in a reduction in nucleation rate. Alternatively, crystallites may be unable to reach the critical size, and thus eventually redissolve, setting themselves and the inhibitor molecule free.[103] This process that sets up a competition between nuclei formation and dissolution is called **nucleation delay**. If inhibitor adsorption efficiently inhibits the formation of nuclei, nucleation delay can prevent or remove the possibility of surface deposition. The effectiveness of an inhibitor in nucleation delay is most commonly evaluated in terms of induction time.[104] However, an accurate model to predict the induction time of $CaCO_3$ polymorphs has not yet been achieved.[105]

The effects of crystal growth inhibition can perhaps be explained using the Kossel's model (Section 1.2.3.4). Growth units diffuse from solution to the crystal face and try to incorporate into an active site, such as kinks and steps. However, if such an active site is not available or is blocked, the growth units may desorb back to the solution. Due to the lack of incorporation area, further growth of the stable nuclei will slow down or eventually stop. This process is **crystal growth inhibition**.

Therefore, the cessation of crystal growth can be caused by two possible reasons[12, 106]: one is the system fails to satisfy the supersaturation level for crystallization, and the another is due to the formation of an equilibrium surface. This equilibrium phase of the surface is caused by blockage of active sites, which results in surface energy stabilization of a crystal (thermodynamics effect) or a change of active sites on growing faces (kinetic effect), or perhaps both,[107] hence, slowing down or completely stopping crystal growth.[12] Theoretically, at any given time, only a small number of kinks are available for incorporation. This is proved by the experimental evidence that less than 1% surface coverage by an additive can completely inhibit the growth of calcite in a lateral movement.[108] This may explain why the very low concentration of impurities or additives accounts for a great growth rate retardation.[19]

1.3.7.3   Crystal Morphology Modification

The inhibition of further growth of stable nuclei exerts two effects on crystals: growth rate reduction and crystal morphology modification. These two effects are correlated. As can be seen

from Figure 1.19, if the additive preferentially adsorbs on face A, it stabilizes this fast growing face markedly by slowing its growth, while other faces are still allowed to grow as normal; an uneven growth of different faces of the crystal leads to the formation of surface complexes (Section 1.3.7.5).[109] The face A is stabilized and expressed in the equilibrium morphology. Moreover, the overall growth rate is determined by the slowest growing face from original face B to face A. When the additive adsorbs, the overall growth rate is reduced.

Gibbs-Wulff theory (see Section 1.2.3.1) provides guidelines for crystal morphology prediction, which is especially useful in explaining changes of crystal morphology if an additive is selectively adsorbed onto one crystal face only. It is not valid for all cases of crystallization, especially crystallization that is kinetically controlled. Water-soluble additives can be inorganic ions, small molecules or polymers. Due to the different structure and size of the additives, there are two modes of specific promotion of nucleation upon the crystal morphology when an additive selectively adsorbs onto only one crystal face.[26] The first mode applies to inorganic ions or small molecules. When they selectively adsorb onto a crystal face, this face is stabilized, while other uncovered faces with high surface energies still grow out and may disappear. The stabilized face is reflected in the equilibrium morphology. Figure 1.20 shows the impact of different ions on the morphology of a calcite based on an atomistic simulation.
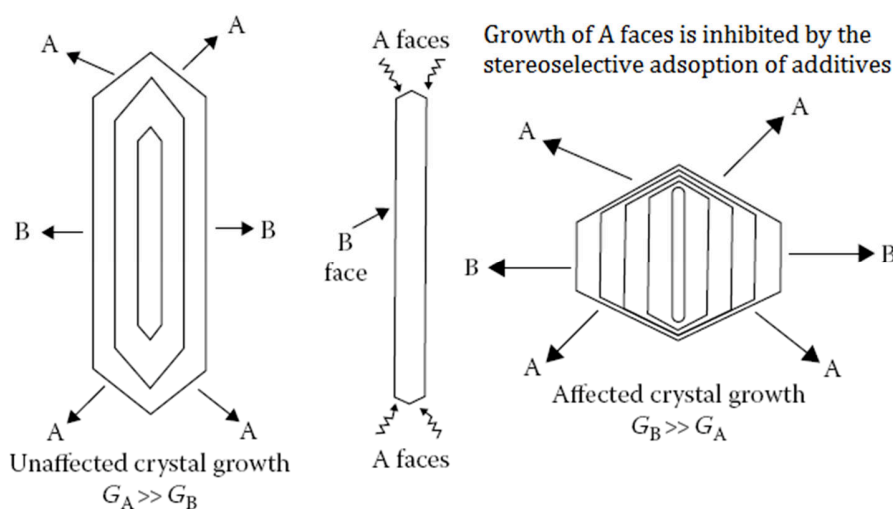
Figure 1.19 Stereoselective adsorption of the additive changes the crystal morphology.[110] (With the kind permission from ref.110. Copyright @ International Union of Crystallography).
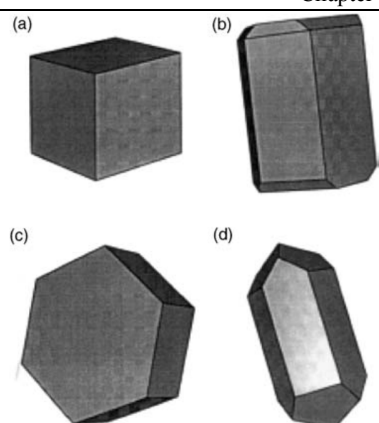
Figure 1.20 Predicted morphologies of calcite surfaces based on atomistic simulation of in the presence of various additives: a) (104) rhombohedral (no additives); b) (100) faces stabilized by Mg^{2+}; c) (100) tabular, stabilized with Li^+; (d) prismatic rhomb (1-10)/(104) stabilized with HPO_4^{2-}. The morphologies are in agreement with experimental results.[111] (Reprinted with the permission of ref.111. Copyright @ Copyright © 1993 Published by Elsevier B.V.)

The second mode of specific nucleation applies to polymers with tails, such as surfactants or double hydrophilic block copolymers. A systematic morphosynthesis of $BaSO_4$ particles has been performed using double-hydrophilic block copolymers (DHBCs), which consist of a hydrophilic solvating block and a hydrophilic binding block, as crystal growth modifiers to direct the controlled precipitation of $BaSO_4$ from aqueous solution. Multiple cone-shaped $BaSO_4$ and $BaSO_4$ fibers were formed in aqueous solution with polyacrylate and monophosphonated poly(ethylene oxide)-block-poly(methacrylic acid) (PEG-*b*-PMAA-PO$_3$H$_2$) as additives, respectively. A possible mechanism has been proposed to explain the how the morphologies developed. The ion-by-ion and particle-by-particle mechanisms are given in Figure 1.21 and Figure 1.22, respectively.[112]
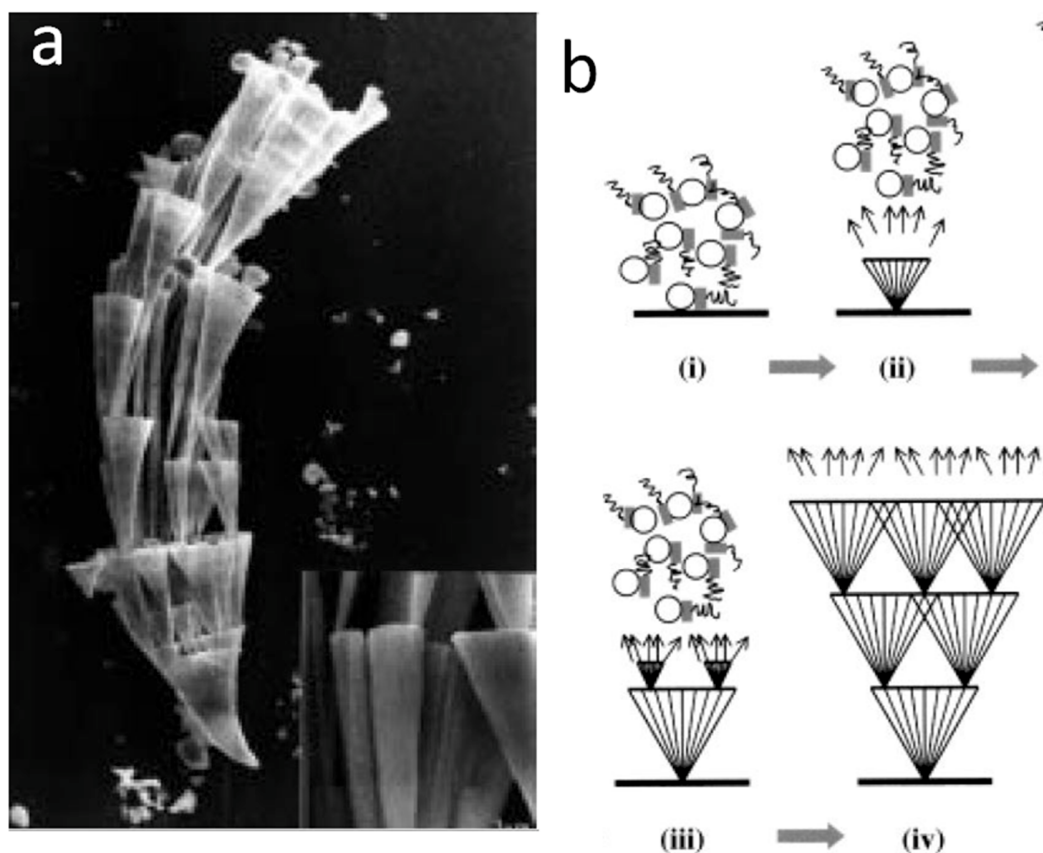
Figure 1.21 The ion-by-ion nucleation on the surface: (A) SEM image of a multiple cone-shaped BaSO₄ particles prepared in the presence of polyacrylate. The inset shows a high magnification image, revealing the internal arrangement of the strands.[112b] (B) The proposed mechanism for the formation of multiple cone-shaped crystals: (i) at the beginning, amorphous particles are formed which are stabilized by the DHBCs; (ii) heterogeneous nucleation of fibres occur on glass substrates and the fibres grow under the control of DHBCs, presumably by multipole field-directed aggregation of amorphous nanoparticles; (iii) the growth is continuously slowed down until secondary nucleation or overgrowth becomes more probable than the continuation of the primary growth. This is a statistical observation and will lead to a distribution of cone sizes. The secondary cone will grow as the first ones have done; (iv) the secondary heterogeneous nucleation taking place on the rim can repeatedly occur depending on the mass capacity of amorphous nanoparticles in the system.[112a] (Reproduced with the permission from ref.112a. Copyright 2002 WILEY-VCH Verlag Gmbh & Co. KGaA, Weinheim)
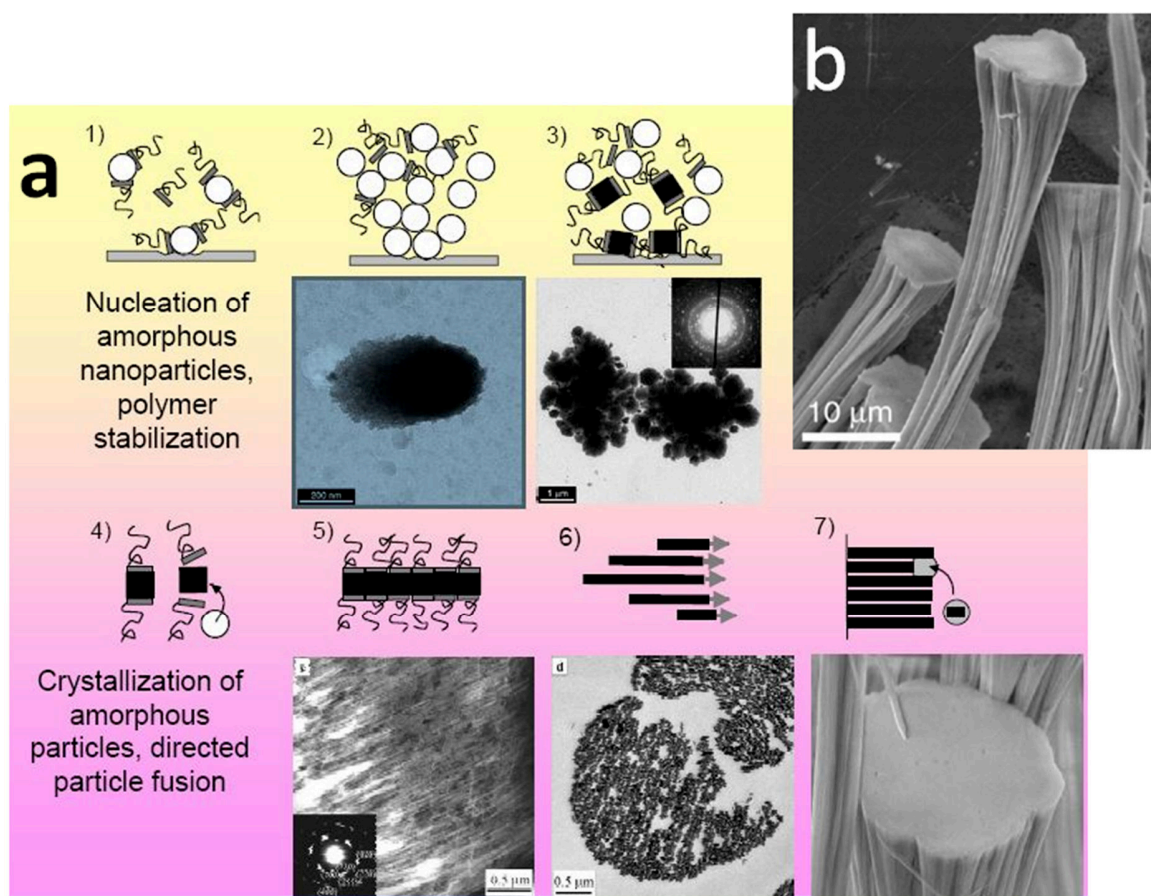
Figure 1.22 Particle mediated nucleation of BaSO₄ nanofilaments on carbon films. (A) The possible mechanism for the development of the bundles of BaSO₄ nanofilaments from the amorphous precursor particles; (1) the polymer-stabilized amorphous particles (2) aggregate into colloidal clusters via van der Waals interactions between the particles. (3-4) Crystallization of BaSO₄ nanoparticles occurs in the aggregates as the amorphous precursors, (4) the anionic polymer chains adsorb selectively to positively charged crystal faces, leads to the formation of an electrostatic multipole field, (5-6) which directs the aggregation of the crystalline BaSO₄ building blocks along one principal axis to produce the nanofilaments, (7) BaSO₄ monofilaments are obtained on carbon films; (B) the full image of the BaSO₄ fibres obtained in the presence of PEG-*b*-PMAA-PO₃H₂ on carbon films with an aging time of 5 days, at pH = 5.[112b] (Reproduced with the permission of ref.112b. Copyright @ 2001 WILEY-VCH Verlag GmbH & Co. KGaA, Weinheim)

1.3.7.4 Polymorph Control

Polymorph selection may occur at the early stage of the transformation based on the observation that the transient amorphous phase already has the nascent order of the polymorph into which it will transform.[113] There are two routes for the stabilization of the less stable forms of $CaCO_3$. One is to prevent the formation of stable form calcite and allow the development of the less stable form. The other one is to stabilize specific plane of vaterite or aragonite such that the transformation into calcite can be prevented or at least delayed. The latter principle is frequently

used for the explanation of the occurrence of polymorphs with the preferred orientation.[53] Additives can employ these two routes and control the formation of the desired polymorph.

Calcite is the final product for most crystallization processes as it is the most thermodynamically stable form of $CaCO_3$.[95] As discussed in Section 1.3.2, calcite tends to be obtained through a kinetic transformation from ACC with one or more of the other less stable forms of $CaCO_3$ as an intermediate. The transformation from ACC to calcite is a process of crystallinity development concurrent with dehydration. The strategies for the stabilization of ACC, hence, are either to keep the size below the critical size for the formation of the crystalline polymorphs or prevent its dehydration. For example: phytic acid (inositol hexakis phosphate) can stabilize amorphous calcium carbonate (ACC) for more than three months with 5 wt.% of additive and 15 wt.% of water in resulting ACC. Vaterite can also be stabilized by the formation of nanocrystalline particles that are below the critical size for calcite formation.[114] Vaterite is mostly obtained by preventing the dissolution-reprecipitation step necessary for its conversion to calcite.[36, 101] This stabilization can be achieved by soluble additives[115] or a template.[100] For aragonite, the routes above do not really apply. When the additives are absent, most kinetic transformation tends to have vaterite as the intermediate and skip aragonite. Aragonite tends to be obtained at high temperature,[67] in the presence of magnesium ions[57b] or a specific plane of aragonite is stabilized by an additive/plane.[116]

The Mollusk shell is an ideal model for the study of polymorph control. The example of mussel shell is shown in Figure 1.23. The calcite and aragonite are present in the neighbouring prismatic and nacreous layers, respectively.[117] It is reported that macromolecules extracted from calcitic shell layers induced mainly calcite formation in vitro, while macromolecules from the aragonitic shell layers induced vaterite in a chitin matrix when silk fibroin is absent. Only when the macromolecules are preadsorbed on a substrate of β-chitin and silk fibroin, can aragonite be obtained and extraneous ions such as magnesium were not required. Therefore we can see that the nucleation of vaterite and aragonite follows different mechanism. The requirement of forming different polymorphs is different. For here, the formation of aragonite even requires a three-dimensional control over the nucleation site, both the macromolecular conformation, as well as the local microenvironment are important.
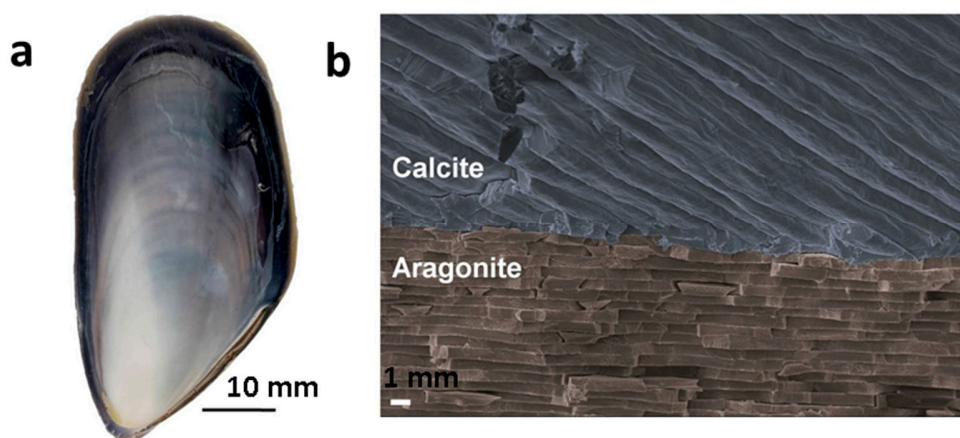
Figure 1.23 Mussel shells: (a) the shell of the Mytilus edulis (commonly known as blue mussel) with a calcitic layer outside (in blue) and aragonitic layer inside (in white). Scale bar = 10 mm; (b) The SEM micrograph of a fractured shell shows the appearance of the outer calcite and inner aragonite layers. Scale bar = 1 micron;[118] (Reproduced with the permission of ref.118. Copyright @ 2013 Springer).

1.3.8 Molecular Recognition at Interfaces

How much and how far the substrate/additive can regulate the crystallization of $CaCO_3$ is dependent on the interaction between the substrate and the growing nucleus. The substrate here can be taken as an insoluble additive. So far, two mechanisms have been proposed to explain the interaction between an additive and growing nucleus: molecular recognition[12] and mutual templating (or induced fit)[119]. In mutual templating, the structure of the nucleus and the structure of the substrate mutually influence each other in such a way that an energetically and structurally optimum interface is realized. It was found by De Yoreo and co-workers that 3- and 4- mercaptophenol monolayers are highly organized before the deposition of ACC. ACC deposition causes SAMs to lose their order. However, SAMs can be ordered again by the mutual templating effect between SAMs and crystallizing ACC moieties.[120] In general, mutual templating and molecular recognition are the same. They are the balancing consequence between the growing nucleus and the additive. Molecular recognition offers some principles to follow. It has been proposed by Mann[12, 121] that the specific promotion of nucleation is possible when there are high electrostatic, structural and stereochemical complementarities between the substrate and the motifs of the forming nucleus. In this section, we will discuss some essential aspects of molecular recognition at interfaces.

1.3.8.1   Electrostatic Interactions between Substrate and Crystal

Firstly, the type of functional group may affect the interaction strength between the substrate and crystals. If the substrates have no effect on nucleation, nucleation may occur randomly in the bulk solution and deposition at the substrate interface is greatly reduced.[60] If the electrostatic interaction is high, the deposition of $CaCO_3$ to the surface will be strong, and the structure of the scale formed should be compact and tough.

The functional groups on a surface affect the crystallization pathway, which is demonstrated by the $CaCO_3$ crystallization on self-assembled monolayers (SAM) with an initial Ca^{2+} concentration of 1 mM.[32, 49, 122] It is shown that the nucleation occurs on the -COOH surface mainly via ion-by-ion mechanism and particle mediated nucleation may also be involved. Nucleation on a surface terminated with –OH, -NH_2 and –CH_3, however, takes place via $CaCO_3$ amorphous clusters, which aggregate in solution and then adsorb onto surfaces. Substrates terminated with -COOH tend to induce the formation of calcite with a distinctive shape and size. A surface terminated with –CH_3 is unlikely to have the same effect and almost no crystals are observed on –CH_3 terminated substrates. On the other hand, surfaces terminated with -OH and -NH_2 direct the formation of vaterite with the preferred orientation. By placing the calcium ion selective electrode around the biomimetic surfaces, it is found that different functional groups affect the electrostatic accumulation of Ca^{2+} concentration near the substrate surface. The Ca^{2+} concentration near a surface terminated with -COOH is 5 mM, which is higher than the other surfaces of 2 mM. If we take the substrate as a two dimensional nucleation site, when the concentration in the solution is low, different functional groups have different abilities to reduce the activation energy. -COOH with higher affinity for Ca^{2+}, is able to attract the lattice ion and create a local high supersaturation. Surfaces terminated with –OH, -NH_2 and –CH_3 are not attractive enough to perform a similar electrostatic accumulation. Crystallization, in this case, tends to follow the course of particle-mediated nucleation. Particles are another form of local high supersaturation. Particle-mediated nucleation also tends to take place at high supersaturation, where the system is thermodynamically unstable and tends to reduce supersaturation by the formation of clusters or amorphous intermediates.[26]

The promotion of the specific nucleation mechanism, based on the ion-by-ion nucleation, and the particle mediated nucleation mechanism are explained by electrostatic interactions as shown in

Figure 1.24 and Figure 1.25, respectively. The former shows how the hexagonal vaterite (001) can be regulated by chitosan gel via ion-by-ion nucleation[100] and the latter is the nucleation within the amorphous phase of $CaCO_3$ on an organic surface, where crystal only grows when the crystal orientation is favorable to the monolayer.[63] The difference lies in the first-step interaction during the induction period. The first step interaction for ion-by-ion nucleation is the electrostatic accumulation, where the functional groups attract the calcium ions, and the bound calcium ions, in turn, attract carbonate ions and form a loosely associated anionic coordination sphere.[121, 123] If the polarity and charge density at matrix nucleation site fit with the electrostatic field surrounding a specific crystal face of a developing nucleus of calcium carbonate, then the calcium ions will be located at a specific point in this crystal lattice, vaterite (001) is stabilized by chitosan gel by this mechanism.[93a] The first step for the particle mediated nucleation on the surface is the aggregation of pre-nucleation clusters on the surface, which form amorphous $CaCO_3$. The crystalline domains are formed within the amorphous phase when in contact with the substrate.[47]
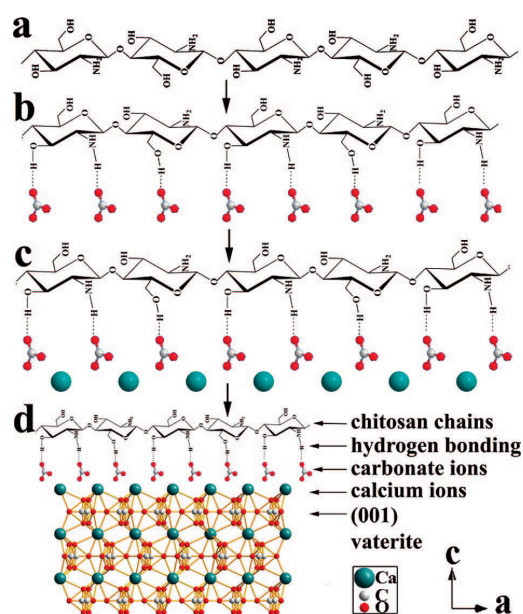
Figure 1.24 The schematic formation process of hexagonal vaterite plates exposed the (001) plane using chitosan gel as a template. (a) Schematic graph of chitosan chains; (b) hydroxyls and amino groups of chitosan chains binding with carbonate ions through hydrogen bonding; (c) carbonate ions bound by chitosan chains attracting calcium ions by electrostatic forces and (d) stereochemical arrangement of carbonate ions in conjunction with Ca^{2+} guiding the formation of vaterite.[100] (Reproduced with the permission of ref.100, Copyright @ 2008, American Chemical Society).
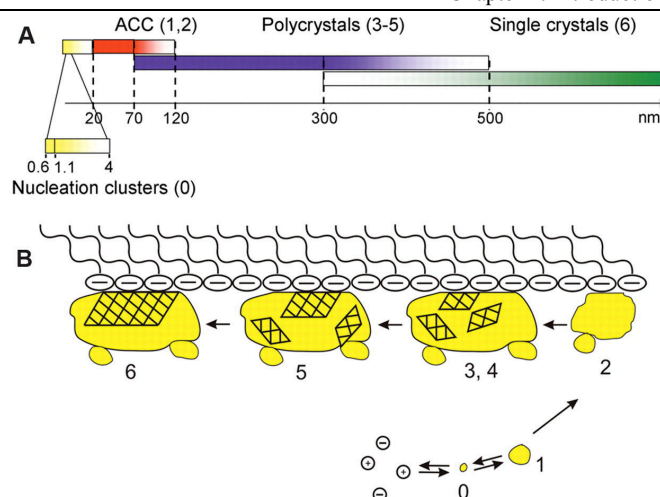
Figure 1.25 Promotion of the specific nucleation of calcium carbonate via particle mediated growth on an organic matrix. (A) The distribution of particle diameters as crystallinity develops at the surface. (B) The schematic pathway of the mineralization of an organic matrix. Step 0: formation of prenucleation clusters. Step 1: aggregation of the clusters to form 30 nm ACC nanoparticles. Step 2: clustering and growth of the ACC particles at the surface of the organic matrix. Step 3: start of the crystallization; formation of poorly crystalline particles. Step 4: formation of nanocrystalline domains inside the amorphous particle. Step 5: the prevalent growth of the crystalline domain stabilized by the template. Step 6: formation and growth of oriented single crystals.[63] (Reproduced with the permission of ref.63, Copyright @ 2009, American Association for the Advancement of Science).

1.3.8.2   Structural Recognition between Substrate and Crystal

One of the well-studied examples is the β-sheet conformation of aragonite (001) found in mollusk nacreous layers.[124] The mollusk nacreous layer is made from β-chitin fibrils and β-sheet silk-fibroin-like protein, which are aligned orthogonally to each other. The resulting aragonite's *a* axis and *b* axis are aligned with the direction of β-chitin proteins and silk-fibroin-like proteins, respectively, indicating the templating effect of the organic matrix controlling the orientation and shape of the resulting crystals. The β-chitin fibrils are sandwiched by two β-sheet silk-fibroin-like protein layers, onto which acidic glycoproteins are located.[123] The acidic glycoproteins, rich in aspartic acids and/or glutamic acids, are responsible for electrostatic interactions.

The electrostatic interactions originated by the functional group and lattice ions, is the first interaction for molecular recognition. Two factors are important for this recognition in biomineralization. There are the properties of the nucleation site and the available number of

active functional groups at the matrix surface. The nucleation site determines the spatial distribution of the functional groups. The available number of functional groups determines the polarity or charge density on the surface. The immobilized acidic glycoproteins with negative functional groups are responsible for the electrostatic accumulation. When aspartic acid binds to the active sites of a crystal face, it exerts structural matching.[125] Figure 1.26 shows the underlining interaction between aspartic acid and aragonite and offers a detailed explanation for structural matching. In Figure 1.26(b), the aspartic acid residues in the nacreous layer are organized in the sequence of Asp-X-Asp (X is a neutral residue) along the β-sheet matrix interface, and are capable of binding to Ca^{2+} by involving two or three ligands. The calcium to calcium (Ca-Ca) distance (4.96 Å) at the a plane of aragonite is similar to the distance of two adjacent aspartic acids in the matrix (4.7 Å). At the b plane, the distance of 6.9 Å of two aspartic acids does not coincide with 7.79 Å of the b plane on aragonite, but in a longer distance, it does commensurate with the Ca-Ca distance in the b plane of aragonite: 7 calcium ions regulated by aspartic acid have an overall distance of 48 Å. This gives an average distance of 8 Å between the two aspartic acid residues, which is commensurate with the Ca–Ca distance in the b plane of aragonite (7.79 Å). Lattice matching may be reasonable as long as the complexation does not distort the molecular structure greatly from the dominant conformation in the unbound state. The study shows the importance of the template adaptability in controlling the specific nucleation. The functional group on the surface is induced to fit the crystal lattice.
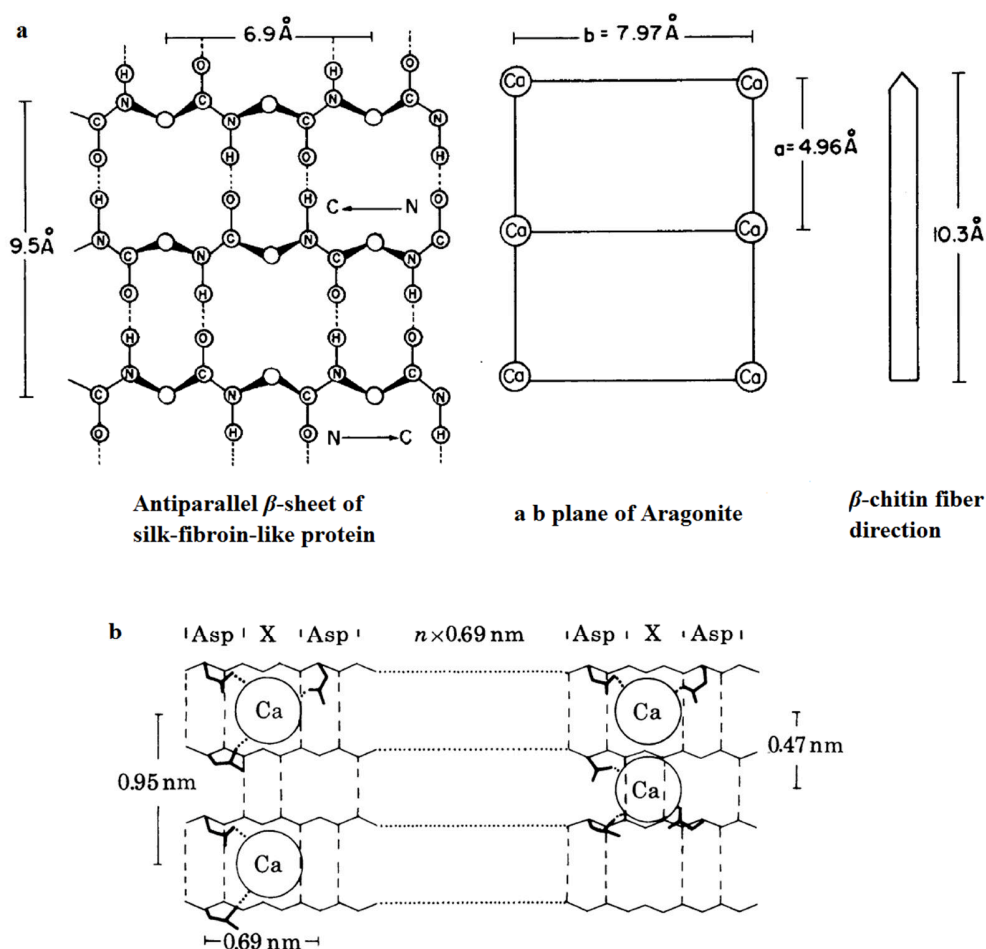
Figure 1.26 The schematic illustration of the lattice complementarities between the aspartic acid residues of the *β*-sheet matrix and Ca atoms in the *ab* plane of aragonite.[126] **(a) The mollusk nacreous layer made from of *β*-chitin fibrils, which are sandwiched by two *β*-sheet silk-fibroin-like protein layers, onto which acidic glycoproteins are located. The acidic glycoproteins, rich in aspartic acids and/or glutamic acids, are immobilized by the protein matrix and act as a core part for spatial control. The aragonite crystal that nucleated along c direction is perpendicular to the surface of the matrix sheets, indicating this preferred orientation of crystal may be relevant to the structure of the *β*-sheet silk-fibroin and acidic glycoproteins on matrix. b) Schematic representation of the modes of calcium binding to the *β*-sheet surface containing aspartic acid residues, which are organized in the periodical sequence of Asp-X-Asp (X is neutral residue) along the *β*-sheet matrix sheet. Two or three ligands are involved in Ca binding, regulating the formation of oriented crystal nuclei along the interface. (Reprinted with the permission of ref.126. Copyright © 2012 Elsevier B.V).**

1.3.8.3 Stereochemical Matching

A functional group generally exerts two effects: electrostatic accumulation and stereochemical matching in the mineral lattice. Anionic coordination matching is the main determining factor in stereochemical matching.[125a,123] In the last section, we discussed the electrostatic accumulation, showing -COOH has a higher affinity for Ca^{2+}, followed by –OH, -NH_2 and –CH_3.[32, 49, 122] Mann and co-workers[127] investigated a complex series of inorganic monofunctional additives: NO_3^-,

SO_4^{2-} and PO_4^{3-}. Phosphate was found to be extremely active in modifying the formation of calcium carbonate even at very low concentrations ([Ca^{2+}]/[additive]=10000), whereas sulfate and nitrate ions have minor or no effects even at high concentrations. From Figure 1.28, we can see that the structure of NO_3^- is stereochemically equivalent to that of the carbonate ion (CO_3^{2-}), but it has no such effects on the modification of CaCO$_3$. Strict stereochemical matching is not the most important factor in crystal nucleation, but electrostatic matching is essential. Take aspartic acid in a nacreous layer for example. The configuration of the binding group (COOH-) in aspartic acid is not very precise compared to the stereochemically equivalent anionic motif (CO_3^{2-}) in the crystal structure of CaCO$_3$, but it still regulates the formation of aragonite (001) through bidentate binding of the calcium sites on the crystal face. Phosphonate ions are more stereochemically equivalent to CO_3^{2-} than COOH and can approach Ca^{2+} in the crystal surface either via a "tripodal" fashion[128] or by bidentate binding.[127, 129]
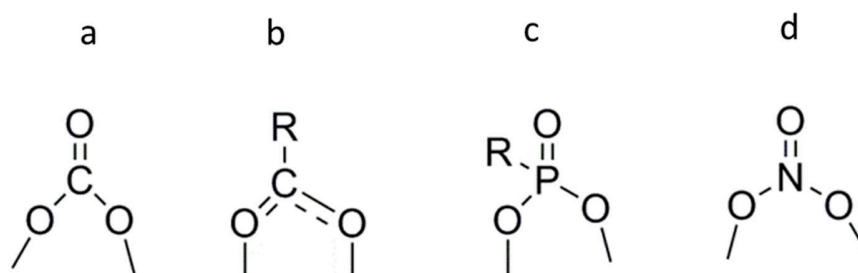
Figure 1.27 The structures of the functional groups: (a) carbonate ion (CO_3^{2-}); (b) carboxylate (-COOH); (c) phosphate ion (PO_4^{3-}); (d) nitrate ion (NO_3^-).

1.4 Inhibition of Calcium Carbonate Growth

1.4.1 Development of a Scale Inhibitor

The applications of scale inhibitors in the industry are found in several fields, such as detergents, industrial water treatment, wastewater treatment, and purification.[82a] Compared to uncharged polymers (such as polyacrylamide) and cationic polymers (which exhibit no inhibition effects)[130], anionic polyelectrolytes are the most effective scale inhibitors. Anionic polyelectrolytes contain one of more of a range of functional groups including: carboxylic acid (-COOH); carbonyl (-CO); acrylamide (-CONH$_2$); sulfonic acid (-SO$_3$H); ester (-COOR); phosphoric acid (-PO$_3$H$_2$) amongst

others.[77b] These functional groups, together with the polymer backbone, can selectively adsorb onto a specific crystal surface through molecular recognition and thus prevent precipitation.

Historically, both natural and synthetic additives have been used to control the size and morphologies of mineral crystals such as calcium carbonate and calcium phosphate. Carboxylic- and phosphate-containing inhibitors are of the utmost importance. Phosphate-containing scale inhibitors, in particular, have been widely applied. However, regulations have been set up to gradually eliminate the use of phosphate agents due to environmental concerns.

Natural macromolecules, such as polysaccharides (starch, cellulose), tannic acid,[131] modified lignin,[132] chitosan,[100] algin[132a] and natural organic acids such as humic acid and fulvic acid[84, 91, 131, 133] have been used as scale inhibitors during the early development.[132b] Natural macromolecules are much more environmentally friendly than their synthetic counterparts, but tend to decompose at high temperature and thus lose inhibition ability. In addition, relatively large amounts of the compounds (50 - 200 mg L^{-1}) are required for satisfactory inhibition.[132b] Given these disadvantages, natural macromolecules have been abandoned and replaced with phosphate-containing inhibitors in the later stage.

Phosphate-containing inhibitors (linear inhibitors) were introduced due to their versatility, low cost, and high performance in both scale and corrosion inhibition.[77b] There are three different types of phosphate containing inhibitor: phosphonates, polyphosphates, and organophosphates. The phosphonate type is an effective calcium sulfate inhibitor but not effective for calcium carbonate inhibition. Sodium tripolyphosphate (STPP) and sodium hexametaphosphate (SHMP) are the most widely used polyphosphates. They can stabilize more Ca^{2+} and Mg^{2+} in solution, and hence supersaturation levels are reduced or eliminated. The inhibition efficiency of polyphosphates and calcium tolerance increase with increasing phosphonate concentration.[134] Unfortunately polyphosphate inhibitors tend to hydrolyze into orthophosphate and lose their inhibition ability, especially at elevated temperatures. Therefore, simple polyphosphate inhibitors in cooling water treatment have been abandoned and replaced with organophosphate inhibitors, such as 1-hydroxyethyidene-1,1-diphosphonic acid (HEDP), phophonobutane-tricarboxylic acid or amino tris-methylene phosphonate (AMP). Inhibition effectiveness for calcite assessed by the turbidity method shows the following order: PBTC >> AMP > HEDP (PBTC: 2-phosphonobutane-1,2,4-tricarboxylic acid).[134] These organophosphate

inhibitors are among some of the most powerful known crystallization inhibitors, but their negative effects on the environment drive the search for inhibitors that are eco-friendly but with similar, if not higher, inhibition ability.[109a]

1.4.2 Aromatic carboxylic acid as Inhibitors for Calcium Carbonate

Non-polymeric inhibitors as candidates for 'green inhibitors' are now under investigation and can be classified into two types: linear and aromatic inhibitors. Aromatic carboxylic acid can be further divided into benzene-based carboxylic acid and cyclo-polycarboxylic acids. The effects of benzene-based inhibitors with other types of linear inhibitor have been compared by Amjad using the constant composition method. He concluded that inhibitors for $CaCO_3$ scale reduction at pH=8.5, T=30 ℃, can have the following order of effectiveness: poly(acrylic acid) (PAA) >> benzene hexacarboxylic acid (BHCA) ~ fulvic acid (FA) > tannic acid (TA) > benzene-1,3,5-tricarboxylic acid (BTCA) ~ salicylic acid (SA).[135] The crystallization rate can decrease by half by using 0.3 mg L^{-1}, 0.2 mg L^{-1}, 0.0175 mg L^{-1} of tannic acid, fulvic acid and poly(acrylic acid), respectively, indicating the effect of dispersion can enhance inhibition efficiency.[131] Focus is shifting to cyclo-polycarboxylic acid inhibitors, which have proved to be more efficient scale inhibitors than linear carboxylic acids.[136] An 80% reduction in growth rate could be achieved by using 0.01 mg L^{-1}. cyclopentanetetracarboxylic acid (CPTCA), though a linear carboxylic acid causes no decrease in growth rate at the same concentration.[136] Carboxylic-containing inhibitors can be candidates to replace the phosphate-containing inhibitors if their production process is suitably environmentally friendly. In this project, the inhibition efficiency of cyclo-polycarboxylic acids for $CaCO_3$ control under dishwasher condition will be explored in Chapter 5.

1.4.3 Inhibition Mechanism

The scale inhibitors in use today generally exert three effects on minerals: chelating, dispersion and lattice distortion. Chelating agents tend to form water soluble complexes with mineral cations so that the solubility product will not be exceeded because of the reduced free cation concentration and hence the system does not reach the supersaturation level required for crystallization. This approach, however, requires at least a stoichiometric quantity of a chelating agent for effective inhibition, which is undesirable. Threshold inhibitors that can achieve the

same or higher inhibition efficiency with considerable less compound than required stoichiometrically, usually parts per million, are more desirable.[132b] This threshold effect has been attributed to surface adsorption and the disruptive ability of the additive rather than complexion.[103a] Both the dispersion and chelation can enhance inhibition efficiency, which is mainly caused by the blockage of active sites.

Firstly, it should be noted that the adsorption phenomenon of the inhibitor is quite different from surface adsorption by surfactants/polymers. The inhibitor molecular is able to interact strongly with the solute and resides within the emerging nucleus, whilst the surfactant or polymer, which are both solute-philic and solvent-philic, reside at the solute/solvent interface to retard nucleation and crystal growth or promote nucleation.[98] Based on molecular simulations, Anwar and coworkers[98] suggest that an efficient inhibitor should firstly have a high affinity for the solute, and the size of the inhibitor should be larger than that of the solute so that the inhibitor can become incorporated into the emerging nucleus and will not be excluded from it. Secondly, it should have a disruptive ability that can ruin the crystal packing, so the critical nuclei size will not be reached. Eventually, the cluster redissolves, setting themselves and the inhibitor molecule free.[103] This is consistent with the statement made by Gill[109a] that the inhibitor adsorption is completely reversible during nucleation inhibition. The disruption effect of the inhibitor can be caused by steric, entropic or energetic effects, which are not very well defined and require future work.[98] Thirdly, inhibitor molecules with high self-affinity should be avoided as these will minimize their interaction with the solute molecules and thus decrease their impact on solute nucleation. Strong additive-additive interactions will only encourage the additive molecules to self-association instead of disrupt crystal packing.[98]

The question now is how an inhibitor can be designed. In molecular recognition studies, we know that the electrostatic and stereochemical matching overrides structural matching in most cases,[53] but it also suggests that even if the strict structural matching is not required, the spacing of functional groups should be complementary to the required polymorph or desired crystal plane. In section 1.3.2, we saw that surface deposition starts from the aggregation of the amorphous phase, which orders to form stable nuclei via coalescence of several subcrystalline nuclei.[53] It suggests that even if the nuclei are subcrystalline, they still have sufficient local order to mimic a

particular crystal plane. Therefore, structural matching between the spacing of the functional group and that on the crystal lattice can ultimately offer some inspiration for inhibitor design.

Now we can rethink the study of the inhibition efficiency comparison of a series of inhibitors for BaSO$_4$ inhibition. The inhibitors of phosphonates are particularly effective for reduction in BaSO$_4$ growth rate,[107, 137] which means that the functional group of the phosphonates has enough affinity for Ba^{2+}. Studies of BaSO$_4$ inhibitors by Black[137] further show that only phosphonates having at least two phosphonic acid groups linked by a three-atom chain can make a change in morphology, such as amino dimethylene phosphonic acid, propane- 1,3-diphosphonic acid, amino trimethylene phosphonic acid and ethane-1,2 diaminotetramethylenephosphonic acid Figure 1.29. With the crystal lattice matching, the dimension/ size of the backbone of the inhibitor structure can be determined. So the only problem now left to consider is which crystal plane(s) occurs first for a specific system. However, this is still largely a mystery, partly because the molecular-level processes involved are inaccessible to experiment.[98]
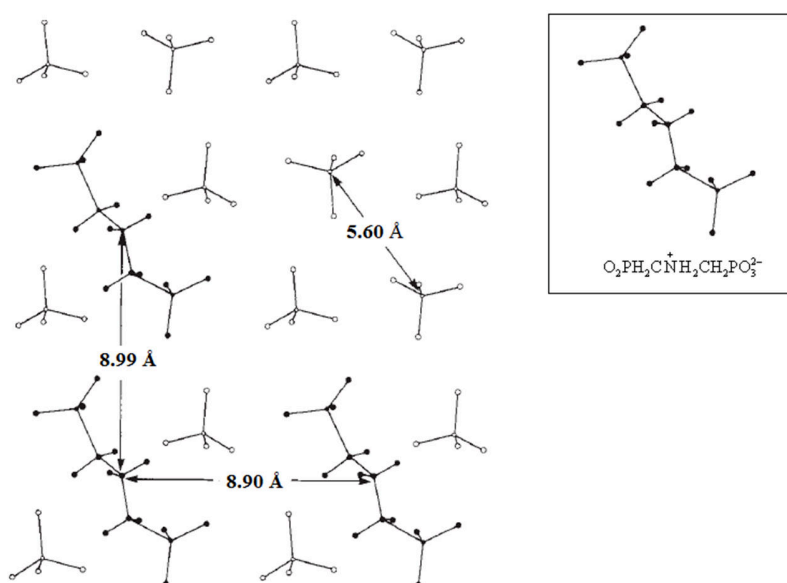
Figure 1.28   Motif replacement on the crystal face (011) of BaSO$_4$ can be carried out by the disphosphonate occupying the two adjacent SO$_4$ binding sites in a similar orientation.[138] (Reproduced with the permission of ref.138, Copyright @ 1969, Royal Society of Chemistry).

1.4.4 Current Design Strategies for CaCO$_3$ Inhibition

Current design strategies for CaCO$_3$ control are more focused on crystal growth, based on molecular recognition.[39, 139, 138, 140] Coveney et al. proposed that an additive capable of binding all

growing faces can be an effective inhibitor.[141] A specific diazo crown ether is designed based on the principle of molecular recognition. It has sufficient conformations and is able to bind all most active crystal surfaces of $BaSO_4$ and results in an almost round shape of the crystals. An inhibitor of this kind may be efficient for one cycle of crystallization as long as the resulting round crystals are invisible to the naked eye. Considering the application of the inhibitor for this project, even if the crystal growth is initially inhibited, a spherical crystal is still left on the surface, which can serve as a nucleator for the next potential crystallization cycle that arises in the dishwashing process. This may not be the most efficient strategy for $CaCO_3$ inhibition inside a dishwasher. Hence, probably the inhibition action should be effective before the nucleation stage. For example, a nucleation delay that extends the width of the metatable zone and delays the formation of nuclei during the washing cycle inside the dishwasher, so that no crystal is formed by the end, can be a possible efficient strategy for the scale control.

One study on HEDP inhibition ability for hydroxyapatite formation shows that HEDP can delay the transformation of amorphous calcium phosphate to hydroxyapatite and inhibit the crystal growth at the same time. The use of 50 μM HEDP is able to delay the transformation of amorphous calcium phosphate to hydroxyapatite for 40 minutes.[142] A similar conclusion has been made by Chen[143] using polyphosphinocarboxylic acid (PPCA: 10 mg L^{-1}) for $CaCO_3$ inhibition. It is shown that PPCA lengthens the induction time of the surface deposition and suppresses calcite formation, resulting in a vaterite-dominated scale. It also causes a change of lattice parameter for both calcite and vaterite crystals. The length of the c-axis of the unit cell increases and the a- and b-axes decrease. The empirical evidence shows a good inhibitor can not only delay the formation of nuclei but also inhibit crystal growth.

Recently, it has been reported that phytic acid (inositol hexakis phosphate) can stabilize the material described as amorphous calcium carbonate (ACC) for more than three months. The stabilized ACC contains 5%wt of additive and 15%wt of water. The inhibition mechanism is suggested being that the phytic acid inhibits the aggregation of the primary particles.[144] Stabilization of ACC can be an inhibition protocol to control crystal growth since ACC has a higher solubility and can be easily flushed away under hydrodynamical conditions. This needs to be further verified by experiment.

Probably an ideal inhibitor is the one that can not only delay the nucleation but at the same time, can stop the transformation of ACC to a crystalline phase. Of course, it is still hard to say what exactly is the inhibition mechanism, or actually whether the best inhibitor is one with multifunction that can not only delay nucleation and inhibit crystal growth but can also stabilize the ACC and inhibit the aggregation of the primary particles. It was proposed by Verch[145] that one additive can have multiple functions during the crystallization process. He also summarized nine different categories of action that an inhibitor/additive may take place during crystallization processes. However, none of the inhibitors of interest in this project were discussed. It may be a good starting point, though, for a systematical study of what an efficient inhibition should behave like in a real crystallization process.

1.4.5 Other Inhibition Methods

Two types of techniques have been applied to reduce mineral deposition. One is to add chemical additives like inhibitors and surfactants as described above. This chemical approach proves to be a more effective method than physical methods.[146] Physical methods like applied magnetic fields, electric fields or ultrasound to reduce mineral deposition are a less expensive method and are very environmentally friendly.[146,147, 148]

In general, the resulting deposits obtained under physical inhibition methods (magnetic field, electric field, and ultrasound) are less tenacious and dense so they can be more easily washed away.[147d, 148] Several underlining mechanisms have been proposed, but an agreement has not been achieved for the physical inhibition methods.[148b]

1.4.5.1   Magnetic fields

Mineral inhibition by magnetic fields (MF) has been used for more than a half-century.[147f] A magnetic field is produced by applying AC or a pulsing current on a magnetic unit.[147b, 148a] The mechanism of MF based inhibition is still controversial. The efficiency-related parameters are also not clearly defined.[147a-c, 147e, 148a, 149] In general, a magnetic field can enhance the Lorenz force and magnetohydrodynamic effects and lead to a faster micellization and thus more effective nucleation.[147f] The following antiscale effects can be achieved by a magnetic field.[148b, 149]

1) Formation of soft scales, which can be more easily washed away.

2) Removing existing scale.

3) Changing the crystal morphology.

1.4.5.2   Electric Field (EF)

The application of electric field exerts three effects: sterilization, intense particle coagulation, and soft, resulting precipitates. The exact mechanism is suggested to involve the electric field altering the activation barrier of nucleation and the polymorph equilibrium[148a, 150] and thus changing the morphology of the crystal.

1.4.5.3   Use of Ultrasound

Ultrasound, in the case of calcium carbonate, enables calcium carbonate to crystallize in solution and significantly reduces scale deposition on the solid surface.[58d] The whole calcium carbonate precipitation processes including ionic association, dehydration, and phase transformation speed have been highly influenced by the intense physical mixing caused by ultrasound. It is found that the pre-nucleation rate is proportional to the ultrasound intensity.[26] Unlike the magnetic field and electric field cases, the resultant morphology of crystals is not affected by the ultrasound. Also, more crystals are observed at the expense of the crystal size.[40, 151]

1.5 Conclusion

We have overviewed two main pathways for mineral crystallization, namely, classical and non-classical crystallization. In doing so, we can have a general theoretical basis for the mineral formation and deposition as well as mineral inhibition for future discussion. The emphasis is placed on the understanding of surface crystallization and deposit control on surfaces with and without additives and how the deposition rate and the properties of the resulting crystals on a surface change under different conditions. These conditions in a dishwasher include the pH and the temperature of the solution, the agitation, the substrate properties and the additives. The three different modes of interaction between the additive and substrate that may affect the growth mode of crystals and resulting morphologies are discussed. They are the substrate-directed nucleation, additive-directed nucleation/inhibition and the crystal growth inhibition/ nucleation resulting from the interplay of substrate and additive. These three modes are highly dependent on the conditions of the specific system applied.

With the understanding of the crystallization mechanism with and without additives, we also review the development of scale inhibitors in history and the poly(carboxylic acids) that we are going to explore as a 'green' alternative for HEDP in this project. An updated view of the inhibition mechanism and current design strategies for an efficient scale inhibitor is also included. Crystal growth inhibition, nucleation delay or a combination of both may be a better explanation for the inhibition of the repeated crystallization situation.

1.6 Project Aims

This project has two main objectives: one is to understand the occurrence of filming and spots on kitchenware (particularly on plastic ware) during dishwasher procedures; another is due to increasing government regulation aimed towards discontinuation of the use of phosphate-containing additives and their replacement with nil-phosphate (nil-P) alternatives. Thus this study aims to develop potential 'green' alternative inhibitors for the scale inhibitor 1-hydroxy ethylidene-1,1-diphosphonic acid (HEDP) under the particular conditions found in a dishwasher (high alkalinity, high ionic strength, and high temperature). To start with, experiments aimed towards the understanding of particularly severe deposition on plastics and glass samples will be carried out. This understanding will focus on the ingredients of the prototype dishwasher detergent and the factors inside the dishwasher. Those factors include the orthophosphate ions, operation temperature in the main wash cycle and the soil from food residues. The inhibition effectiveness of different phosphate-free inhibitors will be compared to HEDP and tested out both in model systems and in a real dishwasher. Based on the understanding of deposition on the surface, an investigation on the relationship between the structure of the inhibitor and its effectiveness to mineral growth inhibition will be carried out to gain a better understanding of the underlying inhibition mechanism. In particular, we will examine the structural chemistry of a range of calcium complexes of oligo carboxylate candidate inhibitors in order to gain insights into the ligand binding site and mode of interaction with the metal ions.

1.7 References

1.   (a) Wang, H.; Alfredsson, V.; Tropsch, J.; Ettl, R.; Nylander, T. *Appl. Mater. Interfaces* **2013,** *5* (10), 4035-4045; (b) Abdel-Aal, N.; Satoh, K.; Sawada, K. *J. Cryst. Growth* **2002,** *245* (1), 87-100.

2.   Mullin, J. B., *Crystallization*. 4th Edition ed.; Butterworth-Heineman: Oxford, 2001; p 587.

3.   *Gi-Xrd Analysis of Glass Slides Washed for 8 Cycles in City Spiked Water*. Procter & Gamble, Newcastle. Unpublished work, 2010.4.   Desiraju, G. R.; Vittal, J. J.; Ramanan, A., *Crystal Engineering: A Textbook*. 1 ed.; World Scientific 2011.

5.   Sabine, H. *Characterization of the Polymer Blend Pmma-Sbr : Combining Confocal Raman and Atomic Force Microscopy*; Witec Wissenschaftliche Instrumente und Technologie GmbH: Ulm, Germany, 2006.

6.   Mann, S.; Webb, J.; Williams, R. J. P., *Biomineralization: Chemical and Biochemical Perspectives*. John Wiley & Sons: 1989.

7.   Sheikholeslami, R. *Desalination* **2004,** *167*, 247-256.

8.   Lide, C., *Handbook of Chemistry and Physics, 2011 Internet Version*. 2012.

9.   Cooper, S. J., Crystallizaion Kinetics. Lecture slide.

10.   Sear, R. P. *J. Phys.: Condens. Matter* **2007,** *19* (3), 033101.

11.   Teng, H. H. *Elements* **2013,** *9* (3), 189-194.

12.   Mann, S., Chemical Control and Biomineralization. In *Biomineralization : Principles and Concepts in Bioinorganic Materials Chemistry*, Mann, S., Ed. Oxford University Press: Oxford, 2001; pp 38-67.

13.   Cooper, S. J. Crystallization Kinetics. http://community.dur.ac.uk/sharon.cooper/lectures/cryskinetics/handoutsalla.html (accessed May 05, 2016).

14.   Wang, L.; Sondi, I.; Matijević, E. *J. Colloid Interface Sci.* **1999,** *218* (2), 545-553.

15.   de Leeuw, N. H.; Parker, S. C. *J. Phys. Chem. B* **1998,** *102* (16), 2914-2922.

16.   Mullin, J. W., Crystal Growth. In *Crystallization (Fourth Edition)*, Butterworth-Heinemann: Oxford, 2001; pp 216-288.

17.   Gautam R. Desiraju; Jagadese J Vittal; Arunachalam Ramanan, *Crystal Engineering : A Textbook*. World Scientific: Singapore, 2011; p 216.

18.   He, G.; Bhamidi, V.; Tan, R. B.; Kenis, P. J.; Zukoski, C. F. *Cryst. Growth Des.* **2006,** *6* (5), 1175-1180.

19.   (a) Burton, W. K.; Cabrera, N.; Frank, F. C. *Philos. Trans. R. Soc. Lond., A* **1951,** *243* (866), 299-358; (b) Myers-Beaghton, A. K.; Vvedensky, D. D. *Phys. Rev. A* **1991,** *44* (4), 2457.

20.   Kossel, W. *Ann. Phys.* **1934,** *413* (5), 457-480.

21.   (a) Stranski, I. N. *Z. Phys. Chem.-Stoch. Ve.* **1928,** *136* (3/4), 259-278; (b) Kossel, W. *Nachr. Ges. Wiss. Göttingen* **1927,** *143*.

22.   Oner, M., Crystal Growth Inhibition of Calcium Sulfate and Calcium Oxalates in Aqueous Systems. In *The Science and Technology of Industrial Water Treatment*, Amjad, Z., Ed. CRC Press 2010: London, 2010; pp Pages 21–38.

23.   Rodriguez-Blanco, J.; Shaw, S.; Benning, L. *Mineral. Mag.* **2008,** *72* (1), 283-286.

24.   (a) Bots, P.; Benning, L. G.; Rodriguez-Blanco, J.-D.; Roncal-Herrero, T.; Shaw, S. *Cryst. Growth Des.* **2012,** *12* (7), 3806-3814; (b) Rodriguez-Blanco, J. D.; Shaw, S.; Benning, L. G. *Nanoscale* **2011,** *3* (1), 265-271; (c) Jada, A.; Pefferkorn, E. *J. Mater. Sci. Lett.* **2000,** *19* (23), 2077-2079; (d) Hardikar, V. V.; Matijević, E. *Colloids Surf., A* **2001,** *186* (1), 23-31; (e) Shen, F.; Feng, Q.; Wang, C. *J. Cryst. Growth* **2002,** *242* (1), 239-244.

25.   Kuntze, R. *Nature* **1966,** *211*, 406 - 407

26.   Cöelfen, H.; Antonietti, M., Nonclassical Crystallization. In *Mesocrystals and Nonclassical Crystallization*, John Wiley & Sons: Chichester, 2008; pp 73-98.

27.   Sreedhar, B.; Vani, C. S.; Devi, D. K.; Rao, M. B.; Rambabu, C. *J. Materials.* **2012,** *2* (1), 5-13.

28.   Merten, H. L.; Bachman, G. L. Stabilized Amorphous Calcium Carbonate. 4237147, 1980.

29.   Loste, E.; Wilson, R. M.; Seshadri, R.; Meldrum, F. C. *J. Cryst. Growth* **2003,** *254* (1), 206-218.

30.   (a) Taylor, M. G.; Simkiss, K.; Greaves, G. N.; Okazaki, M.; Mann, S. *P. Roy. Soc., B* **1993,** *252* (1333), 75-80; (b) Levi‑Kalisman, Y.; Raz, S.; Weiner, S.; Addadi, L.; Sagi, I. *J. Chem. Soc., Dalton Trans.* **2000,** (21), 3977-3982; (c) Hasse, B.; Ehrenberg, H.; Marxen, J. C.; Becker, W.; Epple, M. *Chem. Eur. J.* **2000,** *6* (20), 3679-3685.

31.   Ellis, A. J. *Am. J. Sci.* **1963,** *261* (3), 259-267.

32.   Deng, H.; Wang, X.; Du, C.; Shen, X.; Cui, F. *CrystEngComm* **2012,** *14*, 6647-6653.

33.   Kamhi, S. R. *Acta Crystallogr.* **1963,** *16* (8), 770-772.

34.   Graf, D. L. *Am. Mineral.* **1961,** *46* (11), 1283-1316.

35.   (a) Weiner, S.; Addadi, L. *J. Mater. Chem.* **1997,** *7* (5), 689-702; (b) Meyer, H. J. *Z. Kristallogr.* **1969,** *128* (1-6), 183-212.

36.   Addadi, L.; Weiner, S. *Angew. Chem. Int. Ed. Engl.* **1992,** *31* (2), 153-169.

37.   Cusack, M., Ocean Acidification. The Leverhulme Trust: 2011.

38.   Falini, G.; Fermani, S.; Gazzano, M.; Ripamonti, A. *J. Chem. Soc., Dalton Trans.* **2000,** (21), 3983-3987.

39.   Bendiksen, B.; Gill, J. S., Molecular Modeling in Scale Control-an Experimental Verification and Its Limitations. In *1996 NACE International Annual Conference and Exposition "Corrosion 96",*, NACE International: Houston, Texas, 1996; Vol. 96164.

40.   Meldrum, F. C.; Sear, R. P. *Science* **2008,** *322* (5909), 1802-1803.

41.   (a) Simpson, L. *Electrochimica acta* **1998,** *43* (16-17), 2543-2547; (b) Gao, W.; Ma, X.; Wang, Z.; Zhu, Y. *Colloids Surf., A* **2011,** *389* (1-3), 230-236; (c) Erdemir, D.; Lee, Y. A.; Myerson, S. A. *Acc. Chem. Res.* **2009,** *42* (5), 621-629.

42.   Niederberger, M.; Cölfen, H. *Phys. Chem. Chem. Phys.* **2006,** *8* (28), 3271-3287.

43.   De Yoreo, J. J.; Gilbert, P. U.; Sommerdijk, N. A.; Penn, R. L.; Whitelam, S.; Joester, D.; Zhang, H.; Rimer, J. D.; Navrotsky, A.; Banfield, J. F. *Science* **2015,** *349* (6247), 6760.

44.   Cölfen, H.; Antonietti, M. *Angew. Chem. Int. Edit* **2005,** *44* (35), 5576-5591.

45.   Cöelfen, H.; Antonietti, M., Nonclassical Crystallization. In *Mesocrystals and Nonclassical Crystallization*, John Wiley & Sons: England, 2008; pp 73 -98.

46.   Pichon, B. P.; Bomans, P. H.; Frederik, P. M.; Sommerdijk, N. A. *J. Am. Chem. Soc.* **2008,** *130* (12), 4034-4040.

47.   Gebauer, D.; Völkel, A.; Cölfen, H. *Science* **2008,** *322* (5909), 1819-1822.

48.   Habraken, W. J.; Tao, J.; Brylka, L. J.; Friedrich, H.; Bertinetti, L.; Schenk, A. S.; Verch, A.; Dmitrovic, V.; Bomans, P. H.; Frederik, P. M. *Nat. Commun.* **2013,** *4*, 1507.

49.   Deng, H.; Wang, S.; Wang, X.; Du, C.; Shen, X.; Wang, Y.; Cui, F. *Regener. Biomater.* **2015,** *2* (3), 187-195.

50.   Wang, Q. A Computational Study of Calcium Carbonate. UCL (University College London), 2011.

51.   Aizenberg, J.; Lambert, G.; Weiner, S.; Addadi, L. *J. Am. Chem. Soc.* **2002,** *124* (1), 32-39.

52.   Cölfen, H.; Mann, S. *Angew. Chem. Int. Ed.* **2003,** *42* (21), 2350-2365.

53.   Sommerdijk, N. A. J. M.; With, G. d. *Chem. Rev.* **2008,** *108* (11), 4499-4550.

54.   Vetter, O. J. *J. Pet. Technol.* **1972,** *24* (08), 997-1006.

55.   (a) Sikes, C. S.; Wheeler, A. P., Inhibition of Inorganic and Biological $Caco_3$ Deposition by a Polysaccharide Fraction Obtained from $Caco_3$-Forming Organisms. U.S. Patent 6,563,252: April 29, 1986; (b) Benedetti, E.; Corradini, P.; Pedone, C. *J. Phys. Chem.* **1972,** *76* (5), 790-797.

56.   Richter, A.; Petzold, D.; Hofmann, H.; Ullrich, B. *Chem. Tech. - Leipzig* **1996,** *48* (5), 271-275.

57.   (a) Weiss, I. M.; Tuross, N.; Addadi, L.; Weiner, S. *J. Exp. Zool.* **2002,** *293* (5), 478-91; (b) Zhang, Z.; Xie, Y.; Xu, X.; Pan, H.; Tang, R. *J. Cryst. Growth* **2012,** *343* (1), 62-67.

58.   (a) Nancollas, G.; Reddy, M. *Soc. Pet. Eng. J.* **1974,** *14* (02), 117-126; (b) Chong, T.; Sheikholeslami, R. *Chem. Eng. Sci.* **2001,** *56* (18), 5391-5400; (c) House, W. A. *J. Chem. Soc., Faraday Trans. 1* **1981,** *77* (2), 341; (d) Söhnel, O.; Mullin, J. *J. Cryst. Growth* **1982,** *60* (2), 239-250.

59.   (a) Chen, T.; Neville, A.; Sorbie, K.; Zhong, Z. *Faraday Discuss.* **2007,** *136*, 355-365; (b) Chen, T.; Neville, A.; Yuan, M. *J. Pet. Sci. Eng.* **2005,** *46* (3), 185-194; (c) Chen, T.; Neville, A.; Yuan, M. *J. Cryst. Growth* **2005,** *275* (1), e1341-e1347.

60.   Cheong, W. C.; Gaskell, P. H.; Neville, A. *J. Cryst. Growth* **2013,** *363* (0), 7-21.

61.   Zhang, T. H.; Liu, X. Y. *J. Am. Chem. Soc.* **2007,** *129* (44), 13520-13526.

62.   Zhang, T. H.; Liu, X. Y. *Angew. Chem. Int. Ed.* **2009,** *48* (7), 1308-1312.

63.   Pouget, E. M.; Bomans, P. H.; Goos, J. A.; Frederik, P. M.; Sommerdijk, N. A. *Science* **2009,** *323* (5920), 1455-1458.

64.   Sohnel, O.; Garside, J. *J. Cryst. Growth* **1988,** *89* (2-3), 202-208.

65.   Zhao, X.; Chen, X. D. *Heat Transfer Eng.* **2013,** *34* (8-9), 719-732.

66.   Elfil, H.; Roques, H. *AlChE J.* **2004,** *50* (8), 1908-1916.

67.   (a) Amjad, Z.; Zuhl, R. W., Kinetic and Morphological Investigation on the Precipitation of Calcium Carbonate in the Presence of Inhibitors. In *1996 NACE International Annual Conference and Exposition "Corrosion 2006",*, NACE International: Houston, Texas, 2006; Vol. 06385; (b) Wray, J. L.; Daniels, F. *J. Am. Chem. Soc.* **1957,** *79* (9), 2031-2034.

68.   Koutsoukos, G. P., Calcium Carbonate Scale Control in Industrial Water Systems

In *The Science and Technology of Industrial Water Treatment*, Amjad, Z., Ed. CRC Press Boca Raton Florida: 2010.

69.   Lower, S. K. *Simon Fraser University* **1999**, 15.

70.   Rodriguez-Blanco, J.; Shaw, S.; Bots, P.; Roncal-Herrero, T.; Benning, L. *J. Alloys Compd.* **2012,** *536*, 477-479.

71.   Kitamura, M.; Konno, H.; Yasui, A.; Masuoka, H. *J. Cryst. Growth* **2002,** *236* (1), 323-332.

72.   Kardiman, K.; Muryanto, S.; Bayuseno, A. *Procedia Chemistry* **2016,** *9*, 69-76.

73.   Jiang, J.; Zhang, Y.; Xu, D.; Liu, J. *CrystEngComm* **2014,** *16* (24), 5221-5226.

74.   (a) Hasson, D.; Avriel, M.; Resnick, W.; Rozenman, T.; Windreich, S. *Ind. Eng. Chem. Fundam.* **1968,** *7* (1), 59-65; (b) Hatch, G. *Materials of Protection and Performance* **1973**.

75.   Bott, T. R., General Fouling Problems. In *Fouling Science and Technology*, Kluwer Academic Publishers: Dordrecht, The Netherlands, 1988; pp 3-14.

76.   Walker, P.; Sheikholeslami, R. *Chem. Eng. Sci.* **2003,** *58* (16), 3807-3816.

77.   (a) Supothina, S.; Rattanakam, R. *Mater. Chem. Phys.* **2011,** *129* (1), 439-445; (b) Zeng, S.; Xu, X.; Wang, S.; Gong, Q.; Liu, R.; Yu, Y. *Mater. Chem. Phys.* **2013,** *140* (1), 159-167.

78.   Han, Y. S.; Hadiko, G.; Fuji, M.; Takahashi, M. *J. Eur. Ceram. Soc.* **2006,** *26* (4), 843-847.

79.   Hasson, D., Precipitation Fouling. In *Fouling of Heat Transfer Equipment*, J.G., K., Ed. Hemisphere: New York, 1981; pp 527-568.

80.   Macadam, J.; Parsons, S. *Water Sci. Technol.* **2004,** *49* (2), 153-159.

81.   Calvert, P.; Rieke, P. *Chem. Mater.* **1996,** *8* (8), 1715-1727.

82.   (a) Kim, I. W.; Robertson, R. E.; Zand, R. *Adv. Mater.* **2003,** *15* (9), 709-712; (b) Pokroy, B.; Zolotoyabko, E. *Chem. Commun.* **2005,** (16), 2140-2142.

83.   Garrett-Price, B. *Noyes Publications, 1985* **1985**, 417.

84.   Yang, Q.; Ding, J.; Shen, Z.-Q. In *Sam Heat Transfer Surface Fouling Behavior and Fouling Behaviour and Fouling Fractal Characteristics*, Proceedings of an International Conference on Mitigation of Heat Exchanger Fouling and Its Economic and Environmental Implications, Alberta, Canada, New York: Begell House: Alberta, Canada, 2001; p 239.

85.   Roques, H.; Girou, A. *Water Res.* **1974,** *8* (11), 907-920.

86.   Oliveira, R. *Exp. Therm Fluid Sci.* **1997,** *14* (4), 316-322.

87.   Förster, M.; Bohnet, M. *Int. J. Therm. Sci.* **2000,** *39* (7), 697-708.

88.   (a) Kukulka, D. *Heat Transfer Eng.* **2005,** *26* (5), 42-46; (b) Gunn, D. J. *J. Cryst. Growth* **1980,** *50* (2), 533-537.

89.   Mueller-Steinhagen, H., Heat Exchanger Fouling: Mitigation and Cleaning Technologies. PUBLICO Publication Essen, Germany, 2000; pp 507-532.

90.   Izumi, K.; Takahashi, S.; Sawa, T.; Ikenaga, Y. In *Sludge Deposition and Scale Formation on the Surface of the Heat Transfer Tubes in Multi-Stage Flash Evaporators*, Proceeding of the 6th International Symposium Fresh Water From the Sea, Athens, European Federation of Chemical Engineering. : Athens, 1978; pp 201-209.

91.   Bhushan, B.; Jung, Y. C.; Koch, K. *Philos. Trans. R. Soc., A* **2009,** *367* (1894), 1631-1672.

92.   McGuire, J.; Swartzel, K. R. *Surf. Interface Anal.* **1987,** *10* (8), 430-433.

93.   (a) Mann, S.; Heywood, B. R.; Rajam, S.; Birchall, D. J. *Nature* **1988,** *334* (6184), 692-695; (b) Aizenberg, J.; Black, A. J.; Whitesides, G. M. *Nature* **1998,** *394* (6696), 868-871; (c) Aizenberg, J.; Black, A. J.; Whitesides, G. M. *Nature* **1999,** *398* (6727), 495-498.

94.   Jayaraman, A.; Subramanyam, G.; Sindhu, S.; Ajikumar, P. K.; Valiyaveettil, S. *Cryst. Growth Des.* **2007,** *7* (1), 142-146.

95.   Addadi, L.; Moradian, J.; Shay, E.; Maroudas, N.; Weiner, S. *Proc. Natl. Acad. Sci.* **1987,** *84* (9), 2732-2736.

96.   Donners, J. J.; Nolte, R. J.; Sommerdijk, N. A. *J. Am. Chem. Soc.* **2002,** *124* (33), 9700-9701.

97.   Song, R.-Q.; Cölfen, H. *CrystEngComm* **2011,** *13* (5), 1249-1276.

98.   Anwar, J.; Boateng, P. K.; Tamaki, R.; Odedra, S. *Angew. Chem. Int. Ed.* **2009,** *48* (9), 1596-1600.

99.   Deganello, S. *Acta Crystallogr., Sect. B: Struct. Sci.* **1981,** *37* (4), 826-829.

100.   Junwu Xiao, Y. Z., Yanyan Liu,Huijuan Liu, Yi Zeng,Fangfang Xu,and Lanzhou Wang *Crystal Growth & Design* **2008,** *VOL. 8, NO. 8 2887–2891.*

101.   Cölfen, H., Bio-Inspired Mineralization Using Hydrophilic Polymers. In *Biomineralization Ii*, Springer-Verlag: Berlin, 2007; pp 1-77.

102.   Cody, R. D. *J. Sediment. Res.* **1991,** *61* (5), 1527-1404.

103.   (a) Oner, M., Crystal Growth Inhibition of Calcium Sulfate and Calcium Oxalates in Aqueous Systems. In *The Science and Technology of Industrial Water Treatment*, Amjad, Z., Ed. CRC Press: 2010; p 21; (b) Rodriguezhornedo, N.; Carstensen, J. T. *J. Pharm. Sci.* **1986,** *75* (6), 552-558.

104.   Davey, R. *J. Cryst. Growth* **1976,** *34* (1), 109-119.

105. Van der Leeden, M.; Kashchiev, D.; Van Rosmalen, G. *J. Cryst. Growth* **1993,** *130* (1), 221-232.

106. Lowenstam, H. A.; Weiner, S., *On Biomineralization*. Oxford University Press: New York, 1989; p 336.

107. Karipides, A.; Ault, J.; Reed, A. T. *Inorg. Chem.* **1977,** *16* (12), 3299-3302.

108. Nancolla.G.H.; Reddy, M. M. *Abstracts of Papers of the American Chemical Society* **1973**, 39.

109. (a) Gill, J. S., Development of Scale Inhibitors. In *NACE Corrosion Conference*, NACE International

Houston, United States, 1996; Vol. 229, pp 2-9; (b) Weissbuch, I.; Lahav, M.; Leiserowitz, L. *Acta Crystallogr. Sect. B: Struct. Sci.* **1999**, 166.

110. Weissbuch, I.; Popovitz-Biro, R.; Lahav, M.; Leiserowitz, L.; Rehovot *Acta Cryst. B* **1995,** *51* (2), 115-148.

111. Titiloye, J. O.; Parker, S. C.; Mann, S. *J. Cryst. Growth* **1993,** *131* (3-4), 533-545.

112. (a) Yu, S. H.; Cölfen, H.; Antonietti, M. *Chem. - Eur. J.* **2002,** *8* (13), 2937-2945; (b) Qi, L.; Cölfen, H.; Antonietti, M.; Li, M.; Hopwood, J. D.; Ashley, A. J.; Mann, S. *Chem. - Eur. J.* **2001,** *7* (16), 3526-3532.

113. (a) Politi, Y.; Levi‐Kalisman, Y.; Raz, S.; Wilt, F.; Addadi, L.; Weiner, S.; Sagi, I. *Adv. Funct. Mater.* **2006,** *16* (10), 1289-1298; (b) Hasse, B.; Ehrenberg, H.; Marxen, J. C.; Becker, W.; Epple, M. *Chem. - Eur. J.* **2000,** *6* (20), 3679-3685.

114. Abdel-Aal, N.; Sawada, K. *J. Cryst. Growth* **2003,** *256* (1), 188-200.

115. Hou, W.; Feng, Q. *J. Cryst. Growth* **2005,** *282* (1), 214-219.

116. Nassif, N.; Gehrke, N.; Pinna, N.; Shirshova, N.; Tauer, K.; Antonietti, M.; Cölfen, H. *Angew. Chem. Int. Ed.* **2005,** *44* (37), 6004-6009.

117. Addadi, L.; Joester, D.; Nudelman, F.; Weiner, S. *Chem. - Eur. J.* **2006,** *12* (4), 980-987.

118. Freer, A.; Bridgett, S.; Jiang, J.; Cusack, M. *Mar. Biotechnol.* **2014,** *16* (1), 34-45.

119. Van Der Merwe, J. H. *Metall. Mater. Trans. A* **2002,** *33* (8), 2475-2483.

120. Duffy, D. M.; Travaille, A. M.; van Kempen, H.; Harding, J. H. *J. Phys. Chem. B* **2005,** *109* (12), 5713-5718.

121. Mann, S. *Nature* **1988,** *332* (6160), 119-124.

122. Deng, H.; Shen, X.-C.; Wang, X.-M.; Du, C. *Front. Mater. Sci.* **2013,** *7* (1), 62-68.

123. Weiner, S.; Traub, W.; Parker, S. *Philos. Trans. R. Soc. Lond., B* **1984,** *304* (1121), 425-434.

124. Beveland, G.; Nakahara, H. *Calc. Tiss. Res.* **1969,** *4* (2), 101.

125. (a) Weiner, S.; Traub, W. *Fed. Eur. Biochem. Soc.* **1980,** *111*, 311-318; (b) Weiner, S.; Talmon, Y.; Traub, W. *Int. J. Biol. Macromol.* **1983,** *5* (6), 325-328.

126. Crichton, R., Biomineralisation. In *Biological Inorganic Chemistry (Second Edition)*, Crichton, R., Ed. Elsevier: Oxford, 2012; pp 359-378.

127. Didymus, J. M.; Oliver, P.; Mann, S.; DeVries, A. L.; Hauschka, P. V.; Westbroek, P. *J. Chem. Soc., Faraday Trans.* **1993,** *89* (15), 2891-2900.

128. Heywood, B. R.; Mann, S. *Chem. Mater.* **1994,** *6* (3), 311-318.

129. Buijnsters, P. J.; Donners, J. J.; Hill, S. J.; Heywood, B. R.; Nolte, R. J.; Zwanenburg, B.; Sommerdijk, N. A. *Langmuir* **2001,** *17* (12), 3623-3628.

130. *Acusol™ 588: Polyphosphate and Silicate Scale Inhibitor for Laundry and Automatic Dishwashing Detergents*; Rohm and Haas Company 2008.

131. Beniash, E.; Aizenberg, J.; Addadi, L.; Weiner, S. *Proc. R. Soc. London, Ser. B* **1997,** *264* (1380), 461-465.

132.   (a) Amjad, Z.; Zuhl, R., ,W.; Huang, S., Deposit Control Polymers: Types, Characterization and Applications. In *The Science and Technology of Industrial Water Treatment*, Amjad, Z., Ed. CRC Press Boca Raton, Florida, 2010; pp 447-464; (b) Wucher, B.; Yue, W.; Kulak, A. N.; Meldrum, F. C. *Chem. Mater.* **2007,** *19* (5), 1111-1119.

133.   Rietveld, H. M. *J. Appl. Crystallogr.* **1969,** *2* (2), 65-71.

134.   Gill, J. S.; Varsanik, R. G. *J. Cryst. Growth* **1986,** *76* (1), 57-62.

135.   Amjad, Z.; Pugh, J.; Reddy, M. M., Kinetic Inhibition of Calcium Carbonate Crystal Growth in the Presence of Natural and Synthetic Organic Inhibitors. In *Water Soluble Polymers*, Kluwer Academic Publishers: New York, 2002; pp 131-147.

136.   Reddy, M. M.; Hoch, A. R. *J. Colloid Interface Sci.* **2001,** *235* (2), 365-370.

137.   Chung, J.; Granja, I.; Taylor, M. G.; Mpourmpakis, G.; Asplin, J. R.; Rimer, J. D. *Nature* **2016**, 1-5.

138.   Black, S. N.; Bromley, L. A.; Cottier, D.; Davey, R. J.; Dobbs, B.; Rout, J. E. *J. Chem. Soc., Faraday Trans.* **1991,** *87* (20), 3409-3414.

139.   (a) Wierzbicki, A.; Sikes, C.; Madura, J.; Drake, B. *Calcif. Tissue Int.* **1994,** *54* (2), 133-141; (b) Mann, S.; Didymus, J. M.; Sanderson, N. P.; Heywood, B. R. *J. Chem. Soc., Faraday Trans.* **1990,** *86* (10), 1873-1880.

140.   (a) Bromley, L. A.; Cottier, D.; Davey, R. J.; Dobbs, B.; Smith, S.; Heywood, B. R. *Langmuir* **1993,** *9* (12), 3594-3599; (b) Rohl, A.; Gay, D.; Davey, R.; Catlow, C. *J. Am. Chem. Soc.* **1996,** *118* (3), 642-648.

141.   Coveney, P. V.; Davey, R.; Griffin, J. L.; He, Y.; Hamlin, J. D.; Stackhouse, S.; Whiting, A. *J. Am. Chem. Soc.* **2000,** *122* (46), 11557-11558.

142.   Williams, G.; Sallis, J. D. *Calcif. Tissue Int.* **1982,** *34* (1), 169-177.

143.   Chen, T.; Neville, A.; Sorbie, K.; Zhong, Z. *Chem. Eng. Sci.* **2009,** *64* (5), 912-918.

144.   Xu, A. W.; Yu, Q.; Dong, W. F.; Antonietti, M.; Cölfen, H. *Adv. Mater.* **2005,** *17* (18), 2217-2221.

145.   Verch, A.; Gebauer, D.; Antonietti, M.; Cölfen, H. *Phys. Chem. Chem. Phys.* **2011,** *13* (37), 16811-16820.

146.   Tamer, M. *J. Mod. Phys.* **2013,** *4*, 1149-1157.

147.   (a) Schmidt, U.; Hild, S.; Ibach, W.; Hollricher, O. *Macromol. Symp.* **2005,** *230* (1), 133-143; (b) Borosilicate Glass. https://en.wikipedia.org/wiki/Borosilicate_glass (accessed May 3, 2015); (c) Bhushan, B., Surface Roughness Analysis and Measurement Techniques. In *Modern Tribology Handbook*, CRC Press: London, 2001; Vol. 1, pp 49-119; (d) Anonymous, *Surface Texture (Surface Roughness, Waviness and Lay)*. ANSI/ASME: New York, 1985; Vol. B46.1; (e) Howstuffworks: How Does a Dishwasher Work? http://www.rsc.org/learn-chemistry/resources/chemistry-in-your-cupboard/finish/2 (accessed November 7); (f) Bajpai, D.; Tyagi, V. *J. Oleo Sci.* **2007,** *56* (7), 327-340.

148.   (a) *Knowitall Academic Edition*, version 2005; Bio‑Rad Laboratories: 2005; (Accessed May 05, 2016); (b) Sheldrick, G. M. *Acta Crystallogr. Sect. A: Found. Crystallogr.* **1990,** *46* (6), 467-473.

149.   Goodhew, P. J.; Humphreys, J.; Beanland, R., *Electron Microscopy and Analysis*. CRC Press: 2000.

150.   (a) Wollman, D. A.; Irwin, K. D.; Hilton, G. C.; Dulcie, L. L.; Newbury, D. E.; Martinis, J. M. *J. Microsc.* **1997,** *188* (3), 196-223; (b) Shindo, D.; Oikawa, T., Energy Dispersive X-Ray Spectroscopy. In *Analytical Electron Microscopy for Materials Science*, Spinger-Verlag Tokyo: Tokyo, Japan, 2002; pp 81-102; (c) *Nanoscope Software 6.13 Uer Guide*, version Veeco Instruments Inc.: 2004; (Accessed).

151.   Lin, Y.-P.; Singer, P. C. *J. Cryst. Growth* **2009,** *312* (1), 136-140

Blank Page

2 CaCO$_3$ Crystallization with Nil-HEDP Formula

2.1 Introduction

The precipitated calcium carbonate either suspended in bulk solution or deposited on a solid surface is the result of the combined effects of various factors. These factors include the supersaturation level, temperature, agitation, pH, surface properties and type of additives, among which, the surface-active additives (ions and inhibitors) exhibit the most significant effects.[1] To gain an overall understanding of the formation of CaCO$_3$, it is important to understand CaCO$_3$ crystallization both with and without the presence of additives.

Table 2.1 Nil-phosphate prototype ADW formula (HEDP formula)

Prototype formula	Abbre.	Raw material in water (g 5L^{-1})	Comments
Alkaline Builder			
Trisodium salt of methylglycinediacetic acid	Na$_3$MGDA	2.82	Chelator
Granular sodium carbonate	Na$_2$CO$_3$	9.54	pH buffer
Sodium sulphate	Na$_2$SO$_4$	3.06	Solid diluter
Polymer			
Sulfonated polyacrylates Acusol 588	Acusol 588G	1.29	
Surfactant			
Non-ionic mixture	Non-ionic mixture	1.28	EO and EO-PO
Inhibitor			
1-hydroxyethane 1,1-diphosphonic acid	HEDP	0.1	inhibitor
Enzymes			
Commercial amylase	/	some	No effect on 'shine'
Commercial protease	/	some	No effect on 'shine'
Bleach			
Bleach catalyst	/	some	No effect on 'shine'
Tetraacetylethylenediamine	/	0.35	no effect on 'shine'
Sodium percarbonate	/	1.41	No effect on 'shine'

Figure 2.1 The structure of the key components of the dishwasher detergent: (1) trisodium salt of the methylglycinediacetic acid (MGDA); (2) 1-hydroxyethane 1,1-diphosphonic acid (HEDP); (3) sulfonated polyacrylates Acusol 588 (Acuso 588G).

The motivation of this project is that kitchenware tends to suffer from filming on a surface when there is no CaCO$_3$ inhibitor in solution; in contrast, when using a cleansing formula with inhibitor 1-hydroxyethane 1,1-diphosphonic acid (HEDP), the shine of the kitchenware can be maintained up to 40 cycles. This chapter is a starting point, where we are going to explore how the dishwasher detergent itself retains /deteriorates the shine on surfaces.

The dishwasher detergent (Table 2.1) is a prototype nil phosphate formula which will be referred to as the '**HEDP formula,**' when it contains HEDP and '**Nil-HEDP formula**' or '**full Nil-HEDP formula**' when excludes HEDP. In the following chapters, if not specify, 'Nil-HEDP formula' will be used. The exploration of the 'Nil-HEDP formula' combined with other factors (such as soil, Ortho-P) inside the dishwasher will be presented in the next chapter.

In this chapter, the first two sections are arranged to give an understanding of a real-life dishwasher condition and how a dishwasher cleans the kitchenware. **Section 2.2** describes the substrate properties of glass and plastic that will be used in this project. Two types of plastic substrates are included in this project. They are poly (methyl methacrylate) (PMMA) and polystyrene (PS). **Section 2.3** gives the descriptions of two set-ups that will be utilized for the study of the surface deposition. These two set-ups are: a real-life dishwasher and a model system. The model system is developed in this project and is constructed based on the dishwasher

conditions with an option of involving a pumping system or not. Therefore, it can be used to explore the effects of Nil-HEDP formula itself without considering the agitation effects. **Section 2.4** and **Section 2.5** describe CaCO$_3$ crystallization in the absence and presence of the 'full Nil-HEDP formula,' respectively. An overall screening of the effects of each main component in Nil-HEDP formula has been given in **Section 2.6**, with an emphasized discussion on the polymer. CaCO$_3$ crystallization without additives (Section 2.4) can serve as a comparison for Sections 2.5 and 2.6, where additives are involved.

The deposits on surfaces were investigated with a combination of four different techniques. They are attenuated total reflectance infrared spectroscopy (ATR-IR) for deposit identification, X-ray powder diffraction (PXRD) for polymorph confirmation, scanning electron microscopy (SEM) for imaging morphologies of deposits, and transmission electron microscopy (TEM) for single crystal characterization and confirmation of preferred orientation. Deposits were analyzed in the following sequence: PXRD, SEM, FTIR and TEM. This is because FTIR scanning will break the surface and samples require coating before SEM imaging. The discussion is split into two parts: the shine loss on surfaces of PMMA and glass slides and the variation of polymorph species of CaCO$_3$ under different chemical conditions.

2.2 The Substrates Used: Glass and Plastic

In Chapter one, we have discussed the importance of the surface properties in determining the nucleation rate and the polymorphic form and morphology of the resulting crystals. The possible surface features that affect the surface crystallization include the surface energy, surface roughness, and the surface chemistry. The low-energy surface leads to a lower nucleation rate compared to a high-energy surface.[2] However, there are investigations that negate a direct correlation between surface energy and fouling tendency, and associate the induction time with a degree of roughness on surface[3] and the surface chemistry.[4] Literature evidence[5] also suggests that the surface roughness determines the mass of crystals deposited on surfaces while surface chemistry decides the polymorph distribution. So it is important to understand how different surface properties of the glass and plastic samples impact the surface crystallization of CaCO$_3$. In this project, PMMA slides are used as representative for plastic substrates in both the dishwasher

and the model system. Glass tumblers and microscopy slides are used as representative glass substrates in the dishwasher and model system, respectively. The study of the surface properties of glass samples and plastic samples are summarized in Table 2.3, and will be further discussed below.

2.2.1 The Chemistry of Glass and Plastic

Both glass and PMMA are amorphous solid materials. Glass is mainly made from silicon dioxide (silica).[6] There are various types of glass. In our case, only two types of glass that are relevant. These two types of glass are soda-lime and sodium borosilicate glass. The soda-lime glass with poor resistance to heat is widely used to make windows or tableware, while the sodium borosilicate glass with better durability for high temperature is often utilized as chemical glass, cooking glass or Pyrex.[7] The constituents of both types of glass are listed in Table 2.2. Soda-lime glass is composed of silicon dioxide, sodium oxide from sodium carbonate (soda), calcium oxide (lime), aluminum oxide and small quantities of additives (e.g. sodium sulfate, sodium chloride).[7] Sodium Borosilicate glass is named after its two main constituents: silica and boron oxide. The composition of sodium borosilicate glass includes silicon dioxide, boric oxide, sodium oxide, and aluminum oxide.[7] Microscopy slides (used the substrate in the model system) can be made from both types of glass. The elemental composition of glass and the percentage of each composition in each glass type is a list in Table 2.2. The EDX spectra, as shown in Table 2.3, indicate both the microscopy slides and glass tumblers used in this project are made from soda-lime glass while the crystallization reactor used in the model system is made from borosilicate.[6-7] The Au and Pd signals observed in the EDX spectra belong to the coating material.

Table 2.2 The constituents of the soda-lime[6] and borosilicate glass[7]

Glass type	Soda-lime	Borosilicate
Composition (% from high to low)	SiO_2 (73.0%)	SiO_2 (80.6%)
	Na_2O (14.2%)	B_2O_3 (13.0%)
	CaO (7.0%)	Na_2O (4.0%)
	MgO (4.0%)	Al_2O_3 (2.3 %.)
	Al_2O_3 (2.0 %.)	

Plastic is also an amorphous solid material. The plastic used in this project are poly (methyl methacrylate) (PMMA) and polystyrene (PS). PMMA and PS are synthetic polymers made from monomer methyl methacrylate and monomer styrene, respectively.

PMMA is more prone to scratching under an impact force than conventional inorganic glass but modified PMMA can achieve high scratch and impact resistance.[8] The elemental composition of PMMA is simple with only three elements present: O, C, and H. The chemical structure is as shown in Figure 2.2. The molecular chemical structure of the PMMA surface has been studied by sum frequency generation (SFG) vibrational spectroscopy at the polymer/air interface, showing that the surface of PMMA is dominated by ester methyl groups, while alpha methyl groups are lying down on the surface, and the methylene group has not been observed.[9] If there is an interaction between the Ca^{2+} and the PMMA surface, it will be mainly the interaction between the ester functional group and Ca^{2+}, or the interaction between ester functional groups and additives in solution.
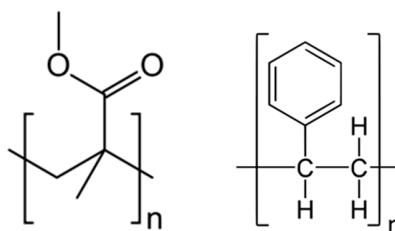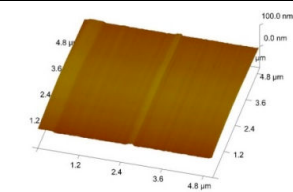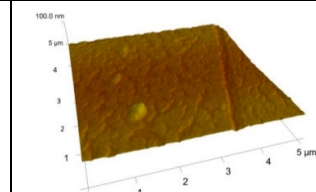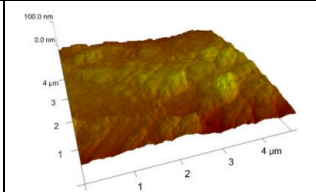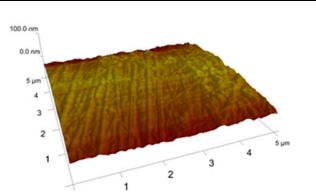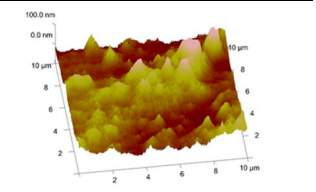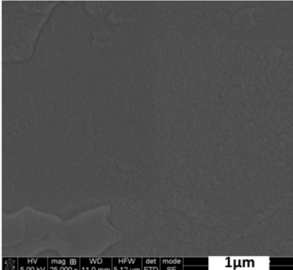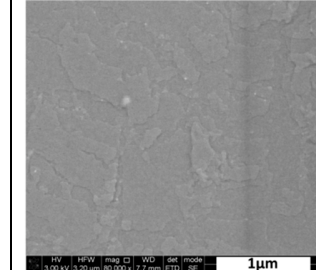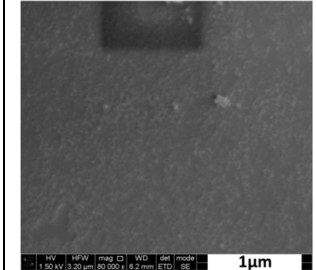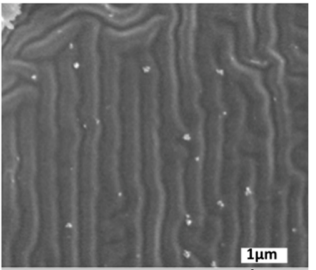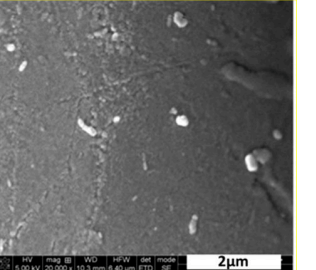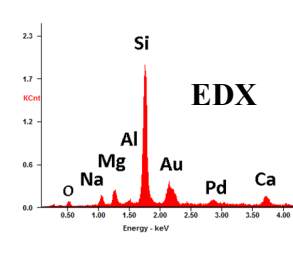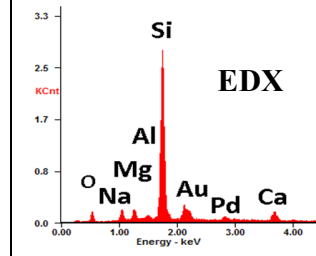
Figure 2.2 The chemical structure of PMMA and PS.

2.2.2 The Surface Roughness of Glass and Plastic

Surface roughness is crucial to surface interaction because surface roughness affects the real area of contact between the substrate and growing nucleus.[10] The actual contact area is affected by the various orders of irregularities on the surface, which is called the surface texture. Surface texture includes (1) roughness (nano- and micro-roughness), (2) waviness (macro-roughness), (3) lay and (4) flaws.[10] Microroughness is defined as "surface roughness components with spacings between irregularities (spatial wavelength) less than about 100 micrometers."[11] The surface roughness in this work is the micro roughness. Micro-roughness of a surface can be studied in three dimensions (3D) by AFM. SEM images, on the other hand, provide two-dimensional (2D) images to confirm the surface roughness observed in AFM. Table 2.3 shows the AFM and SEM

images of three different types of soda-lime glass, the PMMA slide, and a PS tumbler. The surface topography of each sample observed from SEM is consistent with that observed by AFM as can be seen in Table 2.3. The surface of the glass tumbler is the smoothest, while the PS tumbler has the roughest surface. Among the three different types of glass, namely, the glass tumbler, the microscope slide, and the glass dish, the glass tumbler has the smoothest surface. The surface smoothness of the microscope slide even if not as smooth as that of the glass tumbler, is closer to that of the glass tumbler. Hence, the microscope slides are used as glass substrates in the model system.

Table 2.3: AFM and SEM images of glass and plastic surface with element analysis

	Glass tumbler	Microscope slide	Glass dishes	PMMA slide	PS tumbler
AFM Height (100nm)					
SEM Images					
Element present			Not collected, as this substrate will be not used in this research	C, O, H	C,c H

* At the up-left corner of the SEM image of the PMMA slide, it is a there is an impurity other than the surface of PMMA slide.

2.3 Two Set-ups for CaCO$_3$ Crystallization

2.3.1 Dishwasher

For a household automatic dishwasher (ADW), the washing process includes five elements. These are prewash, main wash, cold rinse, heated rinse, and drying. The washing cycle described below is based on the representative Miele GSL R-zeit dishwasher model. The basic layout and the profile of a whole wash cycle are shown in Figure 2.3. In general, fresh water is supplied for each cycle, spraying through both upper and lower spray arms to clean dishes. Dirty water produced in the previous cycle is drained from the bottom of the machine before fresh water fills again. A washing cycle begins with a prewash, where water is not heated. The function of this cycle is to soften and flush away food residuals on surfaces and prepare for the main wash cycle. This step lasts for 9 minutes. In the main wash, fresh water (up to 5 Litre) is added and heated up to 55 ℃ or 65 ℃. The alkaline detergent is added in this step. Detergent is dispersed and contributes to an average pH value of 10.5 in the washing solution. This cycle lasts for half an hour to an hour and is the essential step for an efficient cleaning. The rinses follow the main wash and are composed of a first cold rinse and a second heated rinse. Rinsing helps to flush away residues left from the main wash cycle. Finally, dishes are dried for 30 min in the drying cycle. The drying temperature can be up to 65 ^{o}C. In this project, we mainly explore the crystallization and crystal inhibition in the main wash cycle.
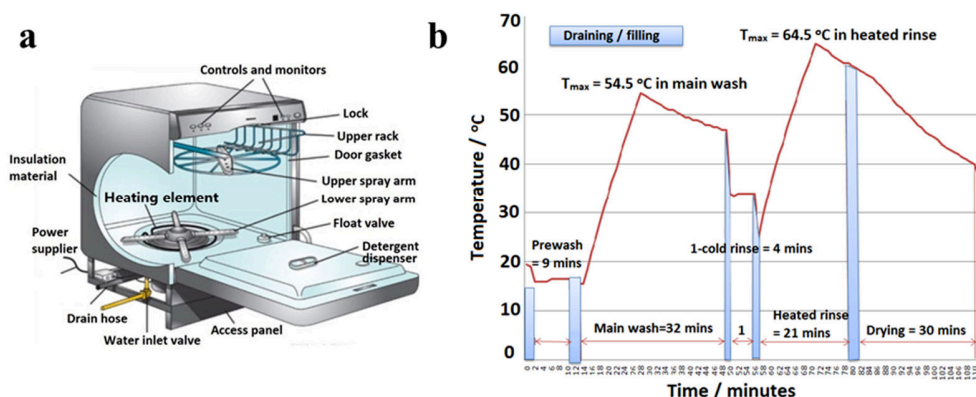
Figure 2.3 (a) The basic layout of a typical household dishwasher[12] and (b) the profile of a typical washing cycle of dishwasher Miele SL R-Zeit[13]. A whole washing process includes five steps: prewash, main wash, cold rinse, heat rinse and drying. The detergent is only applied in the main wash. The timing for each step is 9 min, 32 min, 40 min, 21 min, and 30 min, respectively. The maximum temperature used for the main wash is 55 or 65 ^{o}C and for heated rinse is 64.5 ^{o}C.[13]

2.3.1.1   The Prototype Formula

The detergent added in the main wash cycle is a nil phosphate prototype formula for a household automatic dishwasher (ADW). The ingredient and quantity of this formula are listed in Table 2.4. The formula consists of five main components, which are, builder, polymer, crystal growth inhibitor, surfactant, enzymes and bleach. Both, enzymes and bleach have no effect on 'filming,' so will not be discussed here. For simplicity, the 'prototype formula' will be referred to as the '**HEDP formula**,' while the formula that excludes the inhibitor HEDP will be called the '**Nil-HEDP formula**.'

Table 2.4 nil phosphate prototype ADW formula (or HEDP formula)

Prototype formula	Abbre.	Raw material in water (g 5L^{-1})	Comments
Alkaline Builder			
Trisodium salt of methylglycinediacetic acid	Na$_3$MGDA	2.82	Chelator
Granular sodium carbonate	Na$_2$CO$_3$	9.54	pH buffer
Sodium sulphate	Na$_2$SO$_4$	3.06	Solid diluter
Polymer			
Sulfonated polyacrylates Acusol 588	Acusol 588G	1.29	
Surfactant			
Non-ionic mixture	Non-ionic mixture	1.28	EO and EO-PO
Inhibitor			
1-hydroxyethane 1,1-diphosphonic acid	HEDP	0.1	inhibitor
Enzymes			
Commercial amylase	/	some	No effect on 'shine'
Commercial protease	/	some	No effect on 'shine'
Bleach			
Bleach catalyst	/	some	No effect on 'shine'
Tetraacetylethylenediamine	/	0.35	no effect on 'shine'
Sodium percarbonate	/	1.41	No effect on 'shine'

A detailed review of the development of key ingredients in dishwasher detergent can refer to Tomlinson.[14] In the following section, we will give a small introduction on the builder, the polymer, and the surfactant, which may be related to the growth of CaCO$_3$ in dishwasher system.

The builder is a water softener.[15] The main function of it is to sequester water hardness minerals (calcium or magnesium) by precipitation or complexation, and hence it improves detergent

efficiency and maintains shine. Typical builders are sodium carbonate, binding calcium or magnesium by precipitation. It also helps to maintain high alkalinity for the washing solution in the main wash cycle. Under this pH condition, chelator and inhibitor can exhibit the best cleaning performance.[14, 16] Moreover, it prevents soil redeposition.[15] The trisodium salt of the methylglycinediacetic acid is another builder, which has been widely used because of its biodegradability, thermal stability, and its effectiveness. It removes hard water minerals by forming 1:1 water-soluble complexes. These complexes are stable over a wide pH ranging from 2 to 13.5 but are particularly stable when pH value is around 10.5.[16]

Acusol 588G polymer is a copolymer of acrylic and sulphonic acids with a molecular weight around 12000 g mol^{-1}. This molecular weight range can provide the best chelation ability. The chemical structure is as shown in Figure 2.4. Acusol 588G, according to the manufacturer's data,[17] has the excellent binding capacity for calcium and magnesium, which is based on an ion exchange mechanism. The polymer inhibits the crystallization of CaCO₃. It inhibits the nucleation of a secondary phase from clusters by adsorbing onto the nucleated particles and stabilizing them. Polymers influence the resulting mineral morphology by face specific adsorption, which can be seen from Figure 2.4(a).[18]
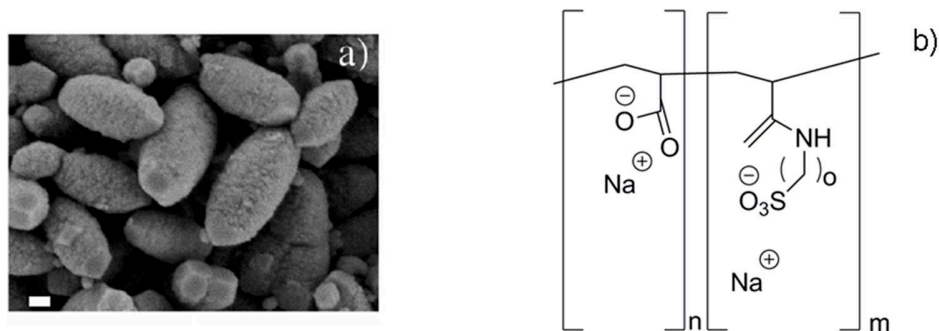
Figure 2.4 (a) The SEM image of CaCO₃ crystals 2 hours after nucleation with the presence of 10 mg L⁻¹ Acusol 588G (scale bar 200 mm); (b) The chemical structure of Acusol 588G.[18]

The surfactant used here is a non-ionic mixture. Non-ionic surfactants do not precipitate with water hardness and help to clean soil. Additionally, they act as a foam depressor, which is ideal for the automatic dishwasher process. It contains mainly two non-ionic surfactants from BASF. Tradenames are SLF180 and TO7. The exact structure of the surfactants is not provided.

2.3.1.2 The Water Chemistry with Presence of Full Nil-HEDP Formula

Apart from the dishwasher detergent, it is also essential to understand the water chemistry inside the dishwasher. The water does not just act as a detergent carrier but also helps to loosen and rinse the soil away with the aid of a spraying system. The presence of hardness ions (Ca^{2+}, Mg^{2+}) in water leads to the deposition of CaCO$_3$ on surfaces. The elemental analysis of by EDX on the deposits found on the surface of PMMA (Figure 2.5), indicates the presence of the CaCO$_3$. In the following discussion, a trace amount of Mg is also observed in some samples. The reason the Mg^{2+} is not detected here is that the crystal that was analyzed by EDX is aragonite. Mg^{2+} is able to access the crystal lattice of calcite but not aragonite, see Section 2.4 and Section 2.5 below. The Au and Pd are from the coating system. The effect of Mg^{2+} is controversial as it is selectively incorporated into different polymorphs of CaCO$_3$. We will further discuss this aspect in the following section. The concentration of the carbonate in solution would account for the carbonate from the prototype formula and any bicarbonate that is present in the water.

Table 2.5 The water chemistries in main wash cycle

Ca^{2+} (mmol L^{-1})	2.75
Mg^{2+} (mmol L^{-1})	0.86
Mg: Ca	0.31
CO_3^- (mmol L^{-1})	18
Detergent	Table 2.4
pH	10.5
Temperature (°C)	65 ^{o}C
Time	60 mins
$SI_{(aragonite)}$	3.37
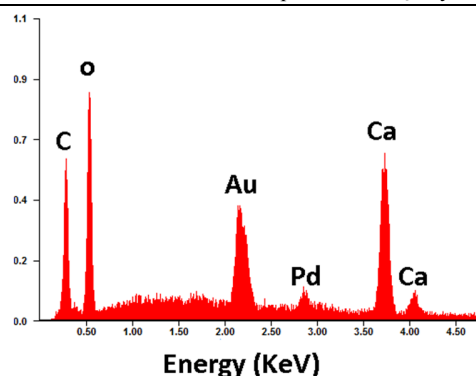
Figure 2.5 The element presents in deposits from the surface of a PMMA slide, which produced with Nil-HEDP formula.

2.3.2 Model System

2.3.2.1 Construction of the Model System

The model system has been set up mainly to mimic the main wash cycle of a dishwasher. Figure 2.6 shows the experimental set-ups with and without a pumping system. The set-up without the pumping system, illustrated in Figure 2.6a, is the main set-up used in this project to explore the growth of CaCO₃ under different chemical conditions. It is very straightforward and easy to operate. The effects of additives can be studied without considering the effects of agitation. In this set-up, substrates are fixed near the top of the glass container, which is made from sodium borosilicate glass. A hot plate with a thermometer is used to maintain the temperature at 65 °C. The stirring speed is kept at a rate of 100 rpm, enough to disperse the detergent but not cause agitation effects. To more closely simulate a real dishwasher, a pumping system was also investigated to spray the washing solution onto the surface of the substrates (Figure 2.6b). This system uses a peristaltic pump (EV8000) from Verderflex. Unlike the way the substrates were kept in solution in Figure 2.6a, substrates in Figure 2.6b are fixed vertically above the solution without direct contact with the washing solution to mimic as how dishes are placed in the dishwasher. In the set-up of Figure 2.6b, the solution is pumped to the reservoir above the lid of the container first, flows back to the container and drops onto the surfaces of the substrates through the holes in the lid. Both set-ups are used to mimic the growth of crystals in a dishwasher. The set-up without the pumping system is the main set-up utilized in this project due to its flexibility and simplicity. Also, it is easy to explore the effects of the additives without

considering agitation effects. From now on, the term '**model system**' refers to the non-pumping set-up if it is not specified.
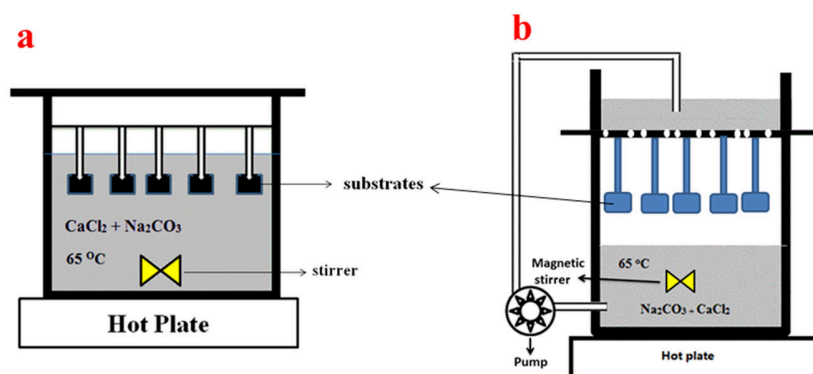
Figure 2.6 Schematic set-ups of model crystallization system without (a) and with (b) the pumping system.

2.3.2.2 Experimental Details for Model System

The detailed experimental procedure for the model system is as follows: PMMA sheets and glass sheets are fixed in pairs near the top of the glass container. The PMMA sheets are cut from a big PMMA slide while glass sheets are cut from microscopy slides. Hard water as used in the real dishwasher is prepared by dissolving $CaCl_2$ (0.1526 g, 2.75 mmol) and $MgCl_2$ (0.04805 g, 0.0806 mmol) in 500 ml deionized water (DI water). This solution is transferred into the glass container and heated up to 65 ^{o}C, before addition of the Nil-HEDP formula. The formula compositions, which are listed in Table 2.4, include Na_2CO_3 powder (0.954 g), Na_2SO_4 (0.306 g), MGDA (0.141g), Acusol 588G (0.129 g), non-ionic mixture (0.175 g) and inhibitors (0.02 g). In the model system, the amount of water and the amount of the formula is ten times less than that used in the dishwasher. To make all the detergent compositions dissolve at a similar speed, all powdered compositions are added simultaneously except the liquid non-ionic mixture, which is added last due to its high dissolution speed. The container then is covered, and the solution is kept at 65 °C for 1 hour. The stirring speed is constant at a rate of 100 rpm from beginning to the end. After crystallization for an hour, the PMMA slides and glass sheets are taken out, rinsed with cold and hot DI water (60 ^{o}C) for one minute, respectively. The substrates are left in the air to dry. The procedure is then repeated. Two sheets of each substrate are retained each time for analysis, and the remainder is replaced in the new solution. Samples for further characterization are analyzed by PXRD, FTIR, SEM and TEM. In future, the effects of different detergent

composition and the effects of candidate inhibitors could be explored in this set-up. For experiments that need to exclude some chemicals or need to add more chemicals, the general procedure is the same: hard water is prepared first, followed by addition of solid chemicals and then the liquid surfactant. The only difference is the change of chemicals added. For example, In Chapter 6, the candidate inhibitors, which are solid powder, are added together with the solid chemicals. Since they are added to replace the inhibitor HEDP and have a similar dissolution speed as the other solid chemicals. The HEDP is therefore excluded.

2.3.3 Differences between the Two Crystallization Set-ups

The key question was to assess the role of agitation in determining the nature of deposits formed on the target substrates in the model systems. To address this question, the results of CaCO$_3$ deposition in the pumped and non-pumped systems were compared. The schematic diagram of both set-ups is shown in Figure 2.7 and Table 2.6 lists the detailed differences between both set-ups. The difference mainly lies in two aspects: the presence of the pumping system and the simplified cycle procedure in the model system. The exclusion of the pumping system in the model system removes the shear effects and agitation effects caused by the spraying action. The model system has a simplified cycle. In the model system, the procedure excludes the prewash cycle, reduces the timing for both cold rinse and hot rinse, and drying is simply in air at room temperature rather than at 60 $^{\circ}$C. Moreover, a rinsing cycle was employed in which DI water was used to clean substrate after crystallization to ensure that the crystals observed on surfaces aroused from deposition from the washing solution in the main wash cycle rather than residues from hard water in the rinsing cycle. In summary, the model system without pumping system has no obvious agitation effects and only has the main wash cycle and a simple rinse cycle.
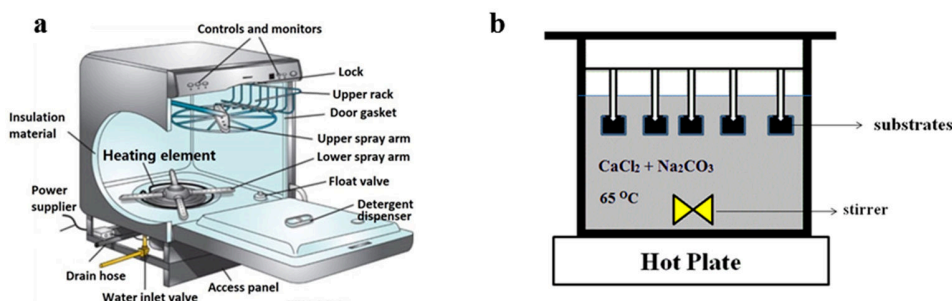
Figure 2.7: Schematic diagram of a typical household dishwasher (a) and the model system without pump (b).

Table 2.6 The set-up differences between a real dishwasher and the model system

Procedure	Model system (no pump)	Dishwasher
Pre-wash	no pre-wash	pre-wash for 9 mins
Main wash	60 mins (500 ml)	60 mins (5.0 L)
Stirring	100 rpm	pumping and spraying systems
T_{max}	65 °C	Ramp up from cold to 65 °C
Cold rinse	1 min with DI water at RT	4 mins (water containing Ca, Mg at RT)
Hot rinse	1 min with DI water at 60 °C	21 mins (water containing Ca, Mg up to 60 °C)
Dry	at RT till dry	30 mins up to 50-65 °C

2.3.4 Sample Preparation

Glass samples and PMMA slides were produced from a dishwasher and the model system under the same chemical conditions. Five different solution compositions with the same supersaturation ratio were used to generate samples. These compositions are 'carbonate only,' 'Nil-HEDP formula,' 'Nil-HEDP formula without polymer ('full minus polymer')' 'Nil-HEDP formula without surfactant ('full minus polymer'),' and 'HEDP formula.' From now on, 'Full' refers to 'Full Nil-HEDP formula.' The involvement of 'Nil-HEDP formula' and 'HEDP formula' can be used to study the difference of crystal growth both with and without inhibitor. The composition of each chemical condition is listed in Table 2.7. The 'carbonate only' sample refers to hard water (Ca^{2+}/2.75 mmol L^{-1}, Mg^{2+}/0.0806 mmol L^{-1}) and CO$_3$$^{2-}$ (18mmol L^{-1}) in the washing solution. The 'carbonate only' conditions are used as a comparison to understand the effects of Nil-HEDP formula on CaCO$_3$ growth. 'Full minus polymer' and 'Full minus surfactant' were intended to study the effects of surfactant and polymer when they are intentionally excluded. The 'simple crystallization' was run to check the effects of Mg^{2+} for 'carbonate only' condition. The samples were run for between 5 to 12 times, depending on experimental objectives.

Table 2.7 The chemical conditions that used to produced samples in the dishwasher and the model system

Conditions	Water		"Filler"/Alkalinity		Builder	Polymer /	Surfactant	Inhibitor
	CaCl$_2$	MgCl$_2$	Na$_2$CO$_3$	Na$_2$SO$_4$	MGDA	Acusol 588	Non-ionic mixture	HEDP
Simple Crystallization	yes	no	yes	no	no	No	no	no
Carbonate only (with Mg)	yes	yes	yes	no	no	No	no	no
Full minus polymer	yes	yes	yes	yes	yes	No	yes	no
Full minus surfactant	yes	yes	yes	yes	yes	Yes	no	no
Full Nil-HEDP formula	yes	yes	yes	yes	yes	Yes	yes	no
HEDP formula	yes	yes	yes	yes	yes	Yes	yes	yes

2.3.5 Data Collection and Analysis

While different deposits may have a different appearance to the naked eye, they may be made up of the same polymorphic form of calcium carbonate and exhibit the same microscale morphology. Bearing this idea in mind, we assume samples sent for analysis are representative. The characterization results of samples from the dishwasher and the model system are summarized in Table 2.13. The information includes the degree of shine loss, the PXRD analysis on polymorph distribution and the morphologies observed in SEM.

Unfortunately, the way in which 'shine' is assessed is different in the dishwasher and the model systems. The clarity of samples from the dishwasher is graded by a camera analysis rating system developed by P&G. Pictures of transparent substrates are taken against a black background in an environment with controlled lighting. The mean film gray level is a measurement of gray level in the range 0-255 and is used to calculate Clarity (%) by normalizing the gray scale to 100%. Thus a clarity index of 100 would occur with a completely dark glass with a gray level of zero and therefore having no film present. In the model system, the shine of samples is rated via a naked eye assessment as the slides from the model system are too small to be used in the analysis camera system. To differentiate them, clarity of samples from the model system was rated from 1 to 10, while samples from dishwasher were rated from 0% to 100%.

Two X-ray powder diffraction patterns were collected for each sample, one *in situ* with the deposit on the substrate and one on free material scraped from the surface of the substrate. The PXRD data shown in the tables is the combined refinement results of the two PXRD patterns. The PXRD pattern collected with substrate indicates the possible preferred orientation of the crystalline material and the powder scraped from the substrate tells gives information on the polymorph distribution ratio.

The morphology of the resulting material is assessed by SEM. TEM is used mainly for the crystal identification for a specific morphology assessment. The samples are coated with gold or carbon before imaging by a HITACHI S-520 type scanning electron microscope (SEM). Typically, a field free mode, operated at a voltage of 5 kV to 10 kV, is used for sample imaging. In EDX (Energy-dispersive X-ray Spectroscopy) mode, a voltage of 10 kV is applied. Samples for TEM were prepared by scraping the material from the substrate, dispersing them in acetone, and dropping them in a holey copper grid. Electron diffraction was carried out on a JEOL 2100F FEG TEM in a transmission mode operating at 200 eV. The EDX data are also collected for each sample in TEM. The diffraction pattern analysis are carried out by the software 'Gatan Digital Micrograph'.[19]

2.4 Surface Deposition of CaCO$_3$ in the Hard Water in Model System

Three classes of parameters in the system affect the surface deposition: (1) system parameters: pH, the temperature of the solution and the flow rate; (2) the nature of the substrate and (3) the solution chemistry. In this subsection, we aim to understand CaCO$_3$ crystallization in hard water with fixed system parameters when additives are absent. The CaCO$_3$ crystallization is carried out in the model system, where the effects of agitation are negligible and hence we can focus on the study of solution chemistry. We will present results of CaCO$_3$ crystallization with and without the presence of Mg^{2+}. The effects of Mg^{2+} on the resulting amount of crystallization and the resulting polymorphic species will be discussed with a focus on the chemistry of the solution. The concentrations of Ca^{2+} (2.75 mmol L^{-1}), Mg^{2+} (0.86 mmol L^{-1}) and CO$_3^{2-}$ (18 mmol L^{-1}) are the same as those detected in the main wash cycle in a real-life dishwasher. This subsection will

help in understanding how Mg^{2+} at this level of concentration affects the growth of CaCO$_3$. It will serve as a comparison section for other sections involving additives.

2.4.1 Supersaturation

Table 2.5 is a summary of the water chemistry in the main wash cycle, listing the possible factors that may contribute to supersaturation of the washing solution. The supersaturation calculated below is the initial supersaturation crystallization starts. As the crystallization goes on, the calcium and carbonate are gradually consumed due to the formation of crystals. For the calculation of saturation index (*SI*) and an explanation of the *SI,* value refers to Section 1.2.1. The *SI* value is a comprehensive consideration of water hardness, temperature, and pH. As discussed in Chapter 1, we know that surface deposition and bulk precipitation are two different processes, and they have different dependencies on the index of supersaturation.[20] The calculation of the *SI* values for aragonite and calcite are shown in Equation 2.1 and Equation 2.2, respectively. When *SI* > 0, the solution is supersaturated and homogeneous precipitation occurs spontaneously. Heterogeneous nucleation occurs more readily than homogeneous nucleation due to a lower activation barrier. In the present case, a solution with a *SI* value of 3.37 in the main wash cycle has a high potential to deposit on surfaces.

$$SI(Saturation\ Index) = log(SR) = log\left(\frac{IP}{K_{sp}}\right) = log\left[\frac{(C_{Ca^{2+}} * C_{CO3^{2-}})}{K_{sp\ (aragonite)}}\right] = 3.37 \qquad \textbf{Equation 2.1}$$

$$SI(Saturation\ Index) = log(SR) = log\left(\frac{IP}{K_{sp}}\right) = log\left[\frac{(C_{Ca^{2+}} * C_{CO3^{2-}})}{K_{sp\ (calcite)}}\right] = 4.51 \qquad \textbf{Equation 2.2}$$
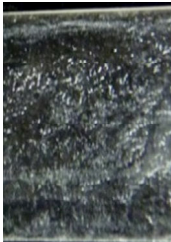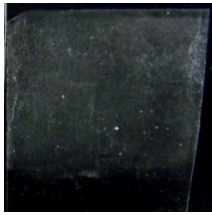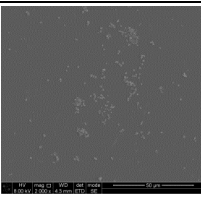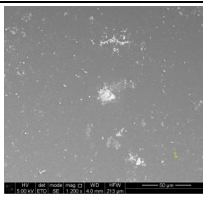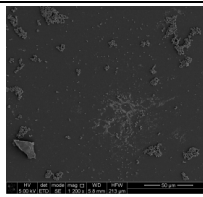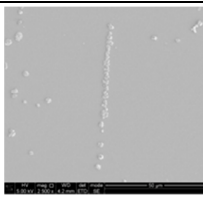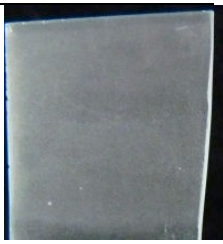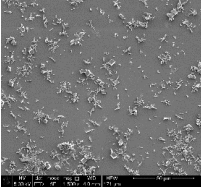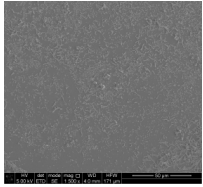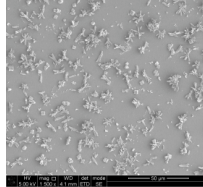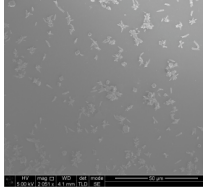
2.4.2 The Effect of Mg^{2+} on Shine Loss

It is known that isomorphic replacement of Mg^{2+} for Ca^{2+} can result in its selective inclusion in the crystal structure of calcite but not in that of aragonite.[21] This inclusion leads to two possible effects on CaCO$_3$ growth, which are the distortion of calcite and the preferential growth of aragonite. These two effects are influenced by the ratio of Mg to Ca in solution.[22] If the ratio of Mg to Ca is higher than 1, the formation of calcite nuclei tends to be disrupted by Mg, leading to the crystallization of aragonite as the aragonite nuclei are not affected by magnesium.[4a] When the ratio of Mg to Ca is smaller than 1, Mg tends to incorporate into the crystal lattice of calcite and leads to the distortion of the crystal structure of calcite.[23] The incorporation of Mg into the lattice of calcite crystal may slow down or stop crystal growth. It has been shown that 30% of inhibition

efficiency can be achieved for surface deposition with a ratio of Mg/Ca = 1/73.[23] In our case, the ratio of Mg/Ca is 3/10 but there is no obvious inhibition effect observed after five cycles. This can be seen from the Table 2.8.

Table 2.8 shows the photographs of PMMA and glass slides after the 2nd cycle and the 5th cycle of crystallization in the absence and presence of Mg^{2+}. It can be seen that there is no obvious difference in shine observed between the Mg-containing and non-Mg crystallization. Moreover, crystals continue to grow with the increase of cycles and cover the surface after five cycles. Mg^{2+} at this level of concentration has little effect on crystal growth inhibition (Only the defects on calcite caused by the presence of Mg^{2+} are observed, see next subsection 2.4.3). This may because even if Mg^{2+} does have an inhibition effect, its effects are on calcite crystals but not both aragonite and calcite crystals at the same time.[24] Hence, with the increase in the number of crystallization cycles, the growth of the crystal, especially the growth of aragonite is evident. It is hard to confirm this with the first two cycles by PXRD as there is not enough film to be analyzed. However, at the 5th cycle, PXRD shows that more aragonite is present than calcite for all samples (see Table 2.8). On the one hand, the high temperature promotes the growth of aragonite and with the presence of Mg, the ratio of aragonite to calcite is increased from 3/2 to 3/1.[22] This is confirmed both by PXRD and SEM (Figure 2.8). Hence, two effects caused by the inclusion of Mg^{2+} in calcite lattice, namely, the distortion of calcite (see next subsection 2.4.3) and the preferential growth of aragonite, are observed in our system. Since Mg^{2+} has no inhibition effects on aragonite, the suggested inhibition effect of Mg^{2+} is not observed, and Mg^{2+} has no effects on retaining shine

Table 2.8 The images of glass and PMMA samples after the 2nd cycle and the 5th cycle of crystallization with and without Mg^{2+} in solution.

		No Mg		With Mg	
	Substrate	PMMA	Glass	PMMA	Glass
	Clarity	6	6	6	6
The 2nd cycle	Optical Image				
	SEM Image				
	Substrate	PMMA	Glass	PMMA	Glass
	Clarity	3	3	3	3
The 5th cycle	Optical Image				
	SEM Image				
PXRD		A/C = 3/2	A/C = 3.7/3.2	A/C = 3/1	A/C = 3/1
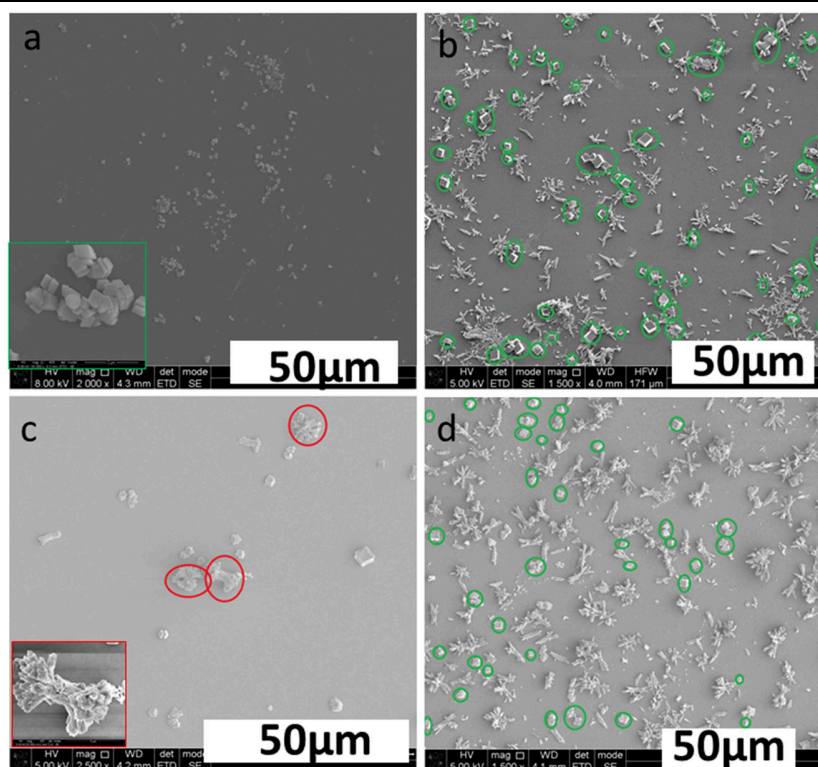
Figure 2.8 The SEM images of crystals found when there is no Mg^{2+} (a & b) and with Mg^{2+} (c & d) in solution on the glass substrates. (a) The 1st cycle: well-formed rhombohedral calcite crystals found when there is no Mg in solution. (b) The 5th cycle: a mix of rhombohedral calcite (in green) and rod-like aragonite discovered in the absence of Mg^{2+} in solution. (c) The 1st cycle: a mix of calcite and aragonite (in the red cycle) in the presence of Mg^{2+} in solution. (d) The 5th cycle: a mix of rhombohedral calcite (in green) and the sheaf-like aragonite observed in the presence of Mg in solution.

2.4.3 The Effect of Mg^{2+} on Polymorph Distribution and Morphology

Even though the inhibition effects of Mg for crystal growth are not observed in the experiments described above, the morphology modification caused by Mg is evident. Mg^{2+} incorporates into the calcite structure, which changes the lateral crystal growth via step pinning[25] or isomorphous replacement[24b] and causes defects in the calcite crystal.[23] When there is only Ca^{2+} and CO$_3^{2-}$ in solution, the crystal shape of calcite can be perfectly rhombohedral (Figure 2.9a) or cubic while aragonite adopts a rod-like shape (Figure 2.9b). When there is Mg^{2+} present in solution, calcite crystals still appear as rhombohedra or cubic but with defects on the surface (Figure 2.9c) and sheaf-like deposits of aragonite are observed (Figure 2.9d). The SEM observation shows that the presence of trace amount of Mg does result in considerable morphology modification on calcite. However, the crystals appear as separated crystals, and tend not to congulate or aggregate.

Probably that is why when applying the cleaning detergent without inhibitor, the films formed on surface are thicker than that when no cleaning detergent are involved.
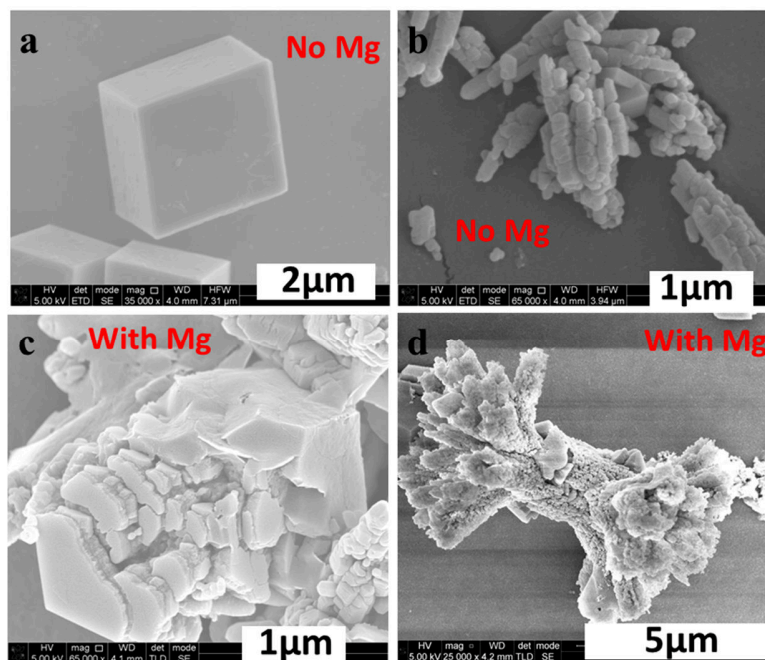
Figure 2.9 The SEM images of crystals found on the surfaces of the substrates when there is no Mg^{2+} (a & b) and with Mg^{2+} (c & d) in solution regardless of the substrate and the number of cycles. (a) Well-formed rhombohedral calcite crystals found when there is no Mg in solution. (b) Rod-like aragonite discovered in the absence of Mg^{2+} in solution. (c) Distorted calcite in the presence of Mg^{2+} in solution. (d) The sheaf-like aragonite observed in the presence of Mg in solution.

2.5 CaCO$_3$ Crystallization with Full Nil-HEDP Detergent

2.5.1 Crystallization for 5 Cycles in Both Set-ups

2.5.1.1 On PMMA

When using 'Nil-HEDP formula', CaCO$_3$ crystals will gradually build up on the surface. After five cycles of crystallization, the deposits become visible, and a homogeneous film can be clearly observed by both naked eyes and PXRD. The PMMA samples produced by both the dishwasher and the model system for five cycles are shown in Figure 2.10. PMMA slides were analyzed by SEM, FTIR, PXRD, and TEM, showing that crystals are of the same type regardless of the apparatus in which they are produced. Figure 2.11 shows the SEM images of crystal morphologies observed on PMMA samples. It can be seen that morphologies observed from the real dishwasher (Figure 2.11 a, c, e, g) and the model system (Figure 2.11 b, d, f, h, i, j) are identical. Two types of flora-like morphologies are observed on PMMA surfaces: Morphology A1 (Figure 2.11 c & d) and Morphology A2 (Figure 2.11 g & h). The Morphology A2 seems to be a small version of Morphology A1. The Morphology A1 is flower-like with several layers of petals. Morphology C1 (Figure 2.11i) and Morphology C2 (Figure 2.11 j) are only observed on PMMA slides from the model system. One has a rice-like morphology (Morphology C1), and the other has a pyramid-like shape (Morphology C2). They are small in size and less in quantity. Morphology A1 and Morphology A2 are the main morphologies observed on both PMMA slides, especially Morphology A1. Morphology C1 and Morphology C2 are the minor morphologies observed on PMMA slides from the model system. Morphology C1 is found on the petals of Morphology A1. It is possible that the morphology C1 is formed via indirect adherence from solution other than from the direct growth of crystals on the surface. A and C represent aragonite and calcite, respectively.
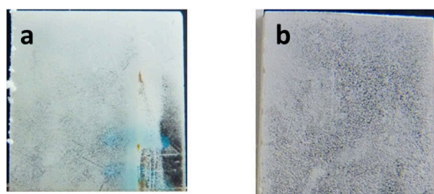
Figure 2.10 The PMMA slides taken out after five cycles of crystallization: (a) from the dishwasher, the blue region is from the marker pen; (b) from the model system.
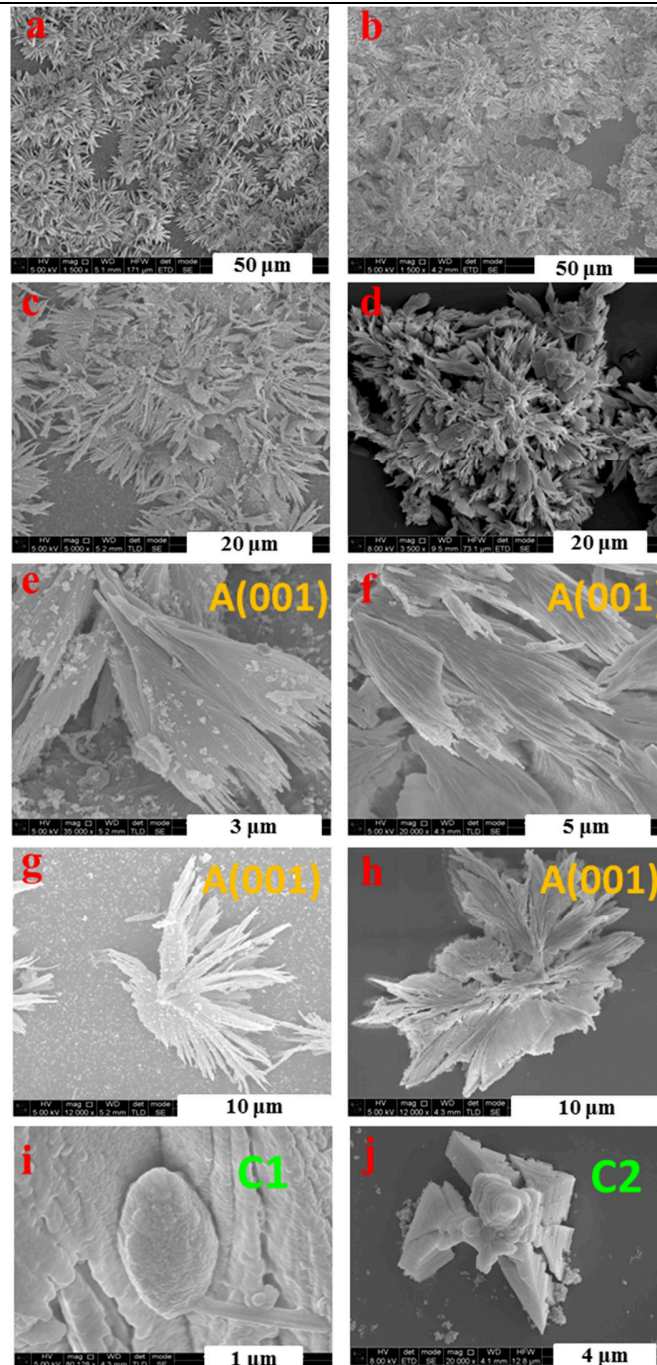
Figure 2.11 Scanning electron micrographs of PMMA samples produced after five cycles from dishwasher (a, c, e, g) and model system (b, d, f, h, i, j). The general distribution of crystals from dishwasher (a) and model system (b) with a scale bar of 50 µm; A flora-like crystal (morphology A1) from dishwasher (c) and model system (d) with a scale bar of 20 µm; one petal of the flora-like crystal from dishwasher (e) and model system (f) with a scale bar of 5 µm; A flora-like crystal (morphology A2) from dishwasher (g) and model system (h) with a scale bar of 10 µm. (i) Morphology C1 with a rice-like shape observed on the petal of Morphology A1 in a model system (j) Morphology C2 with pyramid-like shape from the model system.

114
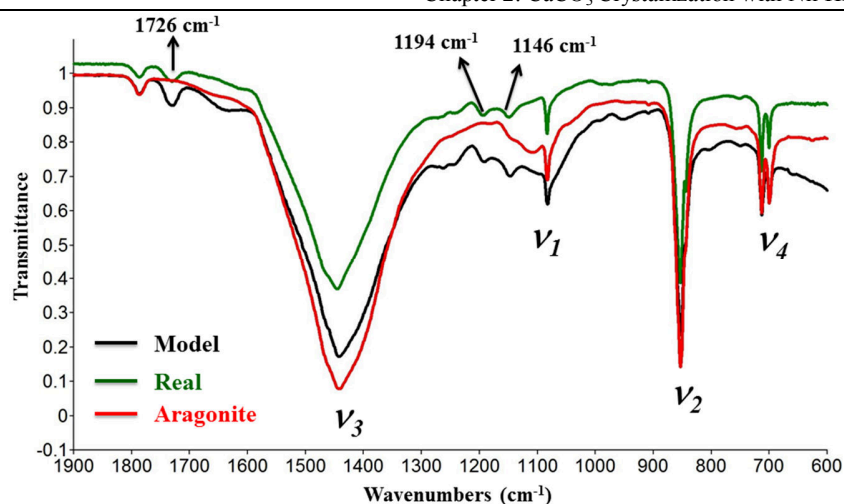
Figure 2.12 The FTIR spectra comparison of the powder scraped from PMMA substrates produced from the model system (in black) and dishwasher (in green), showing aragonite is the only polymorph of CaCO$_3$ observed on the surfaces of PMMA. The spectrum of reference aragonite is shown in red. The three labeled peaks at 1726 cm^{-1}, 1194 cm^{-1}, and 1146 cm^{-1} can be attributed to the functional group of COO^{-1} belonging to PMMA. Apart from these three peaks, other peaks are all fit to the spectrum of reference aragonite.

FTIR spectroscopy has been utilized to identify the film formed on the surface for both PMMA samples (Figure 2.12). FTIR spectra identify the scraped powder from both surfaces of PMMA substrates as aragonite. PXRD validates the results of FTIR that aragonite is the dominating phase and provides more information about the deposits (Figure 2.13). The PXRD patterns collected without and with the substrate are shown in Figure 2.13a and Figure 2.13b, respectively. PXRD patterns of the scraped powder from both samples are shown in Figure 2.13a. It is shown that all peaks belong to aragonite except for one peak, which belongs to the most intense peak of calcite, the calcite (104) reflection. The information on the preferred orientation is obtained by the non-destructive method, where PMMA substrate is loaded intact onto the PXRD instrument. The resulting patterns show aragonite has a preferred orientation (001) (Figure 2.13b). PXRD has a higher sensitivity than FTIR in polymorph identification, especially when one of the polymorphs has a low ratio. PXRD reveals that the deposits on PMMA are aragonite with a trace amount of calcite. Rietveld refinement indicates calcite is less than 1%, and aragonite is the dominant polymorph with preferred orientation (001). The preferred orientation of aragonite (001) is further confirmed by the TEM (see Figure 2.14). The flora-like aragonite is made up from layers of petals. While the petals, as revealed by TEM, are made from single crystals of aragonite, which has a needle-like shape. The growth mechanism of how needle-like

aragonite single crystals developed into a petal, and then further result in a flora-like shape, can refer to Section 1.3.7.3 in Chapter 1.

Combining all of the results together, we can see that both dishwasher and model set-ups produce the same flora-like aragonite and calcite on PMMA slides, but there is more calcite observed in the model system than in the dishwasher. This is probably due to the agitation enhances the transformation toward aragonite.[26] The morphology A is aragonite with preferred orientation (001) and morphology C, and morphology D is calcite.
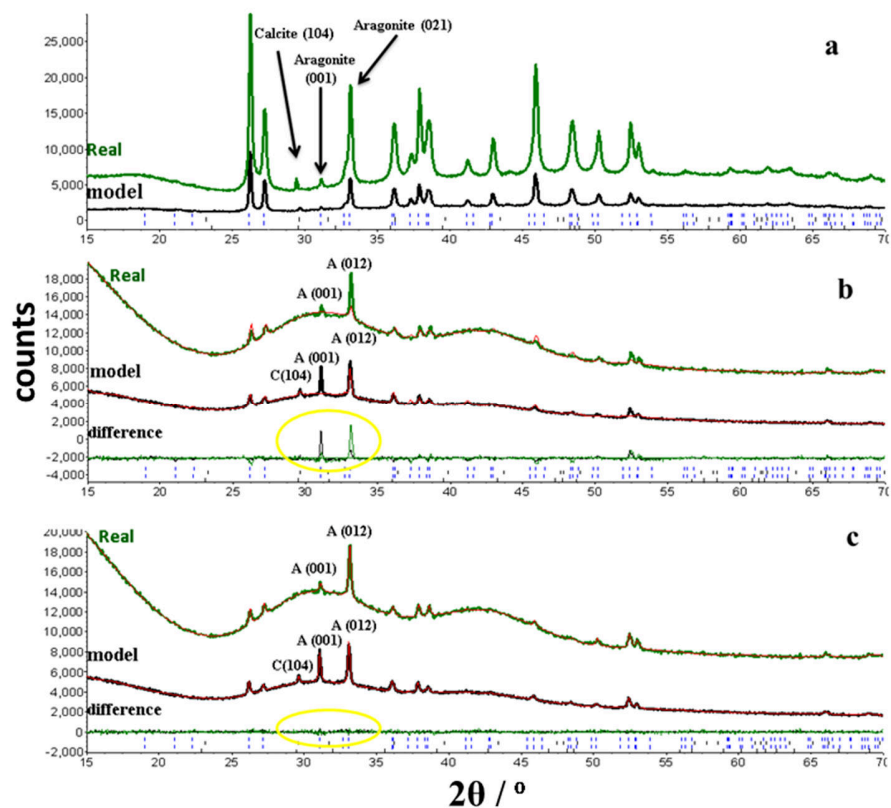
Figure 2.13 PXRD patterns of PMMA samples produced after five cycles without PMMA substrate (a) and with PMMA substrate (b,c), showing crystals on PMMA substrates are mainly aragonite (001) with a trace amount of calcite. The experimental patterns for dishwasher and model system are shown as green and black, respectively. The corresponding green and black lines at the bottom in b and c are the difference lines for the dishwasher and model system, respectively. The red pattern is the simulated pattern. (a) PXRD patterns of scraped powder from PMMA substrates shows all peaks belong to aragonite expect one weak peak from calcite (104), which is the most intense peak of calcite. It can be known that crystals on PMMA are mainly aragonite with trace calcite. (b) and (c) are Rietveld refinement for the PXRD patterns directly collected from PMMA substrates. Rietveld refinement of CaCO₃ crystal peaks before (b) and after (c) applying preferred orientation of aragonite (001), indicating the aragonite crystals on PMMA grows in the direction of the plane (001).
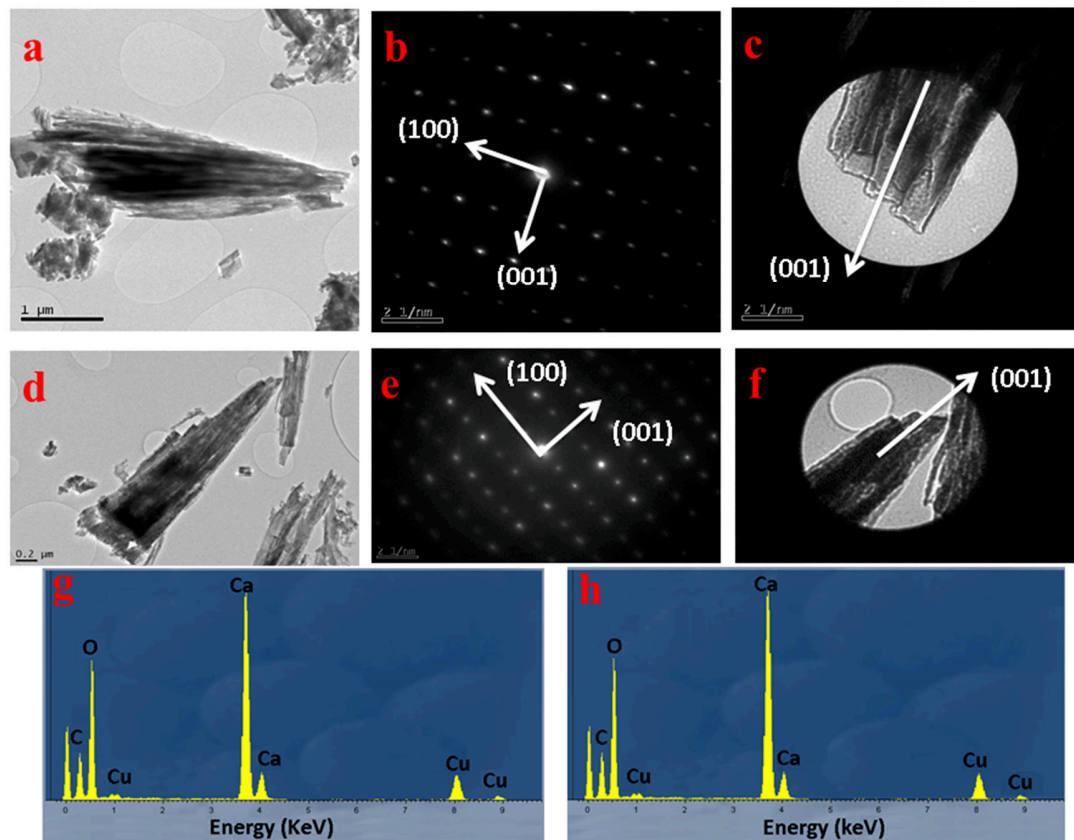
Figure 2.14 TEM observations of the PMMA samples produced after five cycles from the model system (a, b, c and g) and dishwasher (d, e, f and h) confirm the petal-like crystals are made from need-like aragonite single crystal, which has a preferred orientation (001). (a) Bright field image of petal-like crystal that is made from needle-like crystals. (b) TEM diffraction pattern of single crystal shows crystal as aragonite. (c) Shadow image of the tip of crystal in the image (a), confirms the preferred orientation in (001). (d) Bright field image of the petal-like crystal is made from needle-like crystal. (e) TEM diffraction pattern of single crystal shows crystal in (d) as aragonite. (f) Shadow image of the tip of (d), confirms the preferred orientation (001). (g) and (h) are EDX spectrums for crystal observed in (a) and (d), show crystals as calcium carbonate. The Cu counts are from the copper grids.

2.5.1.2   On Glass

The glass samples shown in Figure 2.15 are produced after five cycles by both set-ups with the full Nil-HEDP formula. The film on the glass slide from the model system is visible, but the glass tumbler generated from dishwasher can retain its shine even after five cycles. This may because the surface of glass tumbler has a smoother surface than the microscope slides (Refer to Section 2.2.2). It is easier for the film to build up on a rough surface.[27] Moreover, agitation in dishwasher helps to flush away any amorphous precursors or nuclei formed on a smooth surface.
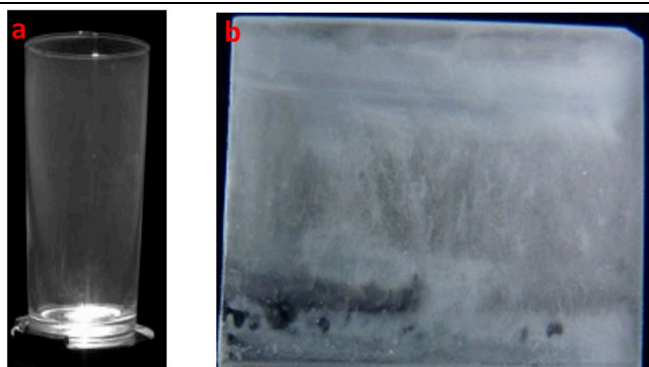
Figure 2.15 The filmed glass samples after five cycles: (a) from dishwasher; (b) from the model system.

Even though the amount of crystals observed on the surface is different, the polymorphic form and the corresponding morphologies found on both glass samples are the same. This is shown by PXRD, SEM, and TEM. Crystal morphologies observed from the dishwasher in Figure 2.16_a1, and the model system in Figure 2.16_d1 are identical. Since insufficient sample can be scraped from glass tumbler, no information of TEM and PXRP is available for the dishwasher sample. The available information is from the SEM. Crystals observed adopt a rice-like morphology (Figure 2.16_d1), EDX in SEM indicates the rice-like crystals to be CaCO$_3$ (Figure 2.16_d2). The rice-like morphologies are also found on the glass slide from the model system but with different shapes. They are either observed as a single crystal of calcite or agglomerated single crystal of calcite. The SEM and TEM with corresponding EDX information of single crystal calcite are presented in Figure 2.16 (a1-3). The agglomerated crystals are shown in Figure 2.16 (b1-3) and Figure 2.16 (c1-3), which are made up from two and ten rice-like calcite crystals, respectively. The PXRD further confirmed that calcite is the only phase observed on the surface of a glass slide (Figure 2.17), no preferred orientation is indicated.
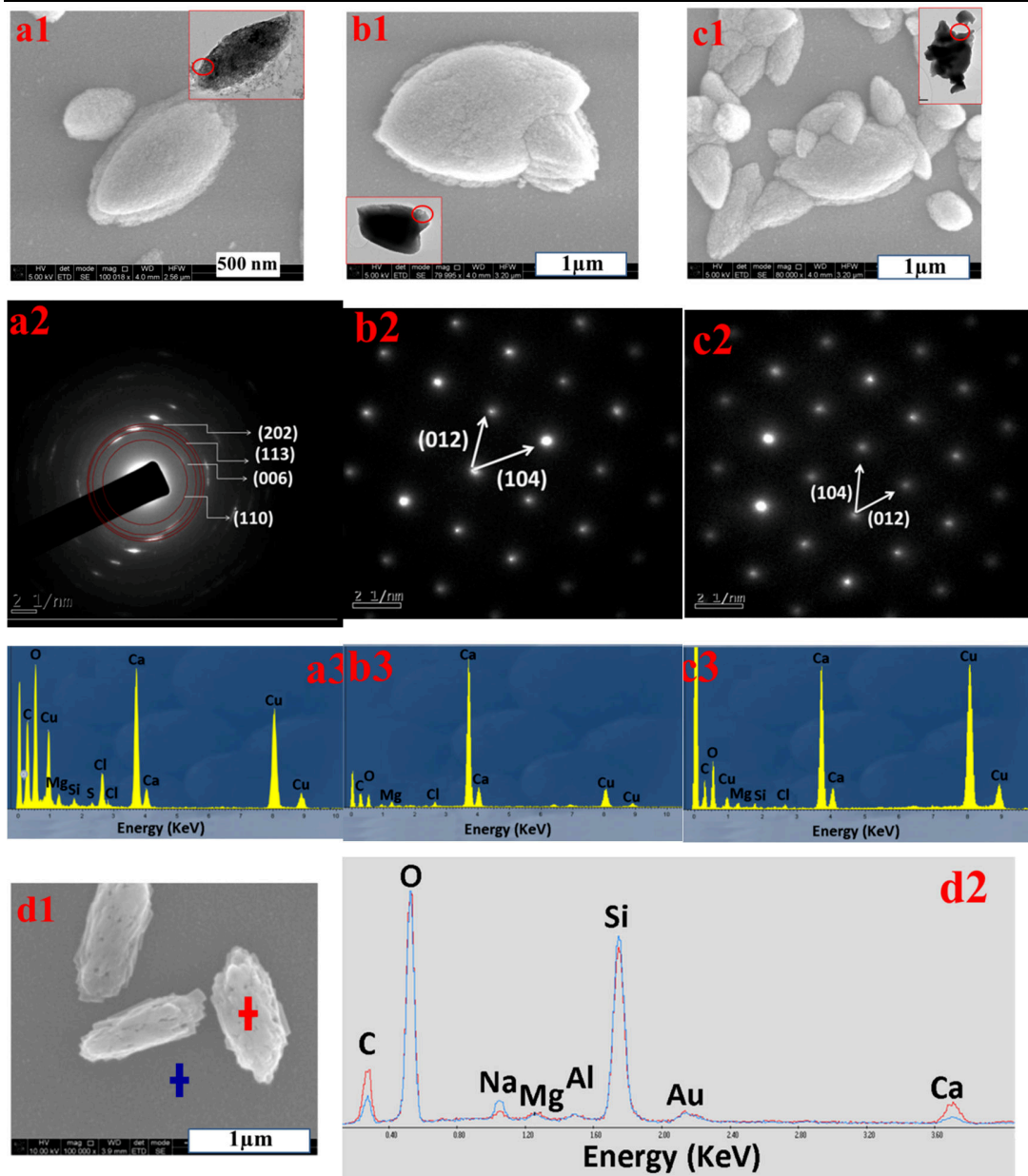
Figure 2.16 The SEM images of morphologies found on the surfaces of glass samples after five cycles, produced by the model system (a, b, c) and dishwasher (d) with corresponding and microanalysis. (a1) SEM image shows crystals as rice-like shape; inset is the TEM image. (a2) TEM diffraction pattern of randomly oriented calcite nanoparticles that were agglomerated up to microns in size. (a3) microanalysis shows crystals in (a1) as calcium carbonate with a trace amount of Mg, Si, S, and Cl. Copper is from the TEM grid. (b1) SEM images of two agglomerated single crystal of calcite. The identification of calcite is confirmed by the SAED pattern in (b2) and microanalysis in (b3). (c1) SEM images of several agglomerated calcite crystals with corresponding TEM pattern in (c2) and microanalysis in (c3). The chemical compositions of a1, a2 and a3 analyzed by EDX in (a3), (b3) and (c3), respectively, revealed the presence of CaCO₃ with traces of Mg, Si, S, and Cl. Those elements are from the detergent. Mg with similar atomic size to calcium can incorporate into the lattice of calcite crystal but not the lattice of aragonite.[4a] (d1) The SEM micrograph of crystals found on the surface of glass tumbler from the dishwasher. (d2) The elemental analysis of (d1) from EXD in the SEM instrument. The patterns shown in red and in blue are the crystal and the background, respectively, indicates crystals in (d1) as calcium carbonate.

119
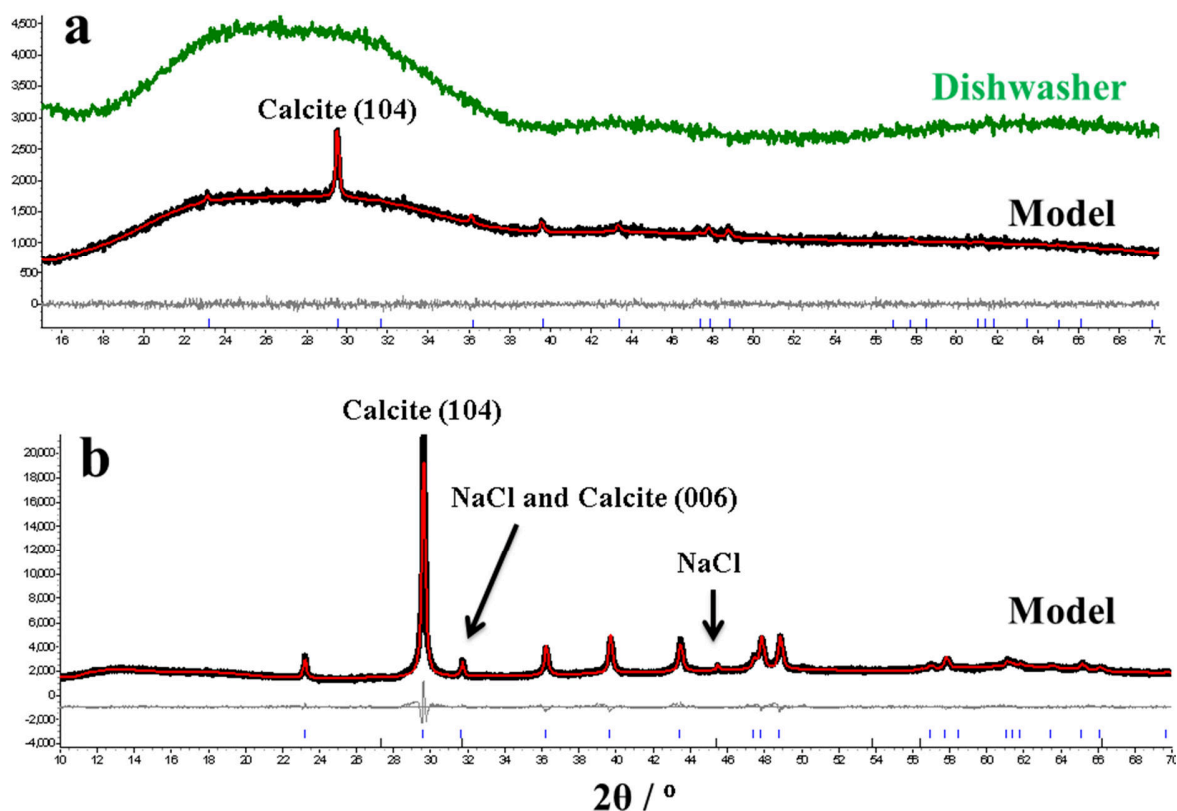
Figure 2.17 The PXRD patterns of glass samples after five cycles from dishwasher and model system with the substrate (a) and without substrate (b). (a) The experimental patterns of glass samples from dishwasher and model system are shown in green and black, respectively. There is no peak observed for a sample from dishwasher due to the lack of sample on surfaces. While glass sample from a model system with more crystals on the surface, shows crystal as calcite with no preferred orientation, this is consistent with the PXRD result of scraped powder, which is shown in (b). (b) PXRD patterns of scraped powder from glass sample of the model system shows all peaks belong to calcite expect two weak peaks. These two peaks belong to NaCl. The peak at 2θ = 32 is overlapping peak of NaCl and calcite (006). Difference lines are shown at the bottom in gray. The red pattern is the simulated line.

2.5.1.3   Crystallization in a Pumped Model System

We confirmed that the model system without a circulating pump produces the same polymorph as the dishwasher. This subsection compares the distribution of crystals on PMMA slides in a model system with and without a pumping system which circulates mother liquor over the substrate in a continuous fashion. Both set-ups are shown in Section 2.3.2.1. For PMMA samples, the involvement of the pump in the model system produces the same polymorphs as when there is no pump. The polymorphs produced are the flora-like aragonite (001) and rice-like calcite (C1 morphology). The pyramid-like calcite (C2 morphology) was not observed. According to our observations, pyramid-like calcite crystals tend to appear in the first several cycles, and can

hardly be observed after 5 or 6 cycles. The SEM observations and the corresponding PXRD characterization for samples produced by the model system with and without pump are shown in Figure 2.18 and Figure 2.19, respectively. From Figure 2.18 (a & b), we can see more crystals observed on PMMA slide produced from model system without a pump. The possible reason may be due to the fact that in the unpumped configuration the PMMA is constantly dipped into the solution while in the pumped system, the solution is dripped onto the surface. Therefore, the build-up of crystals (aragonite) on surfaces is faster when the contact time is longer. In Figure 1.18d, it can be observed that crystals produced with the pumping system are mainly the small version of flora-like aragonite, smaller than the flora-like aragonite seen in the model system without a pump. This is reflected in the peak intensity in the PXRD patterns (Figure 2.19). PXRD refinement reveals there is a greater proportion of aragonite to calcite grows on PMMA surfaces when there is no pump involved. This is consistent with SEM observations. The amount of calcite, on the other hand, on surfaces of both samples is similar. This can be seen from the peak intensity of calcite (104) in both PXRD patterns. However, there is more aragonite observed on PMMA slides produced from the non-pumping model system. However, both systems produced the same aragonite crystals, which are made from the basic unit 'single crystals of needle-like aragonite (001)'. The rice-like calcite crystals in both systems may be from the indirect adherence in solution.

Combining both SEM observations and PXRD analysis results, the model system without the pumping system favors the growth of aragonite in a faster speed. This can be attributed to a reduced interaction time and interaction area between the substrate and the solution in the model system with the pump. Nevertheless, the same polymorphs with the same properties are produced regardless of the pump. Hence the model system without the pump, as a simplified model, is an easy, straightforward, and representative way to study the effects of the chemistries of the solution on CaCO$_3$ growth.
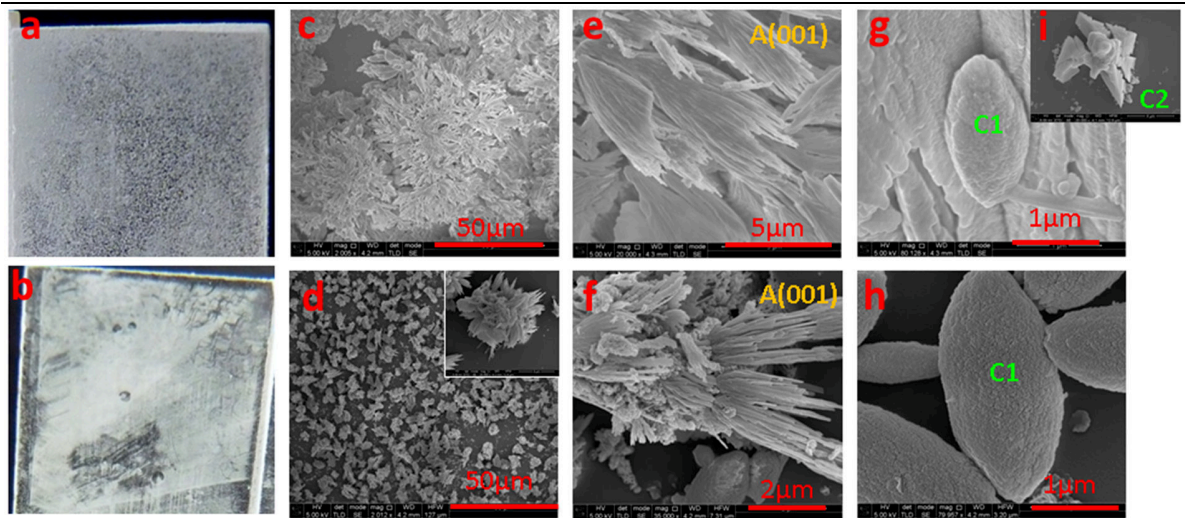
Figure 2.18 The PMMA samples produced with the model system after five cycles with the absence of pump (a, c, e, g) and with pump (b, d f, h). The filmed PMMA samples with no pump (a) and with pump (b); The general distribution of crystals on surfaces of PMMA slides without pump (c) and with pump (d); The needle-like single crystal of aragonite (001) appears like a petal, which is observed when there is no pump (e) and with pump (f); The rice-like calcite (C1) seen in model system without pump (g) and with pump (h). (i) The pyramid-like calcite (C2) discovered in the model system when there is no pump. It is not observed when a pump involved.
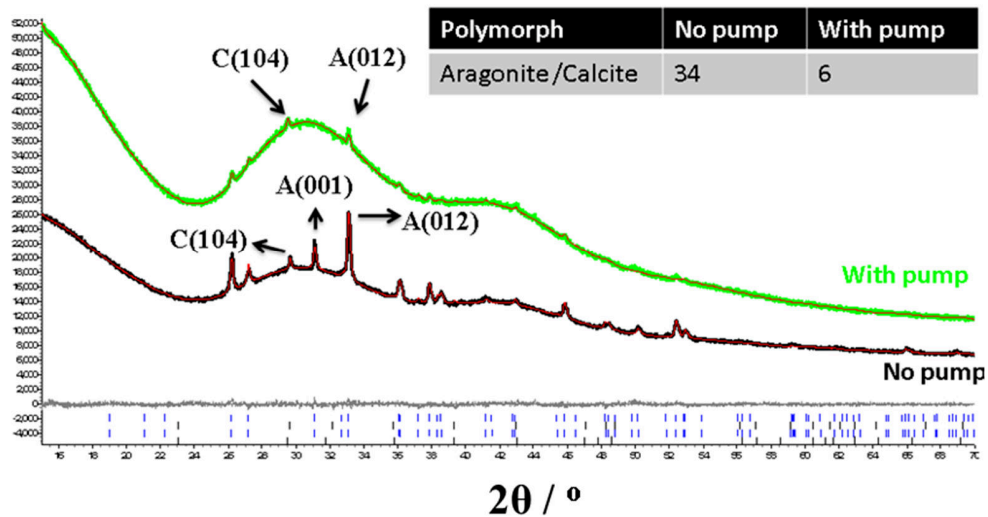
Figure 2.19 The PXRD patterns collected with substrates. The experimental patterns for samples produced in a model system with pump and without pump are shown in in green and in black, respectively. The red line is the simulated pattern generated by the Rietveld refinement. The upright table is to demonstrate the simulation result of the ratio of aragonite to calcite. Pump in the model system.

2.5.1.4   Discussion of Crystallization with Nil-HEDP Formula after 5 Cycles

The ratio of the aragonite to calcite on PMMA slides that are produced from the three different set-ups is different. The PMMA slide in a model system with the pump is placed horizontally, while the substrates in the dishwasher and the model system are placed vertically. Surfaces that are oriented horizontally are exposed to sedimentation; particles formed in bulk solution can adhere to the surface of the PMMA slide. This is probably why there is more rice-like calcite found on PMMA slide from the model system without a pump. While the flower-like aragonite crystals and aggregated, calcite or pyramid-like follows the heterogeneous nucleation. Similar conclusion regarding the growth mechanism on the vertical and horizontal substrate is made by Wang.[28]
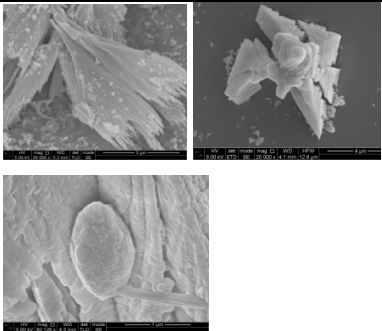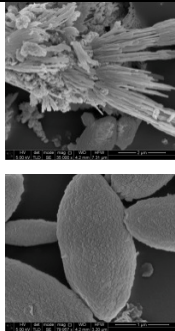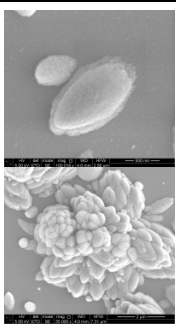
Table 2.9 is a summary of results from Figure 2.12 to Figure 2.17 for PMMA and glass samples. Comparison results for PMMA samples between the dishwasher and model system are shown from Figure 2.10 to Figure 2.14. For glass samples, results are shown from Figure 2.16 to Figure 2.17. A brief comment on each technique has been given in the corresponding column. Technically, we can see that PXRD exhibits certain advantages over the FTIR method: (a) PXRD yields higher detection limit and provides more information regarding polymorph distribution; (b) PXRD can be used for a non-destructive analysis, where information of preferred information can be obtained by applying Rietveld refinement. In subsequent analysis, FTIR will not be applied as PXRD is adequate and preferred for polymorph identification.

When using full Nil-HEDP detergent in solution, the same polymorphs of CaCO$_3$ are observed on the same substrate regardless of what set-up is applied. The difference in the quantity of the crystals grown on glass surface may be due to surface roughness and agitation effects. However, different CaCO$_3$ polymorphs are grown on the different substrate. For PMMA substrate, aragonite (001) with flora-like morphology and pyramid-like calcite or rice-like calcite are observed. The rice-like calcite is believed to grow from indirect adherence from solution, as they are observed either on the surface of flora-like aragonite.[28] For a glass substrate, rice-like calcite is the only polymorph found on the surface. However, from the TEM observations, we know that the basic unit of the flower-like aragonite and rice-like calcite are needle-like aragonite (001) and single crystal calcite, respectively. It indicates that the big crystals found on both substrates may be formed by agglomeration or assebly from those single crystals. For example, the assembly or aggregation of the single crystals of calcite into different shape can be observed in Figure 2.16. It

seems that the resulting shape of calcite depends on how many single crystals of calcite agglomerated together. However, the detailed study on the crystal formation process was not carried out in this project and requires further work.

The ratio of the aragonite to calcite on PMMA slides that was produced from the three different set-ups are different. The PMMA slide in the model system with the pump is placed horizontally, while the substrates in the dishwasher and the model system are placed vertically. Surfaces that are oriented horizontally are exposed to sedimentation, particles formed in bulk solution can adhere to the surface of the PMMA slide. This is probably why there is more rice-like calcite found on PMMA slide from the model system without a pump. While the growth of the flower-like aragonite, the aggregated calcite, and pyramid-like calcite follow the heterogeneous nucleation. Wang[28] made a similar conclusion on the growth mechanism on the vertical and horizontal substrate.

Table 2.9 The summary of sample characterization for PMMA and glass slides produced with the standard Nil-HEDP formula after five cycles.

Substrates	PMMA			Glass	
Systems	Dishwasher	Model system	Model system with pump	Dishwasher	Model system
Images					
Technique					
FTIR	Aragonite (Figure 1.12)		/	/	
PXRD	Aragonite (001) with trace calcite (Figure 2.13)		Aragonite (001) with calcite (Figure 2.19)	100% calcite	
	Aragonite/Calcite =99/1	Aragonite/Calcite =96/4	Aragonite/Calcite=85/14	Calcite (Figure 2.17)	
TEM with EDX	Single crystal of aragonite (001) (Figure 2.14)		Not shown here	Calcite (Figure 2.16)	
SEM with EDX	Flower-like aragonite and calcite (Figure 2.11)		Flower-like aragonite and calcite (Figure 2.18)	Rice-like calcite (Figure 2.16)	
Summary	Flower-like aragonite is made up from layers of petals. The petal is made up from a needle-like single crystal of aragonite (001). $\leq$ 1% calcite is observed with two different morphologies.		Petal-like aragonite crystal is made from a needle-like single crystal of aragonite (001) with more rice-like calcite observed.	Rice-like calcite and calcite observed in an aggregated shape.	

2.5.2 Scale Evolution Study in Model System
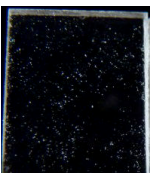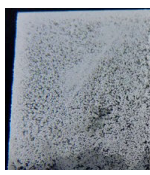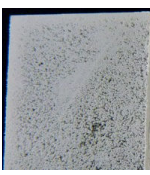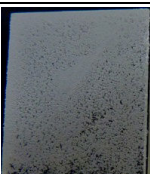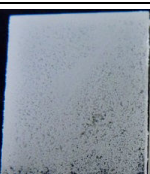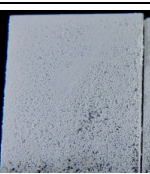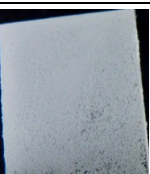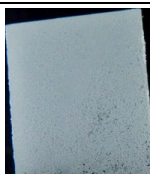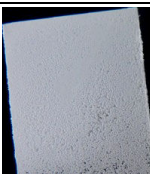
In the previous subsection, we confirmed that the model system without a pump could mimic the growth of CaCO$_3$ crystals in the dishwasher. This section we will discuss how surface scale evolves as the crystallization cycle increases. The understanding of shine evolution and variation of CaCO$_3$ polymorphs distribution may provide an insight into the mechanism of scale formation. Hence, some inspiration for the inhibition of crystal growth.

2.5.2.1 On PMMA Slides up to 12 Cycles

PMMA slides are prepared in Nil-HEDP formula at 65 ^{o}C (See Section 2.3.2.2 for experimental procedure). After crystallization for an hour, the PMMA slides are taken out, rinsed with cold and hot DI water (60 ^{o}C) for one minute, respectively. The substrates are left in the air to dry. The procedure is then repeated. Two sheets of each substrate are retained each time for analysis, and the remainder is replaced in the new solution. Samples for further characterization are analyzed by PXRD, FTIR, SEM and TEM.

The changes of 'shine' on PMMA slides from the 1st cycle to the 12th cycle is evident (Table 2.10). In the first cycle, a small amount of CaCO$_3$ crystals starts to appear on PMMA surfaces, followed by a clear growth in the second cycle. This change may be due to the existing crystals, produced in the first cycle, serving as nuclei seeds for the second cycle. The preexisting nuclei induce growth of crystal without the need to overcome an activation barrier, hence resulting in a faster growth rate under the same initial supersaturation. From the 1st to the 6th cycle, the crystals gradually cover the surface. From the 8th cycle on, original PMMA surfaces can be hardly seen by the naked eye. After 12 cycles of crystallization, the surface becomes completely white.

Table 2.10 The change of surface shininess with the increase of cycle up to 12.

Cycle 1-6	1st cycle	2nd cycle	3rd cycle	4th cycle	5th cycle	6th cycle
Image						
Cycle 7-12	7th cycle	8th cycle	9th cycle	10th cycle	11th cycle	12th cycle
Image						

As discussed in Chapter one, the formation of the first layer of crystals and hence the crystals formed in the first cycle is crucial. The PMMA slide, taken out at the first cycle, was characterized by SEM and TEM (Figure 2.20). Three different morphologies of crystals are observed on PMMA slide at the first cycle. They are flower-like aragonite in the red circle (Figure 2.20 b & c), rice-like calcite in green circle (Figure 2.20 c & d) and pyramid-like calcite in a blue circle (Figure 2.20d). The TEM identification of the first two polymorphs have been shown above in Figure 2.14 and Figure 2.16, respectively. So here we will only show the TEM identification of pyramid-like calcite (Figure 2.20 e, f & g), which is labeled as C2 morphology in green color. This pyramid-like calcite is identified as a single crystal with a trace amount of Mg. (Section 2.4 has already discussed that Mg^{2+} can incorporate into calcite lattice but not that of aragonite)
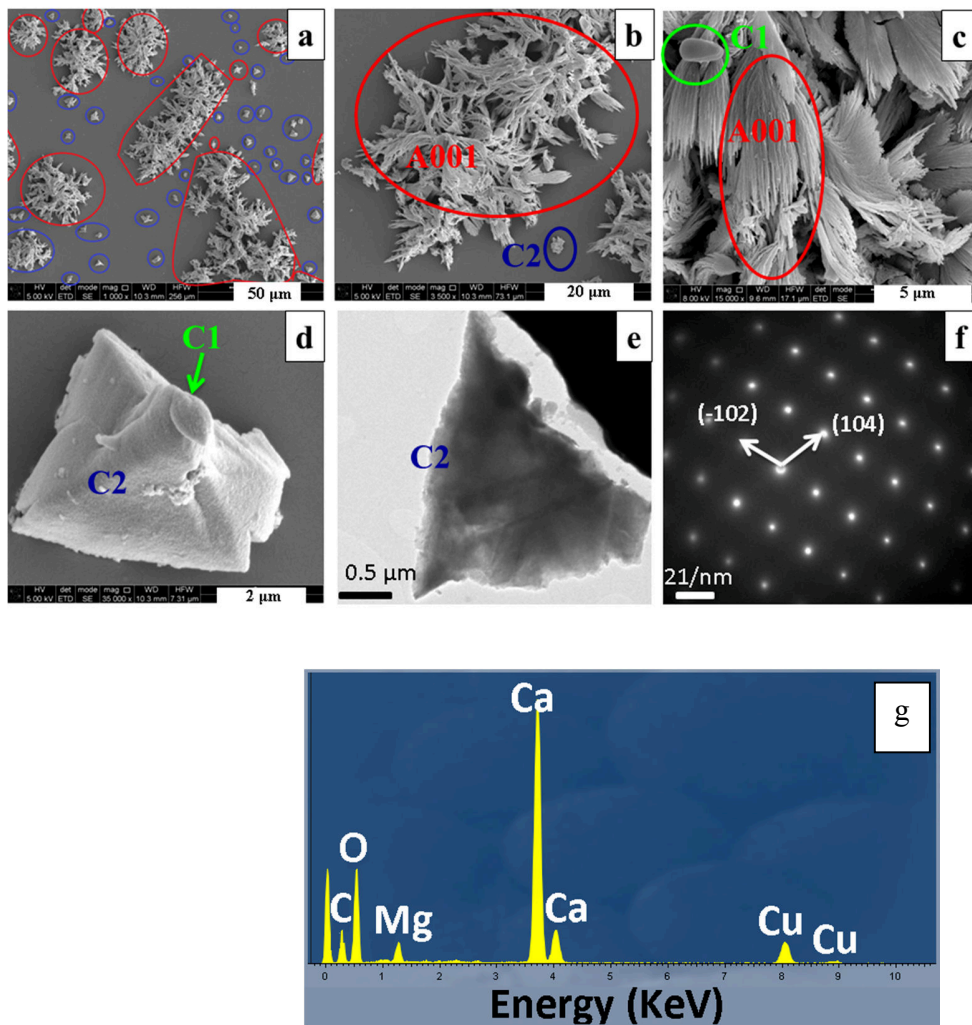
Figure 2.20 The morphologies observed after the first cycle of the crystallization with the standard full Nil-HEDP formula. Three different morphologies of CaCO$_3$ observed in SEM (a, b, c and d) and the TEM identification for pyramid-like calcite (e, f, g). These three morphologies are aragonite labeled as 'A' in red (a, b, c) and two different morphologies of calcite, which are labeled as 'C1' in green and 'C2' in blue, respectively. (a) The general distribution of two main morphologies with a scale bar of 50 µm: flora-like aragonite in red and pyramid-like calcite in blue. (b) The overall morphology of flora-like aragonite with a scale of 20 µm. (c) The petals of aragonite and the rice-like calcite are observed. Scale bar is 5 µm. (d) The overall morphologies of two different calcite. The morphologies of C1 and C2 are also observed in (c) and (b), respectively. (e) Bright field image shows crystal has the similar morphology to that shown in (d). (f) The TEM diffraction pattern shows the crystal observed in (e) as a single crystal calcite. (g) The microanalysis for calcite in (e), shows crystal as calcite with the presence of Mg^{2+}.

Cycle	Ratio of Aragonite to calcite	Errors
1st cycle	0.9	/
2nd cycle	2.2	/
4th cycle	9.3	±8.8%
6th cycle	25.6	±0.26%
8th cycle	58.1	±0.14%
10th cycle	56.2	±0.10%
12th cycle	75.8	±0.11%
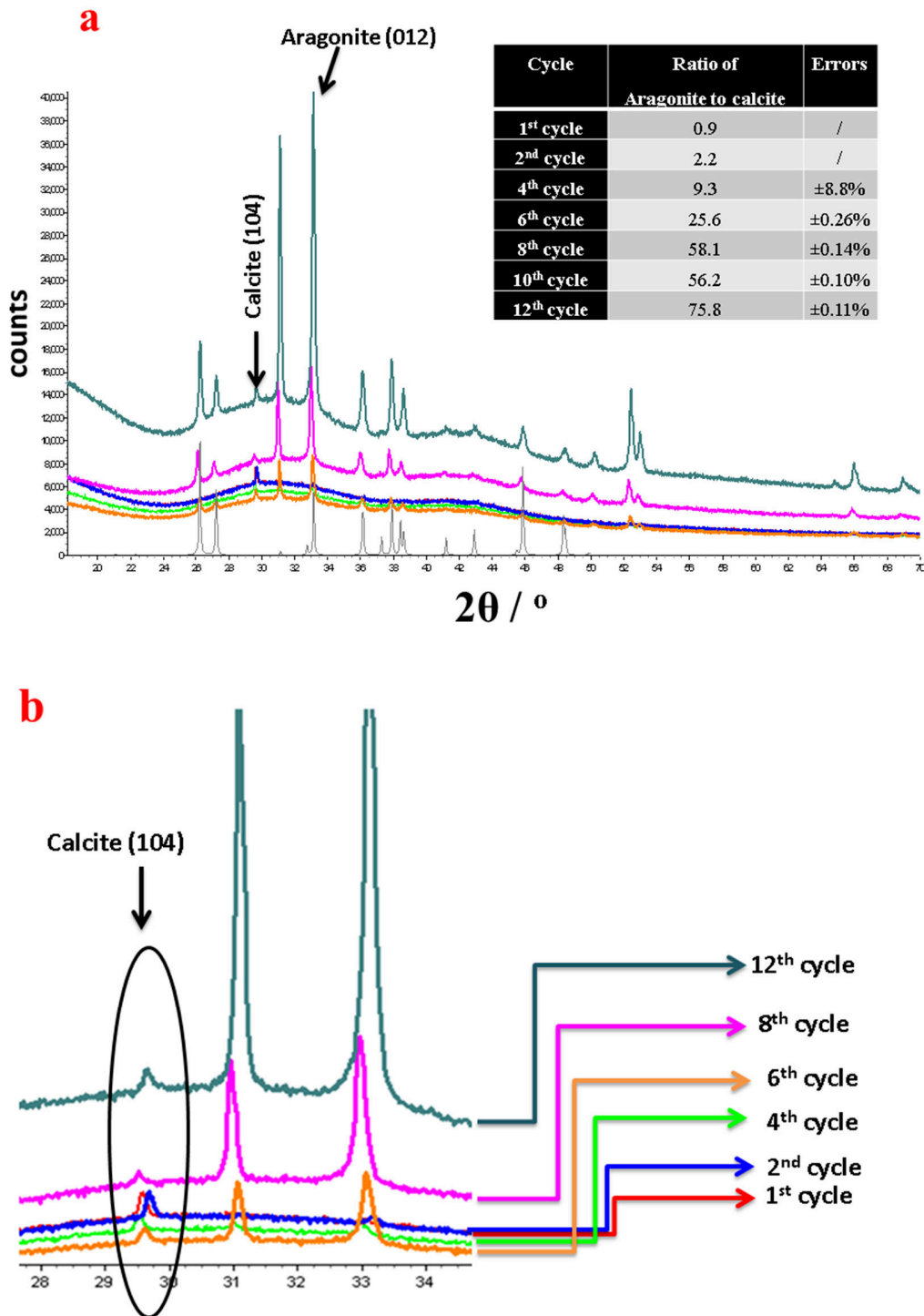
Figure 2.21 The PXRD patterns collected with PMMA substrates of samples taken after the 1st cycle (in red), the 2nd cycle (in blue), the 4th cycle (in green), the 6th cycle (in orange), the 8th cycle (in purple red) and 12th cycle (in aqua). (a) The full reflection of the PXRD patterns of the samples. The gray line at the bottom is the reference pattern of aragonite. All peaks belong to aragonite expect the one peak calcite (104), which is the most intense peak of calcite. The aragonite (012) is the most intense peak when aragonite has a preferred orientation in (001) plane. (b) The enlargement of (a) of 2nd from 28° to 34°, shows that the peak intensity of calcite has no obvious change. While peak intensity of aragonite starts to rise from the 4th cycle on and increases significantly after the 6th cycle.
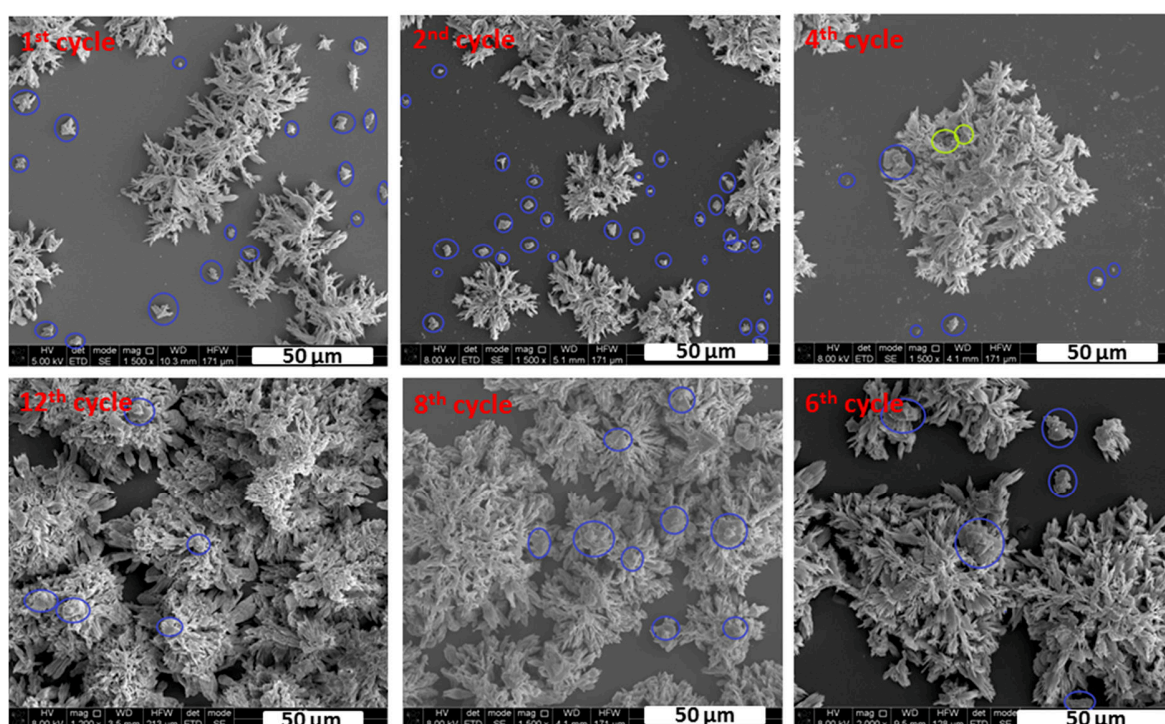
Figure 2.22 The overall distribution of pyramid-like calcite (in blue), rice-like calcite (in green circle) and the flora-like morphology changed with the increase of cycle. The scale bar is 50 μm.

These three morphologies are observed throughout the 12 cycles. According to the PXRD analysis in Figure 2.21, both calcite and aragonite are present in a small quantity at the first cycle. With the increase in the number of cycles, the peak intensity of calcite (calcite 104) hardly changes (Figure 2.21b), while the peak intensity of aragonite increases dramatically. Aragonite (001), with the increase of the number of cycles, becomes the dominant polymorph. The ratio of aragonite is up to 90% on the 4th cycle and 98% after the 8th cycle. The calculation of the ratio of aragonite to calcite is based on the Rietveld refinement and is summarized at the up-right of the Figure 2.21. The exact ratio of aragonite to calcite may not be accurate because the calculation is high at the first two cycles, but the fact that aragonite is the dominant phase is consistent with the observations from SEM as can be seen from Figure 2.22.

The SEM micrographs in Figure 2.22, show more details about the distribution of CaCO$_3$ polymorphs with the increase of cycles. At the 1st cycle, the pyramid-like calcite (in a blue circle) and flora-like aragonite turn up in a similar amount, and they continue to appear in a similar distribution at the 2nd cycle. At the 4th cycle, the size and amount of flora-like aragonite crystals start to increase. At the 6th cycle, the quantity of aragonite increases dramatically as indicated by

both the PXRD and SEM. From the 8th cycle on, aragonite almost occupies the whole surface with a small amount of calcite observed. As shown by PXRD, the amount of calcite crystal has hardly changed, while aragonite crystals increase with crystallization cycle. Therefore, the peak of calcite (104) in PXRD can be allocated to the pyramid-like (rice-like calcite is observed but few), which is constantly observed through 12 cycles.

As a summary for the growth of CaCO$_3$ on the surface of PMMA, pyramid-like calcite, and flora-like aragonite are the two main morphologies found on surfaces at the first cycle, they start to appear on the surface with a small quantity. With the increase of cycle, the aragonite grew dramatically faster than that of calcite and made up of 99% after five cycles of crystallization. The loss of shine on PMMA can be mainly attributed to the growth of aragonite (001). Therefore, an efficient CaCO$_3$ inhibitor should prevent the nucleation of both calcite and aragonite, especially the growth of aragonite.

In Rietveld refinement (Figure 2.21), the calculation error for aragonite to calcite ratio is below 10% at the 4th cycle. At the 5th cycle, the quantity on the surface of PMMA sample is sufficient, resulting in a good PXRD pattern, and hence the error declines to 0.5%. Moreover, distribution of CaCO$_3$ polymorph species, namely, the ratio of aragonite to calcite hardly changes after the 5th cycle. Hence, the first five cycles are enough to study the build-up of deposits on surfaces. Also, the quantity of sample at the 5th cycle is sufficient to be analyzed by PXRD. In the next subsection, the scale evolution on glass samples will only be shown for the first five cycles.

2.5.2.2 On Glass Slides up to 5 Cycles

The changes of 'shine' on glass slides from the 1st cycle to the 5th cycle is evident (Figure 2.23). In the 1st cycle, a small amount of CaCO$_3$ crystals starts to appear on glass surfaces, followed by a clear growth in the 2nd cycle. This is the same growth tendency observed on PMMA substrates. From the 1st cycle to the 5th cycle, the crystals gradually cover the surface. After five cycles of crystallization, the surface becomes almost white. Through the five cycles, only one morphology, namely, the rice-like crystals are observed on the glass slide. This is consistent with PXRD results (Figure 2.24), which identify the crystals on glass as calcite. The SEM micrographs in Figure 2.23 show more details the variation of calcite crystals with the increase of cycles. Calcite crystals start to appear in a small quantity at the 1st cycle. However, calcite crystals do not have a well-defined texture. With more cycles, the rice-like calcite gradually develops and becomes

clear in shape. Crystals observed at the 5th cycle have a much larger size than those found in the 1st cycle. As discussed in Section 2.5.1.2, rice-like calcite crystals tend to aggregate together to form new shapes: cauliflower calcite in the 2nd cycle and bread-like or peanuts calcite observed at the 5th cycle.
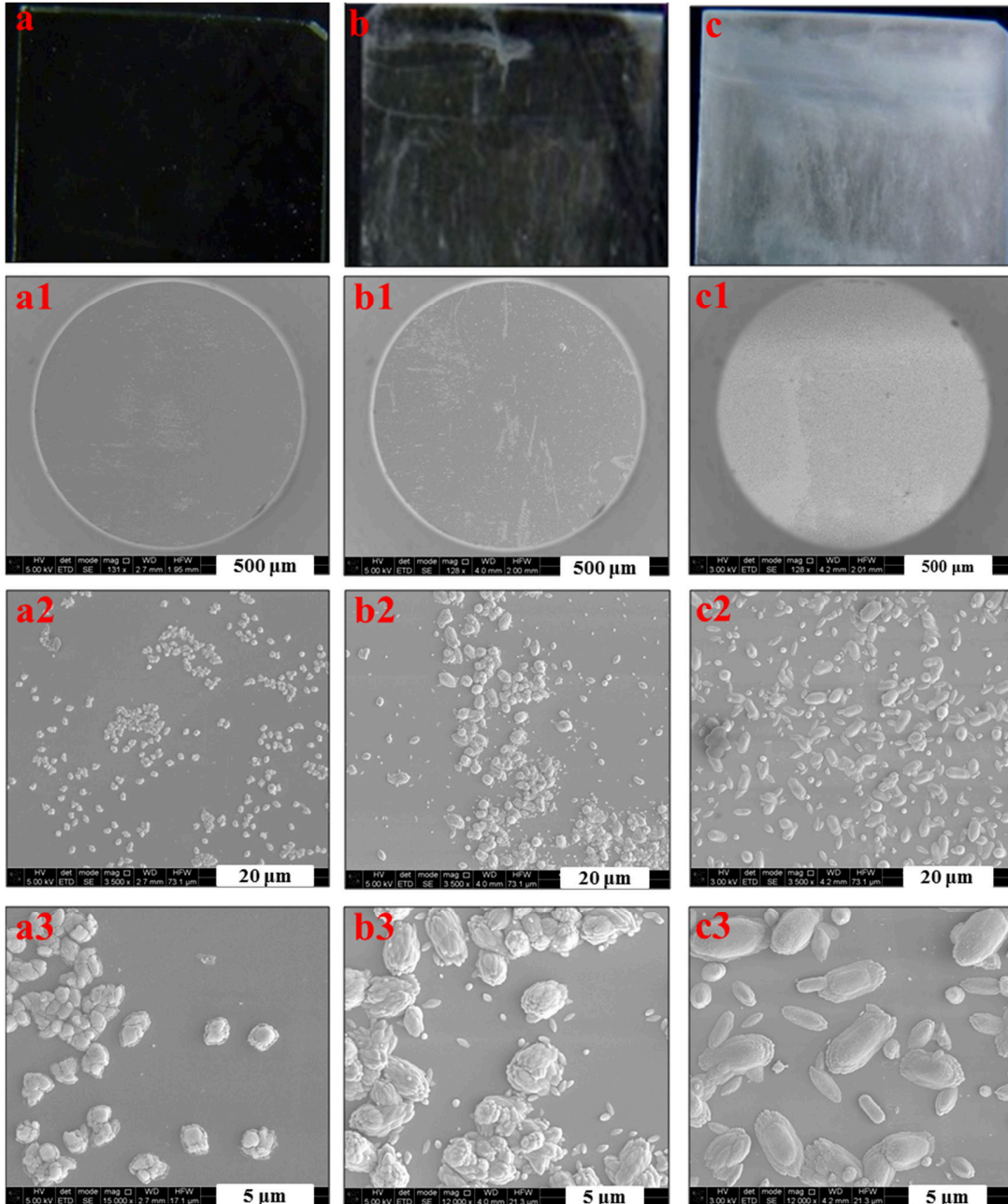
Figure 2.23 The change of surface shininess on glass slides with the increase of cycle up to 5. (a) Sample taken out after one hour; (b) The sample was taken out after two-hour crystallization; (c) sample taken out after five-hour crystallization. Images with number is the corresponding SEM images with a scale bar of 500µm (a1, b1 & c1), 50µm (a2, b2 & c2) and 5 µm (a3, b3 & c3).
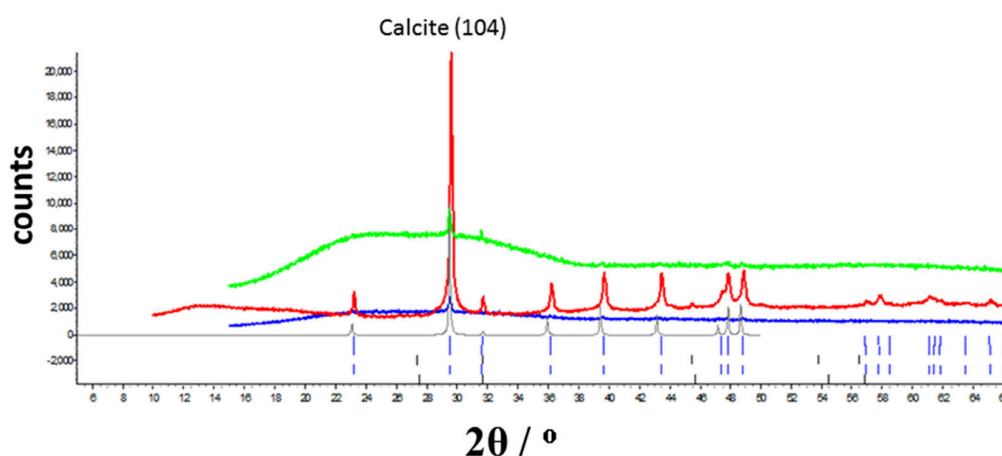
Figure 2.24 The PXRD patterns of glass samples taken out at the 1ˢᵗ cycle (in blue), at the 3ʳᵈ cycle (in green) and at the 5ᵗʰ cycle (in red), showing calcite is the only polymorph found on glass slides. At the third cycle, there are few crystals observed on the surface; the background noise contribution is high and only calcite (104) peak is observed. At the 5ᵗʰ cycle, due to the increased crystal quantity, the peaks belong to calcite is clearly seen. The gray pattern is the calculated pattern of calcite from literature (18164-ICSD).[29]

2.6 The Effects of Polymer on CaCO₃ Crystallization

From sections 2.4 to 2.5, we found that the addition of full Nil-HEDP formula changes the polymorph species of CaCO₃ formed on surfaces. When full Nil-HEDP formula is absent, a mix of the classical shape of calcite and aragonite is observed on PMMA and glass, with a ratio of aragonite to calcite 3/1. It is also observed that the addition of full Nil-HEDP formula changes the polymorphic form of CaCO₃ found on PMMA and glass: aragonite (001) with trace calcite and pure calcite crystals are found on PMMA and glass slides, respectively. It seems that it is the composition of full Nil-HEDP formula that determines this difference rather than the other parameters in the system. Hence, in this section, we will explore what how the composition of the Nil-HEDP formula influences the shine and the polymorphic forms of CaCO₃ on different substrates.

2.6.1 Investigation of the Effects of Polymer in Model System

The effects of the different ingredients in the Nil-HEDP formula have been explored in the model system without the pumping system. One reason for using the no-pupming system is that the effects of agitation are negligible, which have been demonstrated above. The other reason is to

focus on the understanding of the chemistry of the washing solution other than the hydrodynamics.

Five different solution compositions with the same supersaturation ratio were used to generate samples for comparison. These compositions are 'carbonate only,' 'Nil-HEDP formula,' 'Nil-HEDP formula without polymer ('full minus polymer')' 'Nil-HEDP formula without surfactant ('full minus surfactant'),' and 'HEDP formula.' The involvement of 'Nil-HEDP formula' and 'HEDP formula' can be used to study the difference of crystal growth both with and without inhibitor. The composition of each chemical condition is listed in Table 2.11 below. The 'carbonate only' sample refers to hard water (Ca^{2+}/2.75 mmol L^{-1}, Mg^{2+}/0.0806 mmol L^{-1}) and CO_3^{2-} (18mmol L^{-1}) in the washing solution. The 'carbonate only' conditions are used as a comparison to understand the effects of Nil-HEDP formula on $CaCO_3$ growth. 'Full minus polymer' and 'Full minus surfactant' were intended to study the effects of surfactant and polymer when they are intentionally excluded. The samples were run for 5 times.

Table 2.11 The chemical conditions that used to produced samples in the dishwasher and the model system.

Conditions	Water		"Filler"/Alkalinity		Builder	Polymer /	Surfactant	Inhibitor
	$CaCl_2$	$MgCl_2$	Na_2CO_3	Na_2SO_4	MGDA	Acusol 588	Non-ionic mixture	HEDP
Carbonate only (with Mg)	yes	yes	yes	no	no	No	no	no
Full minus polymer	yes	yes	yes	yes	yes	No	yes	no
Full minus surfactant	yes	yes	yes	yes	yes	Yes	no	no
Full Nil-HEDP formula	yes	yes	yes	yes	yes	Yes	yes	no
HEDP formula	yes	yes	yes	yes	yes	Yes	yes	yes

2.6.1.1 On the Shine Loss

Each sample was run five cycles to obtain enough deposits for the analysis by PXRD. The crystal morphologies were recorded by SEM. The clarity on the surface is assessed by visual inspection. The surface characterization of PMMA and glass samples from five different washing solution have been summarized in Table 2.12. The clarity of PMMA and glass slides under different chemical conditions is presented in a column chart as can be seen in Figure 2.25.

We will begin the discussion with the clarity variation on the surfaces of PMMA and glass after five cycles first. As can be seen in Figure 2.25, when using the 'HEDP formula,' the clarity of samples keep the same shine as the original. When in other four washing solutions, PMMA slides suffer from different degrees of filming in different washing solution, while for the glass slides, a similar degree of clarity was retained under all chemical conditions. This may indicate that PMMA slides are more chemistry dependent comparing to glass substrates. PMMA slides suffer from filming most when using the 'Nil-HEDP formula.' When excluding the polymer or surfactant from the 'Nil-HEDP formula,' the shine on the surface of PMMA improved, especially when the polymer is excluded. It can be seen that only the presence of a CaCO$_3$ inhibitor can allow the substrate to retain its shine. Moreover, the presence of polymer promotes the growth of CaCO$_3$, especially for PMMA.
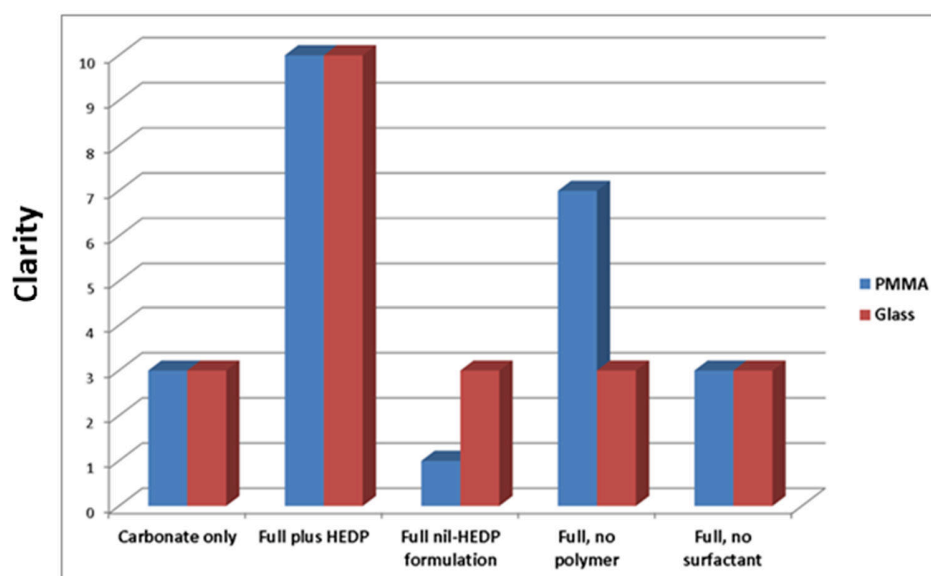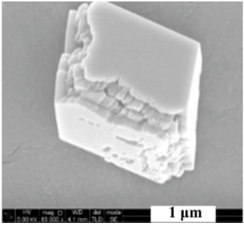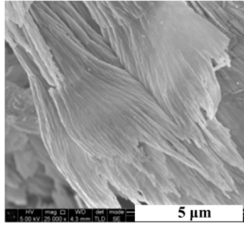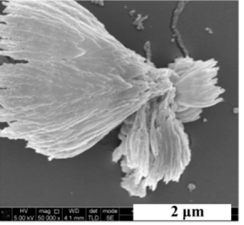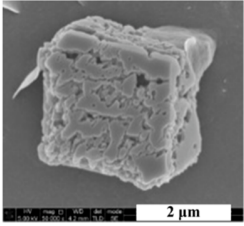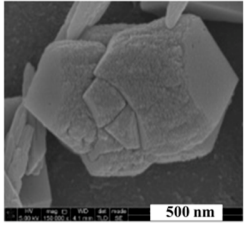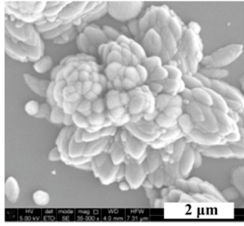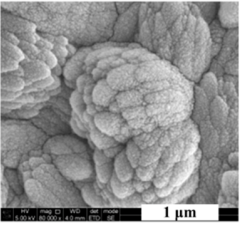
Figure 2.25 The changes of clarity on PMMA and glass slides when using different formulations.

2.6.1.2   On the CaCO$_3$ Polymorphs

The surface characterization of PMMA and glass by PXRD and SEM has been summarized in Table 2.12. It can be seen that the polymer changes the polymorphic form of CaCO$_3$ and the corresponding crystal morphologies. When the polymer is absent, it is shown that a similar ratio of aragonite to calcite, which is 3/1, is detected by PXRD regardless of substrate type and the presence of a surfactant. The morphologies of aragonite and calcite observed on both glass and PMMA slides are similar to the classical morphologies of calcite and aragonite.

Table 2.12 The PXRD analysis for glass and PMMA samples from the model system. To show the full morphology of crystals, the SEM images are not shown in the same scale bar.

	No polymer		With polymer	
	Carbonate only	**Full minus polymer**	**Nil-HEDP formula**	**Full minus surfactant**
PMMA	A/C=3/1	A/C=3/1	A/C=99/1	A/C=99/1
Glass	A/C=3/1	A/C=3/1	Calcite	Calcite

With the presence of polymer in solution, flower-like aragonite with a small amount of calcite tends to grow on PMMA, calcite crystals with cauliflower-like shape grow on surfaces of the glass. Flower-like aragonite is made from needle-like aragonite (001), while calcite observed on glass is made from a rice-like single crystal of calcite. The flower-like aragonite with a size up to 100 μm has not been previously reported in the literature. The only similar shape found is from barium chromate crystals.30 Aragonite (001) crystals with a similar morphology are still observed with the absence of surfactant. Therefore, it can be seen that the presence of polymer changes the polymorphic distribution on surfaces as well as the morphology of calcite and

aragonite. Moreover, the surfactant has no obvious effect on the polymorph distribution or modification of the morphology. In summary, it is the presence of polymer determines the distribution of CaCO3 polymorphic forms other than other ingredients in Nil-HEDP formula.
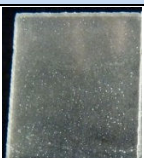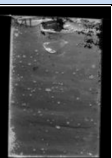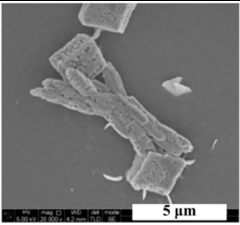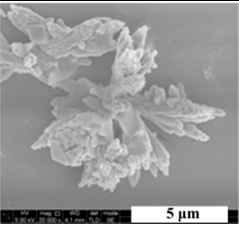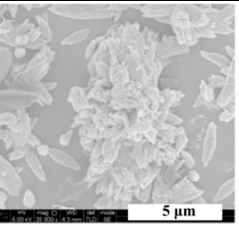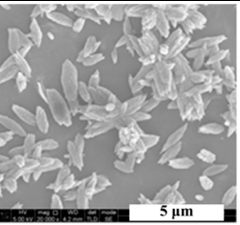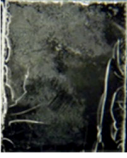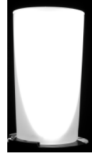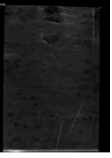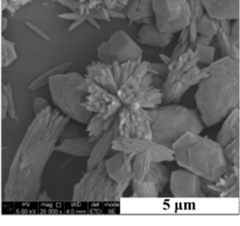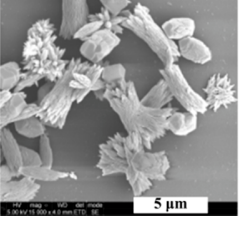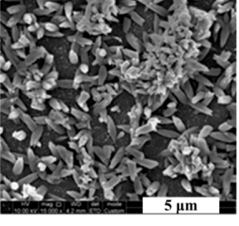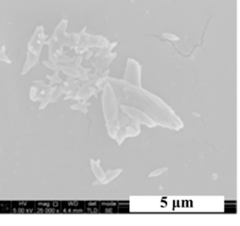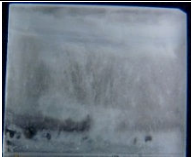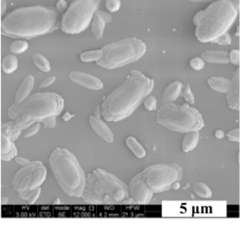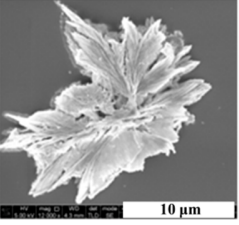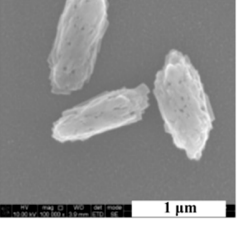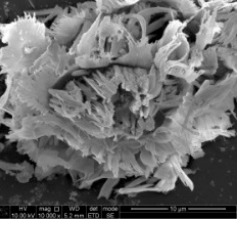
2.6.2 Comparison of Samples from Model System *vs.* Dishwasher

The comparative results of samples produced from the model system and the dishwasher are summarized and shown in Table 2.13. The chemical conditions used to generate the samples are shown in Table 2.12. It can be seen that from the Table 2.13 that the degree of shine loss of samples produced from the model system is similar to those from the dishwasher. The only exception is the glass tumbler produced from the dishwasher when using 'Full Nil-HEDP formula' (Shaded in purple, Table 2.13). The shine loss of PMMA slides that from the model system, and the dishwasher is similar. However, the shine loss of the glass samples of 'Full Nil-HEDP formula' is different. Comparing to the glass sample from the model system, the glass tumbler from the dishwasher can keep the clarity to 75.2% after five cycles. The underlined reason is unclear. However, it may be attributed to surface roughness difference between the glass tumbler and the microscopy slide (the former has a smoother surface than the latter, see Section 2.2.2), and the agitation effects inside the dishwasher. Extra of polystyrene plastic tumblers are also produced in dishwasher under same chemical conditions. It will not be discussed here, for details, see Appendix 3.

Table 2.13 Three chemical conditions that used to produced samples both from dishwasher and model system.

Nil Pv30 formula	water		"Filler"/Alkalinity		Builder	Polymer / CGI	Surfactant
	CaCl$_2$	MgCl$_2$	Na$_2$CO$_3$	Na$_2$SO$_4$	MGDA	Sulfonated polyacrylates	Non-ionic mixture
Carbonate only	yes	yes	yes	no	no	no	no
Full, no polymer	yes	yes	yes	yes	yes	no	yes
Full with polymer	yes	yes	yes	yes	yes	yes	yes

Table 2.14 The characterization summary for glass and PMMA samples produced by the model system and the dishwasher under different chemical conditions.

	Model system		Dishwasher	
	Glass	PMMA	Glass	PMMA
	3	5	0.0	65.8
CO₃²⁻ only				
PXRD	A/C = 75/25 (± 0.74%)	A/C=75/25 (±1.26%)	A/C=81/19 (±0.6%)	A/C=88/12 (±1.3%)
SEM				
	3	8	0.0	86.0
Full minus polymer				
PXRD	A/C=75/25 (± 0.6%)	A/C=70/29	A/C=94/6 (±0.3%)ᴿ	No enough sample
SEM				
	4	1	75.2	15.5
Full Nil-HEDP Formula				
PXRD	Calcite	A/C=99/1 (±0.42%)	No enough sample	A/C=99/1 (±0.1.9%)
SEM				

The CaCO$_3$ polymorph distribution observed on samples from the model system and dishwasher are the same on the same substrate. We have described CaCO$_3$ crystallization under different chemical conditions in a model system in Section 2.5 and Section 2.6.1. When the polymer is present, the CaCO$_3$ polymorph distribution and species are highly dependent on the type of the substrate. Aragonite crystals preferentially grow on surfaces of PMMA slides, while calcite crystals tend to grow on a glass substrate. Without the presence of the polymer, a mix of aragonite and calcite with their classical morphologies are found on surfaces regardless of substrate types. Aragonite crystals are observed as spherulites shape and calcite appears as rhombohedra or cubic. The only difference is the calcite morphologies. This is demonstrated in the column of 'carbonate only,' and 'full minus polymer' in Table 2.13 and is summarized in Figure 2.26. It is shown that the morphology of aragonite crystals observed are similar, but shapes of calcite are slightly different. The morphology of calcite found in the dishwasher has an irregular edge, while the calcite observed in the model system is either cubic or rhombohedral. This may be due to the high shear effect from the fluid which roughens the surface of calcite crystals.[31]
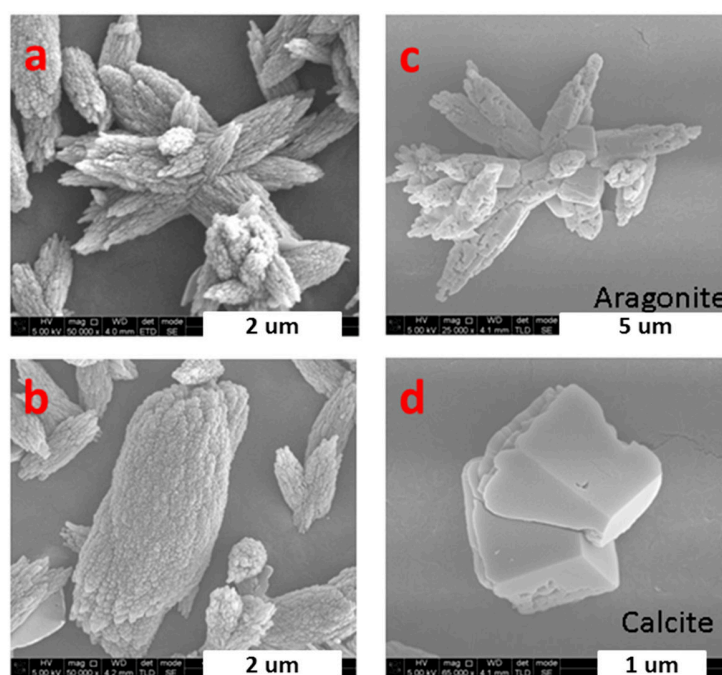
Figure 2.26 The morphologies observed on PMMA from dishwasher (a & b) and model system (c & d) with only Ca, Mg and CO$_3^{2-}$ in solution.

2.7 Conclusion

In this chapter, the ingredients of the Nil-HEDP formula have been explored for their effect on shine loss and the growth of a polymorphic form of CaCO3 on the surface of glass and PMMA slides. It is observed that the growth of polymorphic forms of $CaCO_3$ is similar between the glass and PMMA slides without polymer (acuso 588) addition. The presence of the polymer determines the growth of different polymorphic forms on difference substrates. On glass surface, only calcite is observed, and aragonite (001) is only found on PMMA. The presence of polymer also promotes the crystal growth on the surface, especially for PMMA slides. After only five cycles, the PMMA slides totally lose their clarity. It seems that both big crystals of aragonite and calcite are made up from corresponding single crystals, which further aggregate or assembly into different shapes and the polymer may promote this process. However, due to the limitation of the techniques, this is still lack of direct experimental evidence.

2.8 Analytical Methods

This section describes the different analytical techniques used in this project. The analytical techniques can be split into two sets: crystalline material characterization and single crystal characterization. Crystalline material studies mainly refer to the deposition of $CaCO_3$ on different substrates. Four ex-situ techniques have been employed to investigate the deposits on a surface and the film scraped from the surface. There are attenuated total reflectance infrared spectroscopy (ATR-IR) for deposit identification, X-ray powder diffraction (PXRD) for phase identification, scanning electron microscopy (SEM) with *in situ* energy dispersive X-ray spectroscopy (EDX) for morphology imaging and microanalysis, and transmission electron microscopy for the confirmation of the preferred orientation. The order of characterization carried out on each substrate is as follows: PXRD, SEM, ATR-IR, and TEM. This is because the ATR-IR spectra are collected by pressing the probe against diamond and will damage the sample while imaging in SEM requires a coating to be conductive. TEM is only applied when the preferred orientation of one phase needs to be confirmed, or an unknown morphology needs to be allocated. Atomic force microscopy (AFM) is also used in some cases to study the surface roughness of the substrates. Since PXRD has been the principal technique employed, it is described in the most detail. Relevant aspects of the ATR-IR, SEM-EDX, TEM, AFM and single crystal X-ray crystallography techniques are also briefly explained.

The calcium complexes of candidate inhibitors which formed suitable single crystals were studied using single crystal X-ray diffraction. Infrared spectroscopy, microanalysis and thermogravimetric analysis (TGA) have been used as supporting techniques for further identification of these new crystalline compounds.

2.8.1 X-ray Powder Diffraction

1.1.1.1   Sample Preparation

The preparation of the samples for PXRD is of essential importance for a good quality diffraction patterns and statistics.[32] The samples in this project are mainly produced by two types of experiments: One is calcium carbonate deposition on different substrates (in Chapter 2 and Chapter 3); the other is the synthesis of single crystals of the inhibitor candidates with Ca^{2+} (in Chapter 4). Two types of specimen are loaded into the PXRD instrument: a substrate with

deposits (a layer of thin film) and crystalline material. Filmed substrates are loaded using a bulk sample holder. Crystalline powders are loaded using a zero-background silicon flat plate sample holder. The sample may be scraped films from substrate produced in $CaCO_3$ deposition experiments, or products arising from solution crystallization of candidate inhibitors with calcium salts.

The selection of sample holder is dependent on the properties of the sample and the information required. For the study of calcium carbonate deposits, the polymorph distribution and the preferred orientation of the crystal are of great interest for this project. To acquire the information on preferred orientation, deposits on the substrate are collected as they are produced. No further sample preparation actions are required. The substrates are normally soda-lime glass and poly (methyl methacrylate) (PMMA). They are loaded into the diffractometer with bulk holders. Both glass and PMMA are amorphous material; they have no contribution to the peak intensity, but the background noise will be high. The powder samples, regardless of the experiment types, are all loaded with silicon holders, which offer a 'zero background'. Silicon holders are made from a 511 silicon wafer. Therefore, characterization results regarding the 'filmed substrate' are a combined conclusion from two diffraction experiments, namely, filmed substrate loaded with the bulk sample holder and scraped film loaded with the silicon holder. The former provides the information of preferred orientation; the latter gives the information on phase identification and polymorph distribution.

Good practice in powder sample preparation results in high-quality data for refinement.[32b] The ideal powder sample contains a large number of crystallites in random orientation. The distribution of orientation should be smooth and equally distributed. Thus all possible crystal orientations can be presented to the incident X-ray beam. Large crystals with a size more than $10\mu m$ or crystals with preferred orientation will lead to a change in peak intensity, ultimately resulting in the loss of real information about the samples.[32b] Grinding and sieving can effectively reduce the crystal size, remove the preferred orientation, and ensure sample homogeneity. The procedure for preparing the powder samples is as followed: samples were ground into a fine powder using a pestle and mortar. The powder was passed through a sieve (60, or 80 mesh) and sprinkled onto a silicon holder, which is coated with a thin layer of Vaseline® to prevent powder from falling out of the silicon slide.[32a]

1.1.1.2 Data Collection

The laboratory-based X-ray powder diffractometer 'Bruker D8 Advance', locally known as the "d7," is used to collect high-quality data for Rietveld analysis. It operates at 40 mA and 45 kV, using a nickel-filtered copper X-ray radiation (λ = 1.5406 Å). A Ni filter is used to remove CuK_β from the X-ray beam. Figure 2.27 shows the schematic diagram of an X-ray powder diffractometer. The X-ray beam is produced from the X-ray tube, collimated and directed to the sample by passing Soller slit and divergent slit. The conditioned incident X-ray beam is scattered by the specimen. The scattered X-ray beams pass through a series of receiving-side optics and are directed to a detector, which allows rapid collection of diffraction patterns with high resolution. This process is controlled by the software "Bruker AXS: XRD Commander".[33]
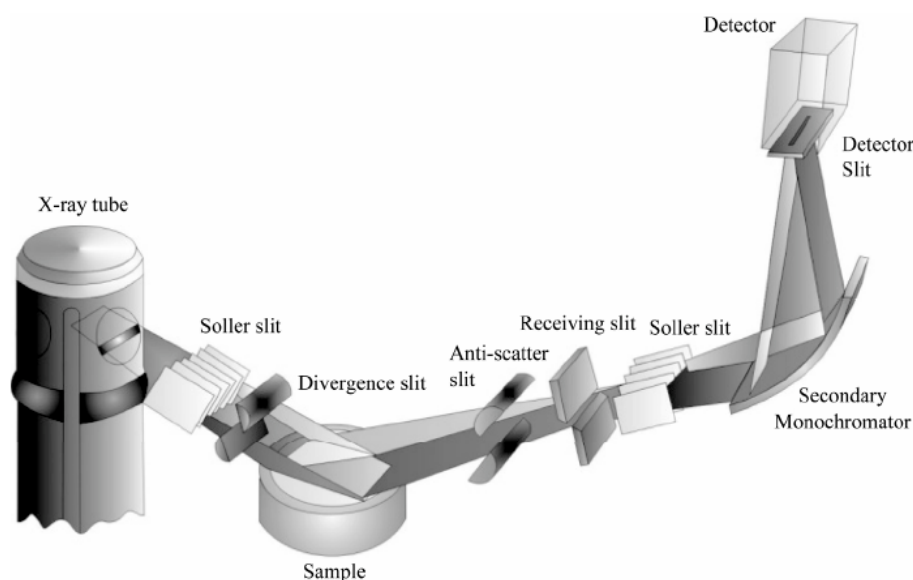
Figure 2.27 Schematic diagram of X-ray powder diffractometer in Bragg-Brentano geometry.[34]

For samples produced from $CaCO_3$ deposition experiments, patterns were recorded with a 2θ range from 15° to 70° at a scan rate of 0.02 step^{-1}. This 2θ range was confirmed at the beginning by scanning $CaCO_3$ from 0° to 90° at different scan rates, where 15° to 70° exert almost all peaks of $CaCO_3$. Moreover, the included crystal structures of $CaCO_3$ polymorphs in Rietveld refinement is also within this 2θ range. For full reflections of single crystals of calcium complexes, the 2θ range is from 2° to 50° with the same scan rate. The collection parameters are set the same as that set in single crystal crystallography. The resulting powder patterns were

given a systematic naming scheme of d*7_nnnnn* (where d*7* defines the diffractometer used and *nnnnn* the pattern serial number).

1.1.1.3   Analysis of X-ray Powder Diffraction Data

The detector records the intensity of the diffracted X-rays which in turn depends on the reciprocal space of the crystal as y_i, at small increments of *i,* where *i* is the 2θ angle between the incident beam and beam reflected, and the data is presented as a 1-D pattern. This resulting pattern can be compared to reference patterns in the Powder Diffraction File (PDF) database[35] through the Bruker EVA interface.[36] Each (crystalline) phase present in a bulk sample will give rise to a characteristic set of peaks. By comparing 2θ position and relative intensity of the reflections, rough phase identification can be obtained. More detailed analysis is carried out by using Rietveld refinement with TOPAS Academic.[37]

Table 2.15 The possible parameters can be refined in a Riveted refinement. [37]

Specimen-specific	Instrument-specific
Lattice parameters	Background
Atomic coordinates	Instrumental profile
Scale factor	Zero point
Isotropic thermal parameters	Height displacement
Anisotropic thermal parameters	
Preferred orientation	
Microstrain	

The Rietveld method is based on the least squares minimization of the difference between a calculated diffraction pattern and one obtained experimentally.[38] It is a structural refinement technique that requires a reasonable starting model so that the global structural minimum is found. Rietveld method uses the entire pattern for refinement. Hence, overlapping peaks pose less of a problem. The inclusion of crystal structure enables the peak profiles to be modelled more effectively. It can be used to model the background, preferred orientation, absorption, solid solutions and peak broadening.[39] For a reasonable structure model, sufficient parameters are

required to ensure the experimental pattern can be reproduced, at the same time the model is chemically sensible. The possible parameters that will be used in a refinement can be divided into specimen-related and instrument-related, which are listed in Table 2.14. The agreement between the observed pattern and the pattern calculated can be assessed by several R factors: R_{wp} or R_{Bragg} or GOF (goodness-of-fit), of which, R_{wp} is most meaningful.[40]

2.8.2 Electron Microscopy

Similar to optical microscopy, scanning electron microscopy (SEM) and transmission electron microscopy (TEM) can provide an 'image' of an object with a high resolution down to nano-scale. Generally, SEM provides images of surface, or near surface structure of bulk specimen, while TEM gives pictures of the microstructure or ultrastructure of thin specimens, with corresponding information of internal structure.[41] Modern TEM and SEM are equipped with energy dispersive X-ray analysis (EDX), which is a non-destructive, semi-quantitative method for elemental analysis.[42] By collecting and measuring the characteristic X-rays escaping from the surface of a sample, the elemental composition can be determined.[43] In the following chapter, if both SEM and TEM information are provided for one sample, EDX data presented is collected together with the TEM data. For samples without TEM information, the EDX data is collected when using SEM.

1.1.1.4   Transmission Electron Microscopy with EDX

TEM is mainly used for the identification of a specific morphology for $CaCO_3$ or to confirm the preferred orientation of one specific polymorph. Samples for TEM were prepared by scraping the material from filmed surfaces of substrates, dispersing them in acetone, and dropping this suspension liquid over a holey copper grid. Electron diffraction was carried out on a JEOL 2100F FEG TEM in transmission mode operating at 200 eV. The EDX data for the samples are collected at the same time. The control of the process and the diffraction pattern analysis are both carried out the software 'Gatan Digital Micrograph'.[19]

1.1.1.5   Scanning Electron Microscopy with EDX

When electrons interact with a sample's atoms, scattered electrons, X-rays and visible light are produced. If these signals are collected and analyzed, a wealth of information about the properties, including morphology, microstructure, and composition can be obtained. SEM in this project is

mainly used to study the morphologies for different CaCO3 crystals. The samples are coated with gold or carbon before imaging by a HITACHI S-520 type scanning electron microscope (SEM). Typically, a mode of field free, operated at a voltage of 5 kV to 10 kV, is used for sample imaging. In EDX mode (Energy-dispersive X-ray Spectroscopy), a voltage of 10 kV is applied.

1.1.1.6   Infrared (IR) Spectroscopy

Data is collected by attenuated total reflectance infrared spectroscopy (ATR-IR). ATR-IR spectra were recorded on a Perkin Elmer Spectrum 100 using a diamond compression cell. The IR spectra were collected by pressing the probe against the diamond in the 4000–400 cm^{-1} region at a resolution of 4 cm^{-1}. Typically, 32 or 64 scans were conducted for a spectrum. The resulting IR spectra were analyzed with the software KnowItAll.[44] Peak intensity is described as strong (s), medium (m) or weak (w).

2.8.2.1   Atomic Force Microscopy

There are three primary imaging modes in AFM: the contact mode, the intermittent, and the non-contact mode. Contact mode is the most appropriate for this project. The advantage of this mode is that it is fast scanning, good for rough samples and can be used in friction analysis.[45] The images were recorded and analyzed by NanoScope software 6.13.[46]

2.8.3 Reference Sample Characterization by AIT-IR and PXRD

Under the ambient condition, there are three different anhydrous CaCO$_3$ polymorphs, which are calcite, aragonite, and vaterite. Amorphous calcium carbonate (ACC), which can be observed both in natural and laboratory work.[47] acts as a precursor phase for anhydrous CaCO$_3$. The most classical way to identify different CaCO$_3$ polymorphs is to use three typical techniques, namely, infrared spectroscopy (IR), X-ray powder diffraction (PXRD) and scanning electron microscope (SEM). IR is used for detecting all the possible substances, while PXRD is to identify all the possible crystalline material, especially different polymorphs of the same kind substance. Characterization of reference CaCO$_3$ is carried out with two purposes: one is to see how the techniques we use agree with literature studies; another is to show how software Topas helps to illustrate the PXRD patterns. The calcite was bought from Sigma-Aldrich, while aragonite was scraped from the sample provided by the P&G.

The FTIR study of the fingerprint region of different $CaCO_3$ polymorphs by various investigator has been summarized by Andersen,[48] showing that CO_3^{2-} anion exhibits four normal vibrational modes in calcium carbonate[68, 48, 191,192]. There is asymmetric stretching mode near 1080 cm^{-1} (v_1), out of a plane bend in 900-850 cm^{-1} region (v_2), a double degenerate asymmetric stretch in 1600 – 1400 cm^{-1} region (v_3) and the double degenerate bending mode in 720-680 cm^{-1} region (v_4). Due to the disagreements among the mid-infrared data in previous reports, infrared spectra of calcite and aragonite were collected with the machine we used and summarized in Table 2.15. The infrared data from literature (in Table 2.15) was selected due to its similarity to the data we collect. According to the literature data, the characteristic peak for calcite is at 877 cm^{-1} and 714 cm^{-1}. Peaks at 854 cm^{-1}, 714 cm^{-1}, and 697 cm^{-1} are attributed to the presence of aragonite, and the peak of both 877 cm^{-1} and 750 cm^{-1} belong to vaterite. There are two different reports to show the characteristic peak of amorphous $CaCO_3$. One is that no obvious peaks observed in v_2 and v_3 but peak near v_3 regions should be split into 2 or 3 peaks and also a broad absorption should be seen near 1086 cm^{-1}. Another observation is listed in Table 2.15, showing the absorption of ACC can be observed in all four vibrational regions but with different peak positions from anhydrous peaks. In the case of our sample, only calcite and aragonite have been collected as a reference since ACC and vaterite are hardly observed in samples. In summary, peaks appearing at 871 cm^{-1} and 700 cm^{-1} should be attributed to calcite, while peaks appear at 853 cm^{-1}, 713 cm^{-1}, and 700 cm^{-1} at the same time belong to aragonite.

Figure 2.29 shows the PXRD patterns for calcite (Figure2.29a) and aragonite (Figure 2.29b). Rietveld refinement of PXRD pattern was carried out by Topas-jedit software[185,186]. In Figure 2.29a, the sample was identified as calcite with a trace amount of aragonite. Only one peak of aragonite (111) was observed, which is the most intense peak of aragonite. The same situation was observed in aragonite sample as shown in Figure 2.29b. All peaks belong to aragonite expect one weak peak of calcite (104), which is also the most intense peak of calcite. The PXRD analysis shows that reference calcite has a trace amount of aragonite, while reference of aragonite has a trace amount of calcite. This 'trace amount' information, however, was not detected by FTIR. PXRD has a higher sensitivity than that of ATR-IR in polymorphs identification, which can provide more information on polymorph species.

The result comparison between PXRD and FTIR confirm that FTIR results are consistent to those of PXRD. PXRD with the advantage of higher sensitivity and providing information of preferred

orientation and the relative ratio of different polymorph is better for the discussion. Therefore, FTIR results will not show in the following discussion for clarity.

Table 2.16 Infrared absorption peaks of calcite and aragonite.

Source	Phase	v_3	v_1	v_4	v_2
This report	Calcite	1392	1090	871, 848	712
	Aragonite	1442	1083	853	713, 700
Literature[183]	Calcite	1420	----	877	713
	Aragonite	1448, 1440	1083	854	713,700
	Vaterite	1487,1445	1089	877,873	746,738
	ACC	1490,1425	1067	864	725,690
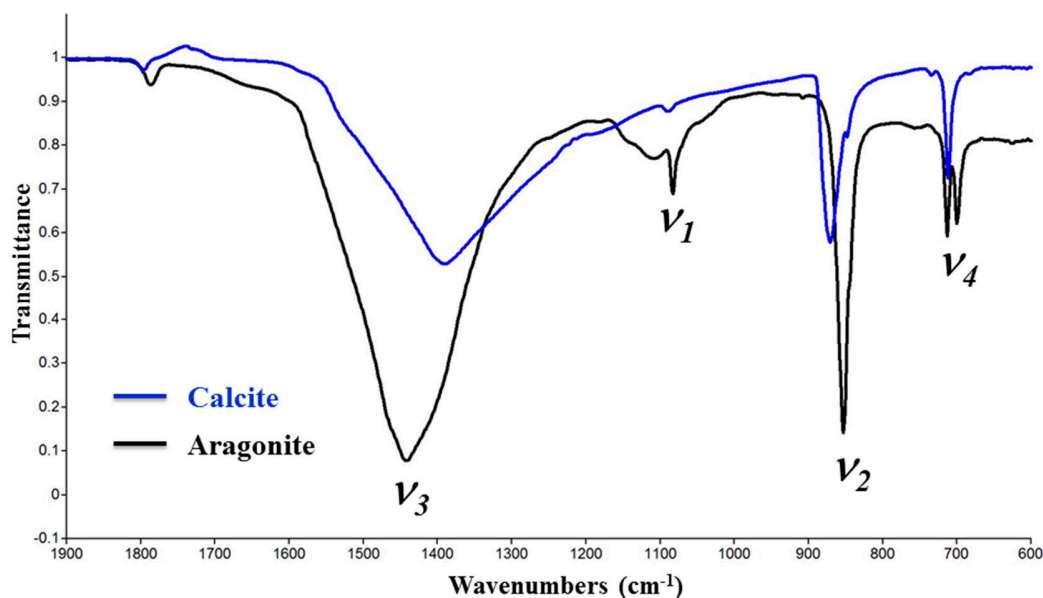
Figure 2.28 Infrared absorption spectra of calcite (blue) and aragonite (black).
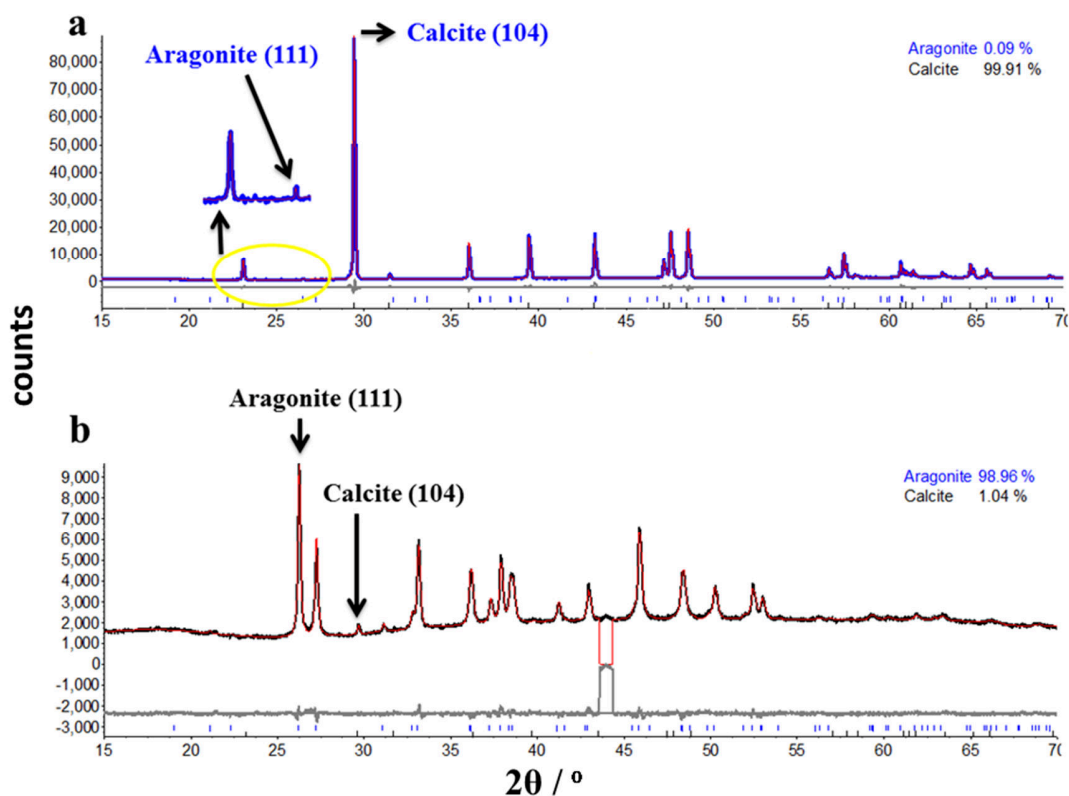
Figure 2.29 **Rietveld fits of calcium carbonate crystal peaks against calcium carbonate X-ray data, showing the presence of calcite (a) with trace aragonite and aragonite (b) with a trace amount of calcite. The final overall Rwp for refinements (a) and (b) are 5.425% and 2.940%, respectively. The figure shows experimental data of calcite in blue and aragonite in black, calculated pattern in red, difference plot in gray. The red pit is the excluded peaks that belong to silicone holder. The right-up data in the image is the relative percent of aragonite and calcite.[49]**

2.9 Reference

1.   Amjad, Z., *The Science and Technology of Industrial Water Treatment*. 1 ed.; CRC Press: 2010; p 532.

2.   Yang, Q.; Ding, J.; Shen, Z.-Q. In *Sam Heat Transfer Surface Fouling Behavior and Fouling Behaviour and Fouling Fractal Characteristics*, Proceedings of an International Conference on Mitigation of Heat Exchanger Fouling and Its Economic and Environmental Implications, Alberta, Canada, New York: Begell House: Alberta, Canada, 2001; p 239.

3.   Förster, M.; Bohnet, M. *Int. J. Therm. Sci.* **2000,** *39* (7), 697-708.

4.   (a) Mann, S., *Biomineralization : Principles and Concepts in Bioinorganic Materials Chemistry*. Oxford University Press: Oxford, 2001; p 198; (b) Mann, S.; Heywood, B. R.; Rajam, S.; Birchall, D. J. *Nature* **1988,** *334* (6184), 692-695; (c) Aizenberg, J.; Black, A. J.; Whitesides, G. M. *Nature* **1998,** *394* (6696), 868-871; (d) Aizenberg, J.; Black, A. J.; Whitesides, G. M. *Nature* **1999,** *398* (6727), 495-498.

5.   (a) Cheong, W. C.; Gaskell, P. H.; Neville, A. *J. Cryst. Growth* **2013,** *363* (0), 7-21; (b) Rechendorff, K. The Influence of Surface Roughness on Protein Adsorption. Ph.D. Thesis, University of Aarhus, 2006.

6.   Soda Lime Glass. http://en.wikipedia.org/wiki/Glass (accessed March 03, 2015).

7.   Borosilicate Glass. https://en.wikipedia.org/wiki/Borosilicate_glass (accessed May 3, 2015).

8.   (a) Bodurov, I.; Vlaeva, I.; Yovcheva, T.; Dragostinova, V.; Sainov, S. *Bulg. Chem. Commun.* **2013,** *45*, 77-80; (b) Poly(Methyl Methacrylate). http://en.wikipedia.org/wiki/Poly(methyl_methacrylate) (accessed March 05, 2015).

9.   Wang, J.; Chen, C.; Buck, S. M.; Chen, Z. *J. Phys. Chem. B* **2001,** *105* (48), 12118-12125.

10.   Bhushan, B., Surface Roughness Analysis and Measurement Techniques. In *Modern Tribology Handbook*, CRC Press: London, 2001; Vol. 1, pp 49-119.

11.   Scheer, B. W.; Stover, J. C. In *Development of a Smooth-Surface Microroughness Standard*, Proceedings of the SPIE, San Diego, CA, United States, International Society for Optics and Photonics: San Diego, CA, United States, 1997; pp 78-87.

12.   Howstuffworks: How Does a Dishwasher Work? http://www.rsc.org/learn-chemistry/resources/chemistry-in-your-cupboard/finish/2 (accessed November 7).

13.   Letzelter, N. *Adw Shine Understanding*. Procter & Gamble, Newcastle upon tyne, UK. Unpublished work, 2011.

14.   Tomlinson, A.; Carnali, J., A Review of Key Ingredients Used in Past and Present Autodishwashing Formulations and the Physic-Chemical Processes They Facilitate. In *Handbook for Cleaning/Decontamination of Surface*, Elsevier: Amsterdam, Netherlands, 2007; Vol. 1, p 197.

15.   Broze, G., Detergents: Technical and Practical Challeges. In *Handbook of Detergents, Part A: Properties*, Broze, G., Ed. CRC Press: 1999; Vol. 82, pp 1-5.

16.   *Organic Chelating Agents Used to Control the Concentration of Metal Ions in Aqueous Systems*; Technical Information of Trilon® M types: BASF Aktiengesellschaft: 2007.

17.   *Acusol™ 588: Polyphosphate and Silicate Scale Inhibitor for Laundry and Automatic Dishwashing Detergents*; Rohm and Haas Company 2008.

18.   Verch, A.; Gebauer, D.; Antonietti, M.; Cölfen, H. *Phys. Chem. Chem. Phys*. **2011,** *13* (37), 16811-16820.

19.   *Digital Micrograph^{tm}*, version 3; Gatan: Pleasanton, CA, 2007; (Accessed May 4, 2015).

20.   Chen, T.; Neville, A.; Yuan, M. *J. Pet. Sci. Eng.* **2005,** *46* (3), 185-194.

21.   Sun, W.; Jayaraman, S.; Chen, W.; Persson, K. A.; Ceder, G. *Proc. Natl. Acad. Sci.* **2015,** *112* (11), 3199-3204.

22.   Morse, J. W.; Arvidson, R. S.; Lüttge, A. *Chem. Rev.* **2007,** *107* (2), 342-381.

23.   Chen, T.; Neville, A.; Yuan, M. *J. Cryst. Growth* **2005,** *275* (1), e1341-e1347.

24.   (a) Lin, Y.-P.; Singer, P. C. *J. Cryst. Growth* **2009,** *312* (1), 136-140; (b) Davis, K. J.; Dove, P. M.; De Yoreo, J. J. *Science* **2000,** *290* (5494), 1134-1137.

25.   Astilleros, J. M.; Fernández-Díaz, L.; Putnis, A. *Chem. Geol.* **2010,** *271* (1), 52-58.

26.   Kitamura, M.; Konno, H.; Yasui, A.; Masuoka, H. *J. Cryst. Growth* **2002,** *236* (1), 323-332.

27.   Keysar, S.; Semiat, R.; Hasson, D.; Yahalom, J. *J. Colloid Interface Sci.* **1994,** *162* (2), 311-319.

28.   Wang, H.; Alfredsson, V.; Tropsch, J.; Ettl, R.; Nylander, T. *Appl. Mater. Interfaces* **2013,** *5* (10), 4035-4045.

29.   Chessin, H.; Hamilton, W. C.; Post, B. *Acta Crystallogr.* **1965,** *18* (4), 689-693.

30.   Yu, S. H.; Cölfen, H.; Antonietti, M. *Chem. - Eur. J.* **2002,** *8* (13), 2937-2945.

31.   Huang, S.; Li, H.; Jiang, S.; Chen, X.; An, L. *Polymer* **2011,** *52* (15), 3478-3487.

32.   (a) Snyder, R.; Jenkins, R., *Introduction to X-Ray Powder Diffractometry*. Wiley-Interscience: 2012; (b) Will, G., General Consideration. In *Powder Diffraction: The Rietveld*

Method and the Two Stage Method to Determine and Refine Crystal Structures from Powder Diffraction Data, Springer-Verlag Berlin Heidelberg: Germany, 2006; pp 1-8.

33.   Bruker-AXS, Diffrac.Suite V2.27: Software for Controlling Bruker Diffractometers 2011.

34.   Tamer, M. *J. Mod. Phys.* **2013,** *4*, 1149-1157.

35.   Powder Diffraction File. International Centre for Diffraction Data: Pennsylvania, 1998.

36.   Bruker AXS, Diffracplus Basic Evaluation Package: Eva 10.0. Karlsruhe, 2004.

37.   Bruker AXS, Topas Academic: General Profile and Structure Analysis Software for Powder Diffraction Data. Karlsruhe, 2000.

38.   Rietveld, H. M. *J. Appl. Crystallogr.* **1969,** *2* (2), 65-71.

39.   Winburn, R. S. *Adv. X-Ray Anal.* **2003,** *46*, 210-219.

40.   Blake, A. J.; Clegg, W.; Cole, J. M.; Evans, J. S. O.; Main, P.; Parsons, S.; Watkin, D. J., Refinement of Crystal Structure. In *Crystal Structure Analysis: Principles and Practice*, 2nd Edition ed.; Clegg, W., Ed. Oxford University Press: New York, United States, 2009; pp 169-188.

41.   Goodhew, P. J.; Humphreys, J.; Beanland, R., *Electron Microscopy and Analysis*. CRC Press: 2000.

42.   Wollman, D. A.; Irwin, K. D.; Hilton, G. C.; Dulcie, L. L.; Newbury, D. E.; Martinis, J. M. *J. Microsc.* **1997,** *188* (3), 196-223.

43.   Shindo, D.; Oikawa, T., Energy Dispersive X-Ray Spectroscopy. In *Analytical Electron Microscopy for Materials Science*, Spinger-Verlag Tokyo: Tokyo, Japan, 2002; pp 81-102.

44.   *Knowitall Academic Edition*, version 2005; Bio‑Rad Laboratories: 2005; (Accessed May 05, 2016).

45.   Introduction to Scanning Probe Microscopy: Basic Theory Atomic Force Microscopy (Afm). Northern Kentucky University, Highland Heights, 2006; pp 1-6.

46.   *Nanoscope Software 6.13 Uer Guide*, version Veeco Instruments Inc.: 2004; (Accessed).

47.   (a) Sikes, C. S.; Wheeler, A. P., Inhibition of Inorganic and Biological $Caco_3$ Deposition by a Polysaccharide Fraction Obtained from $Caco_3$-Forming Organisms. U.S. Patent 6,563,252: April 29, 1986; (b) Neville, A.; Sorbie, K.; Zhong, Z. *Faraday Discuss.* **2007,** *136*, 355-365.

48.   Andersen, F. A.; Brecevic, L. *Acta Chem. Scand.* **1991,** *45* (10), 1018-1024.

49.   Ye, Y.; Smyth, J. R.; Boni, P. *Am. Mineral.* **2012,** *97*, 707-712.

3   CaCO$_3$ Crystallization with Full Nil-HEDP Formula plus Other Factors in Dishwashers

3.1   Introduction

In Chapter 2, the build-up of CaCO$_3$ crystals on different types of substrates by using the 'Nil-HEDP formula' at T_{max} = 65 ˚C was discussed. It was found that the use of 'Nil-HEDP formula' alone did not result in the formation of significant deposits on the glass the way it happens on PMMA. Flower-like aragonite (001) with 1% calcite tends to form on the surface of PMMA, while calcite crystals with a rice-like shape are likely to be seen on the glass substrate (Figure 3.1). The polymer in the 'Nil-HEDP formula' plays a vital role in both the shine loss and the growth of polymorphic form on different substrates. The polymer promotes the growth of aragonite (001) on the surface of plastic but not for glass samples. There is a thicker film observed on PMMA than that on glass.
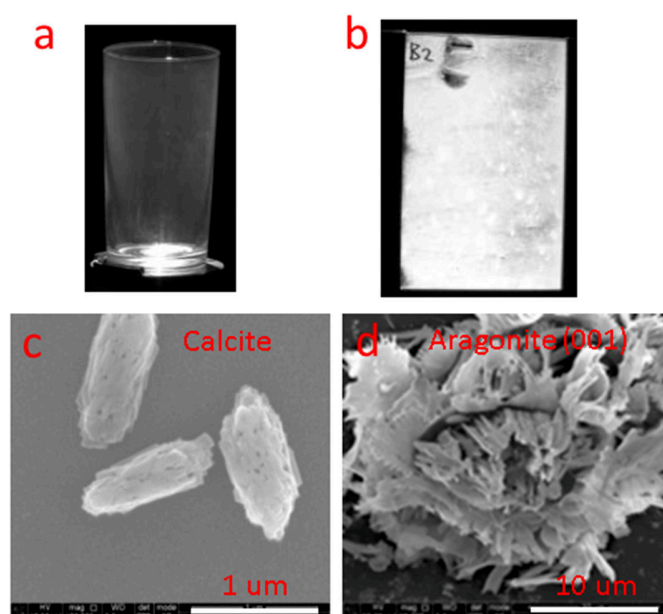
Figure 3.1 The glass tumbler and the PMMA slide produced with the 'full Nil-HEDP formula' at T_{max} = 65 ˚C from a real-life dishwasher after five cycles: (a) a glass tumbler: clarity = 75.2%; (b) one PMMA slide, clarity = 15.5%; (c) rice-like calcite crystals observed on the surface of the glass tumbler; (d) flower-like aragonite (001) crystals found on the surface of the PMMA slides.

In this chapter, other factors in a dishwasher that may affect the function of the 'Nil-HEDP formula' on the 'shine' or the growth of CaCO$_3$ are presented. These factors include the maximum temperature in the main wash cycle (T_{max} = 55 ˚C or 65 ˚C), orthophosphate ions (Ortho-P), and HEDP (CaCO$_3$ inhibitor).

Both, T_{max} = 55 ˚C and T_{max} = 65 ˚C are in the high-temperature range. In the last chapter, samples produced at T_{max} = 65 ˚C with and without the 'Nil-HEDP formula' were presented. It showed that the aragonite and calcite crystals were produced at high temperature and pH when the formula was absent. While, Vaterite was hardly detected, and aragonite was largely identified in the dominant phase, especially in the presence of Mg^{2+} ions in water. This was observed both in the literature[1] and in the model system (Section 2.4).

On the other hand, when 'Nil-HEDP formula' was used flora-like aragonite and calcite were found on both the PMMA and the glass substrates, respectively (Figure 3.1). In this chapter, samples produced at T_{max} = 55 ˚C with the 'Nil-HEDP formula' are discussed. This is presented in the Section 3.31 and Section 3.4.1 sections for glass tumblers and plastic samples, respectively.

About 0.0177 mmol L^{-1} (1.68 mg L^{-1}) of orthophosphate (Ortho-P) is added to the tap water in some countries (the UK in particular) to control the amount of lead leaking from the pipes, by creating an inorganic layer.[2] It has been shown that the time needed for scale formation in solution at 65 ^{o}C with 2.0 mg/L orthophosphate ions is about 17 times longer than in phosphate-free solution.[3] Following elucidations have been proposed to explain the inhibition mechanism of orthophosphate ions. The presence of orthophosphate ions in solution delays the crystallization of CaCO$_3$ by reducing the rate of vaterite crystallization and its subsequent transformation into calcite by interrupting the dissolution-reprecipitation process (However, there is no vaterite observed in our system, see below).[4] Another suggested explanation is that the orthophosphate ions can lead to the blockage of active sites for further crystal growth,[5] which is consistent with another report where phosphate ion adsorption on steps of calcite crystals was observed.[6] The study on biomineralization shows that the amorphous calcium carbonate can be stabilized by phosphate rich protein,[7] as the phosphate functional groups have a high affinity for CaCO$_3$.[8] A recent report demonstrates that the use of phytic acid (inositol hexakisphosphate) can stabilize amorphous calcium carbonate (ACC) for more than three months.[9] Presumably, the orthophosphate can also stifle surface deposition more so than one of the above routes. When orthophosphate ions are present, calcite tends to be the final polymorphic form of CaCO$_3$ in

comparison to a mixture of aragonite and calcite when phosphate is absent.[3] The suggested explanation is that the presence of orthophosphate ions might change the structure of the $CaCO_3$ clusters and/or alter the hydration shell of calcium and thus, it affects the polymorph selection. The effects of phosphate ion on the shine loss, at a concentration level of 0.0177 mmol L^{-1}, will be explored together with other factors within the dishwasher.

Glass tumblers and plastic samples were used in a household dishwasher to study how other factors within the dishwasher affect the function of the 'Nil-HEDP formula' in maintaining/deteriorating the 'shine.' The discussion of the effects of those factors (T_{max}, orthophosphate ions and HEDP) is shown below and is split into two parts: the shine loss on surfaces and the variation of crystal forms of $CaCO_3$ in the early cycles and subsequent excessive cycles. The definition of 'early cycles' and 'excessive cycles' are given in next subsection, together with a brief introduction on how different samples are produced inside the dishwasher.

It should be noted here that the way in which 'shine' was assessed is different for the plastic and the glass samples. The clarity of the glass samples was graded by a camera analysis rating system developed by P&G, while the shine of the plastic samples was rated via a naked eye assessment. To differentiate between them, clarity of the plastic samples was rated from 1 to 10, while glass samples were rated from 0% to 100%. A higher number means a higher clarity of the sample with 10 (plastic) or 100% (glass) indicating no film formation.

The $CaCO_3$ crystals formed under different chemical conditions were investigated with a combination of scanning electron microscopy (SEM), transmission electron microscopy (TEM), and X-ray powder diffraction analysis. The data obtained for most samples except some high shine samples from using these three instruments is available and can be found in the discussion and enclosed CD-ROM. The high shine samples (glass tumblers, in particular) retain a high degree of clarity on the surface and therefore, the level of deposit is too low to be analyzed using PXRD. These samples, in this case, are identified based on the morphologies/shapes observed by SEM. Therefore, in this work, the term 'calcite-like' or 'ACC-like' is used to describe the crystals that have a similar morphology to calcite and ACC in the reported work but have no available PXRD or TEM information. While the presence of ACC cannot be judged by its appearance. The term 'ACC-like' is used here to express the amorphous shape other than it is confirmed by techniques as ACC. The main reason is that ACC-like deposits are almost observed on high shine samples in this project. Hence, no enough samples are available for further analysis.

Moreover, the SEM has its resolution limit and imaging limit. The SEM image is designed to show their appearance but not to provide the information of the internal structure of the crystals. Even its resolution can be as low as 2 nm at a low voltage at 1Kev.[10] However, due to the sample properties, for this project, the resolution is generally around 100 -500 nm. If the sizes of the crystalline forms of $CaCO_3$ are out of this limit or included inside other phases, the information obtained can be limited. The other reason for the difficulty in identifying polymorphs is due to the morphology of the $CaCO_3$ polymorphs themselves which can be similar to one another, particularly when grown in the presence of a complex mixture of additives. Figure 3.2 shows the morphological similarity and differences between vaterite and amorphous calcium carbonate (ACC). The experimental PXRD patterns for some of the selected samples in the present work, are included in the discussion below. The PXRD patterns are only shown when discussion requires details of the peak shape and background information. All the X-ray diffraction data files are available in CDs enclosed.
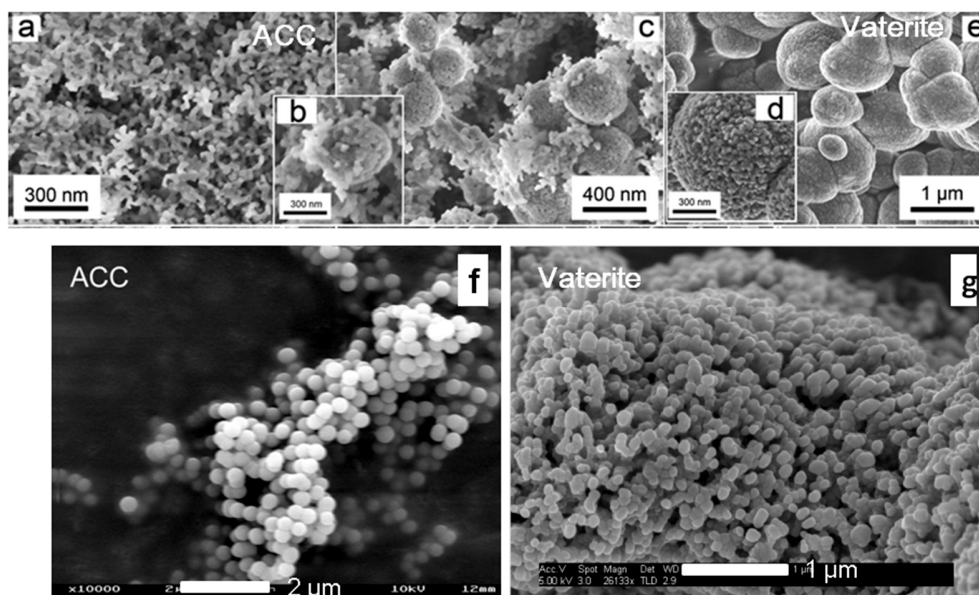
Figure 3.2 Morphologies of ACC and vaterite. SEM images (a - e): the evolution of ACC to vaterite shows the difference in morphology of ACC and vaterite.[11] (a) ACC; (b & c) ACC and vaterite nano-aggregates; (d & e) vaterite nano-aggregates; Images (f, g) shows the similarity between the ACC and vaterite. (f) ACC nano-aggregates;[12] (g) irregular vaterite composed of spherical nanoparticles.[13] (Images a-e are reproduced with the permission of ref.11, Copyright @ 2010, Royal Society of Chemistry; Image f is reprinted with the permission of ref.12, @ Ruhr-Universität Bochum. Image g is reproduced with the permission of ref.13, Copyright 2005 @ Elsevier B.V.).

3.2 How the Samples are Produced in a Dishwasher

This section includes a brief introduction into how samples were produced and labeled in different chemical conditions in a real dishwasher. Samples were generated by the 'Miele GSL' machines with a maximum temperature of either 55 ˚C or 65 ˚C in the main wash cycle. Three different types of substrates were involved, namely, poly (methyl methacrylate) (PMMA) slides, polystyrene (PS) tumblers, and glass tumblers. All the substrates were taken out at the end of the drying cycles. Samples were produced after repeated washing for the following number of repetitions: 5 cycles, 8 cycles, 35 cycles and 39 cycles. For simplicity, the samples obtained after 5 cycles and 8 cycles are referred to as 'early cycles' samples, while samples obtained after 35 cycles and 39 cycles are labeled as 'excessive cycles' samples.

Table 3.1 Nil-HEDP formula

Nil Pv30 formula	Abbre.	Raw material in water (g 5L^{-1})	Comments
Alkaline Builder			
Trisodium salt of methylglycinediacetic acid	Na$_3$MGDA	2.82	Chelator
Granular sodium carbonate	Na$_2$CO$_3$	9.54	pH buffer
Sodium sulphate	Na$_2$SO$_4$	3.06	Solid diluter
Polymer			
Sulfonated polyacrylates Acusol 588	Acusol 588G	1.29	
Surfactant			
Non-ionic mixture	Non-ionic mixture	1.28	EO and EO-PO

The variation in the chemical conditions mainly lies in three parts: the water used, orthophosphate salt and the HEDP. The hard water was made from deionized water and the addition of Ca and Mg salts: Ca^{2+} (2.75 mmol L^{-1}) and Mg^{2+} (0.86 mmol L^{-1}). The orthophosphate sodium salt (0.0177 mmol L^{-1}) was also added to the water to study its effects under dishwasher conditions. In this chapter, when Orthophosphate (Ortho-P) salt was not added to the water is defined as phosphate-free water. Whereas, the presence of Ortho-P salt is referred to as phosphate-containing water. The ratio of Mg^{2+} to Ca^{2+} is equal to 1:3. The Mg^{2+} ions at this

level of concentration at T = 65 ^{o}C favor the nucleation of aragonite. However, it can cause some defects on the surface of calcite. No visible inhibition effects caused by Mg^{2+} ions were observed. This phenomenon has been discussed in depth in Chapter 2. Hence, the inhibition effects of the Mg^{2+} ions will not be taken into consideration in this chapter. Carbonate with a concentration of 18 mmol L^{-1} was added to the main wash cycle, which accounts for both the carbonate from Nil-HEDP formula and bicarbonate present in the water.

A total of 8 different types of samples of each substrate were prepared and labeled as Legs 1–8. Table 3.2 and Table 3.3 describe the conditions in which all of these real dishwasher samples were generated. The composition of the standard Nil-HEDP formula in Table 3.1 were added to all Legs, including Leg3 and Leg7. Samples of Leg1 were produced with 'full Nil-HEDP formula' using phosphate-free water, which has been discussed in Chapter 2.

When other chemicals like Ortho-P and HEDP were added or the T_{max} was changed in the main wash cycle, samples were labeled accordingly (Table 3.2 for plastic samples and Table 3.3 for glass samples).

Hard water for producing samples from Leg1 to Leg4 had no Ortho-P involved, while water used for generating Legs 5 to 8 contained Ortho-P in water. The HEDP was only added in samples of Leg3 and Leg7. All tests were run at T_{max} = 65 ˚C unless specified as T_{max} = 55 ˚C. Leg 4 and Leg 8 were generated at T_{max} = 55 ˚C and will be described below. It should be noted here that the 'with soil' samples, namely Leg2 and Leg6, were also generated but no conclusion has been draw from it. Therefore, 'with soil' samples were not included in the following discussion.

The samples of early cycles were repeated until a significant film formation was observed. For plastic samples, it takes five cycles to produce a visible film except for Leg 4 and Leg 8, which required eight cycles. For glass samples, no obvious film formed even after 20 cycles. For simplicity, all the glass samples of early cycles provided were run for five cycles.

For samples of excessive cycles, all legs of glass samples were run for 39 cycles. Plastic samples from Leg1 to Leg4 were also run for 39 cycles. However, Leg5 to Leg8 were only run up to 35 cycles. For example, samples of Leg3 and Leg7 were produced with HEDP and were run for 39 and 35 cycles, respectively. Leg 4 and Leg 8 were produced at T_{max} = 55 ˚C for 39 and 35 cycles, respectively. In Chapter 2, it was identified that polymorph species on the surface of the

substrate is hardly altered after five cycles. The same polymorphic form of $CaCO_3$ can also be observed on the plastic surfaces after 35 cycles and 39 cycles as long as the chemical conditions are not changed.

Table 3.2 Plastic samples (PMMA slides and polystyrene tumblers) generated from a household dishwasher. Legs 1-3 and Legs 5-7 are generated at 65 ᵒC, while Leg4 and Leg8 are generated at 55 ᵒC. The name 'Leg' is from P&G labeling system. We keep it here for consistency.

		Without Orthophosphate in water				With Orthophosphate in water			
	Leg	**1**	**2**	**3**	**4 (55 ᵒC)**	**5**	**6**	**7**	**8 (55 ᵒC)**
	Cycles	Formula only	With soil	With HEDP	Formula only	Formula only	With soil	With HEDP	Formula only
Early cycles	**5**	yes	yes			yes	yes		
	8				yes				yes
Excessive cycles	**35**					yes	yes	yes	yes
	39	yes	yes	yes	yes				
	Comment	Soil added in legs 1-4 at for excessive samples at cycle 11.				Plastic slides were not included from cycles 11 to 15.			
		HEDP samples of early cycles and 'with soil' samples will not include in discussion							

*Green shade: Formula only; Purple shade: Formula plus HEDP; Red shade: Formula plus soil

Table 3.3 Glass tumblers generated from a household dishwasher. Legs 1-3 and Legs 5-7 are generated at 65 ᵒC, while Leg4 and Leg8 are generated at 55 ᵒC.

		Without Orthophosphate in water				With Orthophosphate in water			
	Leg	**1**	**2**	**3**	**4 (55 ᵒC)**	**5**	**6**	**7**	**8 (55 ᵒC)**
	Cycles	Formula only	With soil	With HEDP	Formula only	Formula only	With soil	With HEDP	Formula only
Early cycles	**5**	yes	yes	yes	yes	yes	yes	yes	yes
Excessive cycles	**39**	yes	yes	yes	yes	yes	yes	yes	yes
Comment	**/**	Soil added in legs1-4 for excessive samples at cycle 11. 'with HEDP' samples of early cycles and 'with soil' samples will not include in discussion							

3.3 Understanding the Shine Loss on the Glass Samples
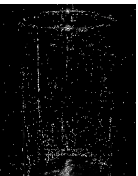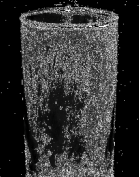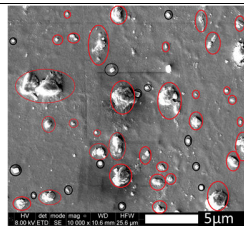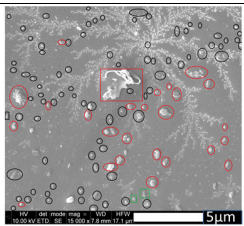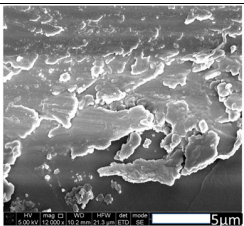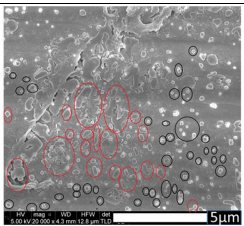
The discussion of the effects of T_{max}, and HEDP is split into two parts: the shine loss on the surfaces of the glass samples and the variation in the polymorph species of $CaCO_3$ under different chemical conditions. The first two sections of this chapter give details about the effects of T_{max}, and HEDP on the 'shine' of glass tumblers and $CaCO_3$ crystal growth. The following two

subsections summarize the general changes in the shine loss and the distribution of different CaCO$_3$ polymorphs under different chemical conditions.

3.3.1 The Effects of Tmax, with and without Ortho-P

This subsection will study the variations of shine and deposited CaCO$_3$ crystals on the surfaces of glass substrates at different T_{max} (T_{max}= 55 ˚C or 65 ˚C) when phosphate ions are present and absent in the hard water. The comparison is carried out among four different types of samples. These four samples are Leg1, Leg4, Leg5, and Leg8. Both the samples of early cycles and excessive cycles are included. The clarity of the glass samples was monitored up to 39 cycles. In the early cycles (i.e. at the end of the 5th cycle), these four samples were found to have approximately the same level of 'shine' as the original state especially for samples produced in the phosphate-containing hard water (Leg5 and Leg8). This was also observed in the samples from excessive cycles. The clarity of Leg5 and Leg8 showed insignificant change after 39 cycles although this was not the case for Leg1 and Leg4. The use of full Nil-HEDP formula without calcium carbonate inhibitor can maintain a clarity of 97 % up to 15 cycles, but the full Nil-HEDP formula loses its inhibition effects as the washing cycle continues. At the end of the 39th cycle, a homogeneous thin film was observed on the surface of the glass of Leg1. It ended with a clarity of 1.1% and showed more loss in 'shine' than that of Leg4. The clarity order of these four Legs at the end of the 39th cycles is as follows: Leg5 (96.2%) & Leg8 (95.1%) > Leg4 (46.6%) > Leg1 (1.1%). It was seen that the presence of inorganic phosphate ions and T_{max} = 55 ˚C encouraged the shine maintenance for glass samples; the former has a more pronounced effect in retaining the shine, which is consistant with the literature that phosphate ions show strong inhibition ability toward calcite.[5] A summary of these four samples can be found in Table 3.4.

Table 3.4 Effects of T_{max} on glass samples in phosphate-free and phosphate-containing solution.

	No phosphate		With phosphate	
Leg	Leg1	Leg4	Leg5	Leg8
5 cycles				
Clarity	98.2%	90.0%	99.2%	99.2%
39 cycles				
Clarity	1.1%	46.6%	96.2%	95.1%
PXRD	Calcite	No peaks observed	No peaks observed	No peaks observed
SEM (5 µm)				
Comments	ACC-like (red), calcite (in black)	ACC-like (red), Calcite-like (in black)	ACC-like, calcite-like	ACC-like (red), Calcite-like (in black)

The SEM images in Figure 3.3(a-d) shows the density and the distribution of the crystals on the surfaces of the glass samples at the end of the 39th cycle in detail. The SEM images in Figure 3.3 (a1 to d3) displays a closer look of the dominant polymorphs observed for the four Legs. In this section, for some of the samples, the morphologies of crystals could not be determined due to lack of sample available for analysis. Hence, no diffraction information could be obtained however it has been reported in the literature that the crystals in this case from these samples are likely to have either ACC-like or calcite-like morphology. At a magnification of 1000X, it was evident that the distribution of crystals on Leg1 (Figure 3.3a) was denser than the other three Legs. The deposit from leg 1 was scraped from the surface of the glass sample and analyzed using PXRD. The PXRD pattern demonstrated that the scraped powder from Leg1 is calcite

(Figure 3.4). No peaks belonging to aragonite or vaterite were observed. The amorphous cluster observed in Figure 3.3-a3 using PXRD is likely to be ACC-like. By evaluating the observations from the SEM images (Figure 3.3-a to Figure 3.3-a3), it can be stated that the single crystals of calcite with a rhombohedral shape (Figure 3.3-a3) and ACC-like clusters (Figure 3.3-a2) were observed on the surface of Leg1. These two dominating morphologies were also seen on the surface of the sample in Leg4. The crystal sizes of both phases found on the surface of the sample from Leg1 (65 ^{o}C) were larger than those from Leg4 (at 55 ^{o}C). This indicates that the variation in T_{max} within the reasonable range has no noticeable contribution to the general distribution of polymorphic forms on the surface. Moreover, a lower temperature leads to a lower crystallization rate on the surface[14]. Hence, crystals observed on Leg1 are denser in distribution and larger in size.

When using phosphate-containing hard water, the clarity was highly improved almost resembling its original state even after 39 cycles (Table3.4). The amount of ACC and calcite (visual observation in SEM during imaging) observed on Leg5 and Leg8 was much less than that on Leg1 and Leg4. The amorphous phases seen on Leg5 and Leg8 looked like a thin film, and those on Leg1 and Leg4 were amorphous clusters (Table 3.4).

Calcite-like crystals observed with round plate-shaped structure were not in their well-defined faces, and this may be due to the presence of phosphate ions or other additives in the solution. The crystals were seen in Leg1 and Leg4 but not Leg5 (Figure 3.3-a3 to Figure 3.3-d3). On the surface of Leg5, amorphous films and few calcite-like crystals with two non-classical shapes were identified in Figure 3.3-c1 and Figure 3.3-c3. Calcite crystals with similar morphologies were also reported in the literature.[15] From the observations on Leg5 and Leg8, it seemed that the phosphate ions not only delay nucleation but also inhibited the crystal growth of calcite.

In summary, calcite or calcite-like crystals and amorphous material were observed in all four samples. However, the amorphous phase found on Leg5 and Leg 8 were more like a film as shown in Figure 3.4 (c2) and Figure 3.4 (d2), while the amorphous cluster observed on Leg1 and Leg4 were more like clusters. It is speculated that the presence of phosphate ions retards the crystallization process of ACC and calcite, in this way, the surface deposition rate is highly reduced. Hence, samples produced with phosphate-containing hard water have a higher clarity.
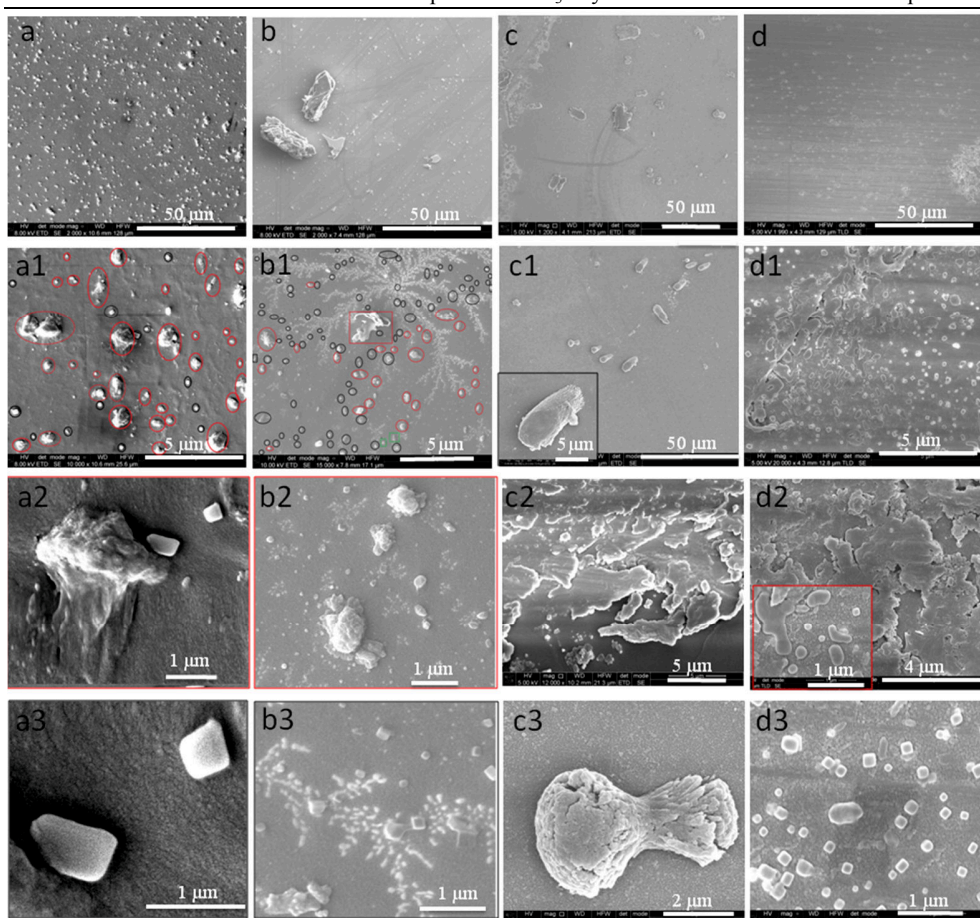
Figure 3.3 The CaCO₃ morphologies on glass samples after 39 cycles when using phosphate-free (a, b) and phosphate-containing (c, d) hard water. (a-a3) Leg1, (b-b3) Leg4, (c-c3) Leg5, (d-d3) Leg8. Images from (a) to (d) are taken at a magnification of 1000X, showing a general distribution of crystals on the surface. Images from (a1) to (d1) show a closer look of the crystals on the surface. The ACC and calcite are circled in red and black (a1), respectively, which are further shown in (a2) and (a3). (b1) The ACC and calcite are circled in red and black, respectively, which are further shown in (b2) and (b3). It can be seen that the crystals observed on Leg1 are bigger than that on Leg4. (c) General distribution of crystals, observed calcite-like crystal with a dumbbell shape is shown in (c3), and ACC is shown in (c2). (c1) distribution of calcite-like crystals with a shape of shooting star as shown in insert image. (d1) The distribution of ACC and calcite, which are further shown in (d2) and (d3). (d2) The ACC film observed on Leg8. Calcite-like crystals with a shape of a round plate-like.
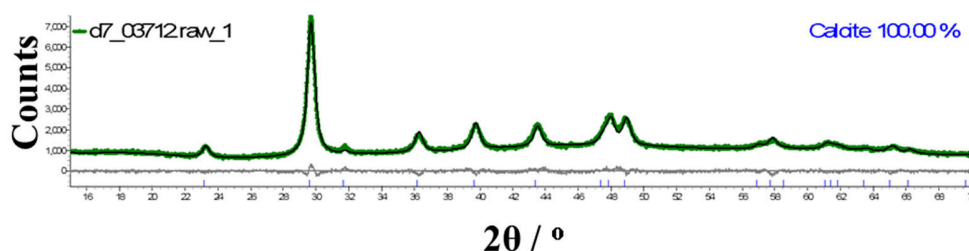
Figure 3.4 Rietveld refinement of scraped powder from glass samples of Leg1, indicating crystals as calcite. The experimental patterns and simulated pattern are shown in dark green and black, respectively. The difference pattern is shown in gray. Refinement statistics for calcite R_{wp} = 4.09%, R_p = 3.25%, $R_{B(calcite)}$ = 1.08 %, GOF = 1.41. Peak broadening due to crystal size and strain is corrected.

3.3.2 The Effects of HEDP, with and without Ortho-P

Table 3.5 shows the inhibition effects of HEDP on the glass samples after 39 cycles when using phosphate-free (Leg3) and phosphate-containing (Leg7) hard water. When HEDP was added to the solution, its contribution to 'shine' on the glass samples was not noticeable in the early cycles (5 cycles) as the use of the 'full Nil-HEDP formula' alone was found to be sufficient to maintain a clarity of 97 % up to 15 cycles. The inhibition effect of HEDP on shine maintenance was apparent after 39 cycles as the clarity on the surface of 'HEDP Legs' hardly altered, regardless of the presence of Ortho-P in solution or not.
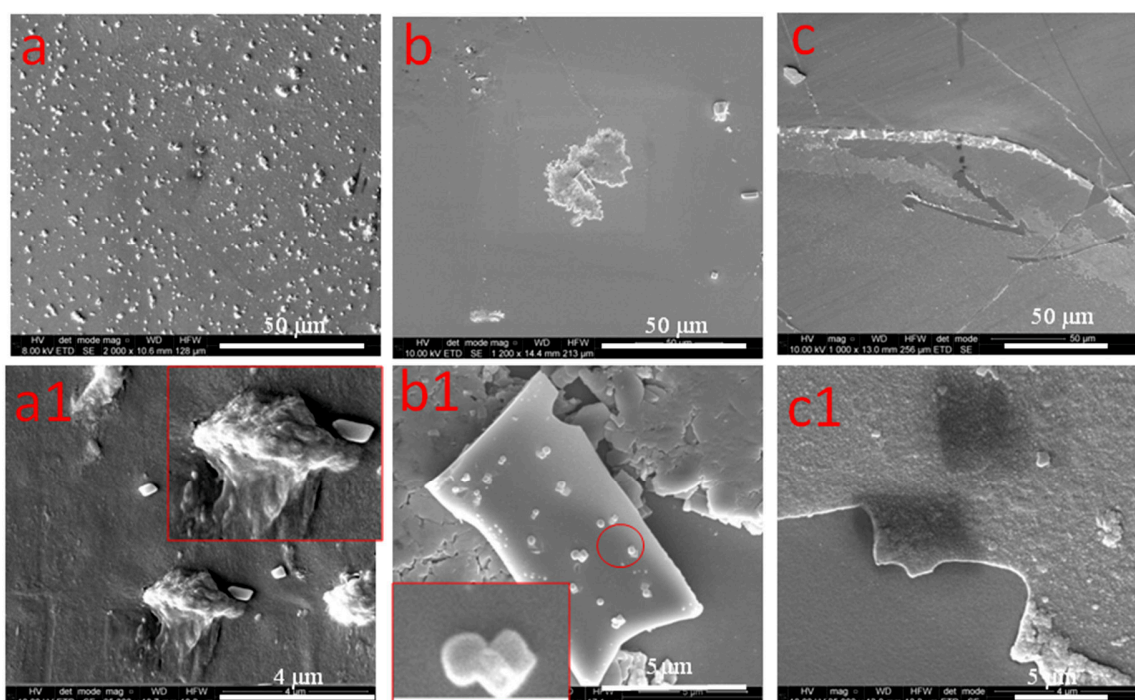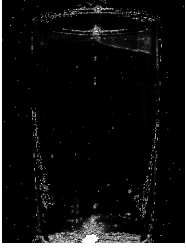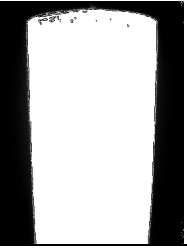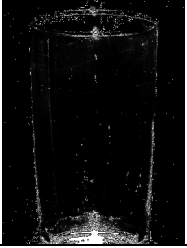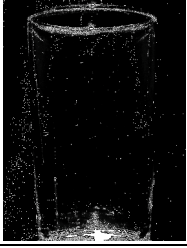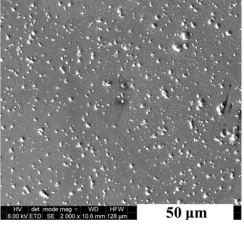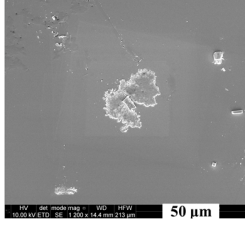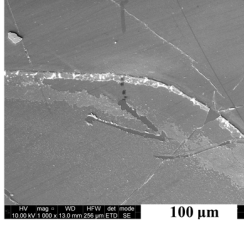
Figure 3.5 Effect of HEDP on the glass samples after 39 cycles. (a) Leg1: ACC-like clusters and single crystals of calcite were observed on leg1, inset is the enlargement of one amorphous CaCO₃ and one rhombohedral calcite, (b) Leg3: an ACC-like film with some rhombohedral calcite-like crystals on top, (c) Leg7: a thin ACC-like film. Images from (a) to (c) shows the general distribution of deposits on the surface. Images from (a1) to (c1) demonstrate details of the crystal morphology observed at a higher magnification.

In the absence of HEDP, a homogeneous distribution of ACC-like clusters and rhombohedral calcite crystals were observed on Leg1. In the presence of HEDP, the crystals found on Leg3 and Leg7 were highly reduced. It should be noted here that very little deposition was seen in Leg3 and Leg7 and the SEM images below for Leg3 and Leg7 only shows the area where deposits can be found. Due to the lack of deposits on the surface, no information could be obtained from the PXRD patterns of either Leg3 or Leg7. Based on the SEM observation, calcite-like crystals, and

an ACC-like film were found on Leg3. On the surface of Leg7, only a thin ACC-like film was observed.

When using the 'full Nil-HEDP formula,' the formation of aragonite and calcite was highly reduced. When HEDP was present, the formation of ACC-like deposits was inhibited or retarded. Hence, a high-shine surface was retained. It seems that an inhibitor that can retard the formation of ACC and prolongs the nucleation until the end of the washing cycle may result in the prevention of surface deposition. A summary of these three samples can be found in Table 3.5.

Table 3.5 The inhibition effects of HEDP on glass samples in phosphate-free and phosphate-containing solution

	No phosphate		With phosphate
Leg	Leg1	Leg3	Leg7
	Formula only	With HEDP	With HEDP
5 cycles			
Clarity	98.2%	97.8%	99.9%
39 Cycles			
Clarity	1.1%	98.4%	97.7%
PXRD	Calcite	One peak calcite (006) or NaCl (002)	No peak observed
SEM			
Comments	**ACC-like, calcite**	**ACC-like, calcite-like**	**A thin ACC-like film**

3.3.3 General Change of Shine Loss on Glass Samples

The samples which suffered from the most severe filming were Leg1 and Leg4 (for this the suffering was slightly less). Other samples, with the involvement of either HEDP or Ortho-P in water, were able to retain a high clarity as the original state even after 39 cycles. The shiniest sample was obtained when HEDP was present in the formula (see Leg1 versus Leg3). All the other samples 'with Ortho-P Legs' have shiny surfaces as the original state. The presence of phosphate ions, which act as a crystal growth inhibitor, helps to retain the clarity of the glass samples. For example, the clarity of Leg1 changes more dramatically than that of Leg5. The change of T_{max} from 65 °C to 55 °C also improves the shine on the surface (e.g. Leg1 versus Leg4), although not as efficiently as in the presence of the phosphate ions. Leg1, with a final clarity equal to 1.1%, loses more 'shine' than that of Leg4, which has a clarity of 46.6% after 39 cycles. Operation at a lower T_{max} improves the shine, and this observation may be due to the intrinsic property of inverse solubility of CaCO₃ and a relatively lower crystallization at T_{max} = 55 °C. The degree of clarity of Leg5 and Leg8 was insignificant in the presence of Ortho-P in the solution, which encourages the shine maintenance.

In summary, two Legs can be classified as filmed surfaces. They are Leg1 and Leg4. However, at a lower T_{max}, the shine can be maintained with extra cycles. The presence of orthophosphate ions in hard water enabled the shine to retain even after 39 cycles. This was consistent with the views from the literature that the presence of phosphate delays the deposition process on surfaces.[3] Samples produced in the presence of HEDP retain the shine almost as the original state of clarity. Therefore, clarity contribution of the different factors can be categorized in the following order: HEDP > Ortho-P >> T_{max} = 55 °C.

3.3.4 Distribution of CaCO₃ Polymorphs on Glass Samples after Excessive Cycles

Table 3.6 below shows all the morphologies observed on the surfaces of the six different glass samples. Morphology (A) is rhombohedral calcite with defects on the surface. It is the most frequently observed morphology of CaCO₃ and was found on the surface of Leg1, Leg3, Leg4 and Leg8. There are two possible reasons: one is that the glass substrate tends to have calcite as the deposited polymorph on its surface. Another is that the orthophosphate ions tend to stabilize calcite as the final polymorph (Leg5 and Leg8). Morphology (B) and Morphology (C) are also

calcite-like crystals but only observed on samples of Leg5. Similar morphologies can be found in the literature, showing Morphology (B) likely to be calcite.[15b] Morphology (C) is similar to the calcite observed in Chapter 2 (Figure 2.18). Morphology (D) has also been reported in the literature.[15a] It is suggested Morphology (D) forms by integrating and merging small CaCO$_3$ nanoparticles together before they transform into discrete calcite crystals with a well-defined edge. The presence of ACC is mainly deduced from the amorphous morphologies seen in SEM as it is difficult to demonstrate from the background in PXRD patterns. Morphology (e) has a tree-like shape and consists of nanoparticles with rhombohedral calcite on top, and is only observed in Leg4. Morphology (E) only has the SEM information available. The amorphous phase was observed for all samples. However, each sample had a different appearance. Morphology (F), Morphology (G) and Morphology (H) were identified by EDX as CaCO$_3$ with no well-defined shape. By summarizing the observations from PXRD, EDX, and SEM, it can be concluded that a mixture of calcite or calcite-like and ACC-like deposits were found on all surfaces of the glass samples except on the shiniest surface of 'Leg7,' where only a thin ACC-like film was observed by SEM. Calcite has been detected by PXRD in the samples of Leg1. The other four samples (Leg4, Leg5, Leg7, and Leg8) have an insufficient amount of crystals on the surface to be identified by PXRD, but the calcite-like crystals are observed by SEM on the surfaces of Leg4, Leg5, and Leg8. The characteristic property of shiny surfaces of Leg3, leg5, Leg7 and Leg8 is that the original surfaces of substrates can still largely be seen. Where deposits can be observed, ACC is the dominant phase found on the surface, and the size of calcite-like crystals is nano-scale. It can be deduced that the HEDP and phosphate ions lengthen the induction time and suppress the formation of both ACC and calcite. Therefore two possible explanations for the inhibition effectiveness of HEDP can be proposed: one is that HEDP inhibits the aggregation of the primary particles.[9] Its effectiveness on suppressing the formation of ACC on the surface reduces the possibility that ACC acts as nuclei for following washing cycles. Another is that ACC which has a higher solubility is stabilized by HEDP and easily flushed away under hydrodynamical conditions, hence will not contribute to the surface deposition.

Table 3.6 Morphologies of CaCO$_3$ observed on the surfaces of glass samples at 39 cycles
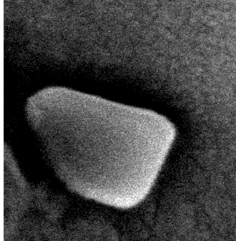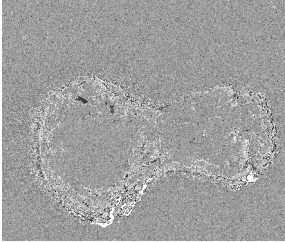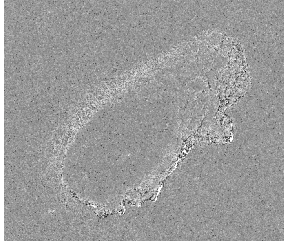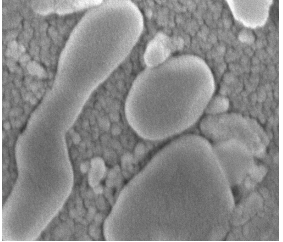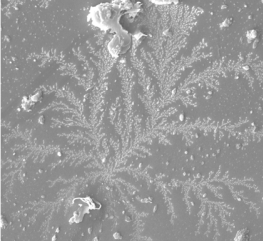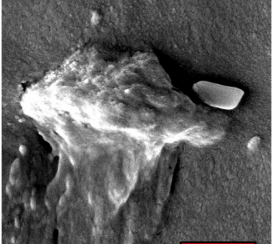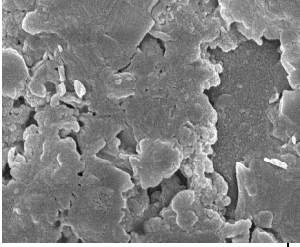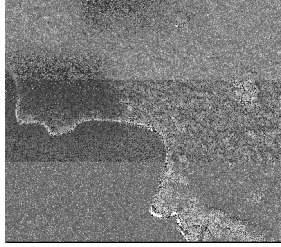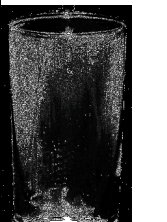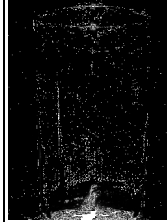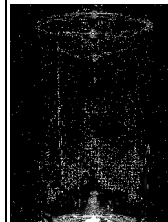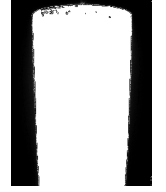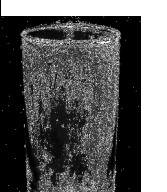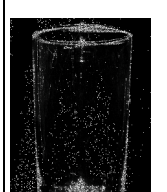
Label	Morphology A	Morphology B	Morphology C	Morphology D	Morphology E
Image					
CaCO$_3$	rhombohedral calcite	calcite-Like (Dumbbell)[15b]	calcite-like (shooting-star)	calcite-like[15a]	calcite-like, ACC-like
Legs	Leg1, Leg3, Leg4, Leg8	Leg5	Leg5	Leg4 and Leg8	Leg4
Label	**Morphology F**	**Morphology G**	**Morphology H**		
Image					
CaCO$_3$	ACC-like	irregular ACC-like film	a thin ACC-like film		
Legs	Leg1 and Leg4	Leg3, Leg5 and Leg8	Leg7		

Table 3.7 Images of glass samples taken after the 5th cycles and the 39th cycles in a dark room and under normal light (the 39th cycles only). The PXRD results are for samples produced after 39 cycles. SEM images of morphology can refer to Table 3.6. The comments part is combined results of PXRD, EDX, and SEM.

	Without Ortho-P			With Ortho-P		
Leg	Leg1	Leg4	Leg3	Leg5	Leg8	Leg7
	Formula only	Formula only	With HEDP	Formula only	Formula only	With HEDP
5 cycles						
Clarity	98.2	90.0	97.8	99.2	99.2	99.9
39 Cycles						
Clarity (%)	1.1	46.6	98.4	96.2	95.1	97.7
PXRD	ACC + calcite	No peaks	No peaks	No peaks	No peaks	No peaks
SEM Table 3.6	A & F	A, E & F	A & G	A, B, C & G	A, D & G	H
Comments	**ACC-like, calcite**	**ACC-like, calcite-like**	**ACC-like, calcite-like**	**ACC-like, calcite-like**	**ACC-like, calcite-like**	**ACC-like film**

3.4 Understanding of the Shine Loss on Plastic Samples

The discussion of the effects of T_{max} and HEDP for plastic samples is split into two parts: the shine loss on the surfaces and the variation in polymorphic species of $CaCO_3$ under different chemical conditions. To be consistent, the first two sections give more details about the effects of T_{max} and HEDP on 'shine' of different substrates and the $CaCO_3$ crystal growth. The following two subsections discuss the general changes of shine loss and distribution of different $CaCO_3$ polymorphs under different chemical conditions. The clarity of plastic samples was rated by visual observation from 1 to 10, with a higher number meaning greater clarity of the sample, i.e.,10 indicating no visible filming.

3.4.1 The Effects of T_{max}, with and without Ortho-P

This subsection describes the variation in shine and deposited $CaCO_3$ crystals on the surfaces of different plastic substrates for 'formula only' samples. Plastic samples were treated under the right-hand side sets of real dishwasher conditions as described in Table 3.2 and labeled 'formula only' (this includes samples which are generated with the standard Nil-HEDP formula only). The comparison was carried out among four samples. These four samples ere Leg1, Leg4, Leg5, and Leg8. The performance of the 'full Nil-HEDP formula' at T_{max}= 55 ˚C and T_{max}= 65 ˚C in phosphate-free (Leg1 & Leg4) and phosphate-containing (Leg5 & Leg8) hard water are compared below (Figure 3.6).
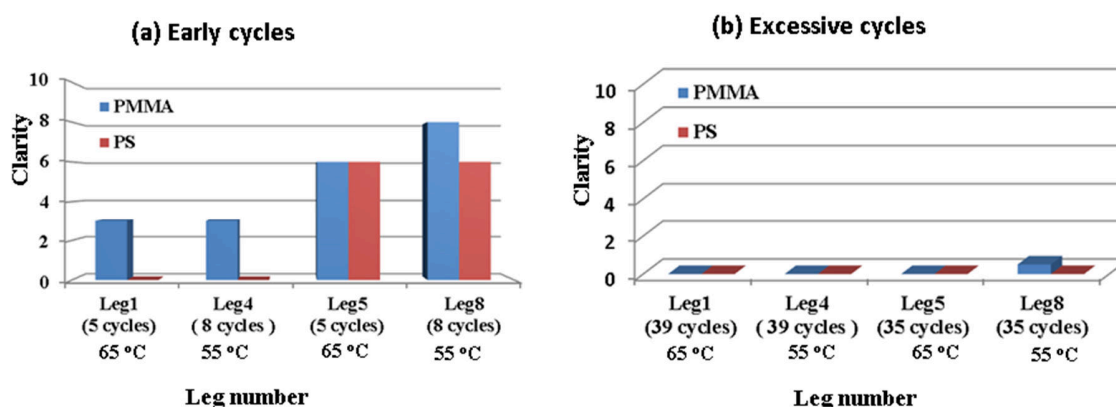
Figure 3.6 The effects of the Tmax on the shine of the plastic samples in the absence (Leg1 and Leg4) and presence (Leg5 and Leg8) of phosphate ions in solution: (a) the early cycles and (b) the excessive cycles.

Unlike the glass samples, none of the 'formula only' samples retain any shine on the surface after 35 cycles (Figure 3.6b). Moreover, samples of excessive cycles were covered with different thicknesses of film. For samples of early cycles (Figure 3.6a), it seemed that either at a lower T_{max} = 55 ^{o}C or the addition of orthophosphate salt in hard water, encouraged the maintenance of shine. This can be observed when comparing Leg1 *vs.* Leg4 and Leg1 *vs.* Leg5. When the T_{max} was changed from T_{max} = 65 ^{o}C to T_{max} = 55 ^{o}C, Leg4 needed to be run for three cycles to achieve a similar shine as Leg1 (Figure 3.6a). This is consistent with the observation on glass samples that a lower temperature retained more shine on the surface.

The presence of orthophosphate ions in the washing solution had a positive effect on retaining the shine for both plastics and glass samples, particularly at the lower T_{max} = 55 ^{o}C. This was noticeable for PMMA samples when comparing clarity of Leg1 to Leg8 (Figure 3.7). Under the same chemical condition, the switch of T_{max} from T_{max} =65 ^{o}C to T_{max} =55 ^{o}C had little effect on the distribution of polymorphic forms of CaCO₃. The dominant phase aragonite and the corresponding morphologies observed in Leg1 and Leg4 were the same, which is represented as morphology (a) in Figure 3.8a. The same calcite crystals were seen Leg5 and Leg8. The only difference between Leg1 and Leg4 lies in the ratio of calcite to aragonite observed in early cycles. There was a slightly higher amount of calcite found on 'Leg4' than 'Leg1' on both PS and PMMA. Apart from the flora-like aragonite (Figure 3.8a), another morphology was also observed on Leg4 of PMMA slide, which corresponds to morphology (b) in Figure 3.8b. Morphology (b) was different from morphology (a) and probably be assigned as calcite. Two different polymorphs were detected by PXRD. The flora-like polymorph belongs to aragonite; morphology (b) can be allocated to calcite.
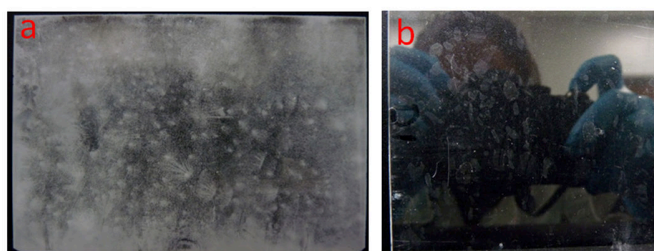
Figure 3.7 The positive effect of T_{max} = 55 ^{o}C with the presence of orthophosphate ions in solution in early cycles. a) PMMA Leg1, T_{max} = 65 ^{o}C, 5 cycles; b) PMMA Leg8, T_{max} = 55 ^{o}C, 8 cycles.

In the study of samples of early cycles, it was learned that the shine was improved by either the presence of inorganic phosphate ions in solution or at lower T_{max} = 55 ^{o}C. Although, the conditions still not sufficient to prevent the formation of a film completely on the surface. However, the ways that Ortho-P and T_{max} retain the shine on the surface are different. The former, according to the literature, functions by interrupting the crystal growth especially for calcite.[4-7] Hence, it was seen that the presence of Ortho-P had a noticeable effect on shine maintenance of the glass surface but not on the plastic surface, where aragonite was observed to grow. The latter, namely a lower T_{max}, leads to a lower crystallization rate, hence a less deposits. However, it is observed that the change to a lower T_{max} has no influence on the final distribution of polymorphic forms.

The effects of orthophosphate ions on polymorphic forms of CaCO₃ on the surfaces can be clearly seen from Table 3.8 below. Polymorphic forms of CaCO₃ on the surfaces were different when using phosphate-free (Leg1 and Leg4) and phosphate-containing (Leg5 and Leg8) water. When using phosphate-free water, the dominant phase observed on the surface was aragonite (001) with a flora-like morphology (Figure 3.8a), regardless of the plastic type and T_{max}. There was only one exception, which were Leg1 and Leg4 of PMMA slides of excessive cycles. When using phosphate-containing water, crystals were stabilized as calcite and the dominant morphology changed from flora-like aragonite (001) (Figure 3.8a) to the coccolith-like calcite (Figure 3.8d). Some deposits of Morphology (f) in Figure 3.8 was observed on PS samples of Leg5 of the excessive cycle.
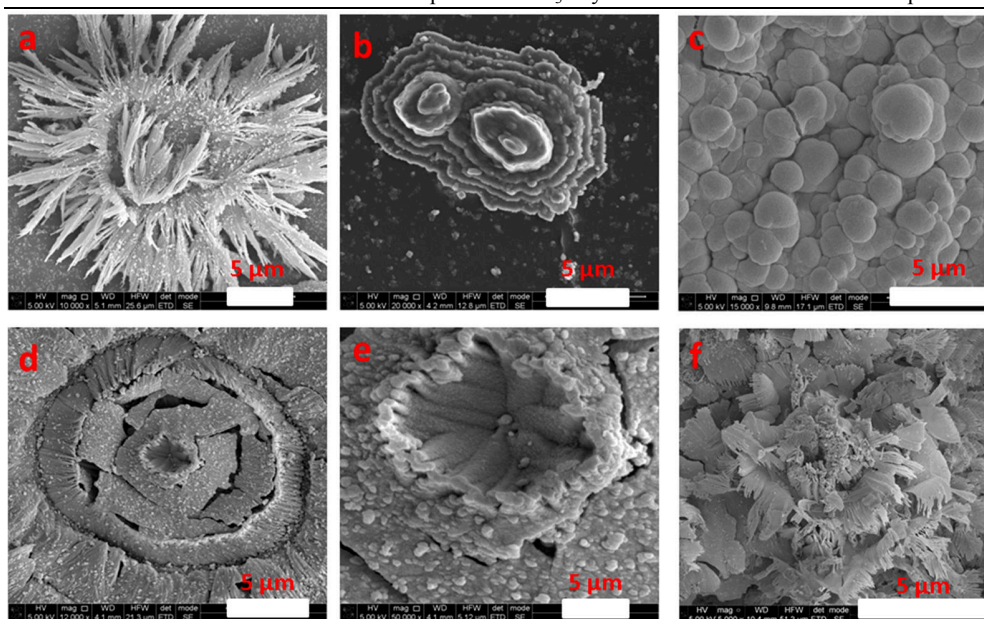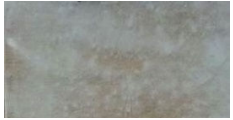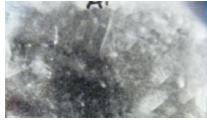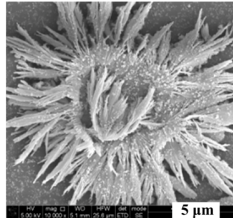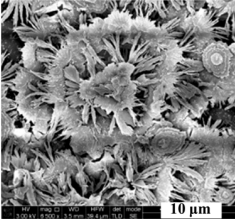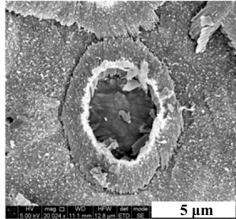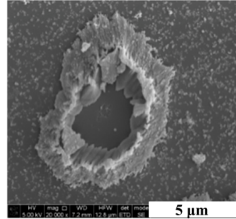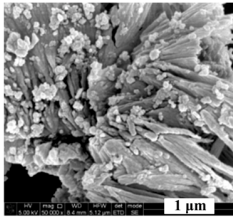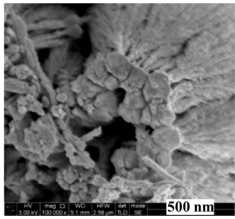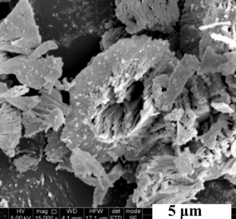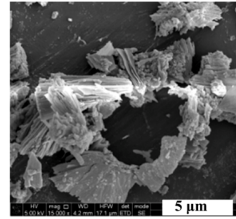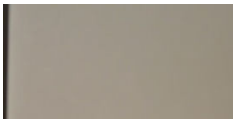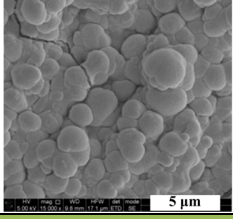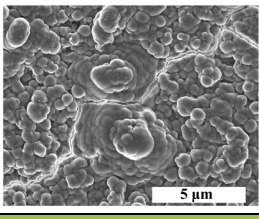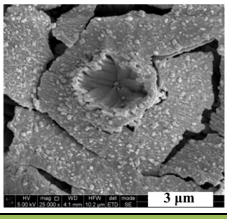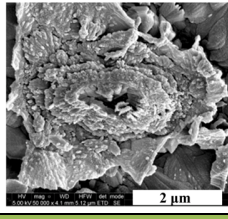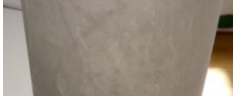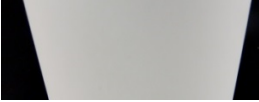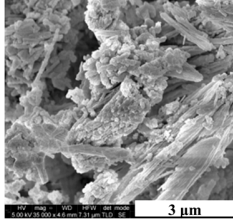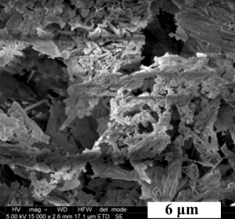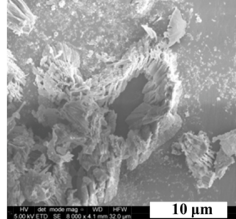
Figure 3.8 The CaCO₃ morphologies observed for 'formula only Legs' on the surface of plastic samples in phosphate-free water (a-c) and phosphate-containing water(d-f) (a) aragonite (001), (b) calcite, (c) a mix of aragonite (001) and calcite (d) calcite (e) calcite and (f) calcite.

For the samples produced using phosphate-free water, there was one exception which was the Leg1 and Leg4 of PMMA slides of excessive cycles. Regardless of T_{max}, the crystals observed on Leg1 and Leg4 were the same. However, the crystals were not flora-like aragonite polymorph as shown in Figure 3.8(a). Instead, the crystals were identified as a mix of aragonite (001) and calcite with a spherical morphology as illustrated in Figure 3.8(c). This may be due to the accidental adding of soil at cycle 10 (soil was accidentally added into legs 1-4 at cycle 10 for plastic samples, see Table 3.2 Table. However, the dominant phase on PS plastic was consistently aragonite (001). Both, samples from the early cycle and excessive cycles were consistent. This is still unknown and requires further exploration.

In summary, the change of T_{max} to T_{max} = 65 °C (Leg1 & Leg5) and T_{max} = 55 °C (Leg4 & Leg8) in the main wash cycle had little effect on the modification of the polymorphic species and morphologies except for when the chemical environment was altered. Phosphate ions in solution can change the crystals from flora-like aragonite (001) to coccolith-like calcite. The exception of the PMMA slides of Leg1 and Leg4 from excessive cycles can be attributed to the accidental addition of soil at cycle 10. The presence of orthophosphate ions in solution or operation at T_{max} = 55 °C retained the shine however this was not sufficient to attain the same level of shine as the

original. The increase in the number of cycles mainly contributed to the increase in the quantity of the crystals rather than the modification of the polymorphic form.

Table 3.8 The effect of T_{max} with and without orthophosphate ions in 'formula only' samples

	Without Ortho-P		With Ortho-P	
	Leg1 (65 °C)	Leg4 (55 °C)	Leg5 (65 °C)	Leg8 (55 °C)
PMMA (Early cycle)				
Clarity	3	3	6	8
SEM				
PXRD	A (001)/C=99/1	A (002)/C=98/2	Calcite	Calcite
PS (Early cycle)				
Clarity	0	0	6	6
SEM				
PXRD	A (001)/C=99.5/0.5	A (001)/C=98.5/1/5	Calcite	Calcite
PMMA (Excessive cycle)				
Clarity	0	0	0	0.5
SEM				
PXRD	A (001)/C=1:1	A (001)/C=3:2	Calcite	Calcite
PS (Excessive cycle)				
Clarity	0	0	0	0
SEM				
PXRD	Aragonite (001)	Aragonite (001)	Calcite	Calcite

3.4.2 The Effects of HEDP, with and without Ortho-P

This subsection will study the inhibition efficiency of HEDP on plastic samples when using phosphate-free (Leg3) and phosphate-containing (Leg7) hard water. The comparison was carried out among three different types of samples: Leg1, Leg3, and Leg7. Leg1 was included for comparison only. The full characterization results are shown in Table 3.9. For consistency, the shine loss on the surfaces of plastic will be initially discussed and then followed by the variation of polymorphic forms of $CaCO_3$ under different chemical conditions.
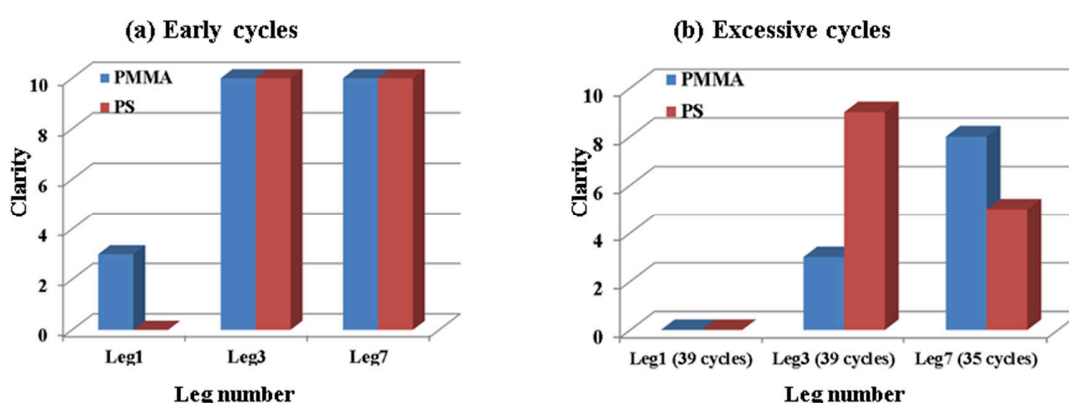
Figure 3.9 The inhibition effects of HEDP on plastic samples in early cycles (a) and in excessive cycles (b).

Clarity comparison for samples of early cycles and excessive cycles are shown in Figure 3.9. In the early cycles, samples of HEDP Legs retained the same shine as the original (Figure 3.9a) and hence, the data for these samples are not provided. The results for samples labeled as 'with HEDP' and from the Legs of excessive cycles, however, are provided. These samples were run until HEDP lost its inhibition ability. It was found that the inhibition ability of HEDP for plastic samples functioned well ≥ 30 cycles. However, at the end of the 35th cycle, the shine loss was apparent for PS Leg7 (Figure 3.9b). Among all 'with HEDP' samples, the PMMA of Leg3 lost most shine, followed by PS of Leg7. The PS of Leg3 and PMMA of Leg7 were visually clean. The latter by eye retained more shine than the former. This was consistent with the observation from the SEM images (Figure 3.10.) At a magnification of 500X, visible crystals were observed on the surfaces of both the 'PMMA Leg3' and 'PS Leg7,' while the deposits on the surfaces of other two samples could not be clearly identified. For 'with HEDP' Legs, the samples produced with phosphate ions in solution did not retain more shine than those produced with phosphate-free hard water i.e. the PS Leg3 vs. PS Leg7. The fact that the presence of phosphate ions has no

effect in enhancing the inhibition ability of the HEDP may indicate that there is a competition between the HEDP and phosphate ions during the crystallization inhibition step, rather than a synergetic relationship.
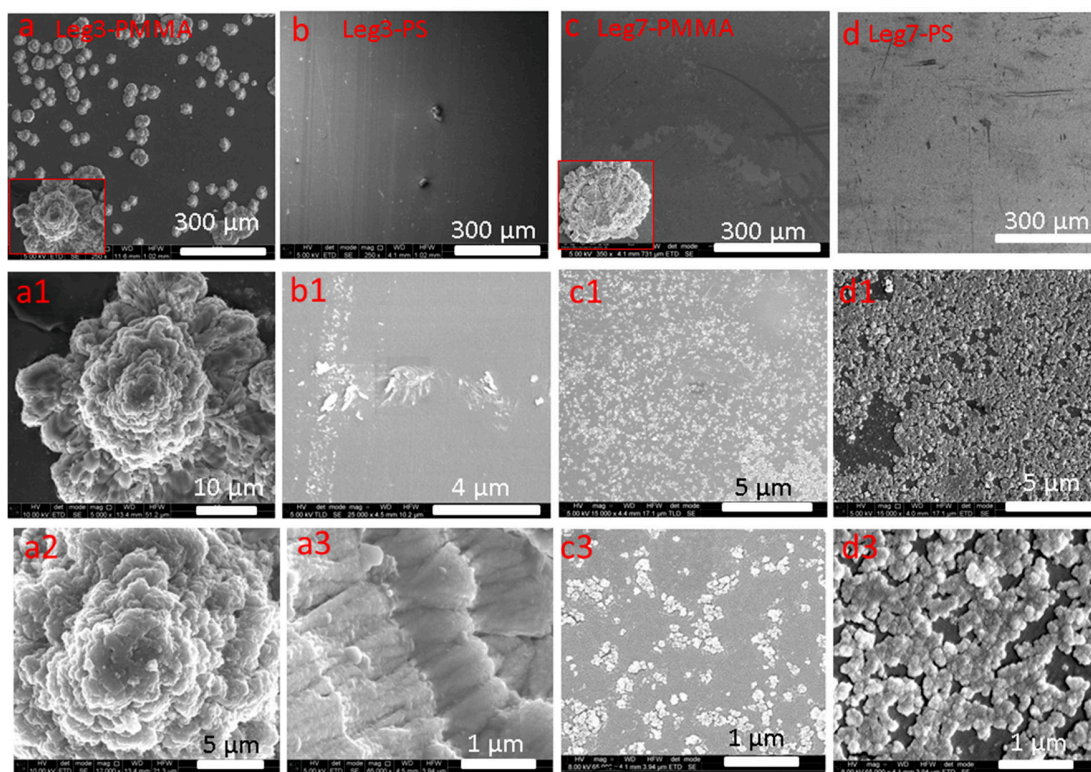
Figure 3.10 The SEM images of 'with HEDP' Legs after 39 cycles. The general distribution of crystals on the surface is shown from (a) to (d).. The corresponding morphologies of the dominant polymorphs are labeled accordingly with the same alphabet letter. (a) Leg3 of PMMA, the insert is the dominant morphology of crystals, a full image is shown in (a1). The texture of (a1) is further shown in (a2) and (a3); (b) PS of Leg3: very few deposits were observed; (c) PMMA of Leg7: a homogeneous film can be clearly seen in (c1) and (c2). The insert crystal is similar to the crystal (a1). (d) PS of Leg7: a homogeneous film observed was thicker than that of PMMA of Leg7.

Figure 3.10 further presents the variation in crystal morphology when involving the CaCO₃ inhibitor HEDP in orthophosphate-free (Leg3) and orthophosphate-containing (Leg7) solution. When using the 'full Nil-HEDP formula,' aragonite (001) crystals were observed on the surfaces. When HEDP was added into the formula, growth of aragonite (001) was inhibited and the shine was highly improved. When HEDP started to lose the inhibition ability, the Morphology (c3) was observed in all 'with HEDP' samples. For example, the 'PMMA Leg7' and 'PS Leg7' exhibited morphology (c3) and morphology (d3) (Figure 3.10), respectively. Morphology (d3) was identified by PXRD as calcite (Figure 3.11) and may contain ACC, as indicated by the broad background of the PXRD pattern. The amorphous shape of morphology (d3) may also confirm

the presence of ACC. Visually, it seems that the crystals of morphology (c3) are similar to those of morphology (d3) and the latter being bigger in size and denser in the amount on the surface. However, due to the lack of deposits, crystalline information of morphology (c3) is unknown. To obtain a shiny surface, the inhibitor should not only retard the growth of $CaCO_3$ crystallites but also restrict the formation of the amorphous phase. When the amorphous phase reaches the critical size and becomes stable, the amorphous phase can spread and gradually build up on the surface. The film will become more visible over a period of time. For example, the homogenous film observed on PS of Leg7.
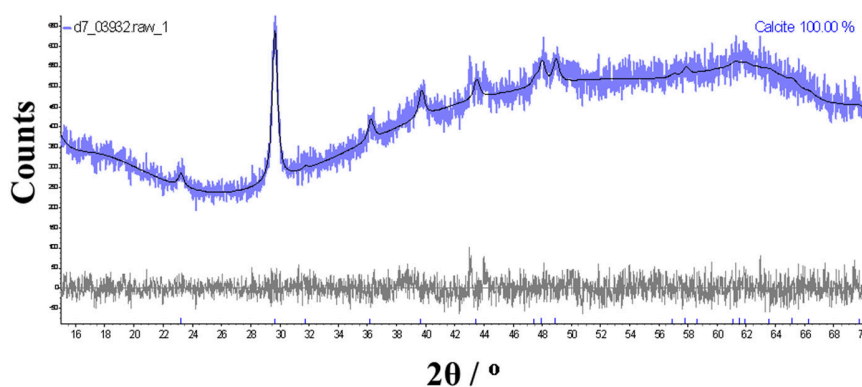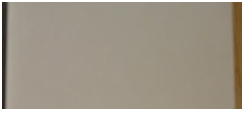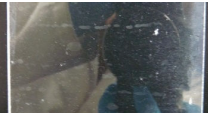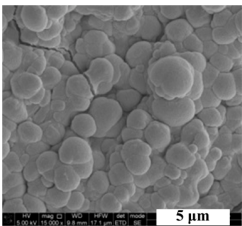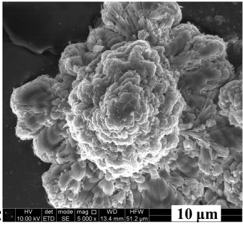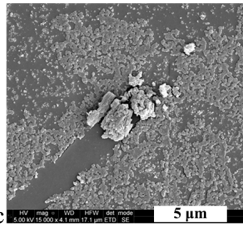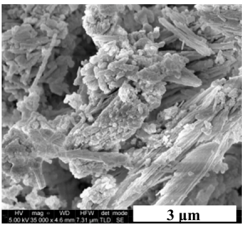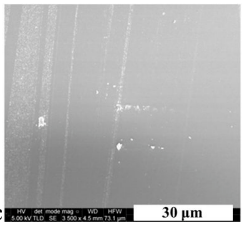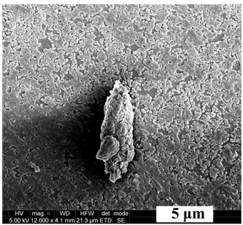
Figure 3.11 Rietveld refinement of scraped powder from PS samples of Leg7, indicates that the deposits are calcite. The low peak intensity is due to the lack of powder sample from the surface of PS. From the observed pattern, it can be seen that calcite is present. The broad background may indicate the presence of amorphous CaCO₃. The experimental patterns and simulated pattern are shown in purple and black, respectively. The difference pattern is shown in gray. Refinement statistics: R_{wp} = 4.97%, R_p = 3.95%, $R_{B(calcite)}$ = 0.50%, GOF = 1.03. The peak broadening of calcite caused by the crystal size and strain is corrected.

'PS Leg3' had the shiniest surface out of all 'with HEDP' Legs, while 'PMMA Leg3' had the most film build up on the surface due to the growth of a mix of aragonite (001) and calcite (morphology a1). A tiny amount of morphology (a1) was also observed on Leg7 of PMMA. Once the crystals grew on the surface, the HEDP lost its inhibition ability quickly. This may indicate that the proposed mechanism for HEDP preventing surface deposition via blocking the active sites in the crystal growth stage may not be entirely accurate. The inhibition action of HEDP probably mainly take place before the stable nucleus is formed. Nucleation delay or inhibition of the aggregation of the primary particles other than the crystal growth inhibition is the main inhibition mechanism of HEDP. Since the focus of this project is to present the properties of deposits observed after dishwasher cycles, the exact inhibition mechanism is not studied.

Table 3.9 The inhibition effects of HEDP on plastic samples of excessive cycles in phosphate-free and phosphate-containing solution.

		Without Ortho-P		With Ortho-P
		Leg1	Leg3	Leg7
		Formula only	With HEDP	With HEDP
Excessive Cycle	PMMA			
	Clarity	0	3	8
	SEM			
	PXRD	A (001):C=1:1	A (001):C=83:17	Caclite, ACC-like
	PS			
	Clarity	0	9	5
	SEM			
	PXRD	Aragonite (001)	ACC-like	Calcite, ACC-like

3.4.3 General Change of Shine Loss on Plastic Samples

This section gives a summary on the shine loss on plastic samples under different chemical conditions. Figure 3.12 shows the clarity changes on surfaces of PMMA and PS of early cycles and excessive cycles. It can be seen that only the presence of the HEDP allowed the substrate to retain the shine after excessive cycles (e.g. Leg3 and Leg7). Other samples lost almost all the shine after excessive cycles. The presence of phosphate ions in solution significantly retain the shine for the glass samples up to 39 cycles. However, the same inhibition effects by phosphate ions were not observed for plastic samples of excessive cycles.

In the early cycles, the presence of phosphate ions improved the clarity for both surfaces of plastic, especially for PMMA when $T_{max}= 55\ ^oC$. Although, the observation was not as noticeable as observed with the glass samples, the overall clarity of samples from Leg5 to Leg8 had a higher clarity than those of Leg1 to Leg4. In general, all the factors benefit the shine maintenance in the early cycles. However, none of them do so sufficiently enough to prevent the formation of a film on the surface. With the increase in number of the washing cycle, different thicknesses of the film were observed to build up gradually. For both the samples of the early cycle and the excessive cycles, only the involvement of CaCO₃ inhibitor HEDP allowed plastic samples to retain the shine in excessive cycles.
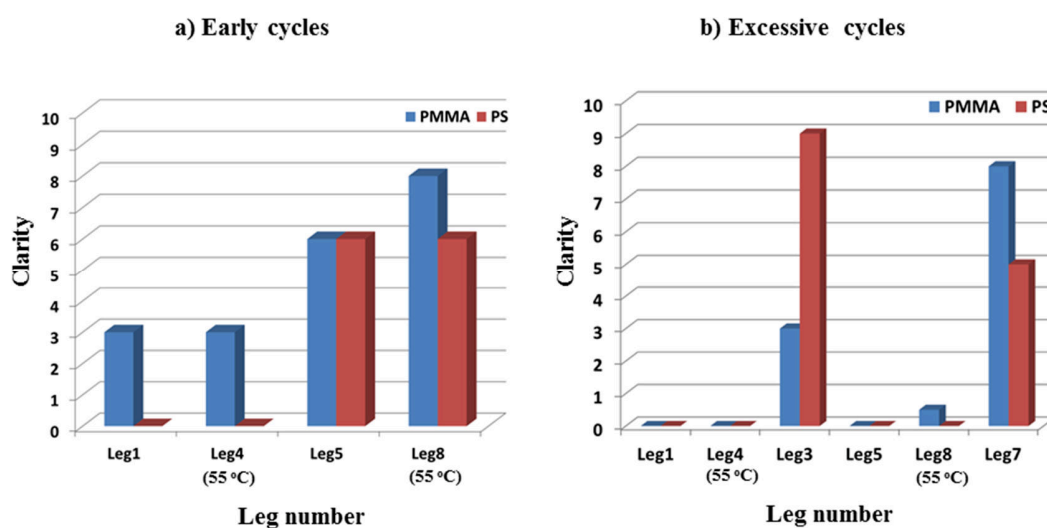
Figure 3.12 The clarity on the surfaces of PMMA and PS samples of early cycles (a) and excessive cycles (b).

3.4.4 Distribution of CaCO₃ Polymorphs on Plastic Samples in the Early Cycles and the Excessive Cycles

A characterization summary by XPRD and SEM for the PMMA and PS samples is shown in Table 3.10. The detailed information for plastic samples of early cycles and excessive cycles are shown in Table 3.11 and Table 3.12, respectively. The most frequently observed CaCO₃ morphologies are attached accordingly. Both the samples of the early cycles and excessive cycles are included.

The CaCO₃ polymorphs observed in plastic samples were different from those found in glass samples. Comparing to glass samples, the polymorphic forms and the morphologies of CaCO₃ found on the plastic samples varied and were highly dependent on the chemical environments.

When using the 'full Nil-HEDP formula' (Leg1 & Leg4), crystals were found to be in the form of flower-like aragonite with a trace amount of calcite (the morphology is shown in Table 3.10a). The flower-like aragonite is made from single crystals of needle-like aragonite (001). The only exception is the PMMA slides of excessive cycles, where crystals were identified as a mix of aragonite (001) and calcite. Moreover, the morphology observed is not the morphology (a) but the spherical-like morphology (d). The reason may be because the soil was accidentally added at cycle 10 during the tests carried out at P&G from Leg1 to Leg4. However, it seems that this 'accidental' soil only had an impact on the PMMA samples but not PS samples. Flora-like aragonite (001) was consistently observed on the surfaces of PS. In summary, flora-like aragonite (001) was the dominant phase on the surfaces of Leg1 and Leg4 up to 39 cycles, with the only exception being the PMMA samples of excessive cycles. Hence, the change of the T_{max} in the main wash cycle had little effect on the resulting polymorphic forms for 'formula only' samples. As the distribution of polymorphic forms observed between Leg1 and Leg4 or between Leg5 and Leg8 are almost the same.

The calcite was observed on Leg5 and Leg8 due to the presence of orthophosphate ions. When using the phosphate-containing water, crystals are stabilized as calcite and observed as morphology (c). With the increase in number of washing cycles, the density and the amount of morphology (c) also increased.

When involving the CaCO₃ inhibitor HEDP (Leg3 and Leg7), morphology (e) was the most frequently observed morphology, and it was seen on the surface of all 'with HEDP' samples. The only exception was the PMMA sample Leg3 where morphology (g) was the dominating phase. A subtle amount of morphology (g) was also observed on Leg7.

From the study on the effects of soil, orthophosphate ions, T_{max} and HEDP on the shine loss and the resulting crystal forms and morphologies of CaCO₃, it is known that the shinier the surface, the ACC tends to be the only polymorph on the surface. Once the CaCO₃ deposits start to build up, the retaining of shine becomes difficult.

Table 3.10: The PXRD and SEM Images of PMMA and PS samples taken from early and excessive cycles. Colour code is the same as Figure 3.1.

	Leg	Without Orthophosphate in water			With Orthophosphate in water		
		Leg1	Leg4 (55 ^{o}C)	Leg3	Leg5	Leg8 (55 ^{o}C)	Leg7
		Formula only	Formula only	With HEDP	Formula only	Formula only	With HEDP
Early Cycle	PMMA	Aragonite (001)^{Calcite}	Aragonite (001)^{Calcite}	Not provided	Calcite	Calcite	Not provided
	SEM	a^e	a^{b,e}	Not provided	c^e	c^e	Not provided
	PS	Aragonite (001)^{Calcite}	Aragonite (001)^{Calcite}	Not provided	Calcite	Calcite	Not provided
	SEM	a^e	a^e	Not provided	c^{e,f}	c^e	Not provided
Excessive cycles	PMMA	Aragonite(001)/ Calcite = 1/1	Aragonite(001)/ Calcite =9/1	Aragonite(001)/ Calcite = 4.8/1	Calcite	Calcite	No peak observed
	SEM	d	d	g^e	c	c	e^g
	PS	Aragonite (001)	Aragonite (001)	No peak observed	Calcite	Calcite	Calcite
	SEM	a	a	e	c	c	e

a) Aragonite (001) b) Calcite c) Calcite d) Calcite & Aragonite f) h) Calcite & Aragonite
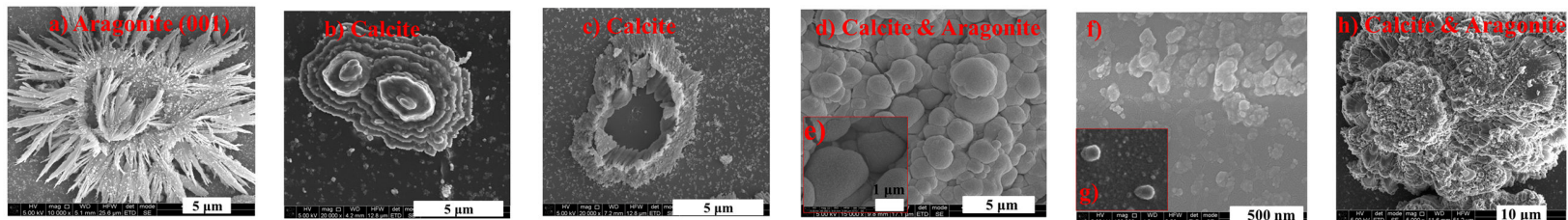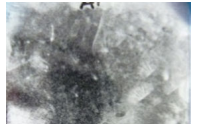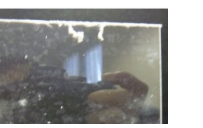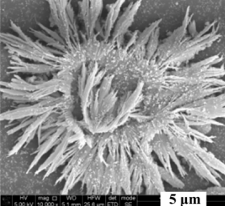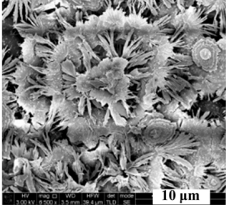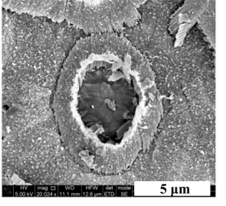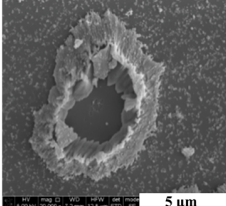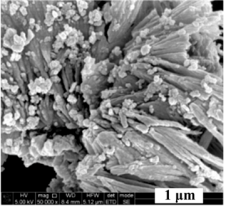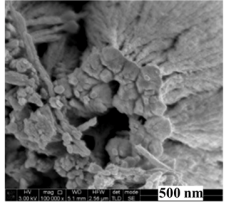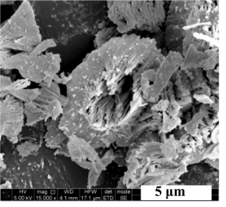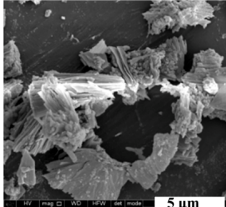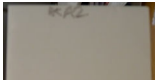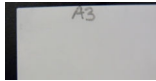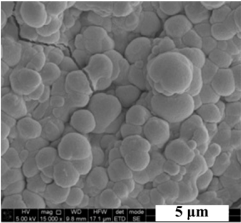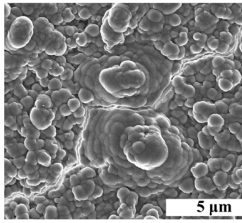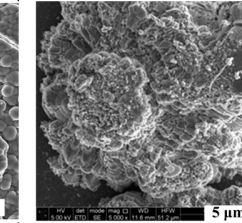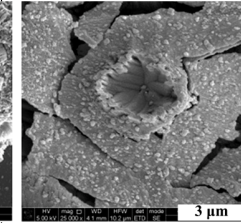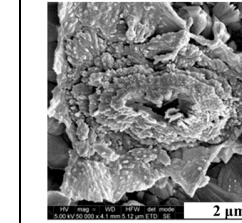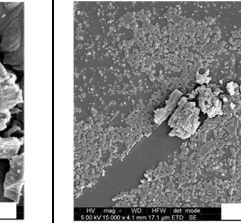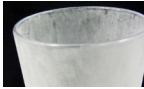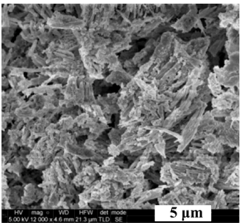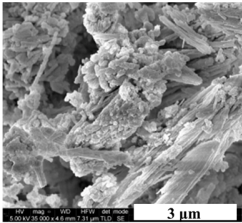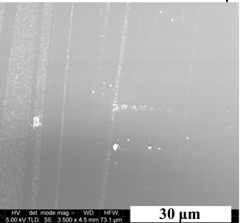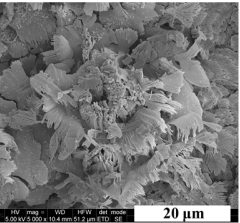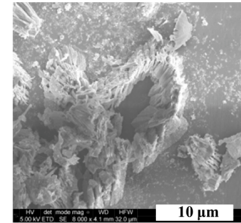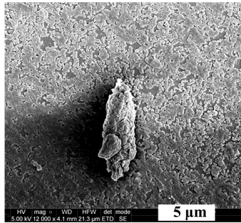
Table 3.11: The plastic samples

	Without Orthophosphate in water		With Orthophosphate in water	
Leg	**Leg1**	**Leg4 (55 °C)**	**Leg5**	**Leg8 (55 °C)**
Substrate	Formula only	Formula only	Formula only	Formula only
PMMA				
Clarity	3	3	6	8
PXRD	Aragonite $(001)^{Calcite}$	Aragonite $(001)^{Calcite}$	Calcite	Calcite
SEM				
PS				
Clarity	0	0	6	6
PXRD	Aragonite $(001)^{Calcite}$	Aragonite $(001)^{Calcite}$	No	Calcite
SEM				

3.12 The plastic samples of excessive cycles

Leg	Without Orthophosphate in water, 39 cycles			With Orthophosphate in water, 35 cycles		
	Leg1	**Leg4**	**Leg3**	**Leg5**	**Leg8**	**Leg7**
Substrate	Formula only	Formula only	With HEDP	Formula only	Formula only	With HEDP
PMMA						
Clarity	0	0	3	0	0.5	8
PXRD	A(001)/C =1:1	A(001)/C =9:1	A(001):C =4.8:1	Calcite	Calcite	No
SEM						
PS						
Clarity	0	0	9	0	0	5
PXRD	A (001)^C	A (001)^C	No	Calcite	Calcite	Calcite
SEM						

3.5 Conclusion

The substrate affects the amount of film deposited and the polymorphic forms of $CaCO_3$, with the latter being highly dependent on the chemical environments. There was much less film formed on the glass tumblers than on the plastic substrates. The glass samples with a clarity above 55% were considered as 'shiny surface' by the naked eye. Shiny surfaces were observed on the glass samples after 39 cycles apart from Leg1. The presence of either HEDP or orthophosphate ions allows attainment of the shinier surface for glass samples.

Samples produced with HEDP was found to maintain the shine almost as the original state. Also, T_{max}= 55 ˚C drives less film formation than that of the T_{max}= 65 ˚C for glass samples. For the glass samples, when the deposits were analyzed, it was always determined to be calcite with either regular shape or irregular shape. Combining the results of PXRD, SEM and EDX, calcite / calcite-like and ACC-like crystals were observed in all samples except Leg7. The deposits observed on the surface of Leg7 were a thin ACC-like film. From the observation on shiny surfaces, it can be seen that the original surface of the substrate which can be largely seen in SEM for a shiny surface. Moreover, ACC-like deposits were the dominant phase for where the deposits were observed on the surface. In summary, the clarity contribution from different variables for glass samples is as follows: HEDP > ortho-P >> T_{max}= 55 ˚C.

Formation of the deposits on plastic samples is highly dependent on the chemical environments. For the 'formula only' samples, aragonite with a trace amount of calcite tends to be the resulting deposits. The presence of orthophosphate stabilizes the sample as calcite as the dominating phase while HEDP generates amorphous $CaCO_3$ on the surfaces if any crystal formation is observed.

For the plastic samples of excessive cycles, there was a significant amount of film formation apart from the two 'HEDP legs' which showed significantly less filming. Other factors had no contribution to retaining the shine when excessive cycles were run due to not being effective enough to prevent the formation of aragonite and calcite. Even though all the factors benefit the shine maintenance in the early cycle, film or deposits can be easily observed after 5 cycles. Therefore, the clarity contribution for plastic samples of the early cycles is HEDP >> ortho-P + T_{max}= 55 ˚C. For samples of excessive cycles, only HEDP worked.

In Chapter 3, the effects of the composition of 'full Nil-HEDP formula' on the shine loss was explored, and it was found that the polymer in the formula promoted film formation on the surface, especially for plastic samples. In this chapter, the possible effects of how other factors affect the function of 'full Nil-HEDP formula' on the shine loss was discussed. The factors included are $T_{max} = 55$ ^{o}C, orthophosphate ions in hard water and HEDP on the shine loss. It was observed that the 'other factors' had a positive effect on the shine maintenance, although to a different extent. In general, the shine for glass tumbler was more readily retained than plastic samples. The polymer in the 'full Nil-HEDP formula' was the main contributor to the build-up of surface crystals more than other factors in the dishwasher. Only HEDP worked to prevent the surface deposition for all types of substrates and hence maintain shine.

3.6 References

1. (a) Wang, H.; Alfredsson, V.; Tropsch, J.; Ettl, R.; Nylander, T. *Appl. Mater. Interfaces* **2013,** *5* (10), 4035-4045; (b) Ren, D.; Feng, Q.; Bourrat, X. *Micron* **2011,** *42* (3), 228-45.

2. Colling, J. H.; Croll, B. T.; Whincup, P. A. E.; Harward, C. *Water Environ. J.* **1992,** *6* (4), 259-268.

3. Noda, S.; Saito, T.; Miya, K.; Furukawa, S.; Clarke, S. M.; Wilson, D. I. In *The Influence of Phosphate on Calcium Carbonate Formation in Hard Water*, The influence of phosphate on calcium carbonate formation calcium carbonate formation in hard water, Budapest, Hungary, Malayeri, M. R.; Muller-Steinhagen, H.; Watkinson, A. P., Eds. Heat Exchanger Fouling and Cleaning: Budapest, Hungary, 2013; pp 165-170.

4. Katsifaras, A.; Spanos, N. *J. Cryst. Growth* **1999,** *204* (1–2), 183-190.

5. Reddy, M. M. *J. Cryst. Growth* **1977,** *41* (2), 287-295.

6. House, W. A. *J. Colloid Interface Sci.* **1987,** *119* (2), 505-511.

7. (a) Simkiss, K. *Biol. Rev.* **1964,** *39* (4), 487-504; (b) Bentov, S.; Weil, S.; Glazer, L.; Sagi, A.; Berman, A. *J. Struct. Biol.* **2010,** *171* (2), 207-215.

8. Didymus, J. M.; Oliver, P.; Mann, S.; DeVries, A. L.; Hauschka, P. V.; Westbroek, P. *J. Chem. Soc., Faraday Trans.* **1993,** *89* (15), 2891-2900.

9. Xu, A. W.; Yu, Q.; Dong, W. F.; Antonietti, M.; Cölfen, H. *Adv. Mater.* **2005,** *17* (18), 2217-2221.

10. Zach, J.; Haider, M. *Nuclear Instruments and Methods in Physics Research Section A: Accelerators, Spectrometers, Detectors and Associated Equipment* **1995,** *363* (1), 316-325.

11. Rodriguez-Blanco, J. D.; Shaw, S.; Benning, L. G. *Nanoscale* **2011,** *3* (1), 265-271.

12. Niedermayr, A.; Immenhauser, A. Trace Element Incorporation and Isotopic Fractionation in Calcium Carbonate Phases (Calcite, Aragonite, Vaterite, Monohydrocalcite, Ikaite and ACC). http://www.ruhr-uni-bochum.de/sediment/forschung.html (accessed May 05, 2015).

13. Nehrke, G.; Van Cappellen, P. *J. Cryst. Growth* **2006,** *287* (2), 528-530.

14. Chen, T.; Neville, A.; Sorbie, K.; Zhong, Z. *Faraday Discuss.* **2007,** *136*, 355-365.

15. (a) Deng, H.; Wang, S.; Wang, X.; Du, C.; Shen, X.; Wang, Y.; Cui, F. *Regener. Biomater.* **2015,** *2* (3), 187-195; (b) Chen, C.; Qi, J.; Tao, J.; Zuckermann, R. N.; DeYoreo, J. J. *Nature* **2014,** *4*, 6266.

4 Syntheses and Structure of Calcium Coordination Compounds of Candidate Inhibitors

4.1 Introduction

Current design strategies for calcium carbonate inhibitors are based on molecular recognition.[1] The proposed inhibition mechanism is mainly described in terms of step-specific or face-specific interactions between the inhibitor and the active sites by evaluating the electrostatic, structural and stereochemical matching at the interface.[2] The understanding of the crystallization process and the structural properties of the inhibitor itself is of equal importance in mineral inhibition. This chapter aims to elucidate the structural nature of the mineral inhibitors and, in particular, the structural chemistry of their calcium complexes, with the hope that some implications of the structural nature of an efficient inhibitor for $CaCO_3$ and hence insight into its mode of action can be obtained. Firstly, a brief review of the structural characteristics of known inhibitors will be given. The newly synthesized calcium complexes with cyclic oligo-carboxylates will be discussed in turns of binding affinity, capacity, effectivity, and their possible docking mode to the mineral surface.
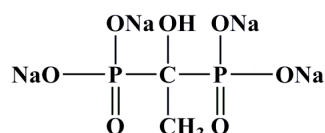

Figure 4.1 Structure of 1-hydroxyethane 1,1-diphosphonic acid (HEDP)

A successful inhibitor such as HEDP (Figure 4.1) consists of calcium-binding functional groups linked by a common organic backbone. For an efficient inhibitor, it had been suggested by Awarccc[3] that the compound should have a high affinity for the solute, and the size of the inhibitor itself should be larger than that of the solute. The affinity of the inhibitor is mainly determined by the functional groups. Binding to cations before docking to a growing particle surface is potentially important, as is the stability of the binding to the surface after docking. Both carboxylic acid and phosphate functionalities are effective in recognizing and modifying crystal surfaces of $CaCO_3$ due to the polarity of the oxygen donor atoms, their full or partial negative

charge, and their similarity to carbonate (see Section 1.3.8.3 in Chapter one). The phosphate functional groups, with their higher polarity, have a better performance than the carboxylate group.[4] Regardless of the presence of polar functional groups, the exposure of the oxygen atoms in the functional groups is also essential. In a study of $BaSO_4$ inhibition,[5] only phosphonate inhibitors with the anions in a doubly unprotonated state are active for inhibition. The number of functional groups, which are attached to the backbone, is also important as they contribute to the overall surface charge density of the inhibitor molecule. Naka[6] shows that sodium acrylate with only one carboxylic acid moiety has no effect on the crystallization of calcite, while the polymerization of this monomer in the early stage of crystallization can lead to the inhibition of calcite, suggesting the importance of a multidentate interaction between the additive and the growing crystal faces. From the study of HEDP, we know that two geminal phosphate-containing functional groups are sufficient for mineral inhibition. However, this may not be the same case for carboxylate groups, which are less polar. Amjad[7] examined benzoic acids with a variable number of carboxylic acids from 2 to 6 and showed that the more carboxylate groups attached to the benzene-derived ring, the better the inhibition outcome for seeded calcite. Benzene-1,2,3,4,5,6-hexacarboxylic acid proved to have the best inhibition performance, followed by isophthalic acid (benzene-1,3-dicarboxylic acid), indicating that two carboxylic acids situated on an aromatic ring can also cause inhibition effects. The position of the carboxylic acid affects the efficiency of the inhibitor. Isophthalic acid is an effective inhibitor while benzene-1,2-dicarboxylic acid and benzene-1,4-dicarboxylic acid exhibit no inhibition effects. In a further study, Reddy[8] examined the effects of two carboxyl groups attached to a single carbon atom in a ring and showed that they are ineffective as growth-rate inhibitors of calcite. Another study which focuses on the inhibition performance of an aragonite inhibitor showed that pyromellitic acid with four carboxylate groups is an effective inhibitor for calcite but not for aragonite, while benzene hexacarboxylic acid (mellitic acid) with a similar structure to pyromellitic acid is an effective inhibitor for both calcite and aragonite.[9] In the case of the cyclic oligo carboxylates, the inhibition ability increases with the increasing charge density which is consistent with the benzoic acids. It has been shown that 1,2,3,4-cyclopentane tetracarboxylic acid, tetrahydrofuran-2,3,4,5-tetracarboxylic acid, and 1,2,3,4,5,6-cyclohexane hexacarboxylic acid are effective inhibitors for seeded calcite.[8, 10] Volkmer *et al.*[4, 11] has related the observation of different polymorphs to differences in charge density (charge density = the number of carboxylate residues

per unit area) in the monolayer and suggested that, above a critical charge density, the crystallization of calcium carbonate switches to these less stable polymorphs. Moreover, in several cases, the compression of the monolayer to higher surface charge densities does not lead to polymorph switching, but inhibition of the crystallization. Hence, the charge density is a more precise way to describe an inhibitor than just stating the number of the functional groups. Charge density for small molecules, if evaluated as a whole, can be roughly expressed as follows: [(polarity of a single functional group) × (number of the functional groups)] / (size of the backbone). The magnitude of the overall negative charge is decided by the types and number of the functional groups. The functional group should be an effective functional group, which participates in docking. Once the functional groups are confirmed, the size of the backbone becomes important.

For the inhibition of barium sulfate, it has been shown by Black[5] that only phosphonates having at least two phosphonic acid groups linked by a three-atom chain show specific effects on morphology modification. The sulfate and carboxylate equivalents of such molecules were ineffective. Therefore, it is not just the types and the number of the functional groups that are essential for an efficient inhibitor but also the backbone, which determines the charge density and the cooperation mode between the functional groups and the backbone. For better molecular recognition, a balance between rigidity and flexibility in the backbone is essential.[12] Rigidity in the backbone can restrict binding by holding the functional groups in an arrangement that does not match the target-growing surface and can prevent possible cooperation between the backbone and the functional groups. Mann[13] studied a series of α,ω-dicarboxylic acids with the general formula $(CH_2)_n(CO_2H)_2$ on the specificity of morphological modification (carboxylic groups are ionized and n<3). The structures are shown in Figure 4.2 (a-h). The comparison was made based on the ability of molecular recognition on calcite (110), which has Ca-Ca distance close to 4 Å. Mann[13] observed that fumarate with a *trans* stereochemical arrangement has no effect on the calcite morphology, while maleate and malonate with a *cis* geometry can preorganize the two carboxylate groups and enable their binding to two different calcium ions on a crystal face simultaneously. Malonate, furthermore, has better performance in molecular recognition than maleate due to its conformation freedom.
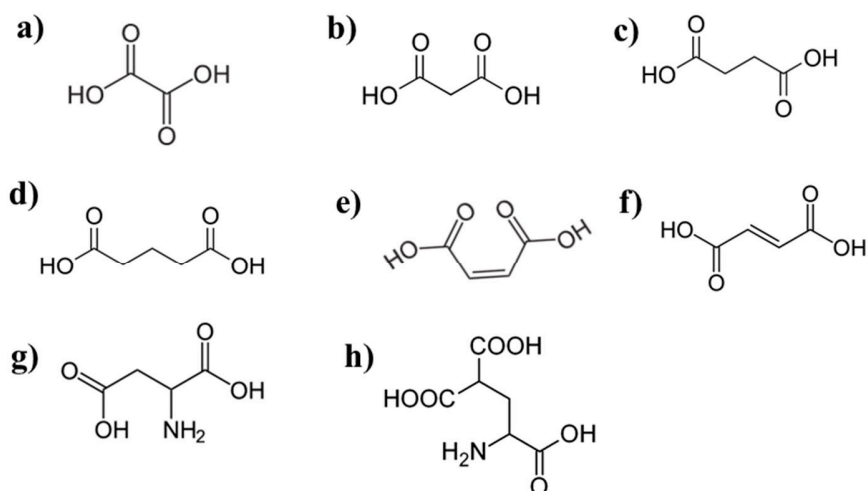
Figure 4.2 The structures of the linear polycarboxylic acids: (a) oxalic acid, (b) malonic acid, (c) succinic acid, (d) glutamic acid, (e)maleic acid, (f) fumaric acid, (g) aspartic acid, (h) γ-carboxyglutamatic acid.

Moreover, additional charge functionalization in the molecule can increase the potency of molecular recognition. For example, both aspartate and γ-carboxyglutamate are more efficient in the stabilization of the prismatic calcite faces than succinate or glutamate, respectively. A similar observation was made for HEDP. The presence of CH_3 and OH in HEDP coupled with the short, one-carbon spacer, restricts the degree of flexibility in the backbone and is helpful in achieving effective metal-ligand interaction.[9] Because the CH_3 group restricts the rotation of the C-P bond, leads to a relatively rigid arrangement, and hence, HEDP tends to be more specific in inhibition than a molecule with flexibility in their structure.[14] It is observed that HEDP is an excellent inhibitor for $CaCO_3$ but not for $CaSO_4$.[14] The presence of OH in HEDP is also believed to enhance the binding affinity and stability.[9] In summary, molecular flexibility allows multiple carboxylate groups to attach to a crystal face,[8] while molecular rigidity, as long as it results in suitable binding preorganization, ensures the correct orientation of functional groups and improves the binding stability.

Mann[13] also observed that the efficiency of dicarboxylate additives is lost at high concentrations where non-specific binding is paramount, which may be because additive-additive interaction becomes increasingly important when the concentration increases.[2] Therefore, the inhibitor molecule should have low self-affinity, as strong additive-additive interactions will cause the additive molecules to self-associate instead of disrupting the crystal packing.[3] It also suggests that

an efficient inhibitor should have the ability to disrupt the crystal packing so that the critical nucleus size will not be reached. Whether this disruptive ability is caused by steric, entropic or energetic effects, however, is still not clear.[3] A summary of the characteristics of an efficient inhibitor is listed in Table 4.1.

Table 4.1 Summary of the structural properties of an efficient inhibitor

General Structure	· larger than the solute[3] · low self-affinity[3]
Functional groups	· high affinity to solute[3] · multiple functional group binding[13] -number of functional groups ≥ 2 -simultaneous bidentate binding · exposed oxygen donor atoms[5]
Backbone	· functional groups linked by 2-5 atoms for cyclic carboxylic acids[15] · balanced rigidity and flexibility[8, 13] · cis-stereochemistry for cyclic carboxylic acids[2] · at least two functional groups are on the same side of the backbone
Side chain	· enhance the preorganization of the functional group · second order short range repulsive and attractive forces

Oligocarboxylates, including linear polycarboxylates, benzene-based oligo carboxylates, and cyclic oligo carboxylates appear to satisfy the requirements of an efficient inhibitor and can potentially be inhibitor replacements for HEDP. Both aromatic oligo-carboxylates and the cyclic aphilic oligo-carboxylates, with four or six carboxylate groups that attached to different carbon atoms in the ring, are excellent inhibitors for seeded calcite.[10, 16] Increasing evidence shows that the surface change density is of foremost importance before the structural and stereochemical requirements. Volkmer[17] shows that a simple charge density correlation exists with calcite inhibition/modification. Considering the molecular flexibility of the cyclic oligo-carboxylates, we would expect that the inhibitors with more conformational freedom may have better inhibition performance than benzene-based oligo carboxylates. Isophthalic acid, with two functional groups, was also found to reduce the growth rate of seeded calcite. Since cyclic polycarboxylic acids have not been systematically studied yet, systems with two or more carboxylate groups will

be investigated. Since the previous studies have been mainly on seeded calcite crystals, whether the inhibitors are efficient in nucleation delay as well as growth inhibition, or whether they are good inhibitors for aragonite in a different system, is unknown. Hence, cyclic polycarboxylic compounds with two or more carboxylate groups will be investigated. The results of testing their inhibition performance in both model and real dishwasher systems will be described in Chapter 6. This chapter reports the synthesis and X-ray crystal structures of a range of newly synthesized calcium compounds with cyclic oligo-carboxylates. Calcium complexes of five different cyclic oligo-carboxylate ligands have been prepared (Figure 4.3). Structural data for calcium compounds of linear polycarboxylic acids[18] and benzene-based polycarboxylates[19] are available in the literature.

CPTCA   **CHTCA**   **CHTTCA**

CHHCA   **CHDAA**
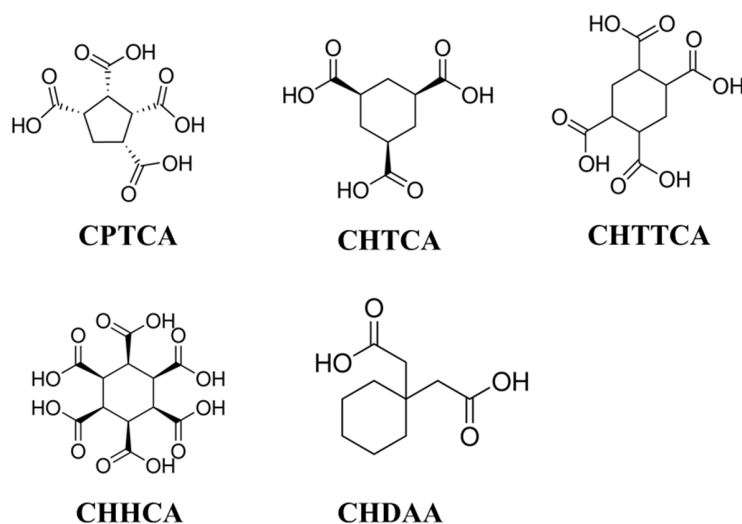
Figure 4.3 Structures of the candidate inhibitors of the cyclic polycarboxylic acid. The full name of the acids as follows: cis,cis,cis,cis-1,2,3,4-cyclopentanetetracarboxylic acid (CPTCA); (1a,3a,5a)-1,3,5,-cyclohexanetricarboxylic acid (CHTCA); cyclohexane-1,2,4,5-tetracarboxylic acid (CHTTCA); 1,2,3,4,5,6-cyclohexanehexacarboxylic acid (CHHCA); 1,1-cyclohexandiacetic acid (CHDAA).

Single crystal structural results on inhibitor calcium complexes may not be representative of the real interaction between the inhibitor and calcium ions or a calcium carbonate crystal surface in the dishwasher system. However, the crystal structures discussed here may be useful for the understanding of the possible structural features for an efficient inhibitor, ligand conformation, functional group spacing and calcium binding mode. Hence, while the analysis of structural data is not an absolute prediction method for an effective inhibitor, it may provide the basis for a discussion of inhibitor selectivity and function.

The structural properties of the cyclic polycarboxylic acids will be compared to HEDP to see if there is any similarity in structure and also in the way they bind to calcium ions, in the hope that understanding the known inhibitor may provide some hints and eventually a common denominator for efficient inhibition. A full assessment of molecular recognition (particularly crystal surface recognition) using molecular simulation is beyond the scope of this project, and we approach the problem in an empirical manner. Detailed complementary computational work inspired by this project is ongoing at P&G. The usefulness of the crystal structures will be assessed in terms of the binding affinity, structural factors and the possible cooperative interaction between the ligand and calcium. The cooperation between the backbone and the functional groups is related to the molecular conformation and the orientation of the functional groups. The discussion of the structural factors will be mainly on the spacing of the functional groups and the donor atoms in the ligand molecule, the geometry of resulting complexes and the possible Ca-Ca distances that the ligand can access. Structural complementarity alone may not be sufficient for molecular recognition, but it does have important implications for the possible molecular recognition between the candidate inhibitors and $CaCO_3$.

4.2 Understanding the Structure of HEDP-Ca

HEDP is an efficient $CaCO_3$ inhibitor and works in the dishwasher system. HEDP fits all the criteria listed in Table 4.1 for being an effective inhibitor. HEDP can offer diverse binding modes to the Ca^{2+} ion, which may be essential for its inhibition efficiency.

The X-ray crystal structure of calcium dihydrogen ethane-1-hydroxy-1,l-diphosphonate dihydrate (HEDP-Ca) has been reported at two different temperatures from two different research groups, both of which are available in the literature (CSD refcode: CAEADP[20] and CAEADP01[21]). Data discussed here is the CAEADP structure that was determind at the room temperature (even though the low-temperature one has a similar structure). Figure 4.4 shows the general eight-fold coordination of a calcium ion bound by oxygen atoms from both the HEDP dianion and three water molecules. The structure is an infinite coordination polymer linked by bridging HEDP dianions and bridging water molecules. The Ca-Op distances (phosphate) range from 2.35 to 2.45 Å and are shorter than the distances from the calcium ion to the water oxygen atoms, Ca-Ow

2.48-2.56 Å. The interaction between the Ca ion and the hydroxyl group (Ca-Oh) is the weakest with a distance of 2.61 Å.

There are three different modes of calcium binding to the phosphonic acid group with three different, yet symmetry-related, HEDP ligands as labeled in Figure 4.4.[22] The first binding mode is a 5-membered chelate ring containing one calcium ion, one hydroxyl group and one phosphonic acid group from the same HEDP ligand(1). The second is a 6-membered chelate ring involving one calcium ion and two phosphonic acid groups from the same HEDP ligand(2). In the third mode, calcium coordinates to one monodentate phosphonic acid group belonging to the HEDP ligand(3). The most strongly bound calcium ion is observed in the six-membered chelate ring (Ca-Op), 2.352 Å; 2.420 Å), followed by the single monodentate phosphonic acid group (Ca-Op, 2.421 Å) and the five-membered chelate ring (Ca-Oh, 2.608 Å; Ca-Op, 2.448 Å). The bidentate binding of two phosphate groups linked by one carbon atom, which also allows the coplanar binding of two phosphates in a similar orientation, may be the preferred adsorption mode of HEDP to growing $CaCO_3$ crystal surface.[7]
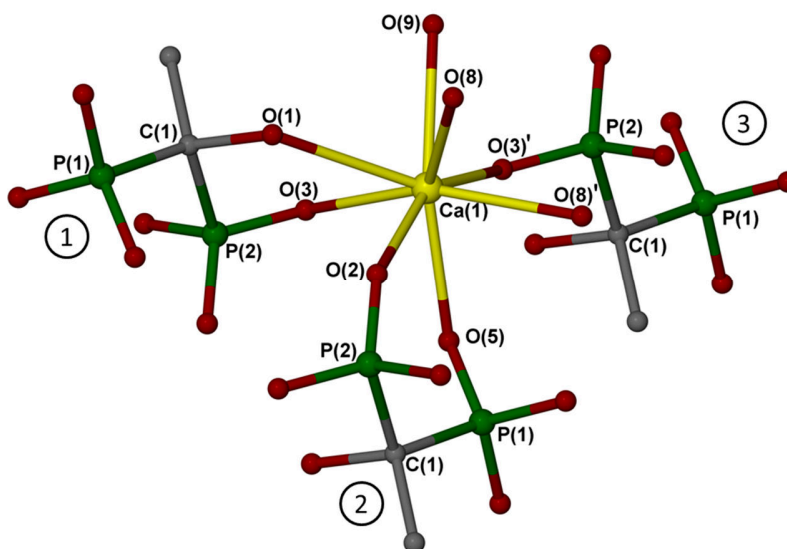
Figure 4.4 The eightfold coordination environment of the Ca ion in HDEP-Ca. Each Ca ion is surrounded by three water molecules, one hydroxyl group from HEDP ligand in 1 and four phosphonate oxygens from three different HEDP ligands, which are labeled as 1, 2 and 3. The HEDP ligand 1 and The HEDP ligand 2 form a 5-membered ring and a 6-membered ring with Ca ion. Replotted from the original data using X-seed.[20]

The software Olex2[23] is used to calculate the Ca-Ca distances that are less than 10 Å of all anhydrous $CaCO_3$ polymorphs and single crystal data of relevant calcium coordination

complexes (see Appendix 4). The smallest Ca-Ca distance for all $CaCO_3$ polymorphs is close to 4 Å. In the six-membered ring of HEDP-Ca, the distances of P1-P2 and O2-O5 between two phosphate groups are 3.074 Å and 2.928 Å, respectively. In the five-membered chelate ring, O1-O3 with a distance of 2.829 Å, is even shorter. The adoption conformation involves one hydroxyl group and one phosphate group can offer another possible binding mode onto the growing faces of the crystal.

In HEDP-Ca, both the phosphonate groups and a hydroxyl group contribute the Ca-Ca bridging. The shortest Ca-Ca distance of 3.825 Å is observed in two symmetry-related phosphonate oxygen atoms. Hence, HEDP can access lattice distances as low as 4 Å or less. Different modes of calcium binding offer different adoption conformations for different $CaCO_3$ polymorphs.

Moreover, it is suggested that the CH_3 group can serve as a hydrophobic and steric side chain to prevent further growth as the CH_3 group can restrict the rotation of the P-C bond. With the methyl group, the cooperativity between the functional group and the backbone is enhanced, while with the hydroxyl group, the possible adoption of a conformation orientated towards to growing faces is increased.

A study on antifreeze proteins (AFP) proposed that van der Waals and hydrophobic interactions play a major role in the inhibition of ice growth, in contrast to earlier proposed inhibition mechanisms that rely almost entirely on a hydrogen bond match between the AFP and ice (lattice matching).[24] Therefore, an efficient inhibitor should be not only attractive enough to bind lattice ions but also, once bound, present a repulsive surface to prevent further incorporation of metal ions onto the crystal surface.

1.1 Syntheses and Structures of Calcium Coordination Compounds

4.2.1 Calcium Complexes with cis,cis,cis,cis-1,2,3,4-Cyclopentanetetracarboxylic Acid

Reactions of Ca(OH)$_2$ or CaO with cis,cis,cis,cis-1,2,3,4-cyclopentanetetracarboxylic Acid (CPTCA) in deionised water (DI) water followed by solvent evaporation after brief sonication to aid dissolution afforded four new crystalline products that were characterised by X-ray

crystallography, $[Ca(\mu\text{-}C_9H_8O_8)(H_2O)_4]_n$ (**1**), $[Ca(H_2O)_8][Ca(C_9H_8O_8)_2(H_2O)_4]\cdot2H_2O$ (**2**), $[Ca(H_2O)_8][Ca(C_9H_8O_8)_2(H_2O)_4]$ (**3**), and $[Ca(C_9H_9O_8)_2(H_2O)_4]$ (**4**). Compound **2** is a hydrate of compound **3** and exhibits two additional lattice water molecules. The product obtained was dependent primarily on the ratio of metal salt and ligand added. Pure products of **1** and **4** can be obtained with metal : ligand stoichiometry 1 : 1, and 1 : 2, respectively. Yields are not relevant to the present structural study and have not been measured, so as not to risk deterioration of the sample by dehydration arising from the removal of the crystalline samples from the mother liquor. However, it is believed that yields are high in all cases, and the crystals isolated represent the bulk product except where discussed. The new complexes **1** and **4** were fully characterized by single crystal X-ray diffraction, X-ray powder diffraction, elemental analysis, IR spectra, and TGA analysis. The new complexes **2** and **3** were side products when crystallization was carried out with a metal : ligand ratio of either 1 : 2 or 2 : 1. Continuing attempts to prepare larger quantities of **2** and **3** have been unsuccessful, possibly because they are less stable phases and transform into **1** or **4** when dried (See Appendix 4). Therefore, only the X-ray structures of the new complexes **2** and **3** are reported without further characterization. See Experimental Section for analytical and crystallographic details for compounds **1**–**4**.

Table 4.2 Calcium complexes of CPTCA-Ca prepared in the present work.

Code	1	2	3	4
Formula	$[Ca(\mu\text{-}C_9H_8O_8)(H_2O)_4]_n$	$[Ca(H_2O)_8]$ $[Ca(C_9H_8O_8)_2(H_2O)_4]\cdot2H_2O$	$[Ca(H_2O)_8]$ $[Ca(C_9H_8O_8)_2(H_2O)_4]$	$[Ca(C_9H_9O_8)_2(H_2O)_4]_n$
Method	slow evaporation	slow evaporation	slow evaporation	slow evaporation
Solvent	DI water	DI water	DI water	DI water
Calcium coordination number	8	8	8	8
Extended structure	1D chain	discrete	discrete	discrete

Table 4.3 Selected bond lengths for complexes 1 – 4

	1			4	
Atom	**Atom**	**Length/Å**	**Atom**	**Atom**	**Length/Å**
O1	C4	1.262(4)	O1	C6	1.244(6)
O2	C4	1.263(3)	O2	C6	1.276(6)
Ca1	O1	2.533(2)	Ca1	O1	2.487(3)
Ca1	O2	2.496(2)	Ca1	O2	2.483(3)
Ca1	O1W	2.438(2)	Ca1	O1W	2.435(4)
Ca1	O2W	2.399(2)	Ca1	O2WA	2.353(11)
			Ca1	O2WB	2.409(6)
	2			**3**	
O1	C6	1.263(9)	O1	C6	1.255(6)
O2	C6	1.278(9)	O2	C6	1.275(6)
O11	C16	1.276(9)	O11	C16	1.285(6)
O12	C16	1.273(9)	O12	C16	1.257(6)
Ca1	O1	2.474(5)	Ca1	O1	2.473(4)
Ca1	O2	2.479(6)	Ca1	O2	2.501(4)
Ca1	O11	2.521(5)	Ca1	O11	2.470(4)
Ca1	O12	2.465(6)	Ca1	O12	2.485(4)
Ca1	O1W	2.440(6)	Ca1	O1W	2.455(4)
Ca1	O2W	2.370(6)	Ca1	O2W	2.361(4)
Ca1	O3W	2.435(6)	Ca1	O3W	2.437(4)
Ca1	O4W	2.452(5)	Ca1	O4W	2.454(4)

The crystal structures of **1–3** contain $C_9H_8O_8^{2-}$, Ca^{2+} ions and water molecules, expect **4**, crystallized out in a more acidic condition, contain $C_9H_9O_8^{1-}$, Ca^{2+} ions and water molecules. Compound **1** features a 1D chain, while **2-4** are discrete molecules. In the eightfold coordination of calcium in all complexes, as shown in Figure 4.5, the calcium ion coordinates to four water molecules and two bidentate carboxylate groups in all structures. The common mode of calcium binding to the carboxylic acid groups involves a four-membered chelate ring containing one calcium ion and one carboxylate group.[25] The carboxylic acid group in CPTCA gives two different C-O distances of 1.22 Å and 1.32 Å.[26] In the presence of the Ca^{2+} ion, the carboxylate group is delocalized. The Ca-O distance in the four-membered chelate ring is around 2.50 Å (Table 1.3)

The nature of the Ca^{2+} ion makes it have a strong affinity for oxygen. The distances from calcium to water oxygen Ca-Ow is in the range of 2.35 - 2.45 Å, which is the normal distance found in other calcium complexes.[25, 27] The distance of the calcium to water oxygen is shorter than that of calcium to the carboxylate oxygen atoms. TGA data shows that loss of water takes place after 60 °C and can occur at temperatures as high as 180 °C, indicating a strong interaction between the Ca ions and water molecules.
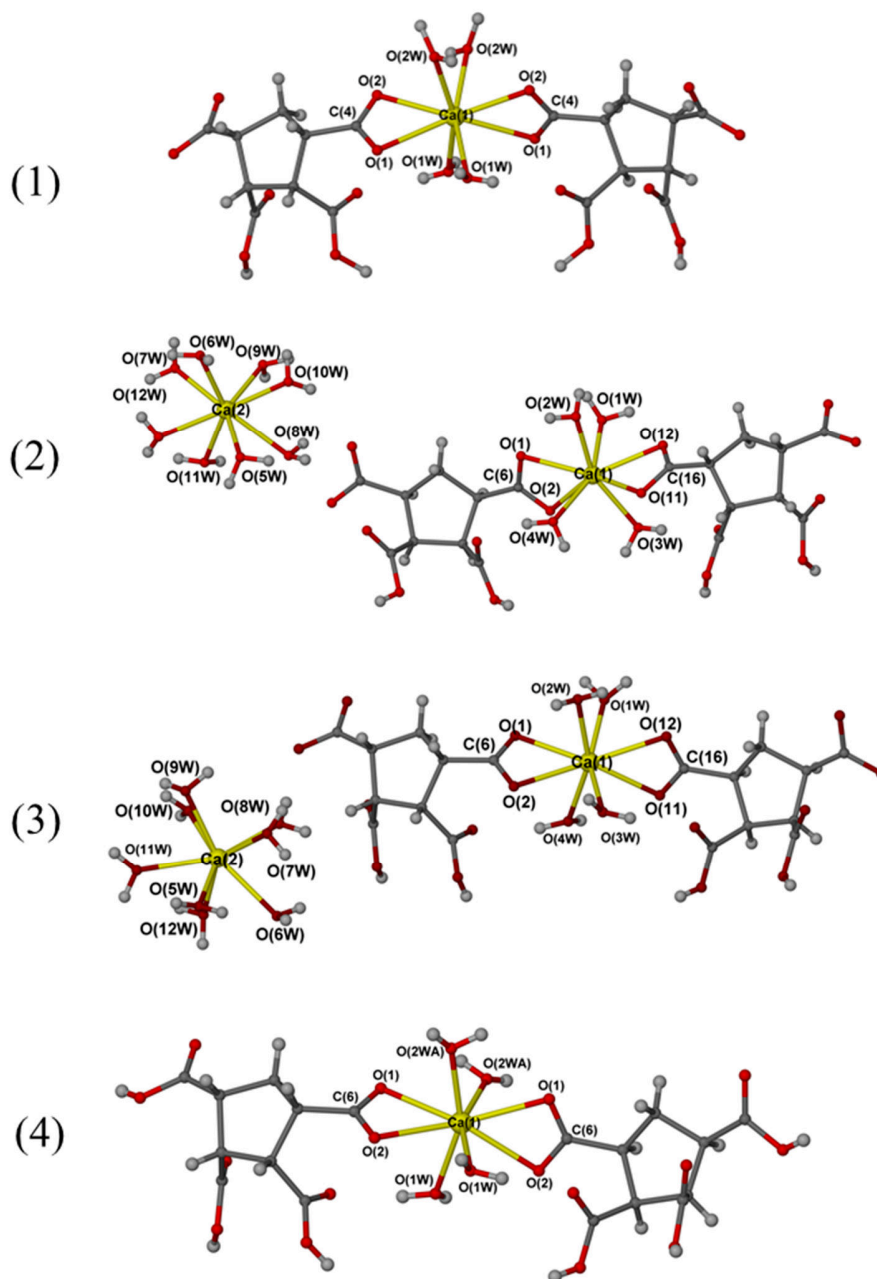
Figure 4.5 The crystal structures of 1-4 are shown from top to bottom in sequence.

The available crystal structures show that the maximum binding sites offered by the CPTCA are no more than 2, and this is only observed in compound **1** (Figure 4.5). However, all crystals were obtained from acidic solution and so the ligands are not fully deprotonated. For the discussion of the Ca-Ca distance and the binding mode, we will take the compound **1** as an example. The extended structure of compound **1** is shown in Figure 4.6 below.
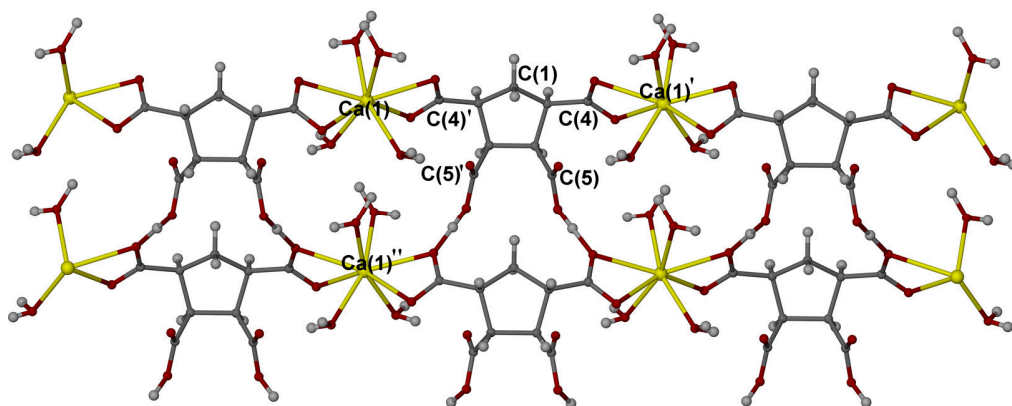
Figure 4.6 The extended structure of compound 1 from the bc face. A hydrogen bond is observed between the carboxylic acid groups. Selected interatomic lengths (Å): C(4)-C(4)' = 3.799 Å, C(5)-C(5)' = 2.690 Å Ca(1)-Ca(1)' =10.203, Ca(1)-Ca(1)" = 5.924.

Unlike Ca-HEDP, there is only one interaction mode observed in the interaction of Ca and CPTCA. One calcium ion binds to one carboxylic acid, forming a 4-membered ring. The delocalization of the carboxylate leads to a much longer Ca-O distance of 2.50 Å. This Ca-O distance is longer than those observed in HEDP-Ca (Ca-O(p)= 2.35 to 2.45 Å), indicating a stronger interaction between Ca and the ligand in Ca-HEDP. Simulation of the docking process of inhibitors to calcium carbonate suggested a substitution of carbonate via carboxylic acid groups.[1, 13] However, whether the docking of the carboxylic acid group to crystal surface is via a monodentate or bidentate mechanism, in reality, is not clear.

A wide range of Ca-Ca distances is also found in Ca-HEDP. The shortest Ca-Ca distances are as low as 3.83 Å. However, the shortest Ca-Ca distance observed in compound **1** is from a dimer, two different 1D chains linked by hydrogen bond and contributes to a Ca(1)-Ca(1)'' distance of 5.924 Å, which is similar to that of aragonite (001) (5.74 Å), while the Ca(1)-Ca(1)' distance which binds to one ligand is 10.203 Å (Table 4.4). The hydrogen bonding is completely intermolecular and occurs between carboxylic acid groups and between water molecules and carboxylic acid groups. It is suggested that interactions through hydrogen bonding between adjacent carboxyl groups on cyclic structures may also influence carboxyl group mobility and adsorption strength on crystal surfaces. Formation of carboxylic acid dimers or trimers (by hydrogen bonding) may also contribute to the growth rate inhibition.[8] However, in our case, at the pH =10, the CPTCA should be all deprotonated. Binding to crystal surface via dimers of CPTCA may not be possible.

The distance between carboxyl groups across a cyclopentane ring is around 1 to 1.5 times of the distance between two phosphate groups in HEDP. Table 4.4 demonstrates that the two neighboring carboxylate groups (C4-C4' and C5-C5') in CPTCA, the later (attached to C5-C5') two carboxylic acid groups have similar distances to those observed in HEDP-Ca (numbers in bold). The distance between the two carboxylate groups in term of O-O distance can range from 3.04 to 7.04 Å, which means CPTCA can access all of the crystal lattices of $CaCO_3$. The CPTCA can adsorb onto growing surfaces vertically or horizontally (Figure 4.7). In a study of the inhibition effectiveness of benzoic acids on seeded calcite, it suggested that the horizontal adsorption is more thermodynamically preferred.[7] If CPTCA approaches a growing surface in an orientation that parallels to the crystal surface, then the docking of CPTCA onto crystal surface will be four carboxylate groups other two carboxylic acid groups. The cyclopentane ring itself can act as a hydrophobic and steric blocking group to prevent further growth. However, the simultaneous docking of four carboxyl groups may result in a rigid conformation in contrast to the more flexible HEDP, which has two polar phosphonate groups. The increase in rigidity may have two consequences: increased specificity of inhibition[28] and ineffectiveness in inhibition.[2] Based on these structural considerations we can suggest that CPTCA may not work as efficiently as an inhibitor as HEDP, though it may exert inhibition ability based on its overall change density.
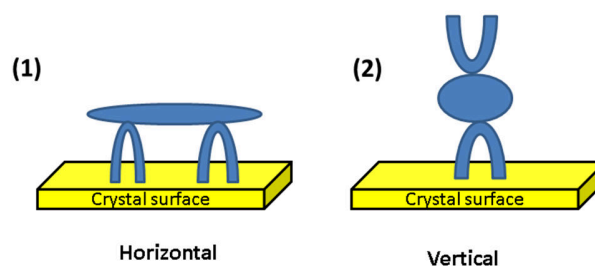
Figure 4.7 Two possible adsorption geometries of CPTCA on to crystal surfaces.

Table 4.4 The comparison of the binding mode of two adjacent functional groups to calcium ion (s) between the HEDP-Ca and the compound 1.

			6-memberred ring in HEDP-Ca (Å)			4-memberred ring in compound 1 (Å)
Ca-O	Ca(1)	O(2)	2.35	Ca(1)	O(1)	2.533(2)
	Ca(1)	O(5)	2.42	Ca(1)	O(2)	2.496(2)
2 neighbouring functional groups	**P(1)**	**P(2)**	**3.074**	C(4)	C(4)'	3.799
	O(2)	**O(5)**	**2.928**	O(2)/O1	O(2)'/O1'	5.486/7.044
				C(5)	**C(5)'**	**2.690**
				O(3)/O4	**O(3)'/O4'**	**3.037/3.146**

4.2.2 Calcium Complexes of 1α,3α,5α-Cyclohexanetricarboxylic acid

Dissolving 1α,3α,5α-cyclohexanetricarboxylic acid (CHTCA) in different solvents, and layering this solution on top of an aqueous solution of $Ca(OH)_2$ and allowing evaporation at room temperature resulted in two new complexes $[Ca_3(C_9H_9O_6)_2(H_2O)_4]\cdot 3H_2O$ (**5**) and $[Ca(C_9H_{10}O_6)(H_2O)_2]\cdot H_2O$ (**6**) which were characterized by X-ray crystallography. The product obtained was dependent primarily on the ratio of metal salt and ligand added and the solvent used. Pure products of **5** and **6** can be obtained with metal : ligand ratio of 1 : 2, and 1 : 1, respectively. Complex **5** was obtained by using either methanol or ethanol (**6** is also observed as the minor phase when using ethanol as solvent, see Appendix 4). **6** was formed when using acetone or ethyl acetate as the solvent. See Experimental Section for analytical and crystallographic details for compounds **5** and **6**.

Table 4.5 Crystallization of calcium complexes 5 and 6 with CHTCA

Code	5	6
Formula	$[Ca_3(C_9H_9O_6)_2(H_2O)_4]\cdot 3H_2O$	$[Ca(C_9H_{10}O_6)(H_2O)_2]\cdot H_2O$
Method	Liquid-liquid diffusion	Liquid-liquid diffusion
Solvent	methanol or ethanol	acetone or ethyl acetate
Calcium coordination number	8 (Ca1) and 6 (Ca2)	7 (Ca1) and 8 (Ca2)
Extended structure	3D	3D

The crystal structures of **5** and **6** contain an infinite array of CHTCA groups, Ca^{2+} ions and water molecules linked together by hydrogen bonding and calcium coordination of the oxygen atoms from both CPTCA and water molecules, forming a 3D inorganic Ca-O-Ca framework. The calcium ions in both compounds **5** and **6** have two different coordination environments. In compound **5** (Figure 4.9), Ca1 has eight oxygen atoms in its primary coordination sphere: seven carboxylate oxygen atoms (O1, O2, O3, O3', O4, O5, O6) from four individual CHTCA ligands and one water ligand (O1w). Ca2 has sixfold coordination connected with four carboxylate oxygen atoms (O1, O1', O4, and O4') from four individual monodentate CHTCA ligands and 2 water ligands (O2w and O2w').
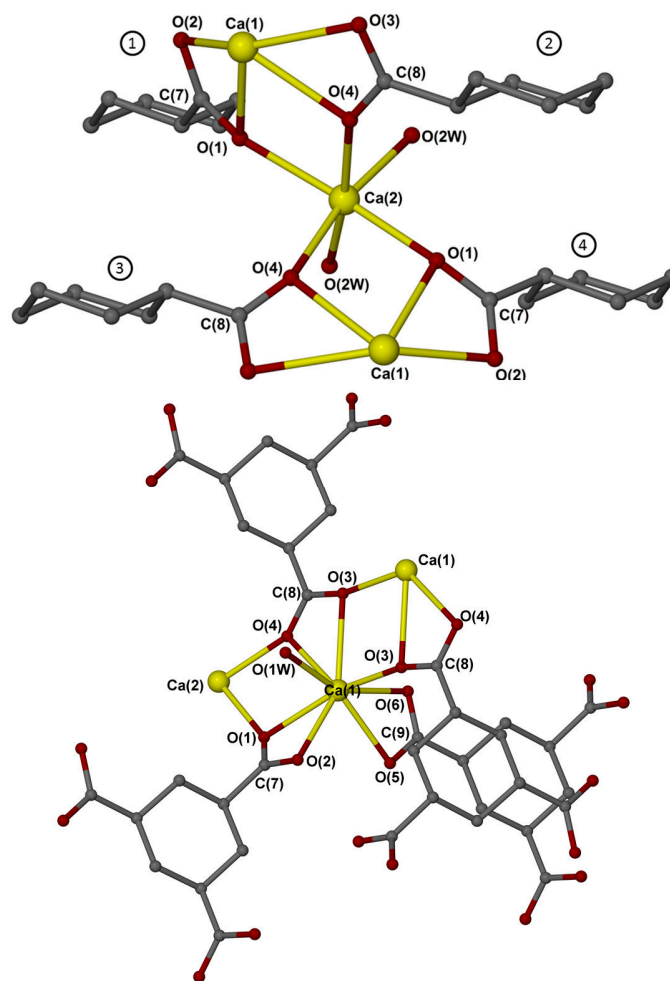
Figure 4.8 The crystal structure of 5 showing the sevenfold coordination of calcium. The attached table shows the corresponding bond length.

Bond Lengths for calcium coordination in 5						
Eightfold coordination for Ca1				Sixfold coordination for Ca2		
Atom	Atom	Length/Å		Atom	Atom	Length/Å
Ca1	O1	2.481(2)		Ca2	O1	2.315(2)
Ca1	O2	2.404(2)		Ca2	O1[4]	2.315(2)
Ca1	O3	2.315(2)		Ca2	O4[2]	2.295(2)
Ca1	O3	2.613(2)		Ca2[6]	O4	2.295(2)
Ca1	O4	2.460(2)		Ca2	O2W	2.341(3)
Ca1	O5	2.503(3)		Ca2	O2W[4]	2.341(3)
Ca1	O6	2.491(3)				
Ca1	O1W	2.439(3)				

In compound **6** (Figure 4.9), Ca1 is seven coordinated with 5 oxygen atoms from four individual CHTCA ligands and two different water ligands (O1w and O2w). Ca2 has eightfold coordination, six carboxylate oxygen atoms (O1, O2, O3, O3', O4, and O9) from four different CHTCA ligands and two different water ligands (O3w and O4w). The distances from calcium to the water oxygen (Ca-Ow) are similar in **5** (2.34 Å-2.50 Å) and **6** (2.38 Å-2.45 Å), which is in the normal range of distances found in other calcium complexes.[25, 27] TGA data shows the loss of free water and coordinated water takes place after 30 ^{o}C and 150 ^{o}C, respectively. The loss of coordinated water can be up to 300 ^{o}C which indicates a strong interaction between the Ca ions and the water molecules. The temperature for the loss of the coordinated water is quite high compared to other compounds. This may be due to the number of water molecules attached to CHTCA ligand in **5** is more than other compounds, which is three free water and four coordinated water. In **5** and **6**, one calcium ion binds to four different CHTCA molecules, and two of the CHTCA molecules are linked together by one calcium ion and form a 2D layer. The two 2D layers are then connected by the other calcium ion(s), forming a 3D structure.
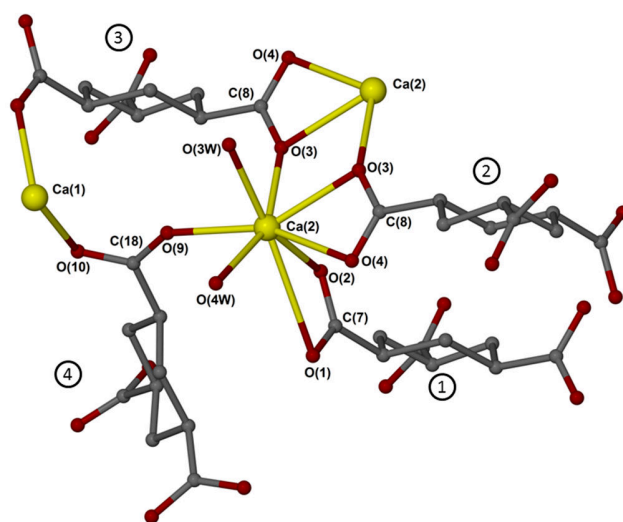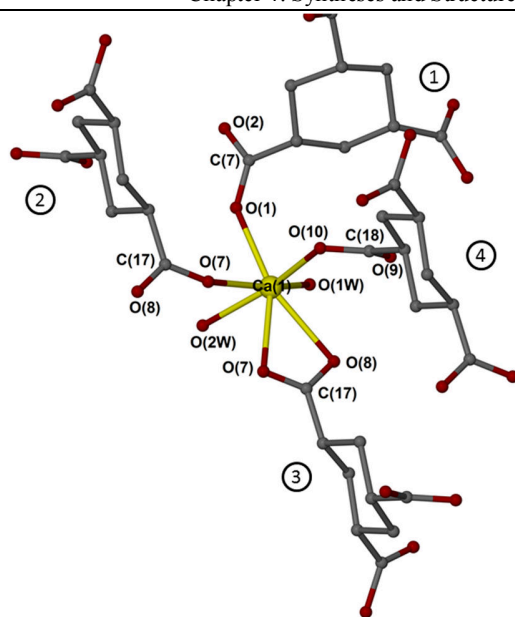
Figure 4.9 The crystal structure of 6 showing the sevenfold coordination of calcium.

Bond Lengths for calcium coordination in 6						
Sevenfold coordination for Ca1				Eightfold coordination for Ca2		
Ca1	O1	2.384(3)		Ca2	O1[4]	3.084(3)
Ca1	O7[1]	2.361(3)		Ca2	O2[4]	2.412(3)
Ca1	O7	2.486(3)		Ca2	O3	2.397(3)
Ca1	O8	2.489(3)		Ca2	O3'	2.461(3)
Ca1	O10[2]	2.395(3)		Ca2	O4	2.498(3)
Ca1	O1W	2.496(3)		Ca2	O9	2.353(3)
Ca1	O2W	2.387(3)		Ca2	O3W	2.385(3)
				Ca2	O4W	2.456(3)

All calcium coordination in both **5** and **6** involve four different individual ligands. The carboxylate group can coordinate monodentate or bidentate to calcium. In the 4-membered ring, one carboxylate group is delocalised and binds bidentate to one Ca ion. In this scenario, the Ca-O distances are in the range of 2.40 to 3.08 Å. The other mode has one calcium ion coordinating to one monodentate carboxylic acid. In Ca1 of **5**, each monodentate carboxylic acid is from each CHTCA. The Ca-O distance is smaller than 2.40 Å. The most strongly bound calcium in **5** is Ca2 (Ca2-O1, 2.30 Å). The weakest bound calcium is observed in the 4-membered ring in Ca2 in **6** **(**Ca2-O1 3.08 Å). The interaction strength between the monodentate carboxylate to calcium is similar to that of Ca-O distance in the 6-membered ring in HEDP-Ca.
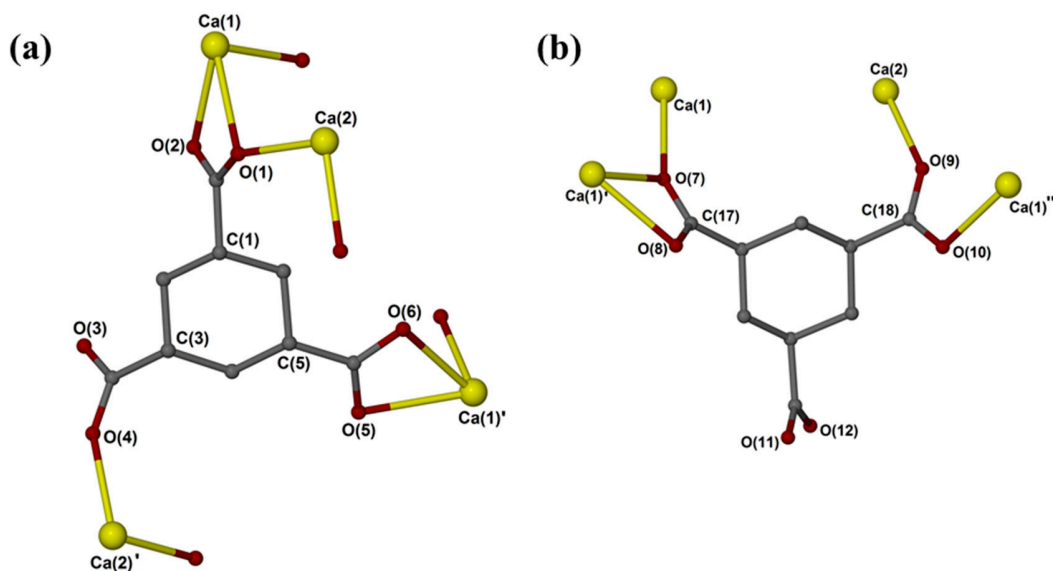
Figure 4.10 The binding of ligand 2 to the calcium ions in 5 (a) and 6 (b). Selected interatomic distances in 5 (Å): Ca(1)-Ca(2)= 3.836, Ca(1)-Ca(1)' = 9.492, Ca(1)'-Ca(2)' = 8.044. Selected bond lengths in 6 (Å): Ca(1)-Ca(2)= 5.095, Ca(1)'-Ca(1)''= 9.377, Ca(1)-Ca(1)'=4.001, Ca(1)''-Ca(2)= 5.192.

All three carboxylate groups in CHTCA participate in the calcium binding (Figure 4.10a). The strength of the Ca-O bond is as strong as that observed in the 6-membered ring in HEDP-Ca (Figure 4.6). However, docking to a surface in a coplanar arrangement may not be possible with CHTCA as the extra carboxyl acid moiety may not allow this arrangement. Adsorption in an orthogonal arrangement through two carboxylate groups seems more sensible. However, the distance between two adjacent carboxylate groups is much larger than that of the two phosphonic acid groups in HEDP-Ca. Taking **6** for example (Figure 4.10b), the distance between carboxyl groups in CHTC-Ca is about 1.5 times larger than that of two phosphonic acid groups in HEDP-

Ca. The minimum Ca-Ca distances between two neighboring functional groups observed in **5**, and **6** are 8.04 Å and 5.10 Å, respectively. This fact indicates that while CHTCA may not be able to access lattices with a Ca-Ca distance smaller than 5 Å, at least HEDP can access a wider range Ca-Ca distance than CHTCA. There are Ca-Ca distances smaller than 4 Å observed in **5** and **6**, but they are two calcium ions which coordinate in a monodentate fashion to one oxygen atom in carboxylate group. This may not satisfy the criterion of multiple carboxylic groups interacting with the crystal surface. Therefore, CHTCA may not work as efficiently as ligand **1**.

Table 4.6 The comparison between HEDP-Ca and compound 6 (Figure 4.10b)

	6-membered ring in HEDP-Ca (Å)			Two carboxylate groups in **6** (Å)		
Ca-O	Ca(1)	O(2)	2.35	Ca(1)	O(7)	2.384
	Ca(1)	O(5)	2.42	Ca(2)	O(9)	2.398
Two neighbouring functional groups	**P(1)**	**P(2)**	**3.074**	**C(18)**	**C(17)**	**4.957**
	O(2)	**O(5)**	**2.928**	**O(7)**	**O(9)**	**5.957**

4.2.3 Calcium Complexes of 1,2,4,5-Cyclohexanetetracarboxylic acid

Reactions of $Ca(OH)_2$ with 1,2,4,5-cyclohexane tetracarboxylic acid (CHTTCA) in DI water followed by solvent evaporation after brief sonication to aid dissolution produced a mixture of two new complexes $[Ca_2(C_{10}H_8O_8)(H_2O)_7] \cdot 2H_2O$ (**7**) and $[Ca(C_{10}H_{10}O_8)(H_2O)_6] \cdot 1H_2O$ (**8**) which were characterized by X-ray crystallography. Complex **7** was obtained as the dominant phase while **8** was a minor phase. A pure sample of **7** and a new crystal form $[Ca(C_{10}H_{12}O_8)_2(H_2O)_4]_n$ (**9**) can be obtained by using a solvent layering method. The product obtained was dependent primarily on the ratio of metal salt to ligand added, and the solvent used. Pure products of **7** can be obtained in ethanol with metal : ligand ratio of 1:2 or 1:1. Product **9** was obtained using methanol with metal : ligand ratio of 1:1.5. See Experimental Section for analytical and crystallographic details for compounds **7 – 9**.

The X-ray crystallographic analysis performed on **7 – 9** revealed that when an aqueous solution containing both trans- and cis-isomers of CHTTCA was used, the Ca ions only crystallized with the all-cis isomer of CHTTCA (Figure 4.11). This phenomenon may be due to the trans- and cis-isomers of CHTTCA having different affinities for calcium ions.[29] It seems that the calcium ions

are capable of isolating the all-cis-isomer of CHTTCA and leaving the other isomer in solution when using a commercially available mixture of isomers.

Table 4.7 Calcium complexes 7-9 of CHTTCA

Code	7	8	9
Formula	$[Ca_2(C_{10}H_8O_8)(H_2O)_7] \cdot 2H_2O$	$[Ca(C_{10}H_{10}O_8)(H_2O)_6] \cdot 1H_2O$	$[Ca(C_{10}H_{12}O_8)_2(H_2O)_4]_n$
Method	slow evaporation (SE) L-L diffusion (LL)	slow evaporation	L-L diffusion
Solvent	DI water for SE Ethanol for LL	DI water	methanol
Calcium coordination number	7 (Ca1) / 8(Ca2)	7	7
Extended structure	3D	Discrete molecules	2D

The crystal structures of **7, 8** and **9** all contain an infinite array of CHTTCA groups, Ca^{2+} ions, and water molecules linked together by hydrogen bonding and oxygen atoms from both CHTTCA and water. Compound **7** features a 3D inorganic framework. Compound **8** and **9** form 2D layer structures. The crystal structures of **7** to **9** are shown in Figure 4.11. The maximum available binding of CHTTCA is observed in compound **7**. CHTTCA binds to two calcium ions in compound **7** and one calcium ion in compound **8**, while in compound **9**, two ligands share one calcium ion. The calcium ions in compound **7** have two different coordination numbers and compounds **8** and **9** have the same coordination number. In the following discussion, compound **7** will be taken as the main model for the understanding of Ca-O distance, binding mode, and Ca-Ca distance.
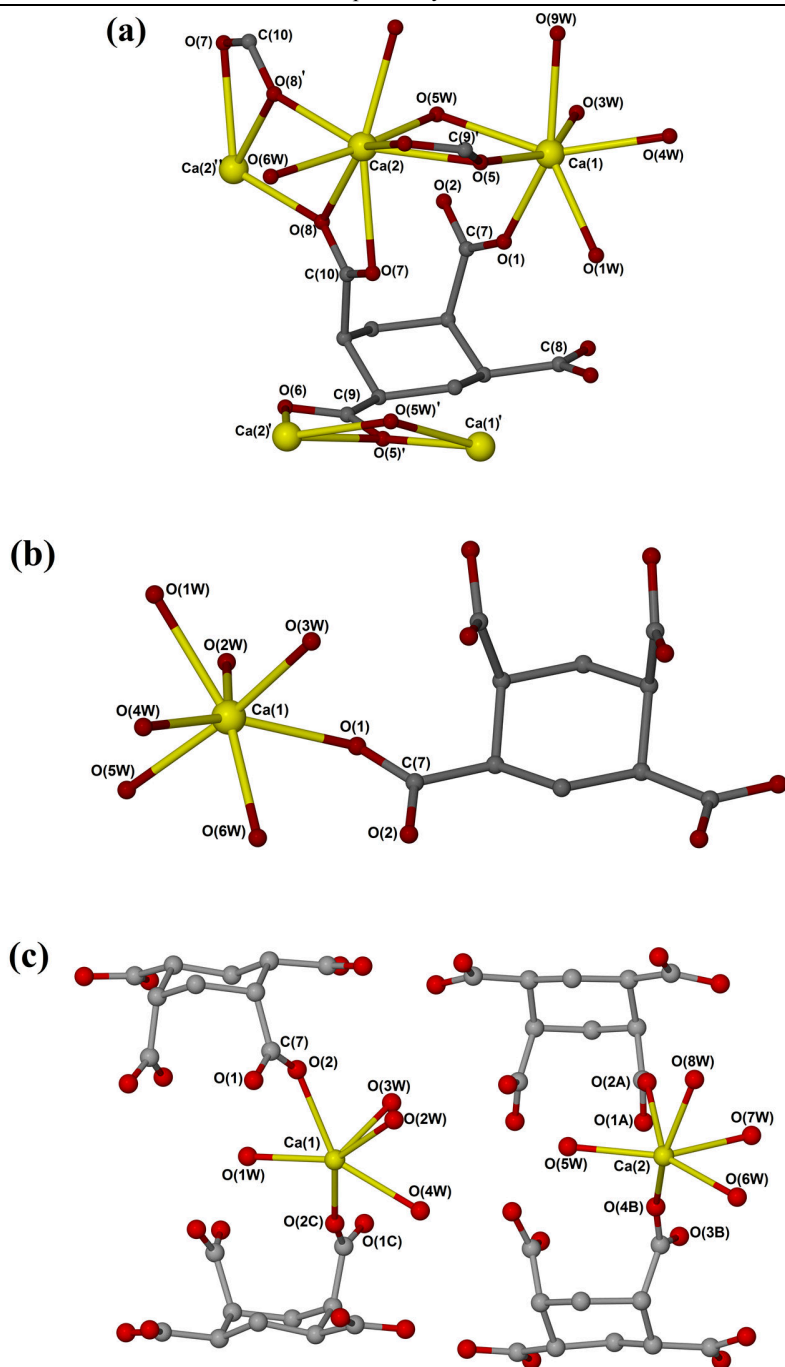
Figure 4.11 Crystal structures of 7, 8 and 9: (a) Selected bond lengths in 7 (Å): Ca(1)-Ca(2) = 3.897, Ca(1)-Ca(2)'= 6.704, Ca(1)-Ca(1)' = 6.704, Ca(2)-Ca(2)'= 6.704, Ca(2)-Ca(2)' = 6.444, Ca(2)-Ca(1)'= 6.729, Ca(2)-Ca(2)''= 3.987; Ca(1)-O(1)= 2.343(2), Ca(1)-O(5)= 2.283(2), Ca(1)-O(1W)= 2.376(2), Ca(1)-O(3W)= 2.347(2), Ca(1)-O(4W)= 2.439(2), Ca(1)-O(5W)= 2.539(2), Ca(1)-O(9W)= 2.471(2); Ca(2)-O(5)= 2.509(2), Ca(2)-O(6)= 2.470(2), Ca(2)-O(7)= 2.551(8), Ca(2)-O(8)= 2.525(2), Ca(2)-O(8)'= 2.350(2), Ca(2)-O(5W)= 2.454(2), Ca(2)-O(6W)= 2.383(2), Ca(2)-O(8W)= 2.520(2). (b) Selected bond lengths in 8 (Å): Ca(1)-O(1)= 2.4252(11). (c) Selected bond lengths in 9 (Å): Ca(1)-O(2)= 2.457(7), Ca(1)-O(2C)= 2.412(6), Ca(1)-O(4C)= 2.408(6); Ca(2)-O(2A)= 2.446(7), Ca(2)-O(2B)= 2.383(6), Ca(4B)-O(2A)= 2.409(6). The hydrogen bond is omitted for clarity.

In compound **7** (Figure 4.11a), Ca1 has seven oxygen atoms in its primary coordination sphere: two carboxylate oxygen atoms (O1, O5) from two individual CHTTCA ligands and five water ligands (O1w, O3w, O4w, O5w, O9w). Ca1 shares O5 and O5w with Ca2. Ca2 has eightfold coordination connected with five carboxylate oxygen atoms (O5, O6, O7, O8 and O8') from three individual CHTTCA ligands and three water ligands (O5w, O6w, and O8w). In compound **8** (Figure 4.11b), the calcium ion has sevenfold coordination with only one carboxylate oxygen atom and six different water ligands. In compound **9** (Figure 4.11c), calcium has seven oxygen atoms in its primary coordination sphere: three carboxylate oxygen atoms from three individual CHTTCA ligands and four aqua ligands. The high water affinity of Ca^{2+} is evident by coordination with CHTTCA in terms of the number of coordinated water molecules. The distance from calcium to the water oxygen, Ca-Ow, is similar in **7** (2.35 - 2.54 Å), **8** (2.38 Å-2.46 Å) and **9** (2.33 Å - 2.47 Å), which is within the normal range of distances found in this report and other calcium complexes.[25, 27] TGA data shows the loss of the 7 coordinated water molecules requires heating up to 250 °C (**7** and **8**), and for the loss of 4 coordinated water molecules (**9**) 175 °C is sufficient.

The strength of interaction between the calcium ion and the carboxylate group is in the range of 2.28 - 2.52 Å. The strongest and weakest Ca-O bonds are observed in compound **7**. We will take **7** as an example to describe the interaction between the calcium ion and CHTTCA, as there are no multiple interactions are observed in **8** and **9**. There are two different modes of calcium binding to the carboxylate groups in compound **7**: the most commonly observed is a 4-membered chelate ring and monodentate binding of carboxylate to calcium.

Table 4.8 shows that distances of the two neighboring carboxylate groups and the two meta carboxylate groups in CHTTCA. The two neighboring carboxylate groups (attached to C9 and C10) have similar distances to those observed in HEDP-Ca (numbers in bold), which means that CHTTCA can access all of the $CaCO_3$ crystal lattices. However, the orientation of these two carboxylate groups is different and maybe not energetically favorable if the simultaneous binding is the docking mode of inhibitors to the mineral surface. In this case, the perpendicular binding of CHTTCA in a coplanar arrangement to the mineral surface should be via two meta carboxylate groups that attached to C7 and C10. The O-O distance in these two functional groups is slightly longer than that of two phosphate groups. The simultaneous binding of these two meta

carboxylate groups contributes to a Ca-Ca distance of 3.90 Å, which is comparable to the smallest Ca-Ca distance observed in $CaCO_3$ polymorphs. The carboxylate group attached to C7 binds to Ca1 via a 4-membered chelation ring, and the other carboxylate group attached to C10 monodentate binds to Ca2. In the 4-membered chelate ring, the delocalised carboxylate groups contribute longer Ca-O distances, which range from 2.51 to 2.55 Å and are longer than that in HEDP-Ca. The interaction strength between the monodentate carboxylate to calcium is similar to that of Ca-O distance in the 6-membered ring in HEDP-Ca (Table 4.8).

If the inhibitor docks to surface in a coplanar orientation, the cyclohexane ring distributes charge density as that of cyclopentane ring and the docking does not require binding from two adjacent functional groups, so CHTTCA should work as efficiently as CPTCA.

Table 4.8 The comparison of the binding of two functional groups to the calcium ion(s) between the HEDP-Ca and the compound 7.

	6-memberred ring in HEDP-Ca (Å)			Bidentate binding in **7** (Å)		
Ca-O	Ca(1)	O(2)	2.35	Ca(1)	O(1)	2.343
	Ca(1)	O(5)	2.42	Ca(2)	O(7)/ O(8)	2.551/2.525
2 neighbouring functional groups	P(1)	P(2)	**3.074**	C(7)	C(10)	3.101
	O(2)	O(5)	**2.928**	O(1)	O(7)/ O(8)	3.398/3.689
				C(9)	C(10)	**3.035**
				O(6)	O(7)	**3.276**

4.2.4 Calcium Complexes of Cyclohexane-1,2,3,4,5,6-hexacarboxylic acid

Dissolving cyclohexane-1,2,3,4,5,6-hexacarboxylic acid (CHHCA) in butan-1-ol laying this solution onto a solution of $Ca(OH)_2$ and allowing evaporation at room temperature, afforded a new complex $[Ca(C_{12}H_{11}O_6)_2(H_2O)_4]\cdot1.25H_2O$ (**10**) characterized by X-ray crystallography. The sample of **10** was obtained with metal : ligand ratio of 1 : 1. Continuing attempts to prepare more crystals of **10** have been unsuccessful. The size of the crystals of **10** was too small for study using a conventional laboratory radiation source. Therefore, the complex was characterized using instrument I19 at the Diamond synchrotron. A side product, $[C_{12}H_{12}O_{12}]\cdot H_2O$ (**11**), was also obtained as a hydrated form of the free acid by using methanol with metal : ligand ratio of 1 : 1. This is the third crystal structure of the free acid form as the other two crystal forms for CHHCA with three and four coordinated water molecules have been previously reported.[30] No difference in CHHCA conformation is observed.

The crystal structure of **10** contains an infinite array of $C_{12}H_{11}O_{12}$, Ca ions and water molecules, all linked together by hydrogen bonding that ultimately forms a discrete molecule. The crystal contains a fair amount of severely disordered solvent; it was not possible to fully resolve this disorder. In the ninefold coordination of calcium, as shown in Figure 4.12, the calcium ion coordinates to five water molecules and two monodentate carboxylate groups and one bidentate carboxylate. CHHCA uses its two neighboring carboxylate groups to coordinate one calcium ion and with the other neighboring carboxylate group connecting to the other ligand compound via hydrogen bond. The distance of the calcium to water oxygen (Ca-Ow) ranges from 2.23 to 2.60 Å, showing different interaction strengths of water molecules to the calcium ion.
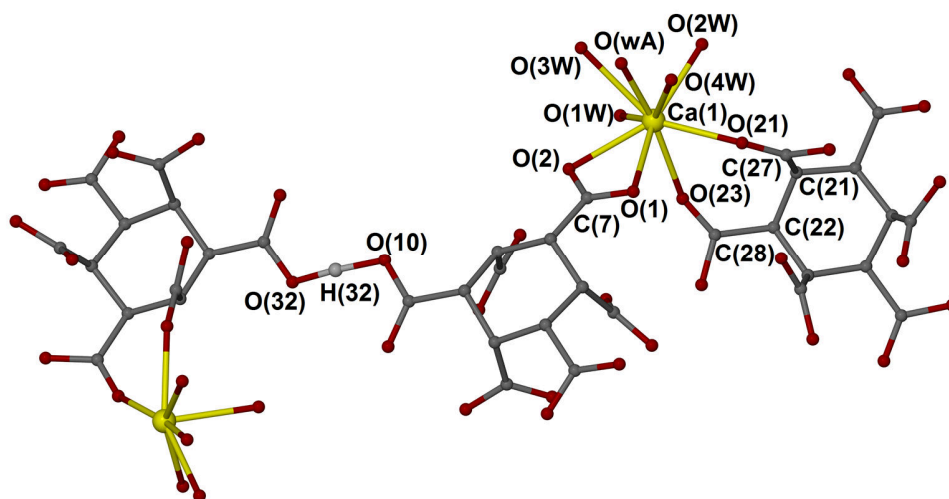
Figure 4.12 The crystal structure of 10 shows the sevenfold coordination of calcium. Selected bond lengths (Å) for ninefold coordination: Ca(1)-O(21) = 2.373(2), Ca(1)-O(23), Ca(1)-O(1W) = 2.386(2), Ca(1)-O(2W) = 2.404(3), Ca(1)-O(3W) = 2.603(3), Ca(1)-O(4W) = 2.420(3), Ca(1)-O(WA) = 2.234(10); Selected bond lengths (Å) for 7-membered ring: Ca(1)-O(21) = 2.373(2), Ca(1)-O(23) = 2.413(2), O(21)-C(27) =1.218(3), O(23)-C(28) =1.215(3), C(21)-C(27) = 1.521(3), C(22)-C(28) =1.518(3), C(21)-C(22) =1.544(3); Selected bond lengths (Å) for 4-memberred ring: : Ca(1)-O(1) = 2.500(2), Ca(1)-O(2) = 2.4550(19), O(1)-C(7) =1.242(3), O(2)-C(7) =1.277(3); Selected bond lengths (Å) for hydrogen bond: O(32)-H(32) =2.480(3).

In compound **10**, there are two modes of calcium binding to the carboxylate group. One is the most commonly observed mode, the 4-membered chelate ring, which involves one calcium ion and one carboxylate group. The other is a seven-membered chelate ring involves one calcium ion and two monocarboxylate groups. Figure 4.12 shows the ninefold coordination of calcium including the 4-membered chelate ring and the 7-membered chelate ring. In free cyclohexane-1,2,3,4,5,6-hexacarboxylic acid (compound **11** and CHXHCA in the CSD[30a]) the carboxylate

group gives two different C-O distances of 1.21 Å and 1.31 Å, which is similar to other carboxylic acids. In the presence of Ca^{2+} ion in the 4-membered ring, the carboxylate group is deprotonated and delocalized, giving Ca-O distances of 2.45 Å and 2.50 Å, which are in the normal range of Ca-O distances observed in other 4-membered rings in the other synthesized compounds. In the 7-membered ring, the carboxylate group is partly deprotonated. The interaction between the Ca ion and the oxygen atom from the carboxylate group is stronger than that in the 4-membered ring Ca(1)-O(21) = 2.37 Å, Ca(1)-O(23) = 2.41Å). The strength of the Ca-O is as strong as that observed in Ca-O distance in the 6-membered ring in HEDP-Ca (Table 4.9). Moreover, the distance of two oxygen atoms, which connect to the corresponding functional groups, is similar (shaded part in Table 4.9). This indicates that the affinity of the functional groups to Ca ions is similar between the carboxylate and phosphonic acid groups when binding in a monodentate fashion. CHHCA also has the potential to access the lattice with smaller Ca-Ca distances similar to HEDP. Among all the new structures, two neighboring carboxylate groups simultaneously binding to one calcium ion is only observed in CHHCA. Figure 4.12 shows that CHHCA not only binds to the calcium ion but also connects to the other CHHCA molecule via a strong hydrogen bond.

Table 4.9 shows that the simultaneous binding of two carboxylic acid groups can access all of the crystal planes which HEDP can access. However, if CHHCA approaches a crystal or cluster surface in a coplanar arrangement, then the docking of CHHCA should also take the other four carboxylate groups into consideration. The cyclohexane ring itself can act as a hydrophobic and steric group preventing further growth. However, the simultaneous docking of 6 carboxyl groups may be not as feasible as the simultaneous interaction of the phosphate groups observed in HEDP. CHHCA is similar to CPTCA, so it may work but may be not as efficient as that of HEDP.

Table 4.9 The comparison of the binding of two neighboring functional groups to one calcium ion between HEDP-Ca and compound 10.

	6-memberred ring in HEDP-Ca (Å)			7-memberred ring in compound **10 (Å)**		
Ca-O	Ca(1)	O(2)	2.35	Ca(1)	O(21)	2.37
	Ca(1)	O(5)	2.42	Ca(1)	O(23)	2.41
2 neighbouring functional groups	**P(1)**	**P(2)**	**3.074**	**C(21)**	**C(22)**	**3.081**
	O(2)	**O(5)**	**2.928**	**O(21)**	**O(23)**	**2.768**

4.2.5 Calcium Complexes of 1,1-Cyclohexandiacetic acid

The reaction of calcium hydroxide with 1,1-cyclohexandiacetic acid (CHDCA) in a 1:2 ratio in DI water followed by solvent evaporation after brief sonication to aid dissolution, gave $[Ca(C_{10}H_{15}O_4)_2(H_2O)_2]_n$ (**12**) at room temperature. Yields have not been measured; however, the experimental PXRD pattern of compound **12** corresponds well with the simulated pattern from the single crystal data, indicating the phase purity of the synthesized compound (see Appendix 4). The new complex **12** was fully characterized by single crystal X-ray diffraction, X-ray powder diffraction, satisfactory elemental analysis, IR spectroscopy, and TGA analysis. See Experimental Section for analytical and crystallographic details for **12**.
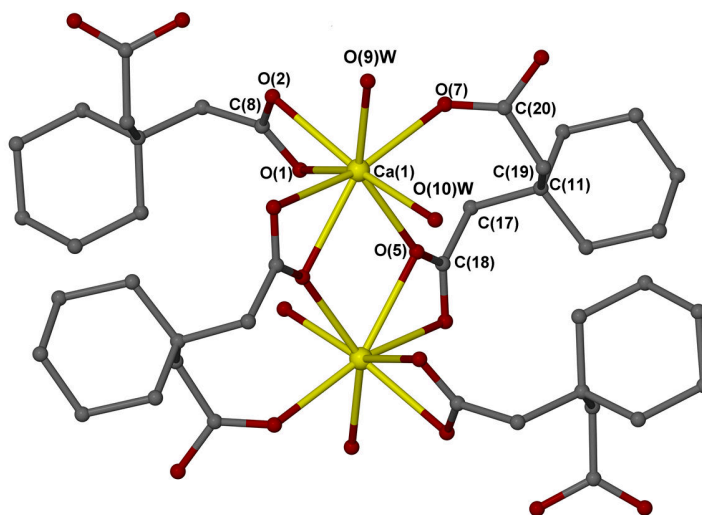
Figure 4.13 The crystal structure of 12.

The crystal structure of **12** contains an infinite array of $C_{10}H_{12}O_4^{2-}$, Ca^{2+} ions and water molecules, linked together by hydrogen bonding and form a 2D layer structure. In the eightfold coordination of calcium, as shown in Figure 4.13, the calcium ion coordinates to two water molecules, to two bidentate carboxylate groups and two monodentate acetate groups. The distance of the calcium to water oxygen, namely, Ca1-O9w, and Ca1-O10w, are 2.34 and 2.38 Å, respectively, are in the normal range of distances yet at the lower end of the range.[25, 27] TGA data (Figure 4.14) shows that water loss takes place after 188 °C, indicating a strong interaction between the Ca ions and water molecules.

There are two modes of calcium binding to the carboxylate group. One is a 4-membered chelate ring involving one calcium ion and one carboxylate group. The other one is an 8-membered chelate ring involving one calcium ion and two carboxylate groups. The carboxylate group in the 1,1-cyclohexandiacetic acid gives two different C-O distances of 1.21 Å and 1.31 Å, which is similar to the other cyclic polycarboxylic acids. With the presence of a Ca^{2+} ion, the C-O distances change. In the 4-membered ring, the carboxylate group is deprotonated and delocalized. The distances of both C-O bonds namely, C(8)-O(1) and C(8)-O(2), become longer and are around 2.6 ± 0.1 Å. The Ca-O distance found in the 4-membered ring is slightly longer than that in the 8-membered ring (Table 4.10) because the carboxylate groups in the monodentate 8-membered ring bind to the calcium ions. However, the binding affinity has no obvious difference from that in HEDP-Ca. With the same type of functional group, the affinity of Ca-O is similar. The emphasis should be on how the backbone preorganises the functional groups for docking.

CHDCA is more inclined to dock to the crystal or cluster surface in an orthogonal arrangement. The methylene-linked carboxylate group may offer some flexibility, but the degree of rigidity is uncertain. Moreover, binding in an orthogonal arrangement may not be as stable and immobile as that in a coplanar arrangement. Even when bound by two separated ligands, the Ca-Ca distance can still be 4 Å. However, the situation is not the same as for CPTCA, in which two CPTCA molecules are linked together by a hydrogen bond. CPDCA may not work as efficiently as CPTCA

Table 4.10 The Ca-O distances in the 4-membered and 8-memberred rings of compound 12.

In 4-memberred ring in 12			In 8-memberred ring in 12		
Atom	Atom	Length/Å	Atom	Atom	Length/Å
O1	C8	1.252(12)	O5	C18	1.266(12)
O2	C8	1.275(13)	O7	C20	1.219(12)
Ca1	O1	2.617(4)	Ca1	O5	2.383(7)
Ca1	O2	2.462(8)	Ca1	O7	2.398(7)
In 5-memberred ring in HEDP-Ca			In 6-memberred ring in HEDP-Ca		
Ca1	O3	2.437	Ca1	O2	2.352
Ca1	O7	2.578	Ca1	O5	2.420

4.3 Conclusion

There are mainly two types of Ca-O distance in HEDP-Ca, that is HCOO-Ca and HO-Ca. Due to the bond properties, the bond length of HCOO-Ca (2.35 to 2.45 Å) is generally shorter than that of HO-Ca (2.57 Å). The bond strength of Ca-O between COOH-Ca and HPO_3-Ca is similar when the functional groups are monodentate connected to calcium ions, is in the range of 2.35 to 2.50 Å. Moreover, the Ca-O distance between the delocalized COO^- and calcium (2.50 to 2.55 Å) is similar to HO-Ca. The interaction affinity is simply determined by the type of functional group. In the case of a carboxylate group, monodentate binding of the carboxylate group to calcium has a similar binding strength to that observed in the six-membered ring of HEDP-Ca. In this case, phosphate groups exhibit little difference from carboxylate groups. However, if both functional groups attach surface via substitution of carbonate group, it is proposed that the phosphate groups and carboxylate groups substitute the carbonate groups in a tripodal fashion and a bidentate mode, respectively. In this case, phosphate groups, which are more negatively charged, are expected to have a stronger interaction with Ca ions than carboxylate groups do. This fact suggests the phosphate acids of the same conformation are better inhibitors than those of carbonate acids.

For cyclic poly (carboxylic acids), the orientation of the carboxylate groups and the docking mode are more important. If the critical charge density does require for an efficient inhibition, the orientation of carboxylate groups and the conformation of the acids including the docking mode will all contribute to the build-up to the critical charge density. For example, If the docking of the inhibitor to the mineral surface is in a coplanar arrangement, and at the same time, the binding of two adjacent carboxylate groups is required, then only CPTCA and CHHCA satisfy this criterion. If just simply from the perspective of the structure factors, the CHHCA and CPTCA have a similar O-O distance to that in HEDP-Ca (bold in Table 4.11). Both ligands may not work as efficiently as HEDP due to their relatively rigid conformation.

The crystal structures of newly synthesized calcium compounds may have no direct indication of the inhibition efficiency of candidate inhibitors or the understanding of the possible inhibition mechanism. However, with the $CaCO_3$ inhibition study goes on, a generic structure characteristics of an efficient inhibitor can be gradually learned. Current understanding of the

molecular recognition at the molecular level in the early stage of nucleation is still at the stage of simulation, the real-life interaction due to the limitation of technique is still inaccessible.[3] In the molecular recognition, the sterochemical, geometrical and electrostatic constraints of an inhibitor dictate their binding to a mineral,[31] hence determining their inhibition ability and efficiency. Those single crystal structures can be useful for the understanding of the inhibitor structure and the corresponding constraints.

Table 4.11 Summary of the interatomic distance between HEDP-Ca and other calcium complexes

	HEDP	CPTCA	CHHCA	CHTCA	CHTTCA
Ca-O (Å)	2.34/2.42	2.50	3.37/2.41	2.38	2.34/2.52-2.55
P-P/C-C	3.074	2.690	3.081	4.957	3.101/3.035
O-O	2.928	3.037/3.106	2.768	5.957	3.34/3.28
Ca-Ca	3.825	5.924/10.203	No	3.897	5.095/ 9.377
Ca-O (Å)	2.45/2.65				
P-P/C-C	1.857				
O-Oh	**2.829**				
Ca-Ca	/				

4.4 Experimental Section

4.4.1 Materials

All reagents were purchased commercially and used without further purification.

4.4.2 Syntheses and Characterization of Coordination Compounds

Synthesis of $[Ca(\mu\text{-}C_9H_8O_8)(H_2O)_4]_n$, **1**. Crystals were grown from evaporation of an aqueous solution of cis,cis,cis,cis-1,2,3,4-cyclopentanetetracarboxylic acid (0.1485 g, 0.05 mol L^{-1}) and Ca(OH)$_2$ (0.4927 g, 0.05 mol L^{-1}) at room temperature. Colorless, plates suiable for X-ray analysis grew whitin three weeks. IR (wavenumber): 3583 cm^{-1}(w), 3313 cm^{-1} (w, b), 2976 cm^{-1} (w) ,2721 cm^{-1} (w), 2479 cm^{-1} (w), 1981 cm^{-1} (w), 1698 cm^{-1} (m), 1512 cm^{-1} (s), 1427 cm^{-1} (s), 1334 cm^{-1} (m), 1312 cm^{-1} (m), 1258 cm^{-1} (m), 1225 cm^{-1} (m), 1208 cm^{-1} (m), 1152 cm^{-1} (w), 1103 cm^{-1} (w), 1090 cm^{-1} (w), 1051 cm^{-1} (w), 1027 cm^{-1} (w), 1010 cm^{-1} (w), 941 cm^{-1} (w), 911 cm^{-1} (w), 867 cm^{-1} (w), 844 cm^{-1} (w), 812 cm^{-1} (w), 799 cm^{-1} (w), 718 cm^{-1} (w), 642 cm^{-1} (W). Microanalysis: calculated for **1**: C, 30.34; H, 4.53. Found: C, 30.28%, H, 4.40%. Water loss in **TGA** calculated for **1:** 20.21% for four water molecules, Found: 21.55%.

Synthesis of $[Ca(H_2O)_8][Ca(C_9H_8O_8)_2(H_2O)_4]\cdot 2H_2O$, **2**. Crystals were grown from evaporation of an aqueous solution of 1,2,3,4-cyclopentanetetracarboxylic acid (0.0347 g, 0.007 mol L^{-1}) and CaO (0.0158 g, 0.014 mol L^{-1}) at room temperature. Colorless plates suitable for X-ray analysis were achieved within three weeks. Not enough crystals were obtained for any further analysis.

Synthesis of $[Ca(H_2O)_8]$ $[Ca(C_9H_8O_8)_2(H_2O)_4]$, **3**. Crystals were grown from evaporation of an aqueous solution of 1,2,3,4-cyclopentanetetracarboxylic acid (0.1484 g, 0.04 mol L^{-1}) and Ca(OH)$_2$ (0.2467 g, 0.02 mol L^{-1}) at room temperature. Colorless plates suitable for X-ray analysis grew within three weeks. Not enough crystals were obtained for any further analysis.

Synthesis of $[Ca(C_9H_9O_8)_2(H_2O)_4]$, **4**. Crystals were grown from evaporation of an aqueous solution of 1,2,3,4-cyclopentanetetracarboxylic acid (0.9850 g, 0.10 mol L^{-1}) and CaO (0.1189 g, 0.05 mol L^{-1}) at room temperature. Colorless plates suitable for x-ray analysis were achieved within three weeks. IR (wavenumber): 3017 cm^{-1}(w), 2971 cm^{-1} (w), 2941 cm^{-1} (w) , 1738 cm^{-1}

(s), 1521 cm^{-1} (m), 1446 cm^{-1} (m), 1406 cm^{-1} (m), 1366 cm^{-1} (s), 1314 cm^{-1} (w), 1287 cm^{-1} (w), 1256 cm^{-1} (w), 1228 cm^{-1} (m), 1217 cm^{-1} (s), 1206 cm^{-1} (s), 1145 cm^{-1} (w), 1115 cm^{-1} (w), 1032 cm^{-1} (w), 1007 cm^{-1} (w), 940 cm^{-1} (w), 876 cm^{-1} (w), 833 cm^{-1} (w), 811cm^{-1} (w), 735 cm^{-1} (w), 707 cm^{-1} (w), 670 cm^{-1} (m), 618 cm^{-1} (m). Microanalysis: calculated for **4**: C, 35.85%; H, 4.32%. Found: C, 36.99%, H, 4.25%. Water loss in **TGA** calculated for **1:** 11.9 % for four water molecules, Found: 11.42%.

Table 4.12 Crystal data and structural refinement of crystal structures 1 to 4.

Identification code	1	2	3	4
Formula weight	356.30	820.69	784.66	602.47
Colour	Colourless	Colourless	colourless	colourless
Temperature / K	120	120	120	120
Crystal system	Orthorhombic	Monoclinic	orthorhombic	orthorhombic
Space group	Abm2	Cc	Pca2$_1$	Pccn
a/Å	5.6391(5)	48.577(3)	11.775(2)	36.2540(18)
b/Å	20.406(2)	5.6824(3)	5.6106(10)	5.5867(3)
c/Å	11.8487(11)	11.5971(8)	45.606(8)	11.6210(6)
α/°	90.00	90.00	90.00	90.00
β/°	90.00	94.016(7)	90.00	90.00
γ/°	90.00	90.00	90.00	90.00
Volume/Å^3	1363.5(2)	3193.3(4)	3013.0(9)	2353.7(2)
Z	4	4	4	4
Density /mg mm^3	1.736	1.707	1.730	1.700
abs coeff / m mm^{-1}	0.526	0.475	0.494	0.368
F(000)	744.0	1728.0	1648.0	1256.0
Crystal size / mm^3	0.2887 × 0.0595 × 0.0297	0.6888 × 0.2092 × 0.0229	0.32 × 0.2 × 0.08	0.24 × 0.22 × 0.04
2Θ range	6.88 to 58°	6.72 to 54°	3.58 to 56.98°	2.24 to 55.98°
Index ranges	$-7 \leq h \leq 7$, $-27 \leq k \leq 27$, $-16 \leq l \leq 16$	$-62 \leq h \leq 62$, $-7 \leq k \leq 7$, $-14 \leq l \leq 14$	$-15 \leq h \leq 15$, $-7 \leq k \leq 7$, $-61 \leq l \leq 61$	$-47 \leq h \leq 47$, $-7 \leq k \leq 7$, $-15 \leq l \leq 15$
Reflections collected	8845	17379	28102	24873
Independent reflections	1863 [R(int) = 0.0622]	6836 [R(int) = 0.0950]	7638 [R(int) = 0.0719]	2837 [R_{int} = 0.0720, R_{sigma} = 0.0457]
Data/restraints/ parameters	1863/1/130	6836/2/477	7638/28/513	2837/0/212
GOF on F^2	1.084	1.044	1.042	1.106
Final R indexes [I>=2σ (I)],	R_1 = 0.0442, wR$_2$ = 0.1001	R_1 = 0.0885, wR$_2$ = 0.1840	R_1 = 0.0663, wR$_2$ = 0.1490	R_1 = 0.0816, wR$_2$ = 0.1894
Final R indexes [all data] ,	R_1 = 0.0521, wR$_2$ = 0.1063	R_1 = 0.1189, wR$_2$ = 0.2058	R_1 = 0.0805, wR$_2$ = 0.1565	R_1 = 0.0954, wR$_2$ = 0.1971
Largest diff. peak/hole/e Å^{-3}	0.69/-0.28	0.81/-0.69	0.71/-0.97	0.53/-0.71

Synthesis of $[Ca_3(C_9H_9O_6)_2(H_2O)_4]·3H_2O$, **5**. Crystals were obtained by layering a solution of 1α,3α,5α-cyclohexanetricarboxylic acid in methanol or ethanol (10 ml, 0.023 mol L^{-1}) onto a solution of $Ca(OH)_2$ in water (5 ml, 0.0233 mol L^{-1}) at room temperature. IR (wavenumber): 3462 cm^{-1}(w, b), 3359 cm^{-1}(w), 2965 cm^{-1} (w), 1601 cm^{-1} (w) , 1543 cm^{-1} (vs), 1464 cm^{-1} (w), 1432 cm^{-1} (s), 1398 cm^{-1} (s), 1364 cm^{-1} (m), 1327 cm^{-1} (w), 1312 cm^{-1} (w), 1296 cm^{-1} (w), 1269 cm^{-1} (w), 1220 cm^{-1} (w), 1139 cm^{-1} (w), 1123 cm^{-1} (w), 981 cm^{-1} (w), 920 cm^{-1} (w), 791 cm^{-1} (m), 738 cm^{-1} (w), 709 cm^{-1} (w), 654 cm^{-1} (m); Microanalysis: calculated for **5**: C, 32.11%; H, 4.75%. Found: C, 31.98%; H, 4.89%. Water loss in **TGA** calculated for **5:** 18.72% for seven water molecules, Found: 17.21%.

Synthesis of $[Ca(C_9H_{10}O_6)(H_2O)_2]·H_2O$, **6**. Crystals were obtained by layering a solution of 1α,3α,5α-cyclohexanetricarboxylic acid in acetone or ethyl acetate (5 ml, 0.023mol L^{-1}) onto the solution of $Ca(OH)_2$ in water (5 ml, 0.0233 mol L^{-1}) at room temperature. IR (wavenumber cm^{-1}): 3517 cm^{-1}(m, b), 3205 cm^{-1} (m, b), 2940 cm^{-1} (m), 2867 cm^{-1} (m, b), 2634 cm^{-1} (w, b), 2381 cm^{-1} (w), 2347 cm^{-1} (w), 2279 cm^{-1} (w), 2162 cm^{-1} (w), 2051 cm^{-1} (w), 1980 cm^{-1} (w), 1701 cm^{-1} (m), 1624 cm^{-1} (w), 1580 cm^{-1} (s), 1548 cm^{-1} (s), 1448 cm^{-1} (m), 1402 cm^{-1} (s), 1356 cm^{-1} (m), 1334 cm^{-1} (m), 1307 cm^{-1} (m), 1286 cm^{-1} (w), 1272 cm^{-1} (w), 1242 cm^{-1} (m), 1185 cm^{-1} (m), 1137 cm^{-1} (w), 1105 cm^{-1} (w), 1034 cm^{-1} (w), 970 cm^{-1} (w), 917 cm^{-1} (w), 894 cm^{-1} (w), 845 cm^{-1} (w), 807 cm^{-1} (w), 773 cm^{-1} (w), 720 cm^{-1} (w), 672 cm^{-1} (w), 664 cm^{-1} (w). Microanalysis: calculated for **6**: C, 35.03%; H, 5.19%. Found: C, 36.69%; H, 5.29%. Water loss in TGA calculated for **6:** 17.52% for three water molecules, Found: 17.21%.

Table 4.13 Crystal data and structural refinement of crystal structures 5& 6.

Identification code	5	6
Formula weight	672.68	308.30
Color	colourless	Colourless
Temperature / K	120	120
Crystal system	monoclinic	triclinic
Space group	C2/c	P-1
a/Å	17.3557(19)	8.5782(9)
b/Å	9.4923(10)	12.5674(14)
c/Å	16.3976(17)	12.8876(14)
α/°	90.00	64.439(3)
β/°	90.882(3)	89.726(3)
γ/°	90.00	89.647(3)
Volume/Å^3	2701.1(5)	1253.3(2)
Z	4	4
Density /mg mm^3	1.654	1.634
abs coeff / m mm^{-1}	0.698	0.541
F(000)	1408.0	648.0
Crystal size / mm^3	0.4 × 0.08 × 0.08	0.32 × 0.24 × 0.06
2Θ range	4.7 to 55°	3.5 to 57°
Index ranges	-22 ≤ h ≤ 22, -12 ≤ k ≤ 12, -21 ≤ l ≤ 20	-11 ≤ h ≤ 11, -16 ≤ k ≤ 16, -17 ≤ l ≤ 17
Reflections collected	11502	13401
Independent reflections	3110[R(int) = 0.0977]	6328[R(int) = 0.0872]
Data/restraints/ parameters	3110/10/243	6328/0/355
GOF on F^2	0.974	1.021
Final R indexes [I>=2σ (I)],	R1 = 0.0516, wR2 = 0.1227	R1 = 0.0835, wR2 = 0.2358
Final R indexes [all data] ,	R1 = 0.0909, wR2 = 0.1424	R1 = 0.1045, wR2 = 0.2567
Largest diff. peak/hole / e Å^{-3}	0.95/-0.51	0.10(7)

Synthesis of $[Ca_2(C_{10}H_8O_8)(H_2O)_7]\cdot 2H_2O$, **7**. Crystals were obtained either by layering a solution of cyclohexane-1,2,4,5-tetracarboxylic acid in ethanol (5 ml or 10 ml, 0.019 mol L^{-1}) onto a solution of $Ca(OH)_2$ in water (5 ml, 0.0233 mol L^{-1}) at room temperature or by evaporation of a solution cyclohexane-1,2,4,5-tetracarboxylic acid (0.0261g) and $Ca(OH)_2$ (0.0087g) in DI water (10 ml). IR (wavenumber): 3570 cm^{-1} (w), 3554 cm^{-1}(w), 3343 cm^{-1}(w, b), 2966 cm^{-1} (w), 2924 cm^{-1} (w), 2347 cm^{-1} (w), 1547 cm^{-1} (m), 1531 cm^{-1} (m), 1449 cm^{-1} (m), 1405 cm^{-1} (s), 1354 cm^{-1} (w), 1327 cm^{-1} (w), 1303 cm^{-1} (w), 1039 cm^{-1} (w), 986 cm^{-1} (w), 925 cm^{-1} (w), 866 cm^{-1} (w), 792 cm^{-1} (w), 775 cm^{-1} (w), 672 cm^{-1} (w), 622 cm^{-1}(w). Microanalysis: calculated for **7**: C, 24.07%; H, 5.21%. Found: C, 23.96%; H, 5.13%. Water loss in TGA calculated for **7:** 32.50% for nine water molecules, Found: 30.46%.

Synthesis of $[Ca(C_{10}H_{10}O_8)(H_2O)_6]\cdot H_2O$, **8**. Crystals were obtained as the minor phase from evaporation of a solution cyclohexane-1,2,4,5-tetracarboxylic acid (0.0261g) and $Ca(OH)_2$ (0.0087g) in DI water (10 ml). IR (wavenumber): 3654 cm^{-1}(w), 3568 cm^{-1}(w), 3444 cm^{-1}(m, b), 3164 cm^{-1} (w, b), 2944 cm^{-1} (w), 2877 cm^{-1} (w), 2543 cm^{-1} (w), 1920 cm^{-1} (w), 1665 cm^{-1} (m), 1586 cm^{-1} (m), 1525 cm^{-1} (s), 1464 cm^{-1} (m), 1450 cm^{-1} (m), 1416 cm^{-1} (m), 1388 cm^{-1} (m), 1337 cm^{-1} (m), 1318 cm^{-1} (w), 1291 cm^{-1} (w), 1275 cm^{-1} (w), 1233 cm^{-1} (m), 1163 cm^{-1} (w), 1035 cm^{-1} (w), 985 cm^{-1} (w), 947 cm^{-1} (w), 672 cm^{-1} (w), 908cm^{-1} (w). 836 cm^{-1} (w), 767 cm^{-1} (w), 749 cm^{-1} (w), 686 cm^{-1} (w), 672 cm^{-1} (w), 637 cm^{-1} (w), 601 cm^{-1} (w). Microanalysis: calculated for **8**: C, 28.28%; H, 5.66%. Found: C, 28.36%; H, 5.57%. Water loss in TGA calculated for **8:** 29.69% for seven water molecules, Found: 30.86%.

Synthesis of $[Ca(C_{10}H_{12}O_8)_2(H_2O)_4]_n$, **9**. Crystals were obtained by layering of a solution of the cyclohexane-1,2,4,5-tetracarboxylic acid in methanol (6 ml, 0.036 mol L^{-1}) onto a solution $Ca(OH)_2$ in water (6 ml, 0.0233 mol L^{-1}). The solution was sonicated before being left to dry. IR (wavenumber): 3465 cm^{-1}(m, b), 2999 cm^{-1} (m), 2970 cm^{-1} (m), 2932 cm^{-1} (m), 2865 cm^{-1} (m), 2767 cm^{-1} (m), 2606 cm^{-1} (w, b), 2381 cm^{-1} (w), 2347 cm^{-1} (w), 2282 cm^{-1} (w), 2050 cm^{-1} (w), 1980 cm^{-1} (w), 1686 cm^{-1} (s), 1636 cm^{-1} (m), 1569 cm^{-1} (w), 1436 cm^{-1} (m), 1409 cm^{-1} (m), 1343 cm^{-1} (w), 1315 cm^{-1} (m), 1285 cm^{-1} (s), 1256 cm^{-1} (m), 1242 cm^{-1} (m), 1219 cm^{-1} (m), 1202 cm^{-1} (m), 1169 cm^{-1} (m). 1064 cm^{-1} (w), 672 cm^{-1} (w), 657 cm^{-1} (w), 601 cm^{-1} (w). Microanalysis: calculated for **9**: C, 38.06%; H, 5.07%. Found: C, 38.23%; H, 4.77%. Water loss in TGA calculated for **1:** 11.42% for four water molecules, Found: 11.42%.

Table 4.14 Crystal data and structural refinement of crystal structures 7-9.

Identification code	13srv063 (7)	13srv089 (8)	14srv008 (9)
Formula weight	498.47	424.37	630.52
Color	colourless	Colourless	colourless
Temperature / K	120	120	120
Crystal system	monoclinic	monoclinic	monoclinic
Space group	P21/c	P21/c	P21/c
a/Å	13.9179(10)	12.3998(3)	23.544(5)
b/Å	11.9925(9)	11.5540(3)	16.359(3)
c/Å	11.7352(9)	12.3824(3)	13.049(3)
α/°	90.00	90.00	90.00
β/°	105.689(2)	108.652(3)	90.05(3)
γ/°	90.00	90.00	90.00
Volume/Å^3	1885.8(2)	1680.81(8)	5025.9(17)
Z	4	4	8
Density /mg mm^3	1.756	1.677	1.667
abs coeff / m mm^{-1}	0.692	0.454	0.348
F(000)	1048.0	896.0	2640.0
Crystal size / mm^3	0.24 × 0.1 × 0.1	0.403 × 0.28 × 0.149	0.31 × 0.22 × 0.03
2Θ range	3.04 to 58°	5.36 to 59°	2.48 to 54°
Index ranges	-18 ≤ h ≤ 18, -16 ≤ k ≤ 16, -16 ≤ l ≤ 16	-17 ≤ h ≤ 17, -16 ≤ k ≤ 15, -17 ≤ l ≤ 17	-30 ≤ h ≤ 30, -20 ≤ k ≤ 20, -16 ≤ l ≤ 15
Reflections collected	22906	32700	46548
Independent reflections	5002 [R(int) = 0.0595]	4669 [R(int) = 0.0458]	10883 [Rint = 0.1089, Rsigma = 0.0910]
Data/restraints/ parameters	5002/23/358	4669/92/331	10883/12/358
GOF on F^2	1.090	1.113	1.061
Final R indexes [I>=2σ (I)],	R1 = 0.0541, wR2 = 0.1253	R1 = 0.0353, wR2 = 0.0779	R1 = 0.0915, wR2 = 0.2245
Final R indexes [all data] ,	R1 = 0.0772, wR2 = 0.1453	R1 = 0.0407, wR2 = 0.0801	R1 = 0.1396, wR2 = 0.2595
Largest diff. peak/hole / e Å^{-3}	0.84/-0.88	0.52/-0.25	1.63/-0.83

Synthesis of $[Ca(C_{12}H_{11}O_6)_2(H_2O)_4] \cdot 1.25H_2O$, **10**. Crystals were obtained at room temperature by layering a solution of l, the 2,3,4,5,6-cyclohexanehexacarboxylic acid in Butanol-1 (8 ml, 0.0108 mol L^{-1}) onto a solution of $Ca(OH)_2$ in water (4 ml, 0.0233 mol L^{-1}). Not enough crystals were obtained for any further analysis.

Synthesis of $[C_{12}H_{12}O_{12}] \cdot H_2O$, **11**. Crystals were obtained by layering of a solution of cyclohexane-1,2,3,4,5,6-hexacarboxylic in methanol (14ml, 0.204 mol L^{-1}) onto a solution $Ca(OH)_2$ in water (20 ml, 0.0233 mol L^{-1}). (As this is a side product, further analysis was not performed)

Synthesis of $[Ca(C_{10}H_{15}O_4)_2(H_2O)_2]_n$, **12.** Crystals were obtained from the evaporation of a solution of 1,1-cyclohexanediacetic acid (0.04 g, 0.2 mmol) and $Ca(OH)_2$ (0.0148 g, 0.1 mmol) in 10 ml DI water. IR (wavenumber): 3520 cm^{-1}(w), 3171cm^{-1} (w) , 2930 cm^{-1} (w), 2854 cm^{-1} (w), 1704 cm^{-1} (m), 1545 cm^{-1} (s), 1483 cm^{-1} (m), 1456 cm^{-1} (s), 1447 cm^{-1} (m), 1420 cm^{-1} (m), 1402 cm^{-1} (m), 1360 cm^{-1} (w), 1317 cm^{-1} (w), 1288 cm^{-1} (w), 1253 cm^{-1} (m), 1203 cm^{-1} (s), 1181 cm^{-1} (m), 1143 cm^{-1} (w), 1126 cm^{-1} (m), 1067 cm^{-1} (w), 979 cm^{-1} (w), 963 cm^{-1} (w), 939 cm^{-1} (w). 928 cm^{-1} (w), 912 cm^{-1} (w), 891 cm^{-1} (w), 866 cm^{-1} (w), 843 cm^{-1} (w), 820 cm^{-1} (w), 758 cm^{-1} (w). 709 cm^{-1} (m), 670 cm^{-1} (m), 601 cm^{-1} (w). Microanalysis: calculated for **12**: C, 50.57%; H, 7.16%. Found: C, 50.69%; H, 7.29%. Water loss in TGA calculated for **12:** 7.59% for 2 water molecules, Found: 7.42%

Table 4.15 Crystal data and structural refinement of crystal structures 10-12.

Identification code	13srv300 (**10**)	13srv196 (**11**)	15srv009 (**12**)
Formula weight	828.07	366.23	474.55
Color	colourless	Colourless	colourless
Temperature / K	100.0	120	120.0
Crystal system	monoclinic	monoclinic	triclinic
Space group	C2/c	P21/n	P-1
a/Å	22.632(5)	7.4792(2)	7.07770(10)
b/Å	10.473(2)	13.6254(3)	11.1674(2)
c/Å	29.189(6)	13.1513(3)	15.7081(3)
α/°	90.00	90.00	106.469(3)
β/°	105.622(2)	90.06(3)	96.639(3)
γ/°	90.00	90.00	101.751(3)
Volume/Å^3	6663(2)	1340.21(6)	1145.63(3)
Z	8	4	2
Density /mg mm^3	1.651	1.815	1.376
abs coeff / m mm^{-1}	0.282	0.170	0.326
F(000)	3436.0	760.0	508.0
Crystal size / mm^3	0.2 × 0.18 × 0.01	0.31 × 0.24 × 0.15	0.3 × 0.25 × 0.09
2Θ range	3.62 to 58°	4.3 to 56°	5.46 to 60
Index ranges	-32 ≤ h ≤ 31, -12 ≤ k ≤ 14, -41 ≤ l ≤ 41	-9 ≤ h ≤ 9, -18 ≤ k ≤ 17, -17 ≤ l ≤ 14	-9 ≤ h ≤ 9, -15 ≤ k ≤ 15, -22 ≤ l ≤ 22
Reflections collected	39546	12993	25088
Independent reflections	9657 [Rint = 0.0403, Rsigma = 0.0383]	3225 [R(int) = 0.1135]	6654 [Rint = 0.0314, Rsigma = 0.0292]
Data/restraints/ parameters	9657/0/517	3225/0/282	6654/6/416
GOF on F^2	1.131	1.049	1.012
Final R indexes [I>=2σ (I)],	R1 = 0.0666, wR2 = 0.2014	R1 = 0.0516, wR2 = 0.1364	R1 = 0.0295, wR2 = 0.0711
Final R indexes [all data] ,	R1 = 0.0813, wR2 = 0.2142	R1 = 0.0639, wR2 = 0.1448	R1 = 0.0378, wR2 = 0.0748
Largest diff. peak/hole / e Å^{-3}	0.92/-1.38	0.61/-0.36	0.47/-0.26

4.4.3 Instrumentation

4.4.3.1 Single- Crystal Structure Determination

All crystallographic data are contained on the CD accompanying this report as .cif and .doc files.

The X-ray single crystal data for all compounds except **10** were collected using graphite monochromated MoKα radiation (λ =0.71073Å). The collection temperature was 120(2) K, maintained using an open flow N_2 Oxford Cryostream device. The data for compounds **11** and **12** were collected on a Bruker D8 Venture (Photon100 CMOS detector, IμS-microfocus source, focusing mirrors) 3-circle diffractometer. Compounds **1**, **2** and **8** were collected on an Agilent XCalibur (Sapphire-3 CCD detector, graphite monochromator) 4-circle kappa diffractometer and compounds **3**, **4**, **5**, **6**, **7** and **9** were collected on a Bruker SMART CCD 6000 3-circle diffractometer (fine-focus sealed tube, graphite monochromator, Monocap (Bruker) optics). The data for the weakly diffracting crystals of **10** were collected at 100 K on a Rigaku Saturn 724+ 4-circle diffractometer at station I19 of the Diamond Light Source synchrotron (undulator, λ = 0.6889 Å, ω-scan, 1.0°/frame) and processed using the Bruker APEXII software.[32] Data sets were corrected for Lorentz and polarization effects and the effects of absorption. All structures were solved by a direct method and refined by full-matrix least squares on F^2 for all data using Olex2[23] and SHELXTL.[33] All non-disordered, non-hydrogen atoms were refined in an anisotropic approximation. In most structures, the hydrogen atoms were placed in calculated positions and refined in riding mode. The structures were visualized using X-Seed.[34] Molecular graphics were produced using POV-Ray.[35]

Crystal data, as well as details of data collection and refinements, are summarized in Table 4.12 for crystals **1−4**, in Table 4.13 for crystals **5 & 6**, in Table 4.14 for crystals **7−9,** in Table 4.15 for crystals **10–12**. Crystal forms obtained from the same acid compound are organized in the same table for clarity except for the single crystals of **12**, which were made from a different acid compound.

4.4.3.2 Elemental Analysis

Microanalysis on compounds **1**, **2** and **8** was performed by London Metropolitan University (London) using a Thermo Scientific (Carlo Erba) Flash 2000 Elemental Analyser. Other samples

were run using an Exeter Analytical E-440 Elemental Analyser (Durham). To keep the coordinated water, selected crystals were dried under ambient condition before submission. The amount submitted ranged from 5mg to 10mg, depending on the availability of sample. The lack of CHN data for some samples is because continuing attempts to prepare suitable bulk quantities for analysis have been unsuccessful.

4.4.3.3   Thermogravimetric Analysis

Thermogravimetric analysis (TGA) were carried out using a Perkin Elmer Pyris 1 TGA coupled with a 500 amu Hiden mass spectrometer (MS), which allows the analysis of the volatiles generated by the thermal degradation of materials. The volatiles monitored by the MS are CO, CO_2, and H_2O. Thermal analysis is carried out from 20 ^{o}C to 500 ^{o}C at a rate of 10 ^{o}C/min. The order of the loss of water starts with the loss of free water, followed by coordinated water and finally the loss of water and CO or CO_2 due to degradation of the cyclic ring and carboxylic acid groups. The water loss is different in different compounds. For the detailed TGA graph, see Appendix 4.

The TGA figures were plot using Pyris manager. Taking the TGA image of compound **12** as an example, the loss of coordinated water takes place after 71 ^{o}C. There is no free water in **12**. Hence we will not observe this. The loss of CO and water takes place after 140 ^{o}C.
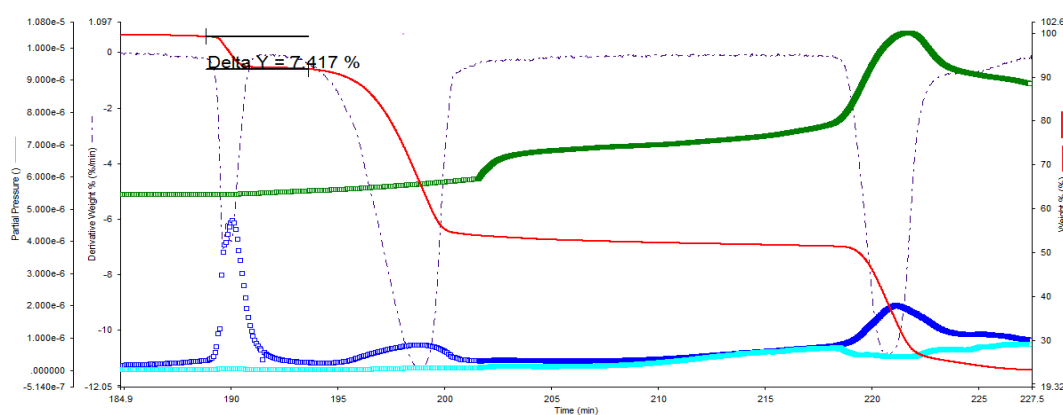
Figure 4.14 TGA with MS for compound 12. Green line for N$_2$ and CO. Blue curve and arctic curves are for water and CO$_2$, respectively. Red and dashed purple lines are for thermal curve and derivative curve, respectively.

4.4.3.4 Infrared Spectroscopy

Data was collected by attenuated total reflectance infrared spectrometer (ATR-IR). ATR-IR spectra were recorded on a Perkin-Elmer Spectrum 100 using a diamond compression cell. The IR spectra were collected by pressing the probe against the diamond and scanning the 4000–400 cm^{-1} region at a resolution of 4 cm^{-1}. Typically, 32 or 64 scans were conducted for each spectrum. The resulting IR spectra were analyzed using KnowItAll.[36] Peak intensity is described as strong (s), medium (m), weak (w), or broad (b).

4.4.3.5 X-ray Powder Diffraction

X-ray powder diffraction patterns were collected on a Bruker D8 Advance powder diffractometer using a nickel- filtered copper X-ray radiation (λ = 1.5406 Å). Powder diffractometer operates at 40 mA and 45 kV. The 2θ range for crystalline material from 2° to 50° is recorded at a scan rate of 0.02^{o} $step^{-1}$. The outcome data was plot in Topas software.[37] The patterns are attached in Appendix 4.

4.5 References

1.   Coveney, P. V.; Davey, R.; Griffin, J. L.; He, Y.; Hamlin, J. D.; Stackhouse, S.; Whiting, A. *J. Am. Chem. Soc.* **2000,** *122* (46), 11557-11558.

2.   Mann, S., *Biomineralization : Principles and Concepts in Bioinorganic Materials Chemistry*. Oxford University Press: Oxford, 2001; p 198.

3.   Anwar, J.; Boateng, P. K.; Tamaki, R.; Odedra, S. *Angew. Chem. Int. Ed.* **2009,** *48* (9), 1596-1600.

4.   Sommerdijk, N. A.; With, G. d. *Chem. Rev.* **2008,** *108* (11), 4499-4550.

5.   Black, S. N.; Bromley, L. A.; Cottier, D.; Davey, R. J.; Dobbs, B.; Rout, J. E. *J. Chem. Soc., Faraday Trans.* **1991,** *87* (20), 3409-3414.

6.   Naka, K.; Keum, D.-K.; Tanaka, Y.; Chujo, Y. *Chem. Commun.* **2000,** *16*, 1537-1538.

7.   Freeman, S. R.; Jones, F.; Ogden, M. I.; Oliviera, A.; Richmond, W. R. *Cryst. Growth Des.* **2006,** *6* (11), 2579-2587.

8.   Reddy, M. M.; Leenheer, J. **2011**.

9.   Berner, R. A.; Westrich, J. T.; Graber, R.; Smith, J.; Martens, C. S. *J. Am. Sci.* **1978,** *278* (6), 816-837.

10.   Reddy, M. M.; Hoch, A. R. *J. Colloid Interface Sci.* **2001,** *235* (2), 365-370.

11.   Fricke, M.; Volkmer, D., Crystallization of Calcium Carbonate beneath Insoluble Monolayers: Suitable Models of Mineral–Matrix Interactions in Biomineralization? In *Biomineralization I*, Springer: 2006; pp 1-41.

12.   Didymus, J. M.; Oliver, P.; Mann, S.; DeVries, A. L.; Hauschka, P. V.; Westbroek, P. *J. Chem. Soc., Faraday Trans.* **1993,** *89* (15), 2891-2900.

13.   Mann, S.; Didymus, J. M.; Sanderson, N. P.; Heywood, B. R. *J. Chem. Soc., Faraday Trans.* **1990,** *86* (10), 1873-1880.

14.   Gill, J. S.; Varsanik, R. G. *J. Cryst. Growth* **1986,** *76* (1), 57-62.

15.   Kuntze, R. **1966**.

16.   Berner, R. A.; Westrich, J. T.; Graber, R.; Smith, J.; Martens, C. S. *J. Am. Sci.* **1978,** *278* (6), 816-837.

17.   (a) Volkmer, D.; Fricke, M.; Agena, C.; Mattay, J. *CrystEngComm* **2002,** *4* (52), 288-295; (b) Volkmer, D.; Fricke, M.; Agena, C.; Mattay, J. *J. Mater. Chem.* **2004,** *14* (14), 2249-2259; (c) Fricke, M.; Volkmer, D.; Krill, C. E.; Kellermann, M.; Hirsch, A. *Cryst. Growth Des.* **2006,** *6* (5), 1120-1123.

18.   (a) Deganello, S. *Acta Crystallogr., Sect. B: Struct. Sci.* **1981,** *37* (4), 826-829; (b) Karipides, A.; Ault, J.; Reed, A. T. *Inorg. Chem.* **1977,** *16* (12), 3299-3302.

19.   (a) Uchtman, V. A.; Jandacek, R. J. *Inorg. Chem.* **1980,** *19* (2), 350-355; (b) Robl, C. *Z. Naturforsch. B Chem. Sci.* **1988,** *43* (8), 993-997; (c) Yang, Y. Y.; Huang, Z. Q.; Szeto, L.; Wong, W. T. *Appl. Organomet. Chem.* **2004,** *18* (2), 97-98.

20.   Uchtman, V. A. *J. Phys. Chem.* **1972,** *76* (9), 1304-1310.

21.   Stavgianoudaki, N.; Papathanasiou, K. E.; Colodrero, R. M. P.; Choquesillo-Lazarte, D.; Garcia-Ruiz, J. M.; Cabeza, A.; Aranda, M. A. G.; Demadis, K. D. *CrystEngComm* **2012,** *14* (17), 5385-5389.

22.   Heywood, B. R.; Mann, S. *Chem. Mater.* **1994,** *6* (3), 311-318.

23.   Dolomanov, O. V.; Bourhis, L. J.; Gildea, R. J.; Howard, J. A.; Puschmann, H. *J. Appl. Crystallogr.* **2009,** *42* (2), 339-341.

24.   Jia, Z.; Davies, P. L. *Trends Biochem. Sci* **2002,** *27* (2), 101-106.

25.   Uchtman, V. A.; Jandacek, R. J. *Inorg. Chem.* **1980,** *19* (2), 350-355.

26.   Lin, J.-L.; Guo, X.-X.; Huang, W.-X. *Acta Crystallogr. Sect. E* **2011,** *67* (8), 1945.

27.   (a) Demadis, D. K.; Sallis, D. J.; Raptis, G. R.; Baran, P. *J. Am. Chem. Soc.* **2001,** *123* (41), 10129-10130; (b) Barnes, J. C.; Paton, J. D. *Acta Crystallogr. Sect. C: Cryst. Struct. Commun.* **1984,** *40*, 1809-1812; (c) DeLucas, L.; Bugg, C. E.; Terzis, A.; Rivest, R. *Carbohyd. Res.* **1975,** *41* (1), 19-29.

28.   Chung, J.; Granja, I.; Taylor, M. G.; Mpourmpakis, G.; Asplin, J. R.; Rimer, J. D. *Nature* **2016,** *536*, 446–450.

29.   Anthonsen, T.; Larsen, B.; Smidsrød, O. *Acta Chem. Scand.* **1972,** *26*, 2988-2989.

30.   (a) Bruckner, S.; Malpezzi Giunchi, L.; Di Silvestro, G.; Grassi, M. *Acta Cryst. B* **1981,** *37* (3), 586-590; (b) Thuery, P., Cyclohexane-1,2,3,4,5,6-Hexacarboxylic Acid Tetrahydrate. Communication, P., Ed. 2012.

31.   Orme, C.; Noy, A.; Wierzbicki, A.; McBride, M.; Grantham, M.; Teng, H.; Dove, P.; DeYoreo, J. *Nature* **2001,** *411* (6839), 775-779.

32.   Bruker Analytical X-Ray Instruments, 1 and Saint Version 7.34: A Data Collection and Processing Software. Madison, WI, USA.

33.   Sheldrick, G. M. *Acta Crystallogr. Sect. A: Found. Crystallogr.* **1990,** *46* (6), 467-473.

34.   Barbour, L. J., Xseed: A Program for the Manipulation and Display of Crystallographic Models. Columbia, MO, USA, 1999.

35.   Persistence of Vision Raytracer Pty., Pov-Ray. 2012.

36.   *Knowitall Academic Edition*, version 2005; Bio‑Rad Laboratories: 2005; (Accessed May 05, 2016).

37.   Evan, S. O. J.; Coelho, A. Topas Academic www.dur.ac.uk/john.evans/topas_academic/topas_main.htm.

5 Inhibition Performance of Candidate Inhibitors

5.1 Introduction

The inhibition mechanism for the crystal growth of mineral formation using substoichiometric amounts of inhibitor is largely unresolved. Known inhibitors are quite specific in their performance, and a universal inhibitor for all types of mineral scale does not exist.[1] Thus, one inhibitor is likely to work for only one system and may not work for other systems. For a given set of conditions, each inhibitor needs to be tested before application.

The use of phosphate-containing inhibitors is gradually being phased out due to the negative environmental impact of phosphorus-containing compounds. In response to recent changes in environmental guidelines, new phosphate-free inhibitors are needed by industry to replace the original HEDP. This chapter presents screening results of the inhibition performance of cyclic poly (carboxylic acids) under the dishwasher conditions. The candidate inhibitors along with a nil-HEDP dishwasher formula were investigated, and the results are reported. The possible inhibition mechanism of HEDP and the new effective inhibitors is also discussed.

5.2 The Inhibition Performance of Candidate Inhibitors

A model system and a real dishwasher (previously described in Chapters 3 and 4) were used to study the inhibition performance of the candidate inhibitors. As discussed in the Section 1.4.4, an effective inhibitor may function in delaying nucleation or as a crystal growth inhibitor, or both. The assessment of the nucleation delay alone or simply just the study of the growth rate reduction on seeded crystals may not be sufficient to evaluate the performance of the inhibitors because the inhibitors may delay nucleation as well as inhibit the growth of the crystals. As a result, the assessment of the inhibition effectiveness of the candidate inhibitors is based on the 'shine' (*i.e.* lack of filming) that the substrate retains over a number of wash cycles.

In general, for an ineffective inhibitor, spots or a very fine film is usually observed in the first cycle. At the second and third cycle, a visible film can be identified. The preliminary performance evaluation of the inhibitors will be carried out in the model laboratory system based

on the HEDP standard. The best performing inhibitors, enable the surfaces of the substrates to retain their shine for up to five cycles and will be further tested under real dishwasher condition.

5.2.1 Candidate Inhibitors

The structural characteristics and the potential inhibition ability of cyclic polycarboxylic acids (CPCA) have been reviewed in chapter 5. A series of CPCA with 5-, 6-, 10- and 12-membered rings have been selected as alternative phosphate-free inhibitors for HEDP (Figure 5.1). Any CPCA with more than two carboxylic acid groups, available in the market, is screened along with standard 'full Nil-HEDP formula' to test their inhibition effectiveness. The schematic structures of the selected CPCA are shown in Figure 5.2.
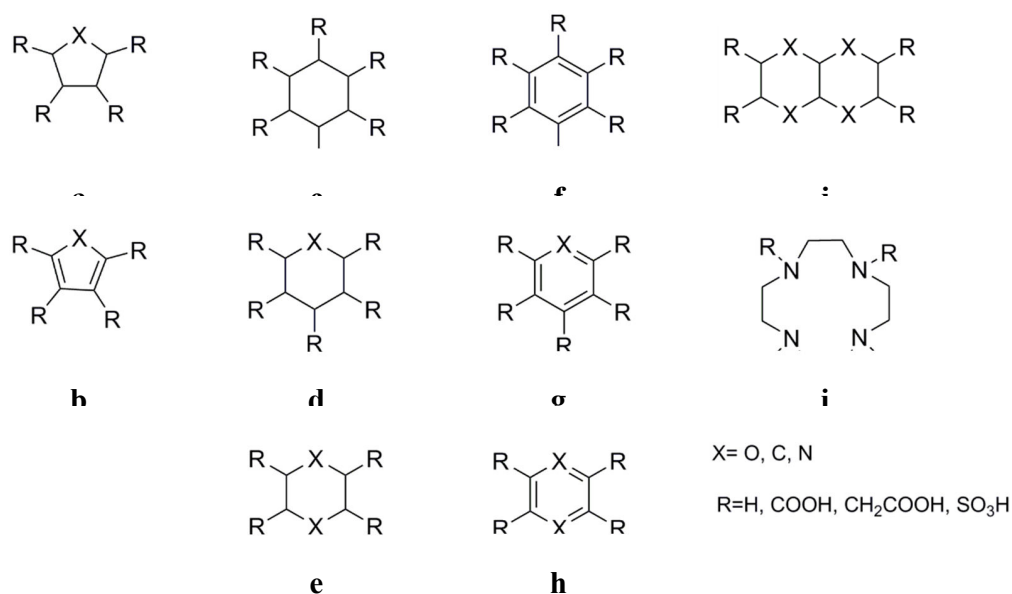
Figure 5.1 The backbones of the candidate inhibitors for the cyclic carboxylic acids.

From evaluating the desirable structural characteristics of an effective inhibitor (see Chapter 5 Section 5.1), it can be suggested that cyclic oligo-carboxylates, as shown in Figure 5.1 **a**, **c**, **d** & **e**, with backbones which allows more conformational freedom, may have better inhibition ability than those with backbones of **b, f, g, h, i** & **j**. The latter are much more conformationally rigid. The inhibition ability increases with the number of carboxylate groups attached to different carbon atoms in the ring, and when the functional groups are all on the same side of the ring plane. Based on these requirements, the inhibition effectiveness of candidate inhibitors can be predicted. Similarly phytic acid (PA) with four phosphate groups on the same side of the ring plane shares many of these favorable characteristics, and it is likely that phytic acid (PA) will have a similar or better inhibition effectiveness than HEDP. It is included here for comparison

despite also being a phosphate-based compound. The suggested rank of the inhibition ability of CPCA based on the number of the functional groups is as follows (see Figure 5.2 for all the structures of the candidate inhibitors): CHHCA > CPTCA > CHTTCA > TPCHTCA ~ CHTCA-135 ~ CHTCA-124 (only CPCA with more than three carboxylic acid groups at one side of ring plane are listed here). The exclusion of the THFTCA is due to the nature of the tetrahydrofuran ring of THFTCA. In THFTCA, two carboxylic acid groups are above the plane of the ring, while the other two carboxylic acid groups are below the plane of the ring. Therefore, it will be a maximum of two carboxylic acid groups docking to surface at a time for THFTCA rather than four carboxylic acid groups.

TMCPDA   CPDA   CPTCA   THFTCA   FA

QA   CHDAA   CHDA   CHTCA-135   CHTCA-124

TPCHTCA   CHTTCA   CHHCA   PA   GTA

DHDAD   GA   PDA-12   PDA-13   SPS

BTCA   BTTCA   BPCA   BHCA   DPA

PZDA   GTDH   TTCDTCA
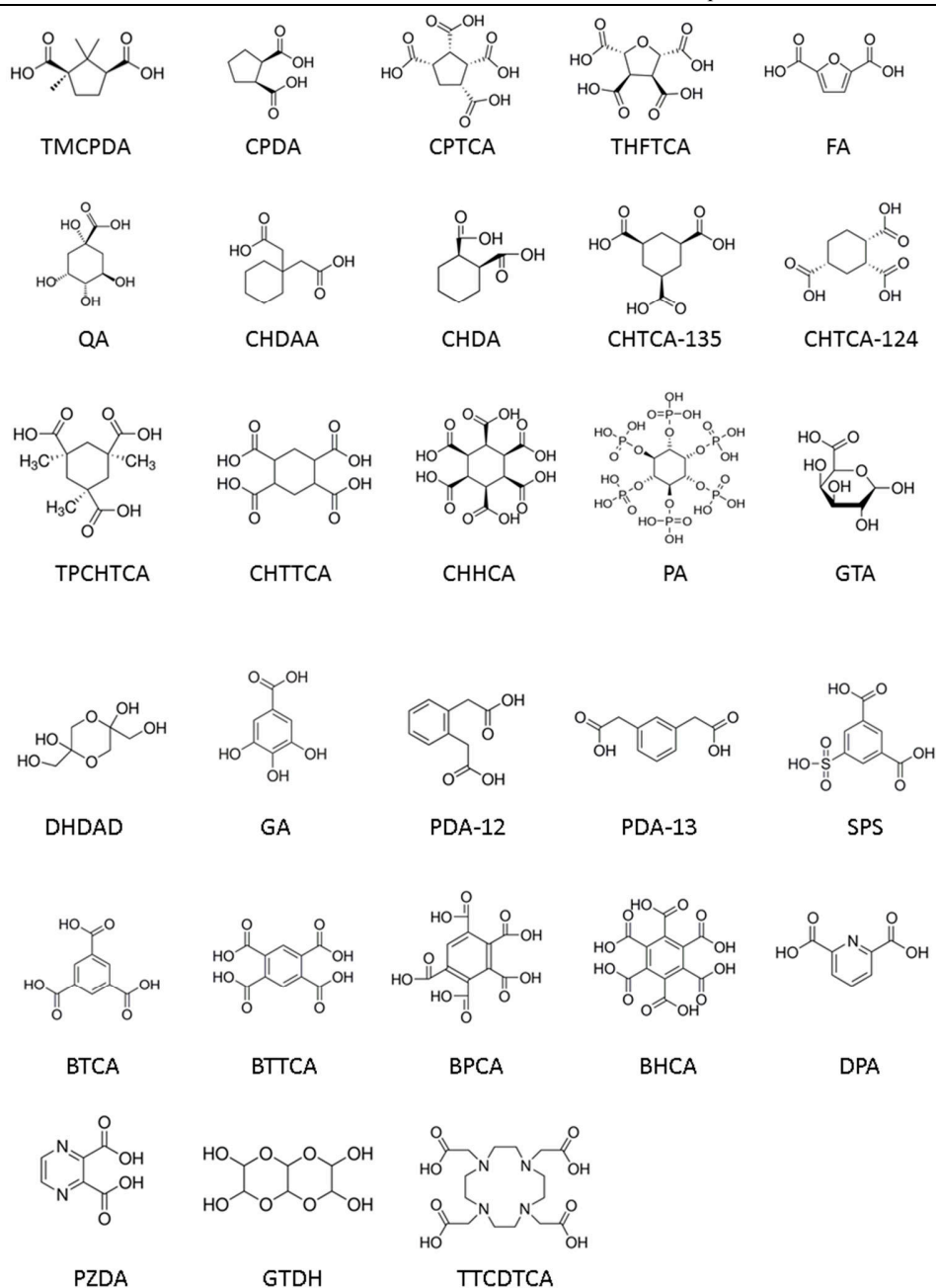
Figure 5.2 Structures of the selected candidate inhibitors. The inhibitors are labeled accordingly based on code number of the backbone as shown in Figure 5.1.

5.2.2 Inhibition Performance Screening in the Model System

The inhibition efficiency of the candidate inhibitors are evaluated along with the 'full Nil-HEDP formula' in the model system. Glass samples and PMMA slides were utilized as test material in the model system. The glass slide and PMMA slide produced with 'Nil-HEDP formula' in the model system after five cycles were used as blank samples (See Section 2.5). The chemical

composition used for the study of the inhibition performance screening is presented in Table 5.1. The samples produced by 'HEDP formula' are also included in Table 5.1 for comparison. The inhibition performance of the selected inhibitors, except the CHTTCA (Figure 5.2), was evaluated at the same concentration as HEDP, which is 0.112 mmol L^{-1}. CHTTCA is a mix of cis- and trans- isomers, hence double the amount of CPTTCA will be used. The applied amount of each of the candidate inhibitors was different and dependent on the molecular weight of each selected inhibitors. The detailed experimental procedure is described in Section 5.5.1.

Table 5.1 The formula used for the screening of the inhibition performance of the selected inhibitors

Conditions	Water		Filler		Builder	Polymer	Surfactant	Inhibitor
	$CaCl_2$	$MgCl_2$	Na_2CO_3	Na_2SO_4	MGDA	Acusol 588	Non-ionic mixture	See below
Nil-HEDP formula	yes	yes	yes	yes	yes	yes	yes	no
HEDP formula	yes	yes	yes	yes	yes	yes	yes	HEDP
Candidate inhibitor + Nil-HEDP formula	yes	yes	yes	yes	yes	yes	yes	candidate inhibitor

*yes: included; no: not included

The inhibition performance of the candidate inhibitors was evaluated by visual inspection. The resulting surfaces after applying the candidate inhibitors will only have two consequences: shine surface or filmed surface. The filmed surface is undesirable. Therefore, the candidate inhibitors will be only classified into two groups: 'effective inhibitors' that can work as efficiently as HEDP and 'ineffective inhibitors' which have no or low inhibition ability on film formation. For an ineffective inhibitor, a visible film can be observed by the naked eye on the surface after 2 or 3 cycles. Film formation can be initially seen during the first cycle, which then becomes visible across the whole surface in the second or the third cycle. The film formation can still occur even if candidate inhibitors have inhibition ability. However, because they are not powerful enough to prevent the formation of the film after three cycles, they will not satisfy the criterion as a calcium carbonate inhibitor under the dishwasher conditions. Candidate inhibitors of this kind will also be classified as 'ineffective inhibitors.' In contrast, an effective inhibitor can maintain the clarity of the surface for up to 5 cycles as HEDP.
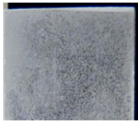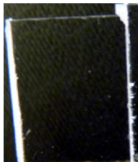
The screening results of the inhibition performance are presented in Table 5.2, showing that the best performing inhibitors are PA and a mixture of CPTCA and CHHCA (CPTCA + CHHCA). All the other candidate inhibitors showed the formation of a film on the surface that was evident after three cycles.

Table 5.2 presents the resulting surfaces and the applied concentration of the best performing inhibitors after five cycles. When using the Nil-HEDP formula, the film formation on the surfaces is obvious. The adding of PA and a mixture of the CPTCA and CHHCA can retain the shine as the original state of charity attained using HEDP. It is interesting to note here that the CPTCA alone only helps to retain shine for the PMMA slide but not for glass surfaces. CHHCA, on the other hand, only retains the shine on glass substrates but not on PMMA slide. Hence, surprisingly, CPTCA and CHHCA are substrate specific. This may be why the concentration of the 'CPTCA + CHHCA' used was twice as much as the HEDP. The glass and PMMA slides exposed to CPTCA and CHHCA separately were examined using PXRD and SEM. The results are shown inFigure 5.4 for CPTCA and Figure 5.5 for CHHCA, respectively. It is shown that as the inhibition of CPTCA and CHHCA for $CaCO_3$ crystals is polymorph specific (see the discussion below).

Table 5.2 The inhibition performance screening results after three cycles. The best-performing inhibitors (HEDP, PA and 'CPTCA + CHHCA') were run for five cycles. 'Yes' means shiny surface, while 'fail' means the film formation on the surface. A concentration of 0.112 mmol L-1 is used in all cases.

No.	Inhibitor	Glass	PMMA	No.	Inhibitor	Glass	PMMA
1	HEDP	yes	yes	16	PA	yes	yes
2	TMCPDA	fail	fail	17	GTA	fail	fail
3	CPDA	fail	fail	18	DHDAD	fail	fail
4	CPTCA	fail	yes	19	GA	fail	fail
5	THFTCA	fail	fail	20	PDA-12	fail	fail
6	FA	fail	fail	21	PDA-13	fail	fail
7	QA	fail	fail	22	SPS	fail	fail
8	CHDAA	fail	fail	23	BTCA	fail	fail
9	CHDA	fail	fail	24	BTTCA	fail	fail
10	CHTCA-135	fail	fail	25	BPCA	fail	fail
11	CHTCA-124	fail	fail	26	BHCA	fail	fail
12	TPCHTCA	fail	fail	27	DPA	fail	fail
13	CPTTCA	fail	fail	28	PZDA	fail	fail
14	CHHCA	yes	fail	29	GTDH	fail	fail
15	CPTCA+CHHCA	yes	yes	30	TTCDTCA	fail	fail

Table 5.3 The inhibition performance screen results after five cycles

Inhibitors	Concentration (mmol L^{-1})	PMMA slides	Glass
No inhibitor	/		
HEDP	0.112		
CPTCA+CHHCA	0.112+0.112		
PA	0.112		

When using the Nil-HEDP formula, both the glass and the PMMA slides showed film formation. As presented in Section 2.5, aragonite (001) with a small amount of pyramid-like calcite was observed to grow on the surfaces of the PMMA samples and calcite crystals were identified on the surfaces of the glass samples. As a matter of convenience, the images are shown below in Figure 5.3.
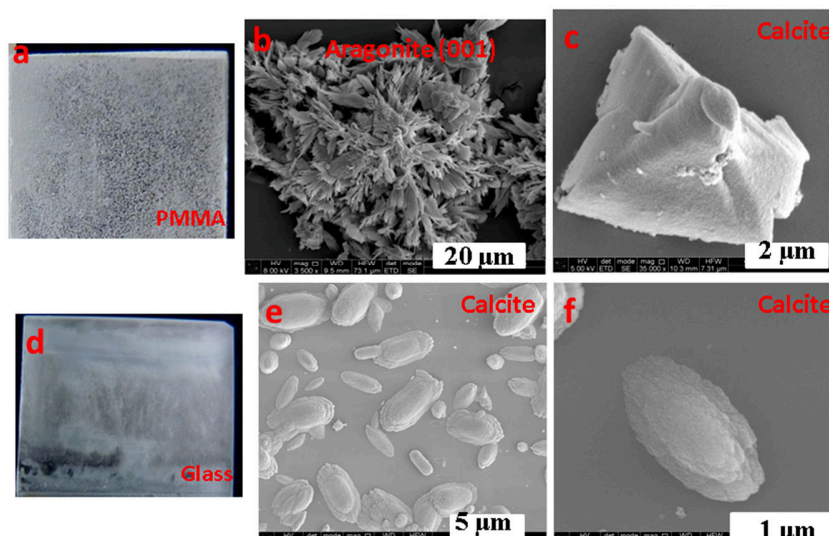
Figure 5.3 The PMMA (a-c) and glass slides (d-f) produced in the model system with 'Nil-HEDP formula.' The flora-like aragonite (001) and pyramid-like calcite observed on PMMA slide. The rice-like calcite observed on the glass slide.

Figure 5.4 presents surface changes due to the application of CPTCA, captured using SEM and PXRD and after three cycles. The observations demonstrate that the flora-like aragonite on the PMMA slide is completely inhibited, and the nucleation of pyramid-like calcite is also suppressed in the presence of CPTCA. However, the inhibition ability of CPTCA is hardly observed for crystals on glass slides. XPRD data as presented in Figure 5.4e confirms that the crystals on the glass slide are calcite. Those calcite crystals (Figure 5.4c & d) have similar morphologies to that observed in blank samples (Figure 5.3e & f). This indicates that CPTCA has strong inhibition effects on crystals grown on PMMA slides but not for glass samples. CPTCA has a specific inhibition ability to aragonite.
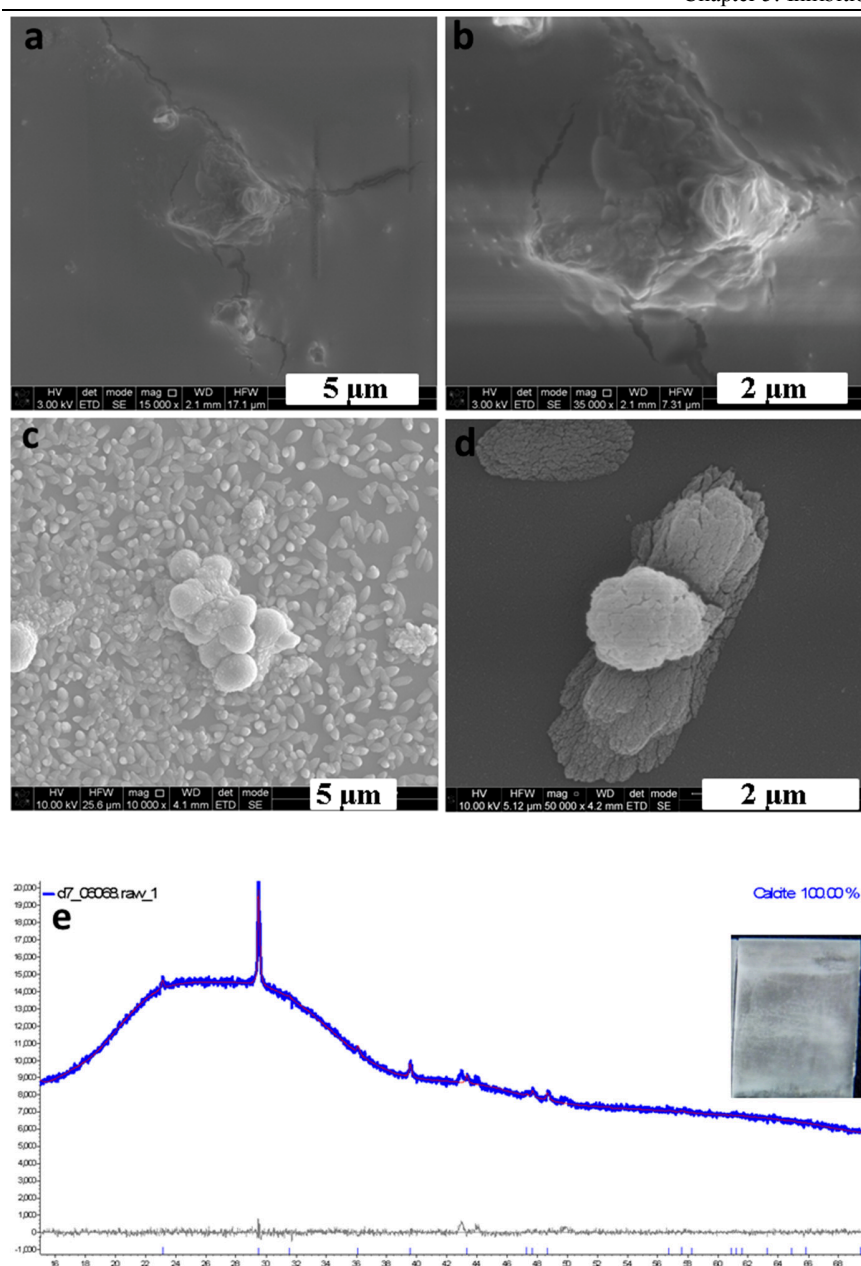
Figure 5.4 The CaCO₃ morphologies on PMMA slide (a&b) and the glass slide (c&d) when applying CPTCA and corresponding PXRD pattern after three cycles for glass slide. (a) Crystals observed with a magnification of 10000x (b) crystals observed at a magnification of 50000X (c) Rietveld refinements of PXRD patterns collected from glass, showing crystals as calcite. Refinement statistics: $R_{wp} = 1.24\%$, $R_p = 0.93\%$, $R_{B(calcite)} = 0.32\%$, GOF = 1.21. The experimental patterns and simulated pattern are shown in blue and red, respectively. The difference in the pattern is shown in gray. (PXRD code: d7_06068)

On the other hand, CHHCA has a similar inhibition effect but are opposite to that of CPTCA. CHHCA inhibits the crystal growth of calcite on glass slides but has no obvious retardation effects for crystals on PMMA slides. The SEM images illustrated in Figure 5.5 shows that the aragonite (001) and calcite on the PMMA slide (Figure 5.5a & b) is similar to those observed in

blank samples (Figure 5.3 b & c). While the inhibitory effect of CHHCA on the glass slide is obvious, only amorphous deposits were observed.
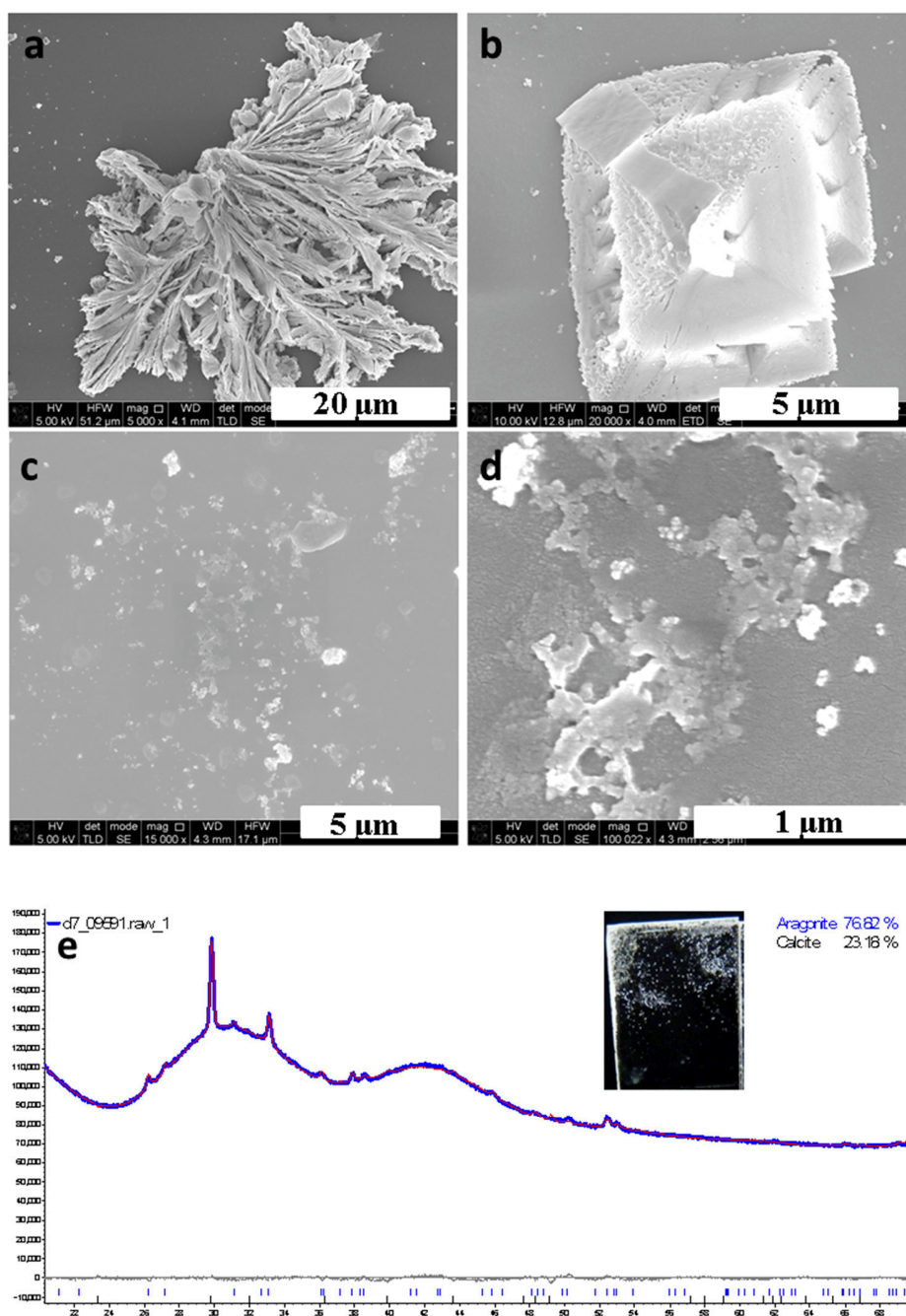
Figure 5.5 Rietveld refinements of PXRD patterns collected from PMMA slide after applying the CHHCA for three cycles shows the presence of aragonite and calcite, with aragonite (001) being dominant. It is indicated that calcite has a preferred orientation as well. Refinement statistics: R_{wp} = 0.62%, R_p = 0.48%, $R_{B(calcite)}$ = 041%, $R_{B(aragonite)}$ = 0.25%, GOF = 1.90. The experimental patterns and simulated pattern are shown in blue and red, respectively. The difference in the pattern is shown in gray. (XPRD code: d7_09591).
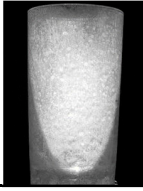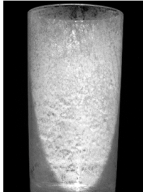
Based on the observations of CHHCA and CPTCA towards the precipitation of $CaCO_3$, it can be seen that CPTCA has a specific inhibition towards aragonite (001) while CHHCA can retard the growth of calcite. The inhibition specificity of additives was also observed with the two different hydration forms of $CaSO_4$ that polyvinyl sulfonate (PVS) and polyglutamic acid (PGA) interact specifically with calcium sulfate dihydrate and calcium sulfate hemihydrates, respectively.[2] The suggested mechanism has been attributed to structural compatibility between the additive and the crystal lattice.

By comparing the structure of CPTCA and CHHCA with HEDP in Chapter 4, the inhibition limitation is probably due to the nature of less negatively charged carboxylic acid groups present in CPTCA and CHHCA and the conformation rigidity of the cyclic ring. PA worked as efficiently as HEDP in the model system can support this assumption. The PA with the same concentration gave a shine similar to HEDP. It can be therefore concluded that the inhibition ability of the phosphate-containing inhibitors with a higher polarity is more superior. However, cyclic poly(carboxylic acids) can make up by applying a combination prescription.

PA is a saturated cyclic acid that can be found in cereals and grains.[3] Previous work has shown that the phytate only manifested toxic effects at very high doses (the LD50 value for male rats was 1.3 mmol kg^{-1} administered orally as sodium phytate.[4] Hence, it is not toxic to mammals at a concentration of 0.112 mmol L^{-1} which has been applied in this study. However, phytate can have a negative impact on the environment (i.e. eutrophication) even at low concentration because it is a phosphate-based compound. The two cyclic carboxylates, CPTCA and CHHCA have no negative environmental impacts that have been reported to this date. Therefore, a mix of CPTCA and CHHCA are proven to be the alternative phosphate-free inhibitors to HEDP and will be further evaluated in a real dishwasher. The full characterization results of the successful inhibitors including SEM images and PXRD analysis are attached in Appendix 5.

5.2.3 Test of the Inhibitors in a Real Dishwasher

Table 5.4 Evaluation of the new inhibitors under real dishwasher condition.

Substrate	Cycles	Nil -HEDP	with HEDP	With CPTCA + CHHCA
		No inhibitor	0.112 (mmol L^{-1})	0.112 +0.112 (mmol L^{-1})
Glass	Cycle 15			
	Cycle 30			
Plastic	Cycle 15			
	Cycle 30			

The two best-performing inhibitors, namely a mixture of CPTCA and CHHCA from a/the initial screening test, was further evaluated in a real dishwasher up to 30 cycles. The inhibition performance of the mixture 'CPTCA and CHHCA' was determined based on the shine that the inhibitors can retain in comparison to the HEDP standard. The resulting surfaces of both the glass and the plastic samples under the conditions of 'No inhibitor,' 'with HEDP,' and 'with CPTCA+CHHCA,' are presented in Table 5.4. The chemical conditions applied are the same as mentioned in Section 5.2.2. The test materials used were the glass tumblers and the polystyrene tumblers. The experimental procedure followed is the same as a standard dishwasher procedure (Section 2.3.1). The wash step was run up to 30 cycles and the test results obtained were in line with the performance observed using the model system, which confirms the inhibition effectiveness of CPTCA & CHHCA. The new inhibitors in combination can maintain the shine as efficiently as the HEDP.

5.3 Nucleation Delay or Crystal Growth Inhibition

In Section 5.2, it is observed that the presence of the HEDP or a mix of 'CPTCA and CHHCA' gives a visibly high shine surface. When observing in SEM, the amorphous clusters of calcium carbonate on the surface can still be observed, which is presented in Figure 5.6. The formation of the observed morphologies may be due to two possible reasons, one is the failure of forming critical nuclei for crystalline phases, and the other is nuclei have been formed, but its growth is severely inhibited to such extent that the surfaces become irregular and crystal growth ultimately stops.
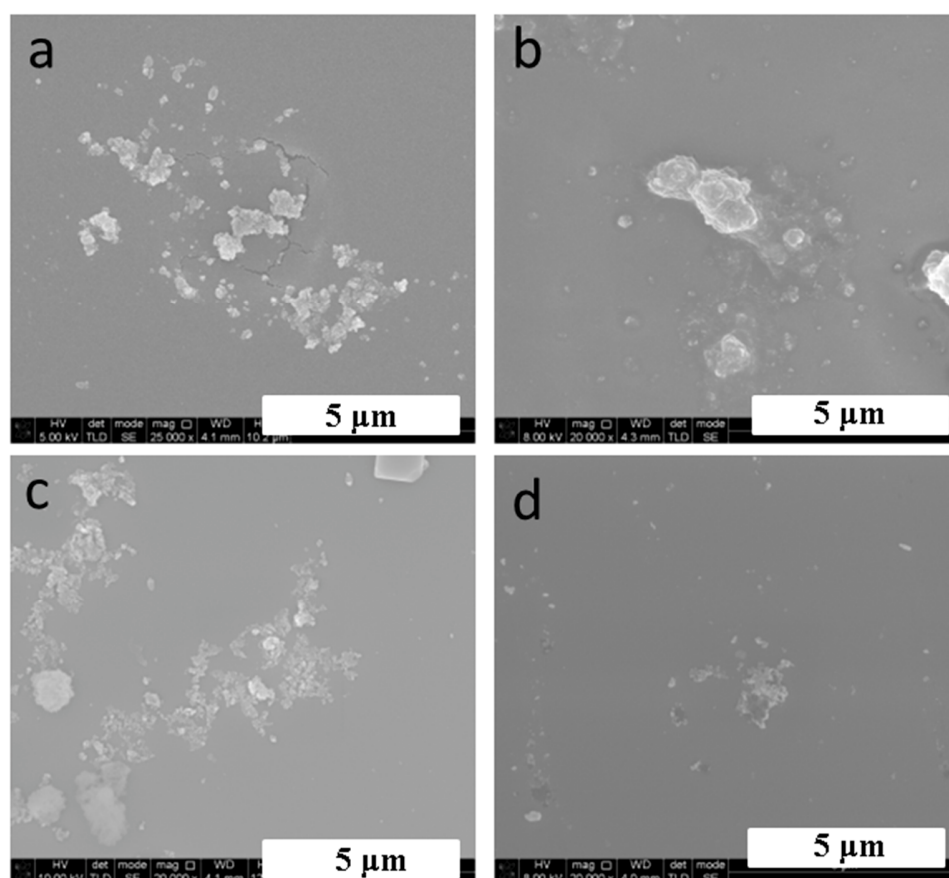
Figure 5.6 The deposits observed in the shining surface after applying HEDP (a&c) and 'CPTCA+CHHCA' (b&d). At a magnification 20000X.

To investigate the underlying mechanism, a simple experiment was carried out to assess whether the inhibitor operates by nucleation delay or as a crystal growth inhibitor. The experimental flow is as shown in Figure 5.7. This experiment is performed in a model system, and the experimental procedure is the same as the inhibition performance screening. The only difference is the

chemical composition (For details of experimental can go to Section 5.5.1). In the first cycles, the standard Nil-HEDP in Table 5.1 is used for generating two glass slides and two PMMA slides. After crystallization for an hour, the PMMA slides and glass sheets are taken out, rinsed with DI water and left in the air to dry. At the second cycle, glass slides and one PMMA slides generated in the first cycle are left in two different solutions, and the procedure is repeated. One solution involves standard Nil-HEDP formula, and the other applies HEDP formula.
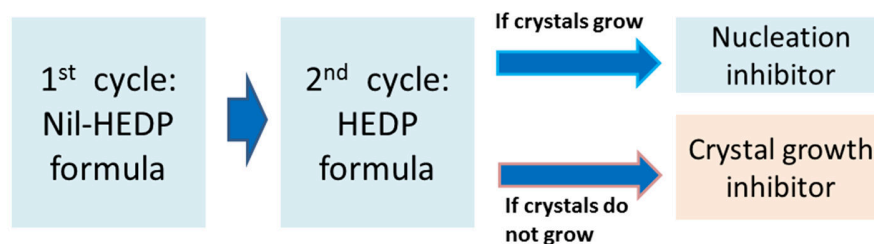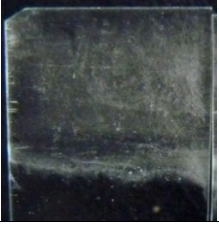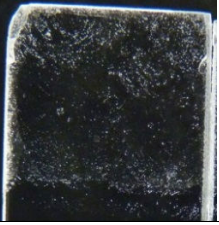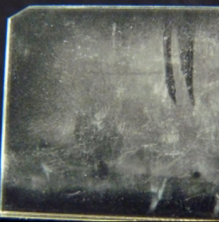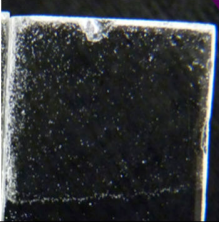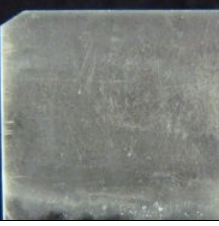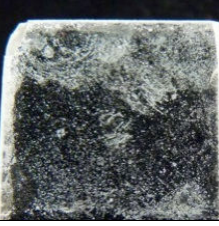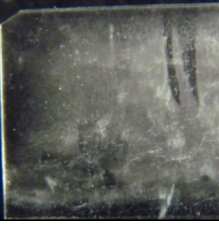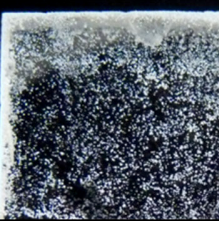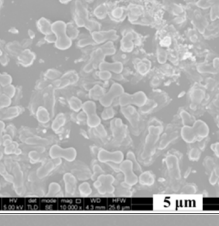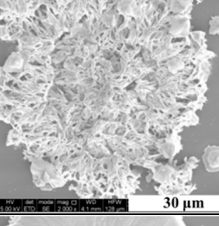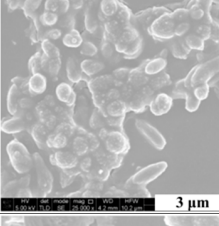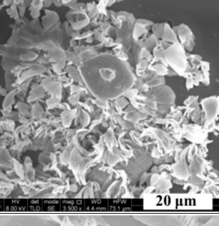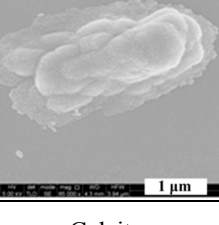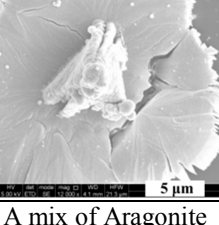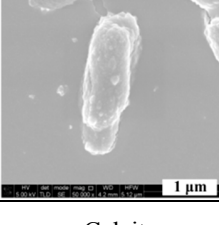
Figure 5.7 The experimental flow for the understanding of inhibition mechanism.

Table 5.5 presents the resulting surfaces after the 1st cycle and the 2nd cycle, which are recorded with a camera. The samples are also sent for the examination by SEM and PXRD. The clarity is assessed by a visual inspection and rated from 0 to 10, with 10 indicating no filming. The results did not give a single answer. Regardless the presence of HEDP, the crystals grow apparently on PMMA but not glass after the 2nd cycle. This means that HEDP has no inhibition effects on aragonite crystals but for calcite. Therefore it can still maintain the shine on the surface of the glass. This is probably because HEDP is an effective crystal growth inhibitor for calcite but not for aragonite.[5] Its inhibition effects on aragonite should have been taken place before the critical nuclei formed. For PMMA, where a mix of pyramid-like calcite and aragonite grow, the inhibition action of HEDP can only operate at the nucleation stage other than at the stage of crystal growth. This is probably why plastic, in particular, suffers more filming in the dishwasher than glass samples. Because HEDP can continue acting as an efficient crystal growth inhibitor for glass samples even though the nuclei of calcite formed.

Table 5.5 The resulting surface with characterization results by SEM and XPRD.

	No inhibitor for both cycles		No inhibitor @ 1st cycle and inhibitor @ 2nd cycle	
	Glass	**PMMA**	**Glass**	**PMMA**
1st Cycle				
Clarity	3	6	3	6
2nd Cycle				
Clarity	0	2	3	1
SEM				
PXRD	Calcite	A mix of Aragonite (001) and calcite	Calcite	A mix of Aragonite (001) and calcite

5.4 Conclusion

Preliminary experiments in model system show that PA and a mixture of CPTCA and CHHCA were found to show similar inhibition performance to HEDP under dishwasher conditions. All other carboxylic acid based inhibitors tested were ineffective. Interestingly, CPTCA and CHHCA are highly substrate specific with CPTCA inhibiting aragonite growth on PMMA while CHHCA inhibits calcite growth on glass. The influence on crystallization by inhibitors has been evidenced by SEM and PXRD analyses. This is further confirmed in a real-dishwasher condition that a mixture of CPTCA and CHHCA can be the phosphate-free alternative for HEDP.

Observation on HEDP also suggests that the inhibition action of HEDP can take place before the nucleation stage for aragonite, but HEDP cannot be a crystal growth inhibitor for aragonite as once aragonite formed on the surface, the presence of HEDP has no effects on its further growth. While HEDP is efficient for inhibition of calcite on glass both before and after nucleation.

5.5 Experimental

5.5.1 Experimental Details of Inhibitor Screening in the Model System

The detailed experimental procedure for the model system is as follows: PMMA sheets and glass sheets were fixed in pairs near the top of a glass container. The PMMA sheets were cut out from a large PMMA slide while the glass sheets are cut from microscope slides. Hard water similar to that used in the real dishwasher was prepared by dissolving $CaCl_2$ (0.1526 g, 2.75 mmol) and $MgCl_2$ (0.04805 g, 0.0806 mmol) in 500 ml deionized water (DI water). This solution was then transferred into the glass container to which the glass and PMMA sheets were attached and heated up to 65 ^{o}C, before adding the Nil-HEDP formula (Table 5.5) and the candidate inhibitor. The concentration of candidate inhibitor (CI) used was equal to that of HEDP, 0.112 mmol/L. The applied quantity of each inhibitor was varied depending on the molecular weight of each CI. The formula compositions, which are listed in Table 5.5, include Na_2CO_3 powder (0.954 g), Na_2SO_4 (0.306 g), MGDA (0.141g), Acusol 588G (0.129 g), the non-ionic mixture (0.175 g) and inhibitor (depends on the molecular weight of the applied inhibitor). In the model system, the amount of water and the formula used is ten times less than in the dishwasher.

<div align="center">Table 5.5 Nil-HEDP formula</div>

Nil Pv30 formula	Abbreviations	Raw material in water (g 5L^{-1})	Comments
Alkaline Builder			
Trisodium salt of methylglycinediacetic acid	Na$_3$MGDA	2.82	Chelator
Granular sodium carbonate	Na$_2$CO$_3$	7.10	pH buffer
Sodium sulphate	Na$_2$SO$_4$	3.06	Solid diluter
Polymer			
Sulfonated polyacrylates Acusol 588	Acusol 588G	1.29	
Surfactant			
Non-ionic mixture	Non-ionic mixture	1.28	

To ensure that all the detergent compositions dissolve at a similar speed, the powdered compositions were added simultaneously. The liquid non-ionic mixture was added last due to its high dissolution speed. The container was then covered, and the solution was kept at constant temperature of 65 °C for 1 hour. The stirring speed was at a constant rate of 100 rpm throughout the crystallization process. After crystallization for an hour, the PMMA slides and glass sheets were taken out, rinsed with cold and hot DI water (60 ^{o}C) for one minute, respectively. Following

this, the substrates were left in the air to dry. The procedure was then repeated until film formation was visible.

5.5.2 Analytical Method:

5.5.2.1 Scanning Electron Microscopy

The samples are coated with gold/ palladium prior to imaging by a HITACHI S-520 type scanning electron microscope (SEM).[6] Typically, a field free mode, operated at a voltage of 5 kV to 10 kV, is used for sample imaging

5.5.2.2 Powder X-ray Diffraction (PXRD):

PXRD patterns were collected on a Bruker D8000 powder diffractometer using a nickel- filtered copper X-ray radiation (λ = 1.5406 Å). Powder diffractometer operates at 40 mA and 45 kV. The 2θ range for calcium carbonate from 16° to 70° is recorded at a scan rate of 0.02 step^{-1}. The outcome data was further analyzed by the Topas software.[7]

5.6 References

1.   Gill, J. S., Development of Scale Inhibitors. In *NACE Corrosion Conference*, NACE International

Houston, United States, 1996; Vol. 229, pp 2-9.

2.   Sarig, S.; Kahana, F.; Leshem, R. *Desalination* **1975,** *17* (2), 215-229.

3.   Lopez, H. W.; Leenhardt, F.; Coudray, C.; Remesy, C. *Int. J. Food Sci. Technol.* **2002,** *37* (7), 727-739.

4.   Grases, F.; Perelló, J.; Isern, B.; Costa-Bauzá, A. *Water SA* **2007,** *33* (5), 749-754.

5.   (a) Jing, X. *Acta Phys. Sin. (Chinese Ed.)* **2006,** *55* (3), 1112; (b) Amjad, Z.; Zuhl, R. W., Kinetic and Morphological Investigation on the Precipitation of Calcium Carbonate in the Presence of Inhibitors. In *1996 NACE International Annual Conference and Exposition "Corrosion 2006",*, NACE International: Houston, Texas, 2006; Vol. 06385.

6.   Edwards, P. Scanning Electron Microscope. www.dur.ac.uk/cmp/research/groups/aim/sem/.

7.   Evan, S. O. J.; Coelho, A. Topas Academic www.dur.ac.uk/john.evans/topas_academic/topas_main.htm.

8.   Oner, M., Crystal Growth Inhibition of Calcium Sulfate and Calcium Oxalates in Aqueous Systems. In *The Science and Technology of Industrial Water Treatment*, Amjad, Z., Ed. CRC Press 2010: London, 2010; pp Pages 21–38.

9.   Chen, T.; Neville, A.; Sorbie, K.; Zhong, Z. *Faraday Discuss.* **2007,** *136*, 355-365.

10.   Berner, R. A.; Westrich, J. T.; Graber, R.; Smith, J.; Martens, C. S. *J. Am. Sci.* **1978,** *278* (6), 816-837.

11.   (a) Katsifaras, A.; Spanos, N. *J. Cryst. Growth* **1999,** *204* (1–2), 183-190; (b) Reddy, M. M. *J. Cryst. Growth* **1977,** *41* (2), 287-295.

12.   Jones, F.; Oliveira, A.; Rohl, A.; Parkinson, G.; Ogden, M.; Reyhani, M. *J. Cryst. Growth* **2002,** *237*, 424-429.

13.   Chung, J.; Granja, I.; Taylor, M. G.; Mpourmpakis, G.; Asplin, J. R.; Rimer, J. D. *Nature* **2016,** *536*, 446–450.

6 Conclusion

6.1 Understanding of CaCO₃ Surfaces Deposition and Control

The deposition of CaCO$_3$ in dishwashers, particularly on plastic, remains a problem. This project was carried out to gain an understanding of the surface crystallization of CaCO$_3$ and its control under dishwasher conditions. Experiments were carried out both in a real dishwasher system and in a convenient laboratory model as shown in Figure 6.1.
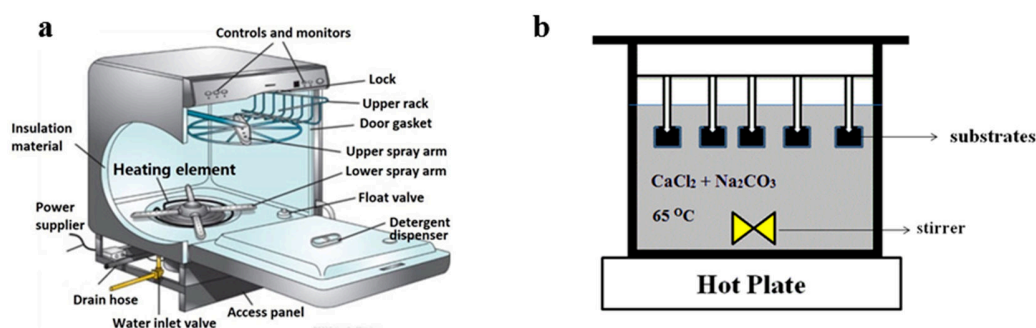
Figure 6.1: (a) A typical household dishwasher; (b) the model system without pump.
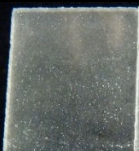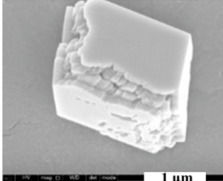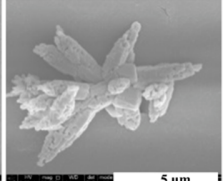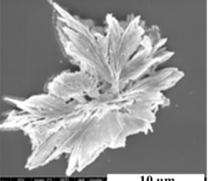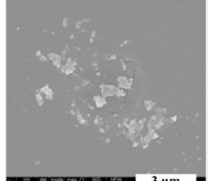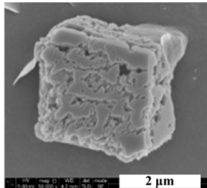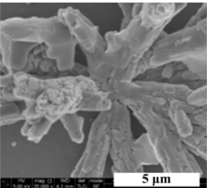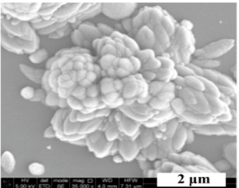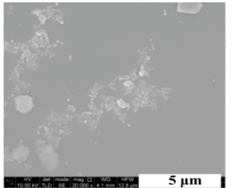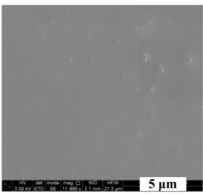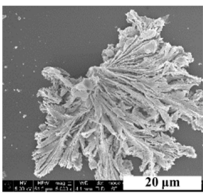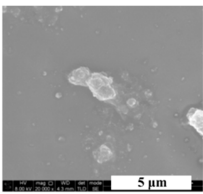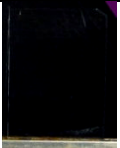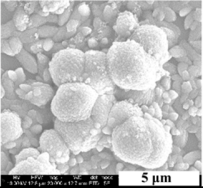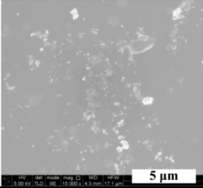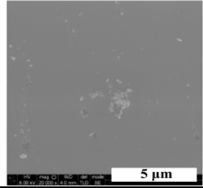
This model system (Figure 6.1b) is constructed based on a household automatic dishwasher (Figure 6.1a). It can be used to explore the factors that affect the surface deposition in a dishwasher. There are three classes of parameters in a dishwasher which affect the surface deposition which have been addressed in this work: (1) the system parameters: pH and temperature of the solution, (2) the nature of the substrate and (3) the chemistry of the solution. Surface-active additives (ions, polymer, and inhibitor) exhibit the most significant effects.[8] Moreover, the model system can be used as a fast and inexpensive way for reproducing mineral deposits and inhibition performance screening. The deposition and screening results have proven consistent with the results which arise in the real dishwasher.

Both the experimental observation and literature evidence[9] show once the first layer of crystals has formed, the growth rate of the crystal increases dramatically and the subsequent growth rate is mainly controlled by the supersaturation level. With the same system parameters, the only

difference in the surface deposition between glass and PMMA substrates is the surface properties. Glass and PMMA have different surface chemistries and the former has a smoother surface than the later. Under dishwasher conditions, with a saturation index = 3.37, high pH and high temperature promote the surface crystallization of $CaCO_3$, especially the growth of aragonite, giving a ratio of aragonite: calcite of 3:2. The presence of Mg^{2+} ions in water further promote the growth of aragonite on the surface, giving a ratio of aragonite: calcite of 3:1. The suggested inhibition effects[10] of the Mg^{2+} ions were not observed in our system. This may be due to the fact that the inhibition action of Mg^{2+} targets calcite crystals but not aragonite.[10] Before the involvement of dishwasher detergent (prototype Nil-HEDP formula provided by P&G Newcastle), the distribution of the polymorphic forms of $CaCO_3$ on glass and PMMA were the same. Both the glass and the plastic substrates, when the dishwasher detergent is absent, suffer from filming. The substrate-specific effects, in terms of surface roughness, were not observed.

When applying the dishwasher detergent without an inhibitor, it is observed that it is the polymer, rather that the other ingredients in the dishwasher detergent, which promotes $CaCO_3$ deposition on the surface, especially for plastic samples. The polymer changes the distribution of the polymorphic forms on both of the glass and plastic surfaces, promoting the aggregation of aragonite (001) on the surface of plastic in an organized way. The loss of shine on plastic surfaces is obvious. On the surface of the glass, only calcite is observed (Table 6.1). There are inconsistencies between the results of the glass samples produced from the dishwasher and those from the model system. However, as can be seen from Chapter 3, it is always easier to retain the shine for glass samples as long as the washing detergent is applied. The presence of orthophosphate ions in solution is also highly effective in shine maintenance, which can be attributed to its ability to inhibit calcite.[11] However, shine maintenance for plastic samples is difficult when the inhibitor is absent. When HEDP is applied, the shine can be retained up to 40 cycles. However, once crystals have formed on the surface HEDP is still effective in stopping the further crystal growth for the glass substrate but not for the PMMA slides. This may be because HEDP is a good nucleation inhibitor and an effective inhibitor for calcite but may not be an effective crystal growth inhibitor for aragonite. This is probably why plastic, in particular, suffers from filming in dishwashers. Therefore, extra attention should be given to plastic samples when choosing the inhibitor and polymer for dishwasher detergent.

Table 6.1 The effects of Nil-HEDP and inhibitors for glass and PMMA samples.

Composition	Ca, Mg, CO$_3^{2-}$	Nil-HEDP Formula	HEDP Formula
PMMA			
Glass			

Composition	CPTCA+ Nil-HEDP Formula	CHHCA+ Nil-HEDP Formula	CPTCA + CHHCA + Nil-HEDP Formula
PMMA			
Glass			

6.2 The Structure Characteristics of an Effective Inhibitor

A mixture of CPTCA and CHHCA exert similar inhibitory effects as HEDP; hence could be a potential, phosphate-free alternative inhibitor to replace HEDP. The inhibition abilities of CPTCA and CHHCA are polymorph specific (Table 6.1). The polymorphs observed were from the completed and repeated crystallization process, rather than the very early stage of crystallization. Hence, detailed information about the formation of the first crystal layer, especially the growing sequence of the crystal planes on different surfaces, is unknown. However, as far as we can see, CPTCA and CHHCA inhibit the growth of aragonite (001) and calcite, respectively (Table 6.1). Interestingly, other related oligo-carboxylates do not show useful inhibition performance.
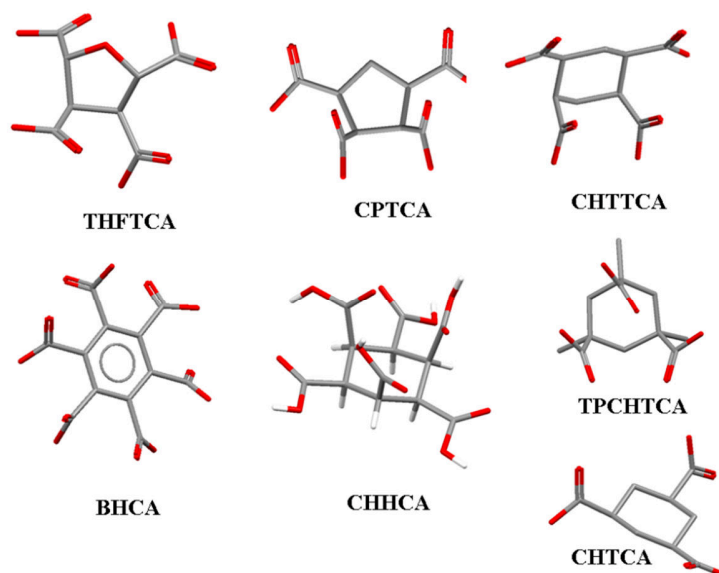
Figure 6.2 The stereochemical arrangement of the cyclic poly (carboxylic acids). THFTCA (CSD-ZEZLEV);[12] CPTCA (CSD-AWUVEU):[13] CHTTCA (CSD-EJEQOZ):[14] BHCA (CSD-MELLIT);[15] CHHCA (CSD-GOHWAD);[16] TRCHTCA (CSD-DEVCOW);[17] CHTCA (CSD-BANGON).[18]

The specificity observed when using a polymer, HEDP, CPTCA and CHHCA may be due to the surface properties of the glass and plastic substrates themselves, substrates whose surface properties have been modified by the polymer, or the polymer changed the interplay of the substrate with mineral ions. The exact cause is unknown. Replacing the old polymer in dishwasher detergent with a new polymer with a similar ability may be beneficial for the shine

maintenance for plastic samples. The compatibility of the new inhibitors and the new polymer should be checked.

Literature evidence shows[19] that the inhibition effectiveness of an inhibitor is related to the number of the functional groups within the molecule. It is known that two gem-diphosphonate functional groups are sufficient for mineral inhibition. However, in the case of carboxylate groups, which are less polar, four or six carboxylate groups attached to different carbons in the ring are required to be effective. It is shown that 1,2,3,4-cyclopentane tetracarboxylic acid (CPTCA) and 1,2,3,4,5,6-cyclohexane hexacarboxylic acid (CHHCA) are effective inhibitors for polymorphs on PMMA and glass, respectively. This is probably related to the very first $CaCO_3$ clusters formed on the surface. Therefore, if molecular modeling can reveal the conformation that HEDP adopted when inhibiting calcite and aragonite and compare it to that of CPTCA inhibiting aragonite and CHHCA inhibiting calcite, some mechanistic insight may be obtained.

In our observation, there are only two types of inhibitors: effective and ineffective inhibitors. It seems that inhibition ability is not proportional to the number of the functional groups. Instead, to inhibit crystallization a critical charge density needs to be achieved or the inhibitor will be ineffective. The charge density of small molecules, if evaluated as a whole, can be roughly expressed as followed: [(polarity of a single functional group) * (number of the functional groups)] / [(size of the backbone)]. The magnitude of the overall negative charge is decided by the type and number of the functional groups. The functional group should be an effective functional group, which participates in docking. Once the functional groups are confirmed, the backbone and the size of the inhibitor becomes important. The size of the backbone affects the magnitude of the overall negative charge, and the nature of the backbone determines the orientation of the functional groups. For example, due to the isomeric form of the tetrahydrofuran-2,3,4,5-tetracarboxylic acid (THFTCA) used, the four functional groups are not on the same side of the ring plane. However, there are two carboxylic acid groups above the plane of the ring and the other two carboxylic acid functional groups below the plane of the ring. The alternative all-cis isomer available for CPTTCA means that it has four functional groups on the same side of the plane (Figure 6.2). It is quite surprising that CHTTCA and CPTCA with the same number of functional groups but subtle difference in isomeric form and backbone lead to

such a substantial change in inhibition efficacy. This is similar to the observation made by Chung.[20]

It seems that even if the critical charge density is achieved, it is still necessary to preorganize the functional groups to fit onto the growing surface. All of the aromatic polycarboxylic acids have rigid conformations. Take BHCA for example (Figure 6.2); the benzene ring restricts the binding by holding all of the functional groups in a planar arrangement making it hard to adopt the conformations required for docking. CHHCA has more conformation freedom, and all of the functional groups are in the all-cis geometry (Figure 6.2). However, functional groups in CHHCA have two different orientations, three carboxylic acid groups vertically attached to the cyclic ring and the other three carboxylic acid groups lay back and lie down. CHHCA seems like a combination of both TPCHTCA and CHTCA. Since both TPCHTCA and CHTCA are not effective inhibitors, we can suspect the docking of CHHCA is via two adjacent carboxylic acid functional groups instead of via the meta-dicarboxylic acid groups or at least the involvement of two adjacent carboxylic acid functional groups in inhibition behavior is essential.

There are two different phytic acid isomers which are available in the market. The phytic acid isomer shown in Figure 6.3b has been studied in this project and shown to work as efficiently as HEDP. Further studies could be carried out on the phytic acid isomer in Figure 6.3a. Detailed structural comparisons of this type may result in insight into the common denominator for an efficient inhibitor for $CaCO_3$ under dishwasher conditions.
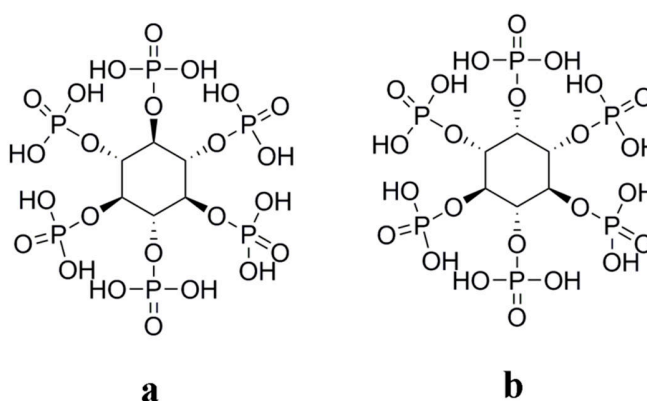
Figure 6.3 Phytic acids

6.3 References

1.   Gill, J. S., Development of Scale Inhibitors. In *NACE Corrosion Conference*, NACE International

Houston, United States, 1996; Vol. 229, pp 2-9.

2.   Sarig, S.; Kahana, F.; Leshem, R. *Desalination* **1975,** *17* (2), 215-229.

3.   Lopez, H. W.; Leenhardt, F.; Coudray, C.; Remesy, C. *Int. J. Food Sci. Technol.* **2002,** *37* (7), 727-739.

4.   Grases, F.; Perelló, J.; Isern, B.; Costa-Bauzá, A. *Water SA* **2007,** *33* (5), 749-754.

5.   (a) Jing, X. *Acta Phys. Sin. (Chinese Ed.)* **2006,** *55* (3), 1112; (b) Amjad, Z.; Zuhl, R. W., Kinetic and Morphological Investigation on the Precipitation of Calcium Carbonate in the Presence of Inhibitors. In *1996 NACE International Annual Conference and Exposition "Corrosion 2006",*, NACE International: Houston, Texas, 2006; Vol. 06385.

6.   Edwards, P. Scanning Electron Microscope.
www.dur.ac.uk/cmp/research/groups/aim/sem/.

7.   Evan, S. O. J.; Coelho, A. Topas Academic
www.dur.ac.uk/john.evans/topas_academic/topas_main.htm.

8.   Oner, M., Crystal Growth Inhibition of Calcium Sulfate and Calcium Oxalates in Aqueous Systems. In *The Science and Technology of Industrial Water Treatment*, Amjad, Z., Ed. CRC Press 2010: London, 2010; pp Pages 21–38.

9.   Chen, T.; Neville, A.; Sorbie, K.; Zhong, Z. *Faraday Discuss.* **2007,** *136*, 355-365.

10.   Berner, R. A.; Westrich, J. T.; Graber, R.; Smith, J.; Martens, C. S. *J. Am. Sci.* **1978,** *278* (6), 816-837.

11.   (a) Katsifaras, A.; Spanos, N. *J. Cryst. Growth* **1999,** *204* (1–2), 183-190; (b) Reddy, M. M. *J. Cryst. Growth* **1977,** *41* (2), 287-295.

12.   Feil-Jenkins, J. F.; Nash, K. L.; Rogers, R. D. *Inorg. Chim. Acta* **1995,** *236* (1), 67-74.

13.   Lin, J.-L.; Guo, X.-X.; Huang, W.-X. *Acta Crystallogr. Sect. E* **2011,** *67* (8), 1945.

14.   Uchida, A.; Hasegawa, M.; Manami, H. *Acta Crystallogr. Sect. E* **2003,** *59* (8), 435-438.

15.   Darlow, S. *Acta Crystallogr.* **1961,** *14* (2), 159-166.

16.   Thuery, P., Cyclohexane-1,2,3,4,5,6-Hexacarboxylic Acid Tetrahydrate. Communication, P., Ed. 2012.

17.   Rebek, J.; Marshall, L.; Wolak, R.; Parris, K.; Killoran, M.; Askew, B.; Nemeth, D.; Islam, N. *J. Am. Chem. Soc*. **1985,** *107* (25), 7476-7481.

18.   Bhogala, B. R.; Vishweshwar, P.; Nangia, A. *Cryst. Growth Des*. **2002,** *2* (5), 325-328.

19.   Jones, F.; Oliveira, A.; Rohl, A.; Parkinson, G.; Ogden, M.; Reyhani, M. *J. Cryst. Growth* **2002,** *237*, 424-429.

20.   Chung, J.; Granja, I.; Taylor, M. G.; Mpourmpakis, G.; Asplin, J. R.; Rimer, J. D. *Nature* **2016,** *536*, 446–450.

21.   Mullin, J. B., *Crystallization*. 4th Edition ed.; Butterworth-Heineman: Oxford, 2001; p 587.

22.   (a) Zhang, X.; Huang, Y.-Y.; Zhang, M.-J.; Zhang, J.; Yao, Y.-G. *Cryst. Growth Des.* **2012,** *12* (6), 3231-3238; (b) Kok, D. J.; Blomen, L. J. M. J.; Westbroek, P.; Bijvoet, O. L. M. *Eur. J. Biochem.* **1986,** *158* (1), 167-172.

23.   Borman, A. H.; Jong, E. W.; Huizinga, M.; Kok, D. J.; Westbroek, P.; Bosch, L. *Eur. J. Biochem.* **1982,** *129* (1), 179-183.

24.   Sato, M.; Matsuda, S. *Z. Kristallogr.* **1969,** *129* (5-6), 405-&.

25.   (a) Verch, A.; Gebauer, D.; Antonietti, M.; Cölfen, H. *Phys. Chem. Chem. Phys.* **2011,** *13* (37), 16811-16820; (b) Gao, W.; Ma, X. Y.; Wang, Z. C.; Zhu, Y. C. *Colloids and Surfaces a-Physicochemical and Engineering Aspects* **2011,** *389* (1-3), 230-236; (c) Cooper, S. J., Crystallizaion Kinetics. Lecture slide.

26.   (a) Silyn-Roberts, H.; Sharp, R. In *Crystal Growth and the Role of the Organic Network in Eggshell Biomineralization*, Proceedings of the Royal society of London. Series B. Biological sciences, London, The Royal Society: London, 1986; pp 303-324; (b) Wray, J. L.; Daniels, F. *J. Am. Chem. Soc.* **1957,** *79* (9), 2031-2034.

27.   Bruker AXS, Topas Academic: General Profile and Structure Analysis Software for Powder Diffraction Data. Karlsruhe, 2000.

Appendix 1

---Supplementary Information Relating to Chapter 1

1. Calculation of the activity (α) of solute in solution.[21]

For non-ideal solutions, the free energy is actually influenced by the active concentration. The activity coefficient (γ) is introduced to correct c to the active concentration by Equation 1.28

$$\alpha = \gamma c \quad\quad\quad\quad \text{Equation 1}$$

A proper estimate of the activity coefficient (γ) in a non-ideal solution is important for predicting the value of solubility. For a solid dissolving in solution, the process can be described as:

$$M_m X_n (\text{solid}) = nM^+ + mX$$
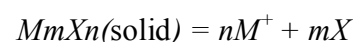
For an electrolyte solution, the mean ionic activity $\alpha_\pm$ is more appropriate to use. It is defined as:

$$\alpha = a_\pm^v = \left(\overline{c}_\pm \gamma_\pm\right)^v = \left(Qc\gamma_\pm\right)^v \quad\quad\quad\quad \text{Equation 2}$$

Where, $\gamma_\pm$ represents the mean ionic activity coefficient, $\overline{c}_\pm$ represents the mean ionic concentration, v is the magnitude of the charge on the ion, c is the concentration. Q is related to the number of ions in solution. The value of v and Q is calculated according to Equation 1.30 and Equation 1.31, respectively.

$$v = v_+ + v_- \quad\quad\quad\quad \text{Equation 3}$$

And

$$Q = \left(v_+^{v_+} v_-^{v_-}\right)^{1/v} \qu\quad\quad\quad \text{Equation 4}$$

The mean ionic activity can be obtained by the electrolytes theory of Debye-Hueckel and is given as:

262

$$\log \gamma_{\pm} = -A \left| z_+ z_- \right| I_s^{1/2}$$

Equation 5

Where A is given by Equation 1.33

$$A = \frac{e^3 \left(2000 \times N_{\mathrm{A}} \right)^{1/2}}{8\pi \left(\varepsilon \varepsilon_0 k_B T \right)^{3/2} \ln(10)}$$

Equation 6

Where e is the charge on an electron, ε_r, ε_0 are the relative permittivity and vacuum permittivity, respectively k_B, is Boltzmann's constant, N_A is Avogadro's constant and T is temperature. A = 0.509 for aqueous solutions at 298 K.

Ionic strength is related to the species concentration and their corresponding charges (z) and is given as:

$$I_s = \frac{1}{2} \sum c_i z_i^2$$

Equation 7

Table 1 Crystallographic information for calcium carbonate polymorphs
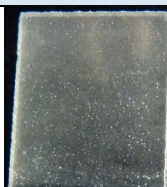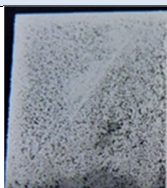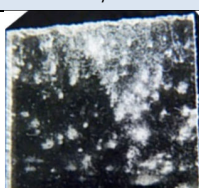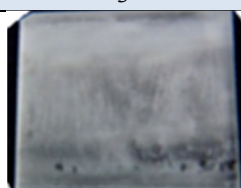
Polymorph	Crystal system	Unit cell (Å)	Density (g cm^{-3})	Info.
Calcite[22]	Hexa	a = 4.99 b = 4.99 c = 17.1	2.71	$\alpha = \beta = 90°; \gamma = 120°$ rhombohedra
Aragonite[22a, 23]	Ortho.	a = 4.96 b = 7.96 c = 5.74	2.94	$\alpha = \beta = \gamma = 90°$ needle-like
Vaterite[22, 24]	Hexa.	a = 4.13 b = 4.13 c = 8.48	2.54	$\alpha = \beta = 90°; \gamma = 120°$ spherical shape
HCC[25]	Mono.	a = 8.87 b = 8.23 c = 11.02	1.80	$\alpha = \beta = 90; \gamma = 110.02°$ prismatic crystal; 30 x 30 x 15 μm
MCC[25a, 26]	Hexa.	a = 10.54 b = 10.54 c = 7.56	2.38	D = 100 nm to 100μm spherical shape
ACC[22a]	/	/	/	little spheres; D = 1nm to 1 μm

*Hexa.= Hexagonal; Mono = Monoclinical; Ortho = Orthorhombic; D = diameter

Appendix 2

− Supplementary Information Relating to Chapter 2

Table 2 The shininess of PMMA and glass samples produced by model system after five cycles

Row label	formula	PMMA with clarity	Glass with clarity
A	HEDP formula	10	10
B	Carbonate only	3	3
C	Full Nil-HEDP Formula	1	3
D	Full, no polymer	7	3
E	Full, no surfactant	3	3

Polystyrene samples from the real-life dishwasher

A summarized characterization results by PXRD and SEM of three different substrates is shown Table 3. The polymorphs information is collected by PXRD and analyzed by the software called

jedit-TOPAS.[27] It can be seen from Table 3 that when polymer absent ('carbonate only' and 'full minus polymer'), the $CaCO_3$ polymorphs observed among these three samples are similar, namely, the aragonite crystals with a similar morphology are the dominant polymorph. When polymer present ('full with polymer'), the polymorphs observed on surfaces are different substrates are different. Since both the glass tumbler and PMMA slides have been discussed in Chapter 2, Section 2.6.2, only the study on the polystyrene samples will be mainly discussed here below.

When using the Nil-HEDP formula ('full with polymer'), the characterization results for both sides of the polystyrene plastic are shown in Table 4. The film observed on both sides is not evenly distributed, and the film on some area is much thicker than other parts. Hence, both sides including the thin and thick film areas of each side, are collected. It is observed that there is a mix of calcite and aragonite detected by PXRD on the thick film area, regardless of the side. For the thick film parts of both sides, aragonite is observed to be the dominant phase, where the aragoite crystal also has a preferred orientation of (001). The detection made by PXRD is consistent with the SEM observations as can be seen in Table 4 (see images a, b, e and f). The only difference is the thicker film from the inside of the polystyrene tumbler has a higher ratio of aragonite to calcite (A/C) than that of outside surface.

For the area with thin films of the both sides, no peaks of PXRD observed due to the lack of samples. However, based on the observation from SEM and comparing to the polymorphs observed on thick area, it can be seen that only one $CaCO_3$ morphology is observed but the morphologies observed on both sides are different (Table 4, Image c, d g and h). The crystals observed by SEM in the thin film of the inner surface have aragonite-like morphologies (Table 4 Image g and h). This observation is similar to what we found on PMMA surfaces, which is aragonite (001) with trace calcite. However, the crystals observed on the outer surface of PS are caclite-like crystals. As a summary, thick film part of both sides of the polystyrene (produced by full formula with polymer) is a mix of aragonite (001) and calcite, with aragonite being the dominating phase. For the thin film part of both sides, the morphologies of the crystals are different. The aragonite-like and calcite-like morphologies are observed on the inner and outer surfaces of polystyrene plastics, respectively.

Table 3 The samples of different substrates produced from a real-life dishwasher
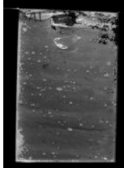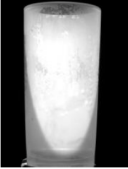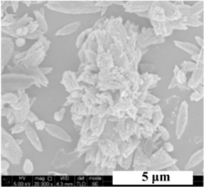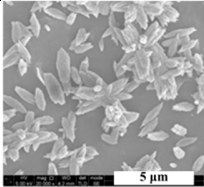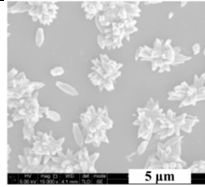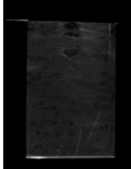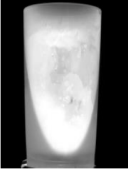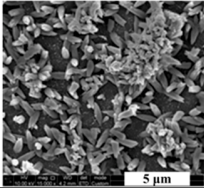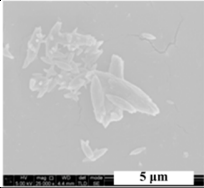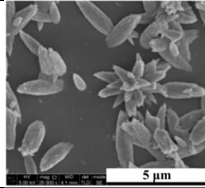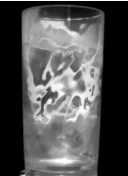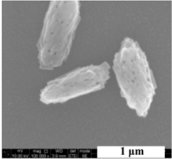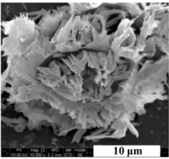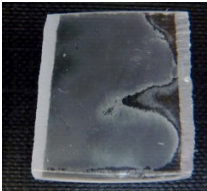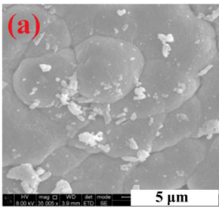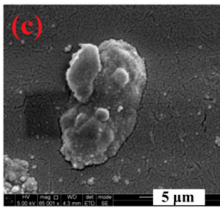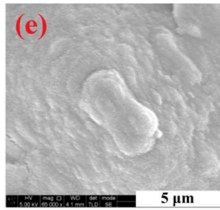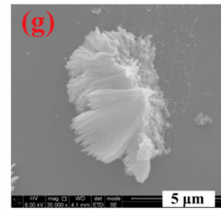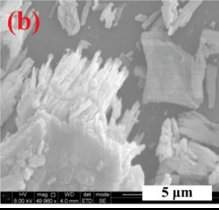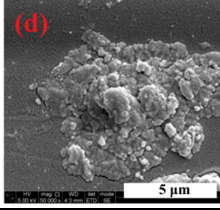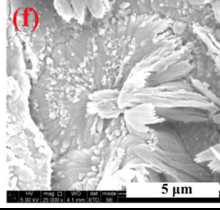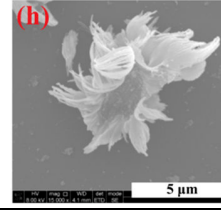
Carbonate only		Glass	PMMA	Polystyrene
Images with clarity (%)		**0.0**	**65.8**	**6.0**
PXRD	On substrate	A/C =96/4 (±3.2%)	Caclite	A/C = 86/14(±3.7%)
	Scraped powder	**A/C=81/19 (±0.6%)**	**A/C=88/12 (±1.3%)**	**A/C=75/25 (±0.5%)**
SEM				
Full minus polymer		Glass	PMMA	Polystyrene
Images with clarity (%)		**0.0**	**86.0**	**11.0**
PXRD	On substrate	A/C=93/7 (±6.0%)	No peak observed	No peak observed
	Scraped powder	**A/C=94/6 (±0.3%)[R]**	**No enough sample**	**A/C=89/11 (±0.4%)**
SEM				
Full with polymer		Glass	PMMA	Polystyrene
Images with clarity (%)		75.2	15.5	42.5
PXRD	On substrate	No peak observed	aragonite (001)	See Table 5 for details
	Scraped powder	**No enough sample**	**A/C=99/1 (±0.1.9%)**	**See Table 5**
SEM				See Table 5 below for detals

Table 4 The PXRD and SEM results of the outer and th inner surfaces of polystyrene plastic produced by full Nil-HEDP formula after 5 cycles from the real-life dishwasher.

SAN plastic, full		Outside of the SAN plastic		Inside of the SAN plastic	
Description		The thick film part: A mix of calcite and aragonite (001) The ratio of A/C= 3/2. The thin film part: Calcite-like morphology. The PXRD is unavailable due to the lack of sample.		The thick film part: A mix of calcite and aragonite (001) with a ratio of A/C = 6/1. The thin film part: Aragonite-like morphology. The PXRD is unavailable due to the lack of sample.	
		Outside of SAN plastic, thick film	**Outside of SAN plastic, thin film**	**Inside of SAN plastic, thick film**	**Inside of SAN plastic, thin film**
Image					
PXRD	On substrate	A (001)/C = 60/40 (±11.5%)	No enough sample	A (001)/C = 89/11 (±7.6%)	No enough sample
	Scraped powder	A/C = 63/37 (±1.2%)	No enough sample	A/C = 86/14 (±0.9%)	No enough sample
SEM					

Appendix 3

− Supplementary Information Relating to Chapter 3

Information for PXRD patterns:

The powder X-ray diffraction data that related to Chapter 3 are enclosed in a CD-ROM, which includes raw. and inp. files. The inp. files can be open by TXT. The structure refinements were performed using the TOPA academy.[1,2] The refinement details are given in inp. files. The following tables show below are the file names and the corresponding refinement results. For each sample, two PXRD patterns are collected: one collected with substrate showing the information of preferred orientation (above), the other is scraped powder indicates the ratio of aragonite to calcite (below).

Glass samples

Table 5 Summary of glass samples after 39 cycles. The slash part means samples is not available.

	Leg	Without Ortho phosphate in water			With Ortho phosphate in water		
		Leg1	**Leg4 (55**	**Leg3**	**Leg5**	**Leg8 (55 °C)**	**Leg7**
		Formula only	Formula	With HEDP	Formula only	Formula only	With HEDP
On substrate	Raw file	d7_03256	d7_03258	d7_03307	d7_03534	d7_03565	d7_03564
	simulation	No peaks	No peaks	No peaks	No peaks	No peaks	No peaks
Powder	Raw files	d7_03712	/	/	/	/	/
	simulation	Calcite	/	/	/	/	/
	R Value	$R_{wp} = 4.09\%$, $R_p = 3.25\%$, $R_{B(calcite)} = 1.08\%$, GOF = 1.41.	/	/	/	/	/
overall	**Conclusion**	**Calcite**	/	/	/	/	/

Table 6 Summary of PMMA samples the early cycles.

		With Ortho phosphate in water		With Ortho phosphate in water	
	Leg	**Leg1**	**Leg4 (55 ºC)**	**Leg5**	**Leg8 (55 ºC)**
On substrate	Raw file	d7_02759	d7_02629	d7_02910	d7_02908
	simulation	Aragonite (001)	Aragonite(001)/calcite= 86% (±1.3%)/14%	one peak calcite (104)	one peak calcite (104)
		R_{wp} = 1.22%, R_p = 0.95%, $R_{B(aragonite)}$ = 1.18%, GOF = 1.27.	R_{wp} = 0.84%, R_p = 0.69%, $R_{B(calcite)}$ = 0.32%,$R_{B(aragonite)}$ = 0.95%, GOF = 1.21	one peal may not worth refinement. No preferred orientation observed	one peal may not worth refinement. No preferred orientation observed
Powder	Raw files	d7_04707	d7_04176	d7_03902	d7_03909
	simulation	Aragonite/Calcite= 99% (±0.01%)/1%	Aragonite/Calcite = 98% (±0.2%)/2%	calcite	calcite
	R value	R_{wp} = 2.67%, R_p = 1.92%, $R_{B(calcite)}$ = 1.42%, $R_{B(aragonite)}$ = 1.18%, GOF = 2.76.	R_{wp} = 3.71%, R_p = 2.90%, $R_{B(calcite)}$ = 0.45%, $R_{B(aragonite)}$ = 1.02%, GOF = 1.29	R_{wp} = 4.45%, R_p = 3.32%, $R_{B(calcite)}$ = 1.52%, GOF = 1.85	R_{wp} = 2.97%, R_p = 2.32%, $R_{B(calcite)}$ = 0.72%, GOF = 1.17
overall	**Conclusion**	**Aragonite (001)/ Calcite= 99% (±0.01%) /1%**	**Aragonite (001) /Calcite = 98% (±0.2%) /2%**	**calcite**	**calcite**

Table 7 Summary of PMMA samples of the excessive cycles.

		Without Ortho phosphate in water			With Ortho phosphate in water		
	Leg	**Leg1** Formula only	**Leg4 (55 °C)** Formula only	**Leg3** With HEDP	**Leg5** Formula only	**Leg8 (55 °C)** Formula only	**Leg7** With HEDP
On substrate	Raw file	d7_03463	d7_03279	d7_03278	d7_03493	d7_03501	d7_03494
	simulation	A(001)/C= 56%(±1.8%)/44%.	A(001)/C= 31%/69%(±2.0%)	A(001)/C= 70%(±3.5%)/30%	Calcite (104)	Calcite (104)	No peaks
	R value	$R_{wp}=1.5\%$, $R_p=1.22\%$, $R_{B(calcite)}=0.33\%$, $R_{B(aragonite)}=0.36\%$, $GOF=1.39$	$R_{wp}=1.46\%$, $R_p=1.16\%$, $R_{B(calcite)}=0.34\%$, $R_{B(aragonite)}=0.45\%$, $GOF=1.28$.	$R_{wp}=1.28\%$, $R_p=1.02\%$, $R_{B(calcite)}=0.65\%$, $R_{B(aragonite)}=1.20\%$, $GOF=1.20$.	One peak	One peak	/
Powder	Raw files	d7_03856	d7_03931	d7_05203	d7_03927	d7_09208	d7_03922
	simulation	A/C= 52% (±1.5%) /49%	A/C= 16%/84% (±1.3%)	A/C= 83%(±0.65%)/17%	Calcite	Calcite	No enough sample
	R value	$R_{wp}=4.20\%$, $R_p=3.32\%$, $R_{B(calcite)}=0.81\%$, $R_{B(aragonite)}=0.96\%$, $GOF=1.18$	$R_{wp}=4.66\%$, $R_p=3.73\%$, $R_{B(calcite)}=0.50\%$, $R_{B(aragonite)}=1.46\%$, $GOF=1.06$.	$R_{wp}=4.11\%$, $R_p=3.17\%$, $R_{B(calcite)}=1.20\%$, $R_{B(aragonite)}=1.27\%$, $GOF=1.27$.	$R_{wp}=3.93\%$, $R_p=3.11\%$, $R_{B(calcite)}=0.94\%$, $GOF=1.42$.	$R_{wp}=6.76\%$, $R_p=5.43\%$, $R_{B(calcite)}=1.15\%$, $GOF=1.12$.	/
overall	Conclusion	**A (001)/C=52% (±1.5%) /49%**	**A(001)/C=16%/84% (±1.3%)**	**A(001)/C= 83%(±0.65%)/17 %**	**Calcite**	**Calcite**	**No enough sample**

Table 8 Summary of polystyrene samples of the early cycles. The slash part means samples is not available.

		With Ortho phosphate in water		With Ortho phosphate in water	
	Leg	**Leg1**	**Leg4 (55 °C)**	**Leg5**	**Leg8 (55 °C)**
On substrate	Raw file	d7_02758	d7_02734	d7_02977	d7_09253
	simulation	Aragonite (001)	Aragonite(001), and may other preferred orientation	calcite	No peak observed
	R value	R_{wp} = 0.97%, R_p = 0.76%, $R_{B(aragonite)}$ = 0.24%, GOF = 1.02.	R_{wp} = 2.11%, R_p = 1.67%, $R_{B(aragonite)}$ = 1.21%, GOF = 1.11.	R_{wp}= 1.64%, R_p = 1.28%, $R_{B(calcite)}$ = 0.20%, GOF = 1.36.	/
Powder	Raw files	d7_03926	d7_09185	d7_02906	d7_03909
	simulation	A/C= 99.7% (±0.1%)/0.3%	A/C = 98.50% (±0.06%) /1.5%.	calcite	calcite
	R value	R_{wp} = 4.06%, R_p = 3.18%, $R_{B(aragonite)}$ = 1.20%, GOF = 1.42.	R_{wp} = 9.33%, R_p = 7.45%, $R_{B(calcite)}$ = 1.68%, $R_{B(aragonite)}$ = 1.55%, GOF = 1.07.	R_{wp} = 8.46%, R_p = 6.67%, $R_{B(calcite)}$ = 1.15%, GOF = 1.21	R_{wp} = 5.28%, R_p = 3.99%, $R_{B(calcite)}$ = 1.27%, GOF = 1.30.
overall	**Conclusion**	**A(001)/C= 99.7% (±0.1%) /0.3%**	**A(001)/C= 98.50% (±0.06%) /1.5%**	**Calcite**	**Calcite**

Table 9 Summary of PS samples of excessive cycles. The slash part means samples is not available.

			Without Ortho phosphate in water			With Ortho phosphate in water		
		Leg	**Leg1** Formula only	**Leg4 (55 °C)** Formula only	**Leg3** With HEDP	**Leg5** Formula only	**Leg8 (55 °C)** Formula only	**Leg7** With HEDP
PS (excessive cycle)	On substrate	Raw file	d7_03266	d7_03269	d7_03263	d7_09254	d7_03515	d7_03502
		simulation	Aragonite(001)	Aragonite(001)	No peaks observed	Calcite	Calcite	No peaks observed
			R_{wp} = 2.07%, R_p = 1.56%, $R_{B(aragonite)}$ = 1.43%, GOF = 1.46	R_{wp} = 1.75%, R_p = 1.18%, $R_{B(aragonite)}$ = 0.76%, GOF = 1.62.	/	R_{wp} = 1.71%, R_p = 1.34%, $R_{B(calcite)}$ = 0.27%, GOF = 1.17.	R_{wp} = 1.25%, R_p = 0.99%, $R_{B(calcite)}$ = 0.44%, GOF = 1.26.	/
	Powder	Raw files	d7_03714	d7_03715	/	d7_09251	d7_09233	d7_03922
		simulation	Aragonite	Aragonite	No enough	Calcite	Calcite	Calcite
			R_{wp} = 4.89%, R_p = 3.88%, $R_{B(aragonite)}$ = 2.18%, GOF = 1.85	R_{wp} = 4.64%, R_p = 3.69%, $R_{B(aragonite)}$ = 1.94%, GOF = 1.75.	/	R_{wp} = 6.33%, R_p = 5.04%, $R_{B(calcite)}$ = 1.76%, GOF = 1.28	R_{wp} = 6.70%, R_p = 4.78%, $R_{B(calcite)}$ = 2.29%, GOF = 2.29.	R_{wp} = 4.97%, R_p = 3.95%, $R_{B(calcite)}$ = 0.50%, GOF
	overall	**Conclusion**	Aragonite(001)	Aragonite(001)	No enough sample	**Calcite**	**Calcite**	**Calcite**

Appendix 4

– Supplementary Information Relating to Chapter 4

Table 10 The Ca-Ca distance (< 10 Å) of the calcium carbonate polymorphs and the calcium complexes with candidate inhibitor, calculated by Olex2.

	Polymorphs	~ 4 Å		~ 5 Å	~ 5.5 Å	~ 6 Å	~ 7 Å	~ 8 Å		~ 9 Å	~ 10 Å
CaCO₃	Calcite	4.03		4.99				8.06			9.82
	Aragonite	3.89/3.95/4.11		4.96	5.74	6.06	7.58 / 7.67	7.97/8.06		9.17	9.82
	Vaterite	4.13				5.91 / 5.92	7.15 / 7.16	8.25 / 8.26		9.28/9.4	
Inhibitors											
2-PO₃H₂	0-HEDP	3.79	4.11		5.42		7.58 / 7.62	8.08		9.15	9.79
3-COOH	4-BCA	one calcium only				5.99	7.48			8.89	9.63
	3-CCA	3.96	4.00	5.10				8.10		9.38	9.62
4-COOH	11-BHTCA	3.92			5.82	6.08		7.81			9.79
	6-CHTCA	3.90	3.97	5.13			7.64				9.58
	1-THFTCA	3.97		4.96			7.82	7.93	8.10	9.14	9.86
	2-CPTCA	one calcium only			5.61	5.89		8.12			9.75
6-COOH	14-BHHCA	3.98	4.06					7.95		9.14	9.83
	13-CHHCA	one calcium only						7.92			

TGA Data

June 24 2016
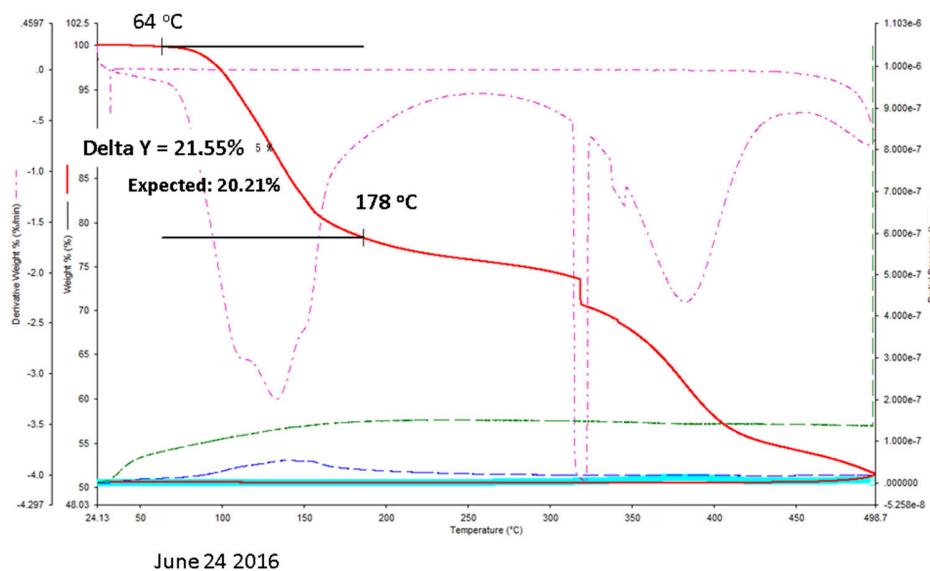
Figure 1 TGA with MS for compound 1. Green line for N₂ and CO. Blue curve and arctic curves are for water and CO₂, respectively. Red and dashed purple line are for thermal curve and derivative curve, respectively.
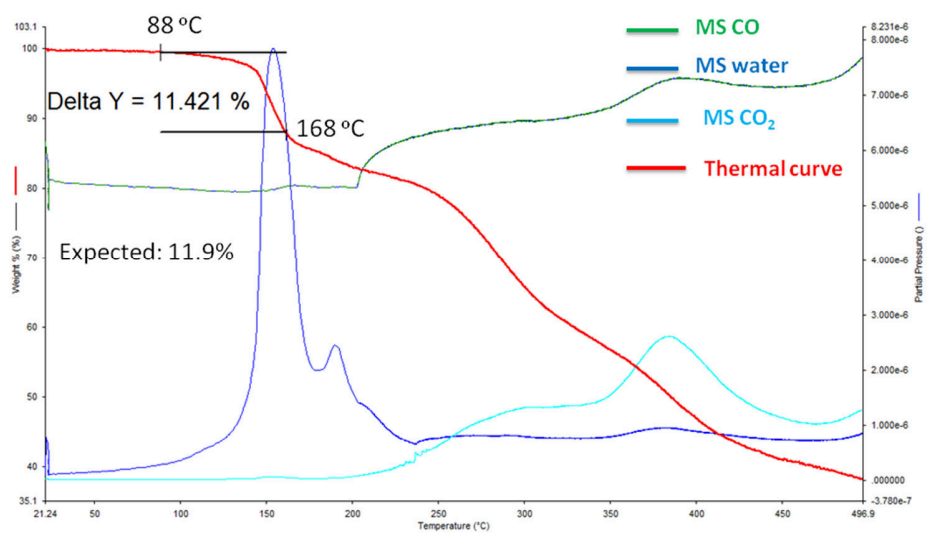
Figure 2 TGA with MS for compound 4. Green line for N₂ and CO. Blue curve and arctic curves are for water and CO₂, respectively. The red curve is for thermal curve and derivative curve, respectively.
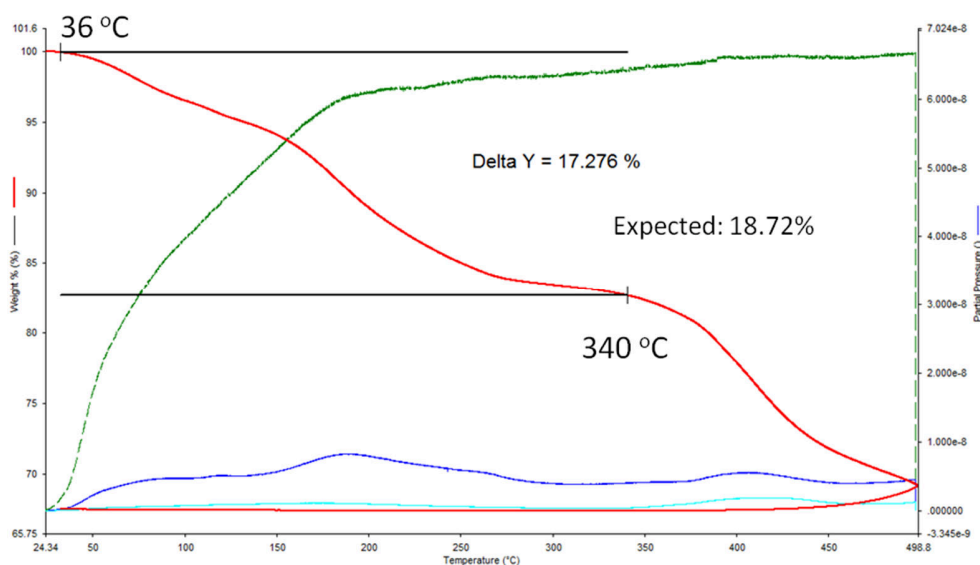
Figure 3 TGA with MS for compound 5. Green line for N₂ and CO. Blue curve and arctic curves are for water and CO₂, respectively. The red curve is for thermal curve and derivative curve, respectively.
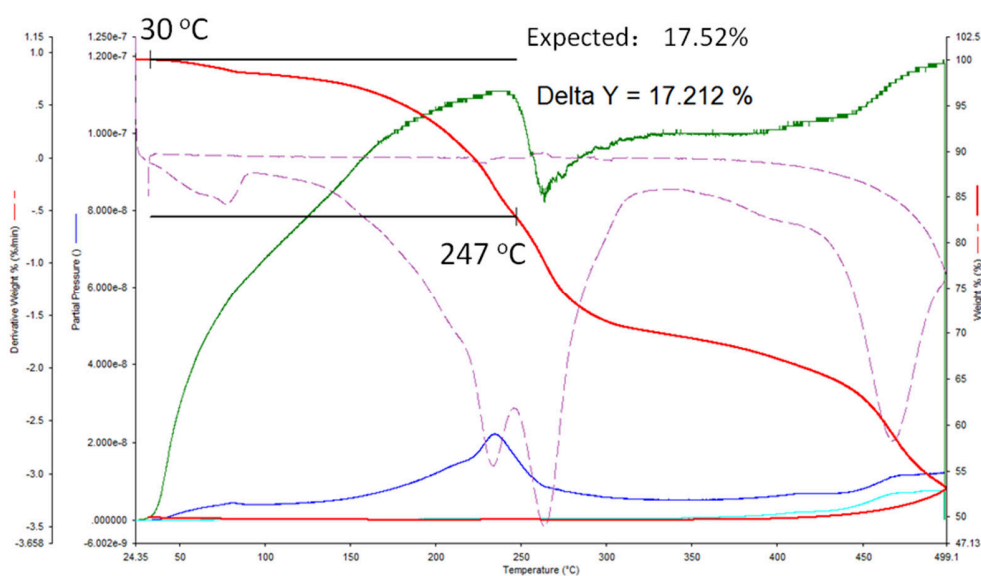
Figure 4 TGA with MS for compound 6. Green line for N₂ and CO. Blue curve and arctic curves are for water and CO₂, respectively. Red and dashed purple line are for thermal curve and derivative curve, respectively.
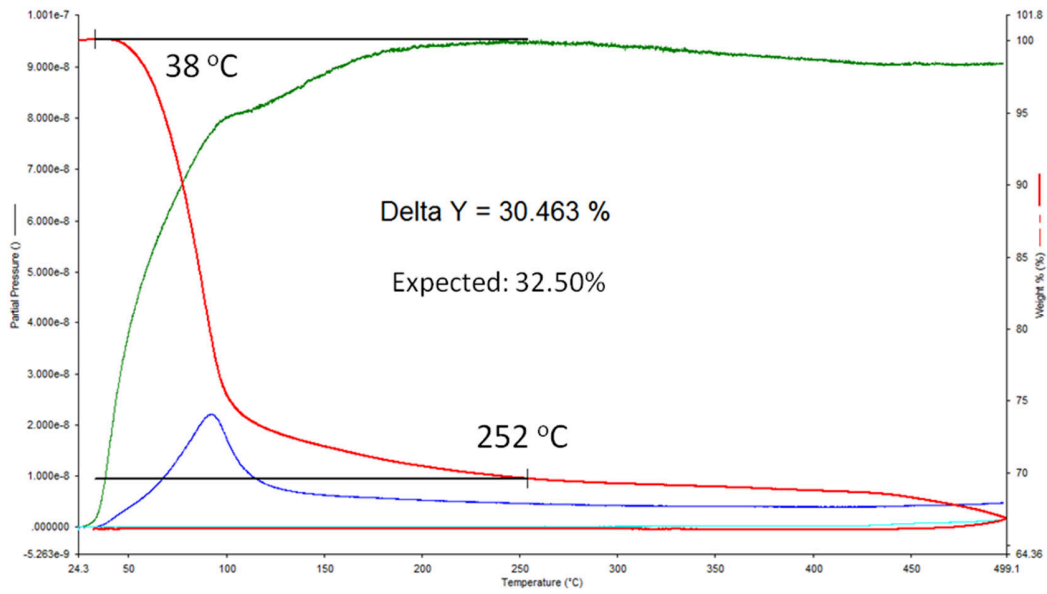
Figure 5 TGA with MS for compound 7. Green line for N$_2$ and CO. Blue curve and arctic curves are for water and CO$_2$, respectively. The red curve is for thermal curve and derivative curve, respectively. The difference in percentage may be due to the loss of free water.
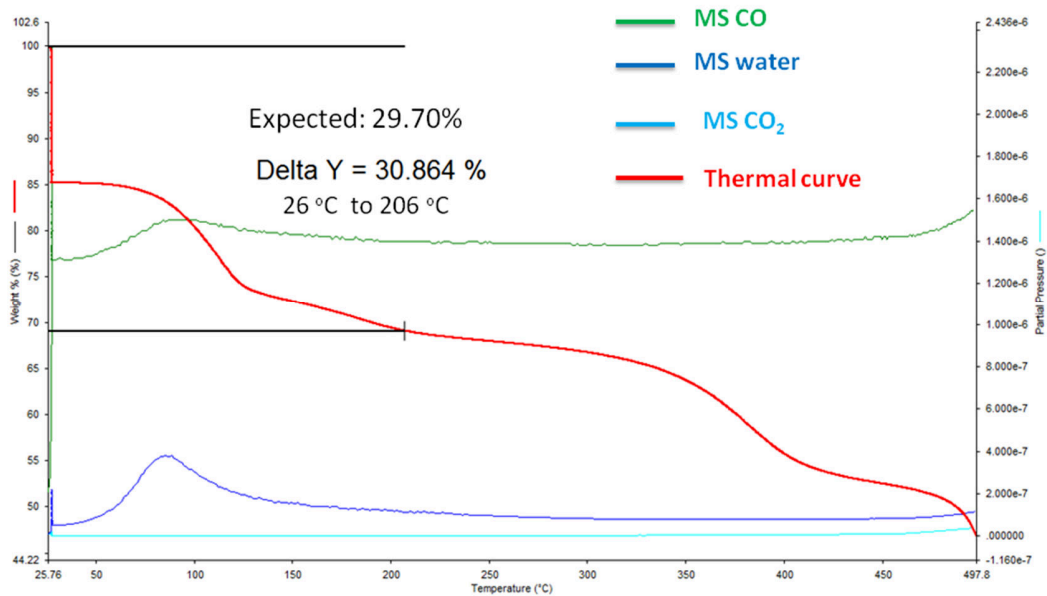
Figure 6 TGA with MS for compound 8. Green line for N$_2$ and CO. Blue curve and arctic curves are for water and CO$_2$, respectively. The red curve is for thermal curve and derivative curve, respectively.

278
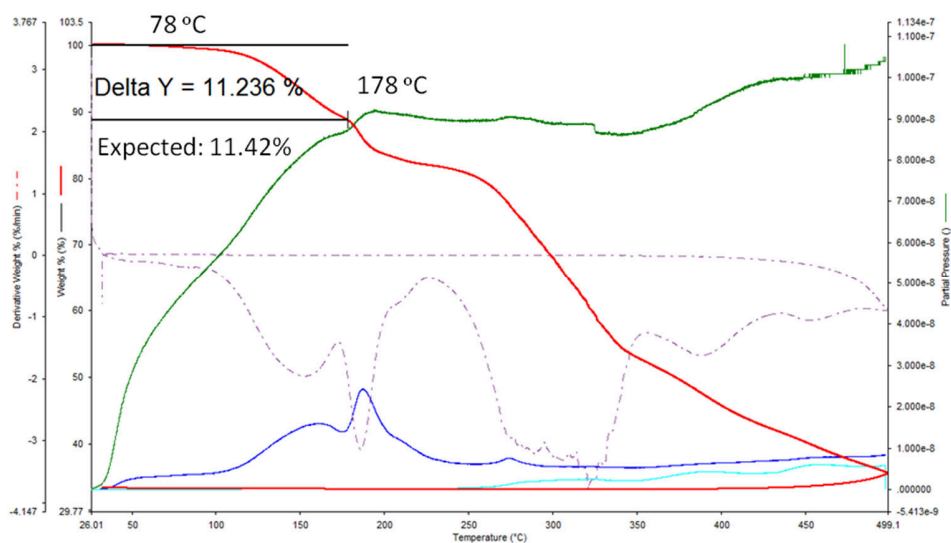
Figure 7 TGA with MS for compound 9. Green line for N₂ and CO. Blue curve and arctic curves are for water and CO₂, respectively. Red and dashed purple line are for thermal curve and derivative curve, respectively.
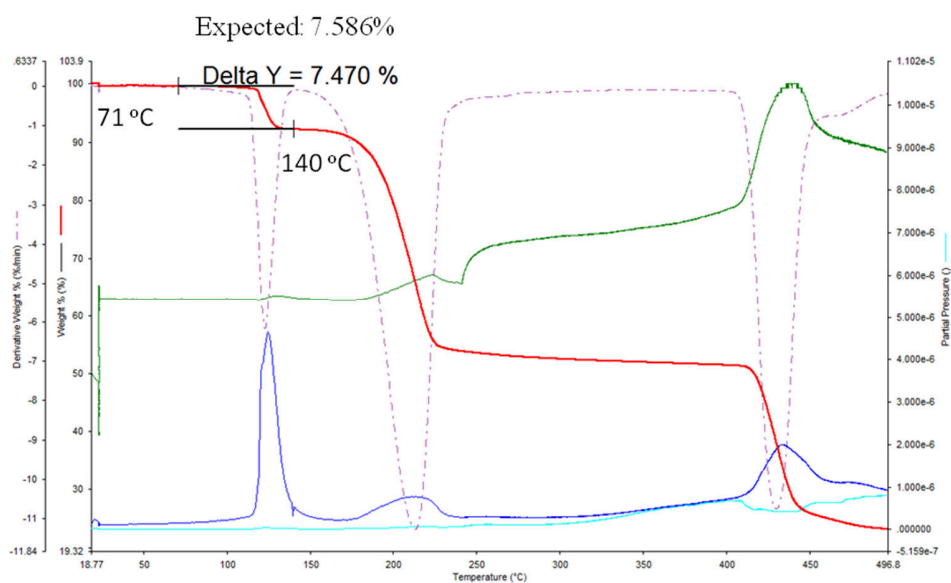
Figure 8 TGA with MS for compound 12. Green line for N₂ and CO. Blue curve and arctic curves are for water and CO₂, respectively. Red and dashed purple line are for thermal curve and derivative curve, respectively.

PXRD Patterns

Crystals 1-4
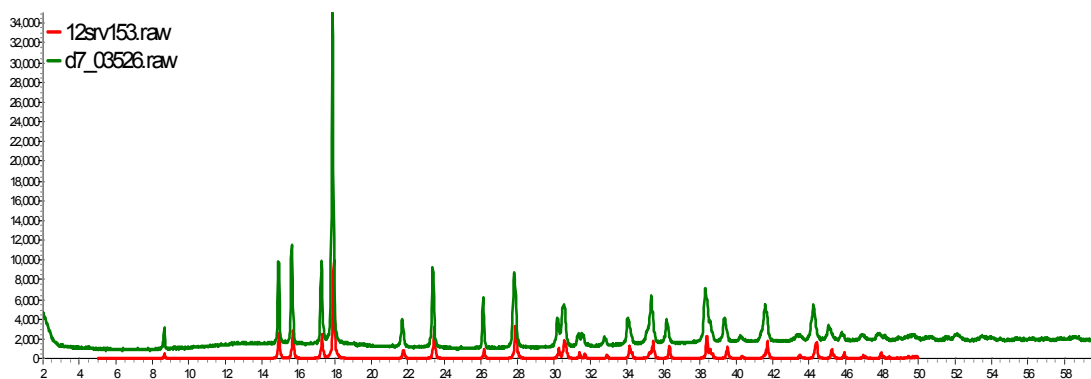
Figure 9 PXRD patterns for compound (1). Experimental pattern and simulated pattern are shown in green and red, respectively. The peak positions correspond well with the results simulated from the single crystal data, indicating the purity of the synthesized samples.
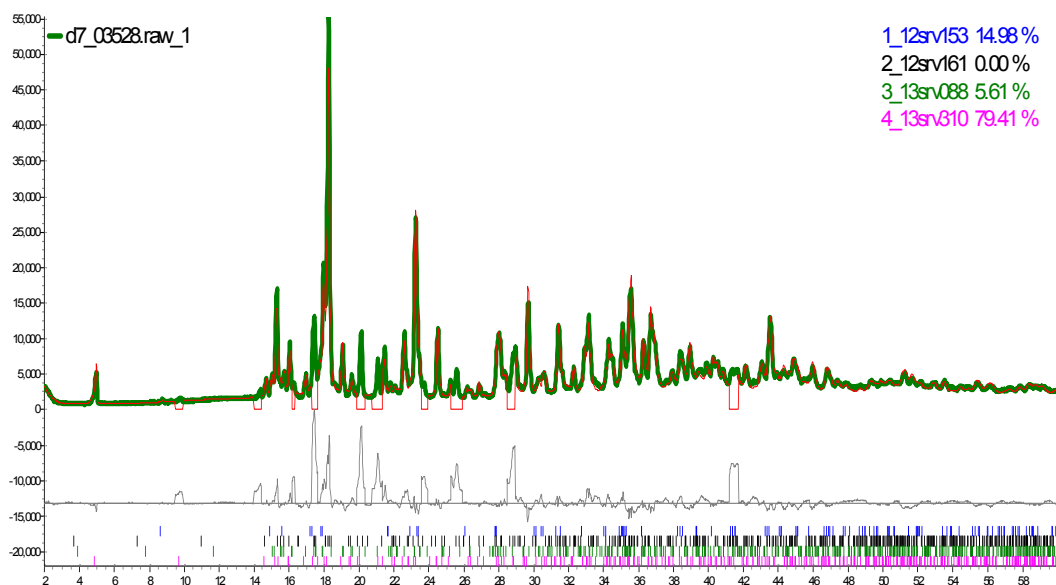
Figure 10 Rietveld refinement indicates a mix of 3 different polymorphs, which are 1, 3 and 4. No polymorph was indicated (P45-2:1, ratio of Ca (OH)$_2$ / CPTCA =2:1). The unit cell of all three polymorphs is refined. Refinement statistics for calcite R_{wp} = 10.8%, R_p = 8.0%, $R_{B(1)}$ = 11.76%, $R_{B(3)}$ = 10.38 %, $R_{B(4)}$ = 8.72 %, GOF = 6.45. The experimental patterns and simulated pattern are shown in green and red, respectively. The difference pattern is shown in grey. The peaks in difference pattern belong to excluded peaks. The excluded peaks belong to the CPTCA acid.
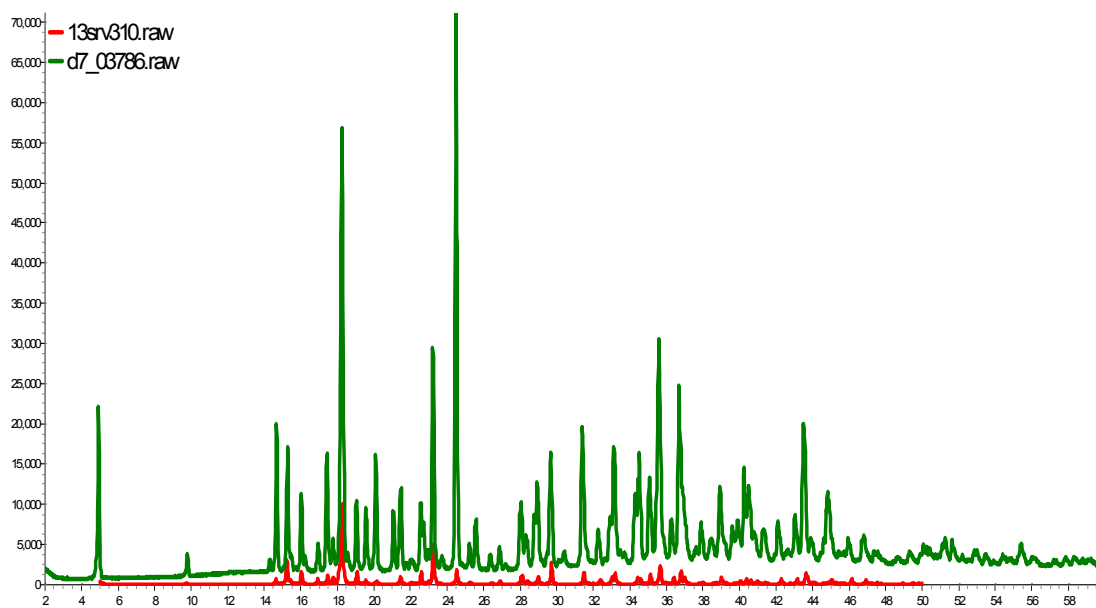
Figure 11 PXRD patterns for compound (4). Experimental pattern and simulated pattern are shown in green and red, respectively. The peak positions correspond well with the results simulated from the single crystal data, indicating the purity of the synthesized samples.

Crystal 5-6
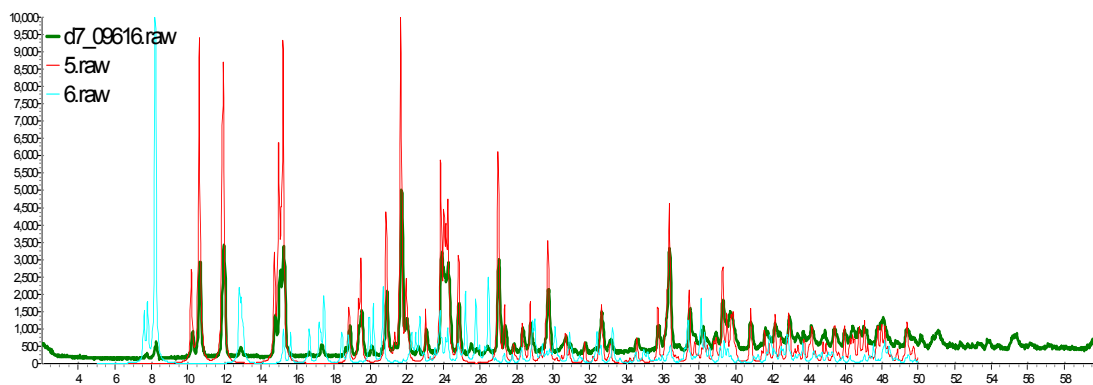
Figure 12 PXRD patterns for compound 5. The peak positions of the experimental pattern correspond well with simulated from the single crystal data of 5 and 6, indicating a mix of 5 and 6 formed in the bulk sample. The experimental pattern and simulated patterns of 5 and 6 are shown in green, red, and arctic, respectively.
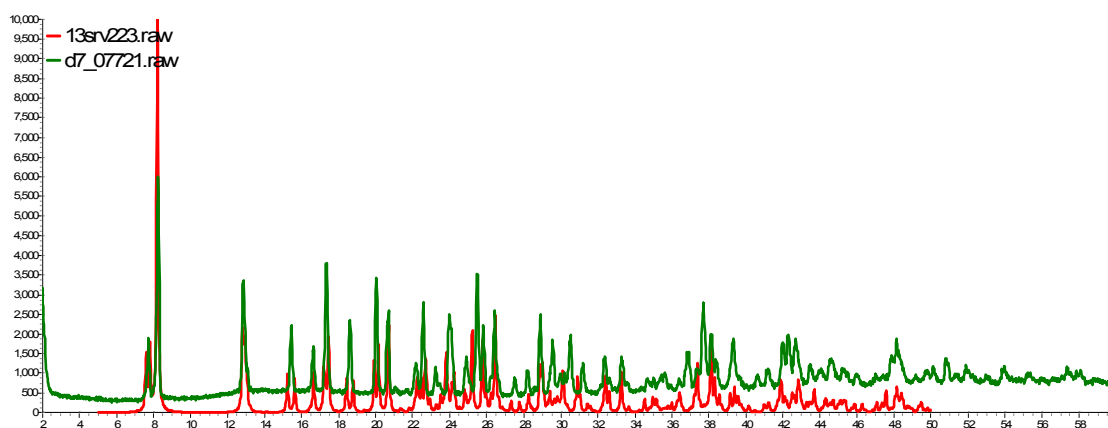
Figure 13 PXRD patterns for compound 6. The peak positions of the experimental pattern correspond well with simulated from the single crystal data, indicating the purity of the synthesized samples. The experimental pattern and simulated pattern are shown in green and red, respectively.

Crystal 7-9
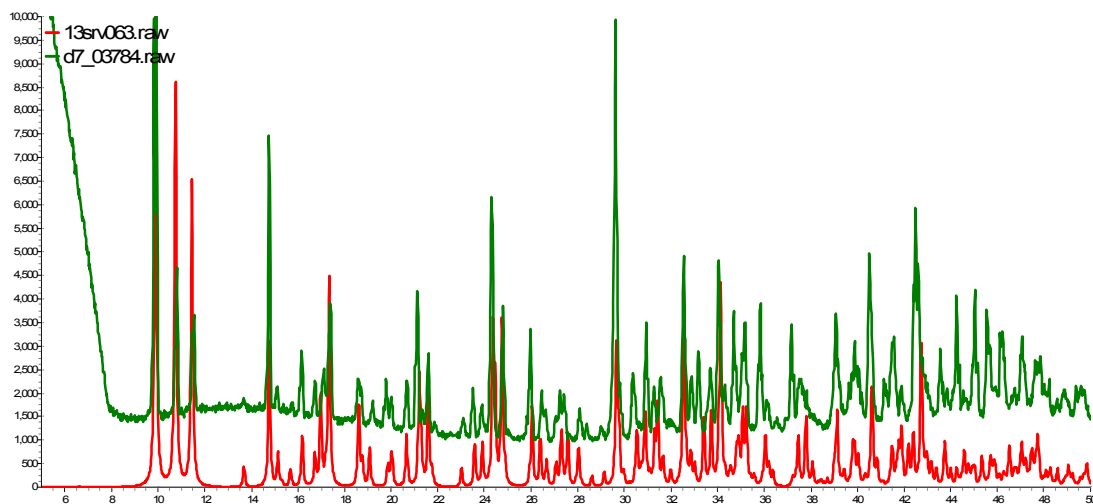
Figure 14 PXRD patterns for compound 7. The peak positions of the experimental pattern correspond well with simulated from the single crystal data, indicating the purity of the synthesized samples. The experimental pattern and simulated pattern are shown in green and red, respectively.
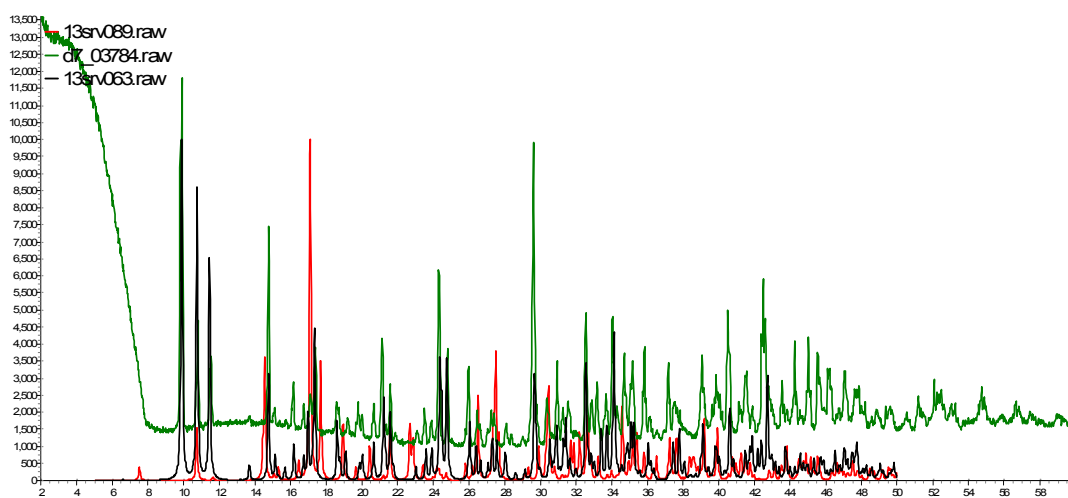
Figure 15 PXRD patterns for compound 8. The peak positions of the experimental pattern show both the presence of the 7 (in black) and 8 (in red). The experimental pattern is shown in green.
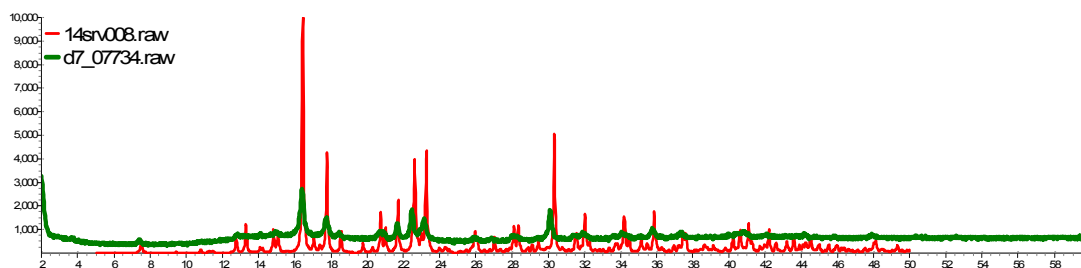
Figure 16 PXRD patterns for compound 9. The peak positions of the experimental pattern correspond well with simulated from the single crystal data, indicating the purity of the synthesized samples. The experimental pattern and simulated pattern are shown in green and red, respectively.

Crystal 12
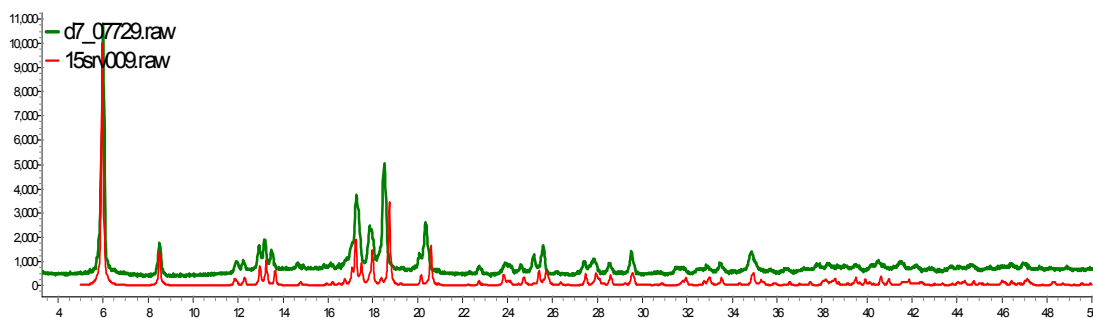
Figure 17 PXRD patterns for compound 12. The peak positions of the experimental pattern correspond well with simulated from the single crystal data, indicating the purity of the synthesized samples. The experimental pattern and simulated pattern are shown in green and red, respectively.

The NMR elucidation for phytic acid

The phytic acid exists in different stereoisomers. The position and the nature of the proton in cyclohexane ring were determined by 1D ^{1}H NMR, 1D ^{13}C NMR, 2D NOESY, 2D COSY, 2D HSQC, 2D HMBC, 2D 31P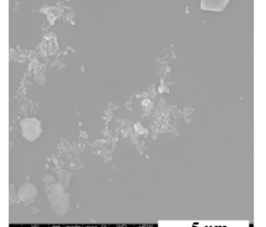 (omega 1)-half-filtered COSY and 2D 31P-relayed COSY spectra. Four different of protons is deduce by combining data from the 1D ^{1}H NMR, 1D ^{13}C NMR, 2D NOESY, 2D COSY, 2D HSQC, and 2D HMBC. The stereoisomers of phytic acid is limited to 2 types of stereoisomers, which is myo- and epi-. The position and the nature of the proton in cyclohexane ring were determined from 2D 31P (omega 1)-half-filtered COSY and 2D 31P-relayed COSY spectra.
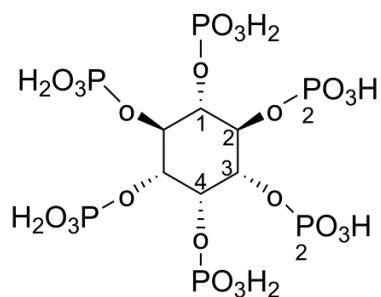
Figure 18 The structure of phytic acid
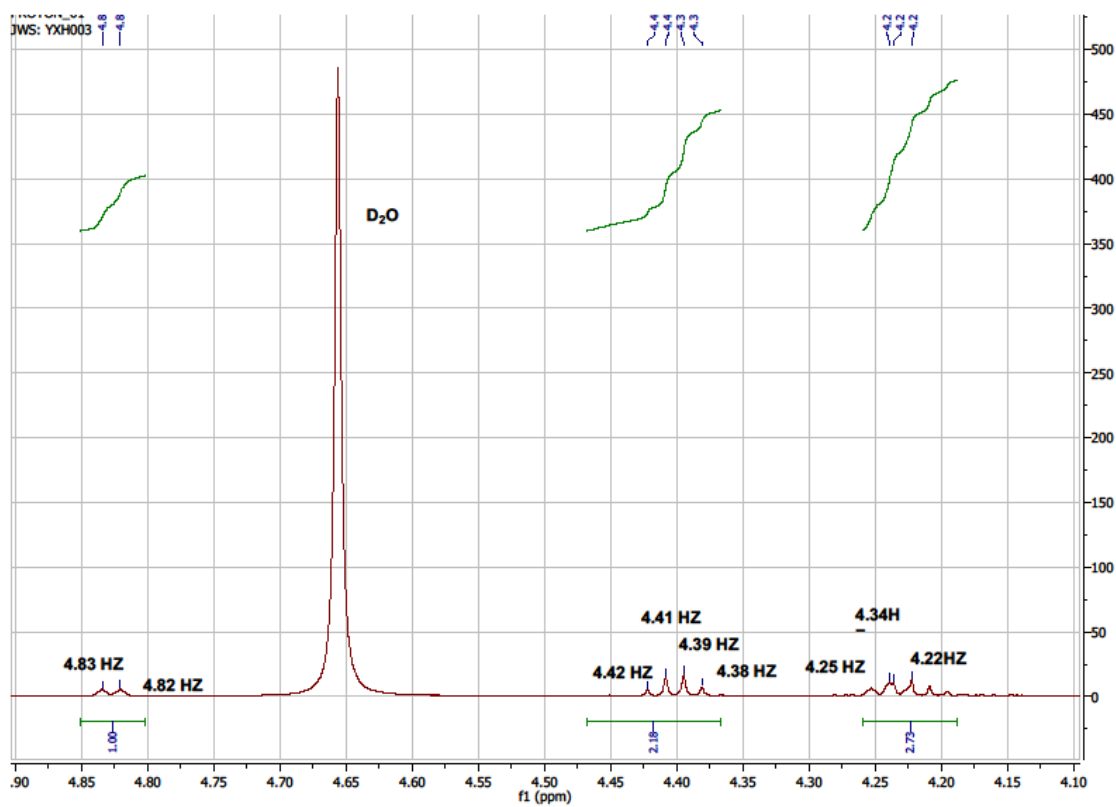
1D ^{1}H NMR
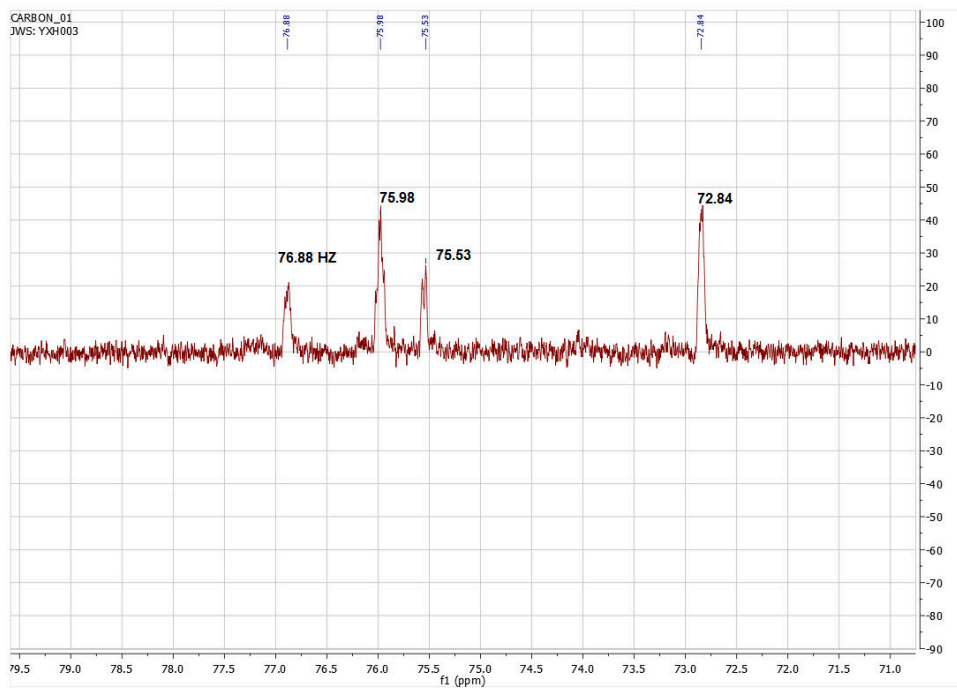
, 1D ^{13}C NMR
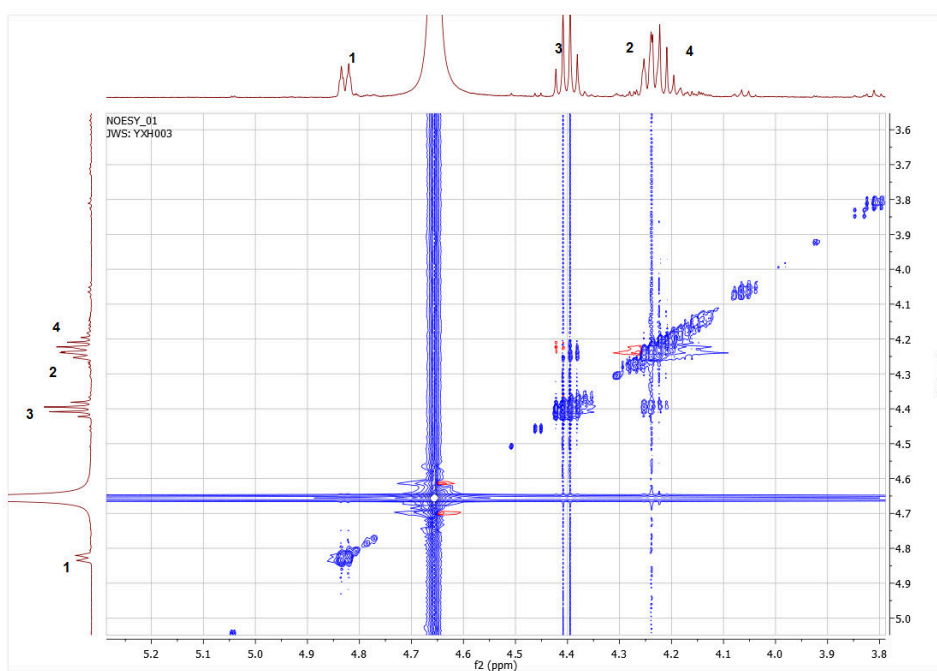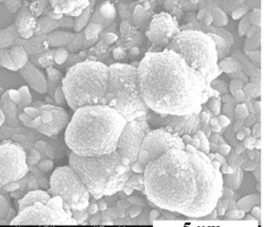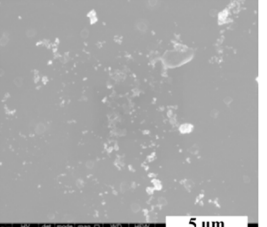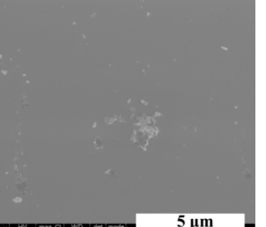

2D NOESY,
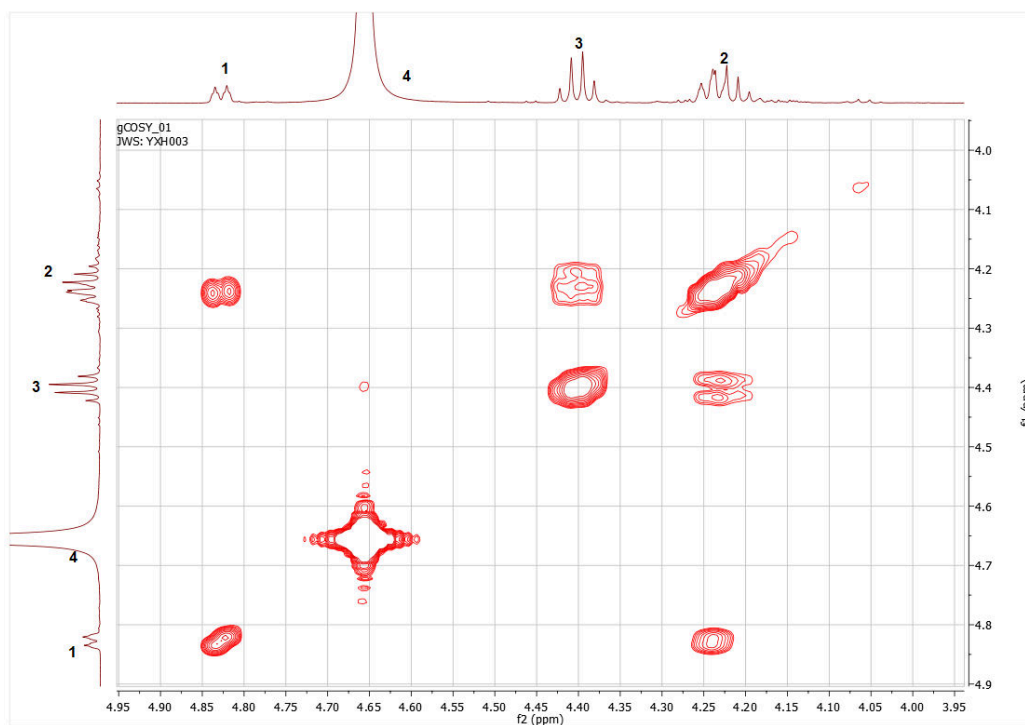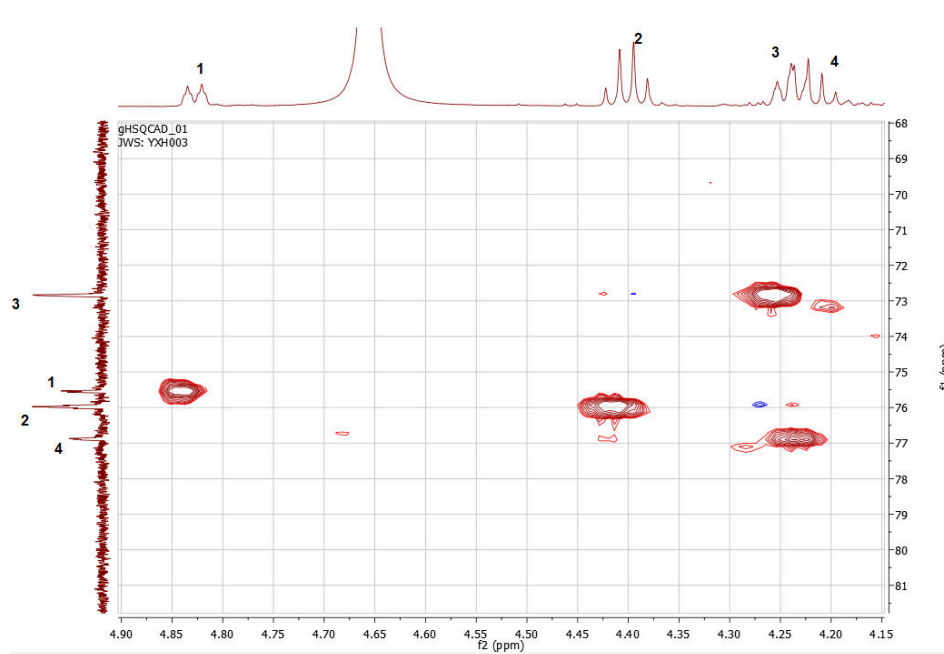
2D COSY,

2D HSQC,
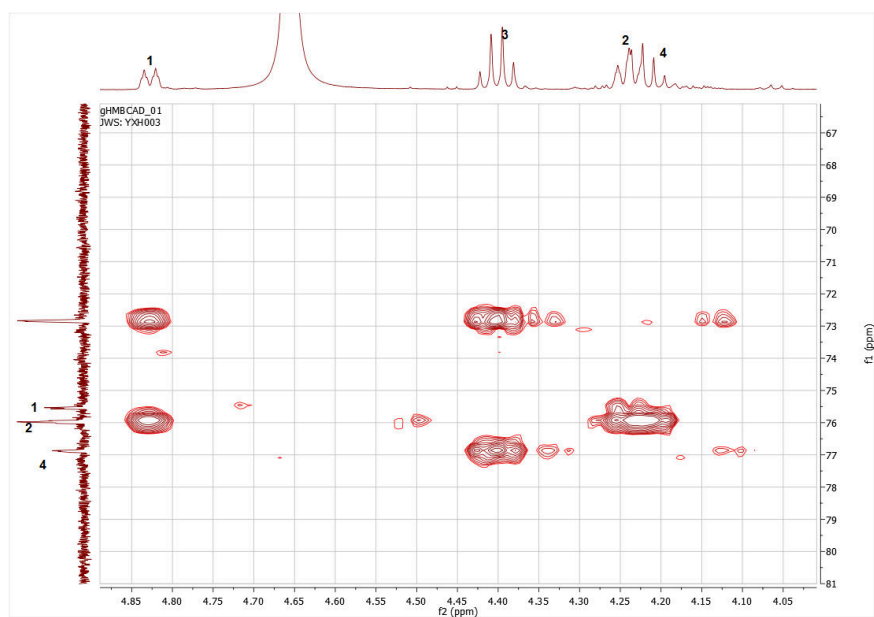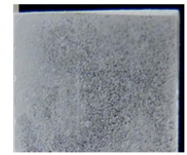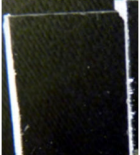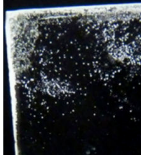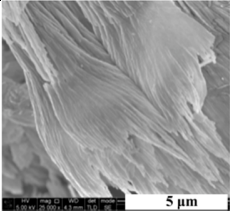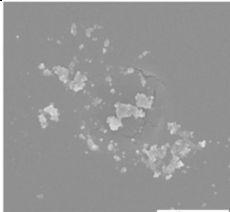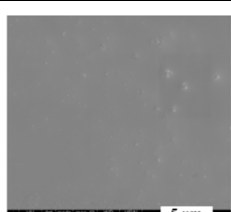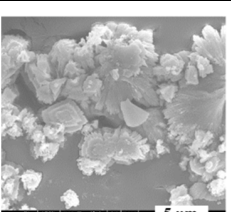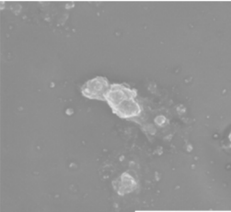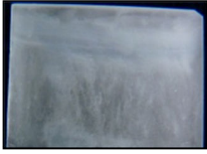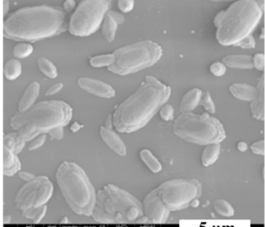
2D HMBC
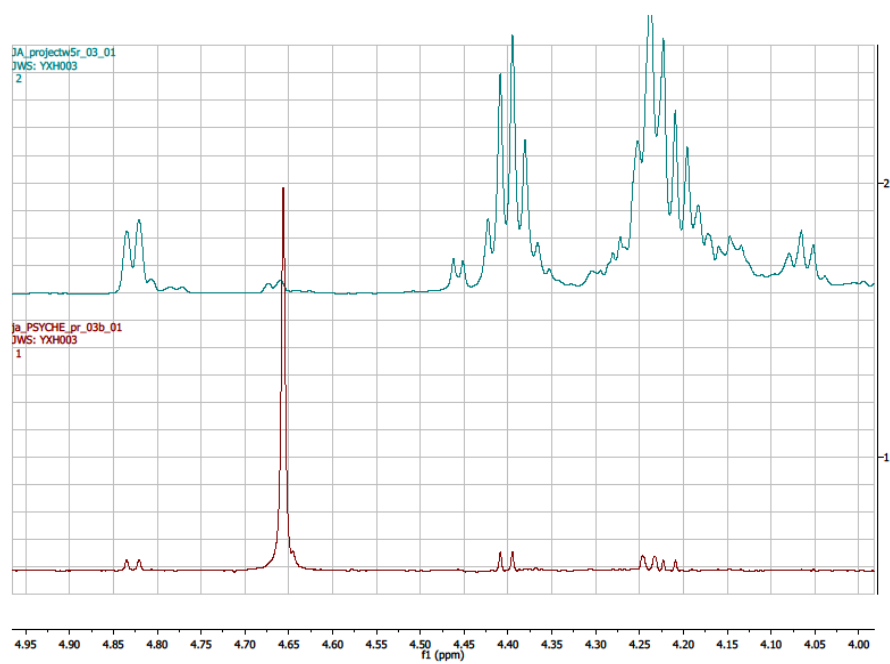
2D 31P (omega 1)-half-filtered COSY and 2D 31P-relayed COSY spectra.

Appendix 5

Table 11 A summary of the effective inhibitors. SEM images were collected with a magnification of 20000X for Chapter 5

	No inhibitor	HEDP	CPTCA	CHHCA	CPTCA+ CHHCA	PA
PMMA	Aragonite (001)^C	ACC-like	ACC-like	A/C=7/2	ACC-like	/
						Not collected
Glass	calcite	ACC-like	Calcite	ACC-like	ACC-like	/
						Not collected

This Ph.D. thesis is accompanied by a CD-ROM which includes crystallographic information for all new crystals for Chapter 4 as res. cif. and doc. Files, which may be viewed using the standard crystallographic software.

The X-ray powder data for Chapter 3 and Chapter 5 are included as raw. and inp. files. The inp. files can be viewed by TXT.

Blank Page